

**CONTROLLED GROWTH OF ZINC OXIDE  
NANOSTRUCTURES FOR MULTIFUNCTIONAL  
APPLICATIONS**

**Ph.D. Thesis**

**By**

**AMIT KUMAR RANA**



**DISCIPLINE OF PHYSICS  
INDIAN INSTITUTE OF TECHNOLOGY INDORE  
JULY, 2018**



**CONTROLLED GROWTH OF ZINC OXIDE  
NANOSTRUCTURES FOR MULTIFUNCTIONAL  
APPLICATIONS**

**A THESIS**

*Submitted in Partial Fulfilment of the Requirements for the  
Award of the Degree of*

**DOCTOR OF PHILOSOPHY**

By

**AMIT KUMAR RANA**

**Roll No. PHD1401151002**



**DISCIPLINE OF PHYSICS**

**INDIAN INSTITUTE OF TECHNOLOGY INDORE**

**JULY, 2018**



*“Research is what I’m doing when I don’t  
know what I’m doing”*

*- Werner von Braun*





## INDIAN INSTITUTE OF TECHNOLOGY INDORE

### CANDIDATE'S DECLARATION

I hereby certify that the work which is being presented in the thesis entitled **CONTROLLED GROWTH OF ZINC OXIDE NANOSTRUCTURES FOR MULTIFUNCTIONAL APPLICATIONS** in the partial fulfilment of the requirements for the award of the degree of **DOCTOR OF PHILOSOPHY** and submitted in the **DISCIPLINE OF PHYSICS, Indian Institute of Technology Indore**, is an authentic record of my own work carried out during the time period from July, 2014 to July, 2018 under the supervision of Dr. Parasharam M. Shirage, Associate Professor and Ramanujan Fellow, Discipline of Physics and Discipline of Metallurgy Engineering and Materials Science.

The matter presented in this thesis has not been submitted by me for the award of any other degree of this or any other institute.

Signature of the student with date  
(**AMIT KUMAR RANA**)

-----  
This is to certify that the above statement made by the candidate is correct to the best of my knowledge.

Signature of Thesis Supervisor with date  
(**Dr. PARASHARAM M. SHIRAGE**)

-----  
**AMIT KUMAR RANA** has successfully given his Ph.D. Oral Examination held on

.....

Signature of Chairperson (OEB)  
Date:

Signature of External Examiner  
Date:

Signature of Thesis Supervisor  
Date:

Signature of PSPC Member #1  
Date:

Signature of PSPC Member #2  
Date:

Signature of Convener, DPGC  
Date:

Signature of Head of Discipline  
Date:

-----



## ACKNOWLEDGEMENTS

*First and foremost, I would like to express my deep and sincere gratitude to my supervisor Associate Professor Dr. Parasharam M. Shirage, IIT Indore, for giving me the opportunity to do research and providing me with profound comments, guidance and constant encouragement, and support throughout my Ph.D. study. His dynamism and enthusiasm towards work have deeply encouraged me to work more energetically and passionately.*

*I would like to extend my sincere gratitude to my PSPC member Prof. K. R. Mavani, HOD, Dr. Preeti Bhoje, Discipline of Physics and Dr. Rupesh S. Devan, MEMS, IITI, for their encouragement and invaluable suggestions. I also thank Dr. S. Sen, Dr. Sunil Kumar and their group for providing suggestions and help during the experimental work.*

*During my Ph.D. years, I was fortunate enough to get financial support from IIT Indore and MHRD, Govt. of India for providing me the fellowship as a teaching assistant. I also owe my sincere thanks to Discipline of Physics, IITI for providing the generous funding, laboratory facilities and rich environment to explore new ideas. I am also grateful to all the academic and administrative staff of IITI for providing practical support with friendly enthusiasm and grace. I thank Mr. Kinney Pandey and Nitin Upadhyay for helping me in the technical works at SIC Indore.*

*I am incredibly grateful to Dr. Rajashree Das with whom I learnt the experimental works. I thank her for her constant encouragement and contribution in accomplishing my research. It has always been a great pleasure for me to work with her. I am also thankful to my friends and lab mates for their co-operation and support during my Ph.D. work.*

*I gratefully acknowledge Dr. P. Rajput, S. N. Jha, D. Bhattacharyya, RRCAT Indore and BARC Mumbai for permitting me to use the facilities at their institute. I would like to acknowledge IISER Bhopal, Pune University, IUC Indore for the various kinds of characterizations facilities. I am also grateful to Prof. G. Neri and S. G. Leonardi, University of Messina, Italy for providing the characterization facilities.*

*I am always thankful to my best buddies Harisankar S., Arvind Khuntia and Dhananjaya Thakur for their moral support during my good as well as awful times and being my constant source of encouragement, tenderness and confidence.*

*Most importantly, I owe my heartfelt gratitude to my immediate family; Mother, Father, and siblings (Dimpal and Sumit) and extended family, without whom none of this will be possible. My family has been a continuous source of love, concern, care and strength during these years.*

*On a very special and personal note I extend regards from the core of my heart to my Maa (Mother) and Papa (Father) for their encouragement and inspiration. It is their love and trust that served as a beacon through the long nights at IITI. I owe you everything!*

**Date: 16/07/2018**

*Amit Kumar Rana*



*Dedicated*

*To my beloved parents*

*Lajwanti Rana & Mahabir Singh Rana*



## LIST OF PUBLICATIONS

### PAPER - 1

**Amit K. Rana**, Yogendra Kumar, Parasmani Rajput, Shambhu Nath Jha, Dibyendu Bhattacharyya, Parasharam M. Shirage, Search for origin of room temperature ferromagnetism properties in Ni doped ZnO nanostructures, *ACS Applied Materials and Interfaces*, **9(8)**, 7691 – 7700, 2017.

### PAPER - 2

**Amit K. Rana**, Prashant Bankar, Yogendra Kumar, Mahendra A. More, Dattatray J. Late, Parasharam M. Shirage, Synthesis of Ni-doped ZnO nanostructures by low temperature wet chemical method and their enhanced field emission properties, *RSC Advances*, **6(106)**, 104318 – 104324, 2016.

### PAPER - 3

**Amit K. Rana**, Rajasree Das, Yogendra Kumar, Somaditya Sen, Parasharam M. Shirage, Growth of transparent  $Zn_{1-x}Sr_xO$  ( $0.0 \leq x \leq 0.08$ ) films by facile wet chemical method: Effect of Sr doping on the structural, optical and sensing properties, *Applied Surface Science*, **379**, 23 – 32, 2016.

### PAPER – 4

Parasharam M. Shirage, **Amit K. Rana**, Yogendra Kumar, Somaditya Sen, S.G. Leonardi, G. Neri, Sr- and Ni-doping in ZnO nanorods synthesized by simple wet chemical method as excellent materials for CO and CO<sub>2</sub> gas sensing, *RSC Advances*, **6(86)**, 82733 – 82742, 2016.

### PAPER – 5

**Amit K. Rana**, Yogendra Kumar, Arjunan M. S., KV Adarsh, Somaditya Sen, Parasharam M. Shirage, Enhancement of two photon absorption with Ni doping in dilute magnetic semiconductor ZnO crystalline nanorods, *Applied Physics Letters*, **107(23)**, 231907, 2015.

### PAPER – 6

**Amit K. Rana**, Yogendra Kumar, Niharika Saxena, Rajasree Das, Somaditya Sen, Parasharam M. Shirage, Studies on the control of ZnO nanostructures by wet chemical method and plausible mechanism, *AIP Advances*, **5(9)**, 097118, 2015.

### PAPER – 7 (equal contribution)

Yogendra Kumar, **Amit K. Rana**, Prateek Bhojane, Manojit Pusty, Vivas Bagwe, Somaditya Sen, Parasharam M. Shirage, Controlling of ZnO nanostructures by solute concentration and its effect on growth, structural and optical properties, *Materials Research Express*, **2(10)**, 105017, 2015.

### PAPER – 8

Rajasree Das, **Amit Kumar**, Yogendra Kuma, Somaditya Sen and Parasharam M. Shirage, Effect of growth temperature on the optical properties of ZnO nanostructures grown by simple hydrothermal method, *RSC Advances*, **5**, 60365-60372, 2015.



## LIST OF CONFERENCE/WORKSHOP ATTENDED

1. Poster presentation at “*19<sup>th</sup> International Workshop on The Physics of Semiconductor Devices (IWPSD)*”, Indian Institute of Technology (IIT) Delhi, India 11<sup>th</sup>-15<sup>th</sup> December 2017.
2. Oral presentation at “*2<sup>nd</sup> International Conference on Advances in Functional Materials*”, Jeju Island, South Korea, 08<sup>th</sup>-11<sup>th</sup> August 2016.
3. Poster Presentation at “*National Conference on Study of Matter Using Intense Radiation Sources and Under Extreme Conditions*”, UGC-DAE Consortium for Scientific Research (UGC-DAE CSR) University Campus, Khandwa Road, Indore, 03<sup>rd</sup>-06<sup>th</sup> November 2016.
4. GIAN workshop on “*High-Pressure Synthesized Materials: A Chest of Treasure and Hints*”, at IIT Indore, 11<sup>th</sup> to 19<sup>th</sup> July 2016.
5. GIAN workshop on “*Chemical Sensors: Principles, Technologies and Applications*”, at IIT Indore, 1<sup>st</sup> to 9<sup>th</sup> July 2016.
6. Poster presentation at “*2<sup>nd</sup> International Conference on Materials Science and Technology (ICMST)*”, St. Thomas college Palai, Kerala, 05<sup>th</sup>-08<sup>th</sup> June 2016.
7. Poster presentation at “*International Conference on Nanoscience and Technology (ICONSAT)*”, Indian Institute of Science Education and Research (IISER), Pune, February 29<sup>th</sup> -2<sup>nd</sup> March 2016.
8. Poster presentation at “*Ramanujan Conclave*”, 22<sup>nd</sup>-23<sup>rd</sup> December, 2015 at IIT Indore.
9. Poster presentation at “*18<sup>th</sup> International Workshop on The Physics of Semiconductor Devices (IWPSD)*”, Indian Institute of Science (IISc), Bangalore, India 7<sup>th</sup>-10<sup>th</sup> December 2015.



## TABLE OF CONTENTS

<b>Acknowledgements</b>	i
<b>List of Publications</b>	v
<b>List of Conference/Workshop Attended</b>	vii
<b>List of Figures</b>	xiii
<b>List of Tables</b>	xxi
<b>Nomenclature</b>	xxiii

### **CHAPTER 1: Introduction to Nanostructured Materials**

1.1. Background and motivation.....	4
1.1.1. Overview of nanostructured materials.....	4
1.1.2. Zinc oxide (ZnO): The material of interest.....	5
1.2. Synthesis/Growth of ZnO nanostructures.....	10
1.3. Application of zinc oxide.....	16
1.4. Scope and goal of thesis.....	17
1.4.1. Thesis objectives.....	17
1.4.2. Thesis outline.....	17
References.....	20

### **CHAPTER 2: Experimental Techniques**

2.1. Wet chemical synthesis: Chemical bath deposition.....	32
2.2. Substrate preparation procedure.....	35
2.3. Analytical characterization tool.....	36
2.3.1. X-Ray diffraction.....	36
2.3.2. X-Ray absorption spectroscopy.....	38
2.3.3. X-Ray photoelectron spectroscopy.....	41
2.3.4. Raman spectroscopy.....	42
2.3.5. UV-Visible spectroscopy.....	45
2.3.6. Photoluminescence spectroscopy.....	46

2.3.7. Field emission scanning electron microscopy.....	47
2.3.8. Transmission electron microscopy.....	49
2.3.9. Secondary ion mass spectroscopy.....	51
2.3.10. Two Photon absorption.....	53
2.3.11. Field electron emission.....	54
2.3.12. Gas sensing experiment.....	56
References.....	58

### **CHAPTER 3: Controlled Growth of Zinc Oxide (ZnO) Nanostructures**

3.1. Materials and Method.....	65
3.2. Results and discussion.....	66
3.2.1. Effect of pH.....	66
3.2.2. Effect of concentration.....	68
3.2.3. Effect of temperature and time.....	73
3.3. Growth mechanism.....	76
3.4. Effect of morphology on optical and vibrational properties of ZnO.....	80
3.5. Summary.....	88
References.....	90

### **CHAPTER 4: Effect of Doping on Zinc Oxide (ZnO) Nanostructures**

<b>4(A). Effect of Strontium (Sr) Doping on ZnO Nanostructures.....</b>	<b>99</b>
4(A).1. Materials and method.....	99
4(A).2. Results and discussion.....	100
4(A).2.1. Morphological properties.....	100
4(A).2.2. Structural properties.....	102
4(A).2.3. Optical properties.....	110
<b>4(B). Effect of Nickel (Ni) Doping on ZnO Nanostructures.....</b>	<b>114</b>
4(B).1. Materials and method.....	115
4(B).2. Results and discussion.....	115
4(B).2.1. Morphological properties.....	115
4(B).2.2. Structural properties.....	117

4(B).2.3. Optical properties.....	125
4.3. Summary.....	129
References.....	131
<b>CHAPTER 5: Multifunctional Applications of Zinc Oxide (ZnO) Nanostructures</b>	
5.1. Multifunctional applications.....	142
5.1.1. Dilute magnetic semiconductor application.....	142
5.1.2. Field emission (FE) application.....	145
5.1.3. Two photon absorption.....	151
5.1.4. Gas sensing application: CO and CO <sub>2</sub> sensing tests.....	155
5.2 Summary.....	165
References.....	167
<b>CHAPTER 6: Conclusion and Scope of Future Work</b>	
6.1. Thesis summary.....	178
6.2. Outlook and future prospects.....	179



## LIST OF FIGURES

### CHAPTER – 1

<b>Figure No.</b>	<b>Figure Caption</b>	<b>Page No.</b>
<b>1.1</b>	Types of nanostructures materials by size: 0D (zero dimensional), 1D (one dimensional), and 2D (two dimensional).	<b>5</b>
<b>1.2</b>	Stick and ball representation of the ZnO crystal structures, cubic rocksalt, cubic zinc blende and hexagonal wurtzite (O = red and yellow ball, Zn = white and dark green ball).	<b>8</b>
<b>1.3</b>	Unique properties and diverse applications of ZnO nanostructures.	<b>16</b>

### CHAPTER – 2

<b>Figure No.</b>	<b>Figure Caption</b>	<b>Page No.</b>
<b>2.1</b>	Schematic diagram of chemical bath deposition.	<b>33</b>
<b>2.2</b>	Scheme of different components of an XRD. The dotted circles represent the goniometer where the sample is placed in the centre. A divergent source of X-rays is focused on the flat plate sample which then diffracted and collected by the detector. The diffraction pattern is recorded by rotating both the source and the detector at an angle $\theta$ , while the sample is kept fixed.	<b>37</b>
<b>2.3</b>	XFAS spectrum with EXAFS and XANES regions.	<b>39</b>
<b>2.4</b>	Schematic of the X-ray photoelectron spectroscopy showing its basic components.	<b>42</b>
<b>2.5</b>	Raman transitional scheme (a) An electron is excited from ground state and falls back to the original position (b) An electron is excited from the ground state and falls to a vibrational level (c) An electron is excited from a vibrational level and falls to the ground level.	<b>44</b>
<b>2.6</b>	Schematic diagram of UV-Visible spectrophotometer.	<b>45</b>
<b>2.7</b>	Schematic diagram of Photoluminescence spectrometer.	<b>47</b>
<b>2.8</b>	Schematic representation of electron-sample interaction in an SEM.	<b>48</b>

2.9	Schematic representation of electron-sample interaction in a TEM.	50
2.10	Ion ejection process in SIMS.	52
2.11	Illustration of single photon absorption (left) and two photon absorption (right) for a sample.	54
2.12	Schematic of field emission set up.	55
2.13	Schematic of the gas sensing setup used for the detection of various gases.	56
 <b>CHAPTER - 3</b>		
<b>Figure No.</b>	<b>Figure Caption</b>	<b>Page No.</b>
3.1	Technique for synthesis of nanomaterial top-down and bottom-up approach.	64
3.2	Represent the XRD pattern of the ZnO nanostructure of different pH (a) Zn1 (pH=9), (b) Zn2 (pH=10), (c) Zn3 (pH=11), (d) Zn4 (pH=12).	67
3.3	SEM images of ZnO nanostructure at different pH (a, a1) pH-9, (b, b1) pH-10, (c, c1) pH-11, and (d, d1) pH-12.	68
3.4	XRD patterns of ZnO nanostructure different concentrations, (a) 50 mM, (b) 100 mM, (c) 150 mM, (d) 200 mM, (e) 250 mM, inset of figure shows the relative position of (002) peak (*related to Zn(OH) <sub>2</sub> phase).	69
3.5	(a) Rietveld refinement of ZnO film deposited at a concentration of 250 mM, (b) The lattice parameter variation in ZnO films at different concentrations.	70
3.6	SEM images of ZnO deposited on glass substrates at different concentrations of (a) 50 mM, (b) 100 mM, (c) 150 mM, (d) 200 mM, and (e) 250 mM.	71
3.7	Schematic diagram representing the effect of concentration on the growth process of the ZnO nanostructures.	72
3.8	(a) Typical cross sectional TEM image of a single ZnO nanorod inset of figure shows selected area electronic diffraction (SAED) pattern of the nano-rod structure, (b) The	73

	HRTEM image of nano-rod (arrow indicates the growth direction of the nano-rod).	
<b>3.9</b>	(a) XRD pattern of ZnO grown at different temperature (a) ZN1 (70°C) (b) ZN2 (80°C) (c) ZN3 (90°C) (d) ZN4 (100°C) (e) ZN5 (110°C) (f) ZN6 (120°C) nanostructures, (b) shows the relative shift in (002) peak position.	<b>74</b>
<b>3.10</b>	(a) Rietveld refinement of ZnO deposited at 90°C with deposition time of 120 min. (b) The effect of deposition temperature on lattice parameter of ZnO.	<b>74</b>
<b>3.11</b>	FESEM images of ZnO nanostructures (a) ZN1 (b) ZN2 (c) ZN3 (d) ZN4 (e) ZN5 (f) ZN6 for deposition time of 120 min.	<b>75</b>
<b>3.12</b>	Schematic diagram (a) shows idealized growth process of nano-rod with tapered tip. Schematic diagram of growth of (b) Nano-needle (c) Splitting of nano-rod into small nano-rods (d) layer formation along <i>c</i> -axis (e) Nanotube.	<b>77</b>
<b>3.13</b>	ZnO film deposited at 70°C with deposition time (a) 30 min (b) 60 min (c) 90 min (d) 120 min and 120°C with deposition time (e) 30 min (b) 60 min (c) 90 min (d) 120 min.	<b>79</b>
<b>3.14</b>	FESEM images of nanostructures (a) Formation of the needle like structure at 70°C for 120 min and (b) rod like structure at 120°C for 30 min (c) tubes at 120°C for 120 min. The SEM clearly indicates the screw dislocation nucleation mechanism as marked at the central part of the rods and tubes.	<b>80</b>
<b>3.15</b>	Room temperature UV-Vis reflection spectra of ZnO nanostructures. Inset image shows (a) Tauc plot of ZN1 and (b) Variation in bandgap with synthesis temperature.	<b>81</b>
<b>3.16</b>	(a) Room temperature UV-Vis reflection spectra measured on ZnO nanostructures films deposited on the glass substrates at different concentrations, (b) shows the variation on band gap of ZnO nanostructures with concentration.	<b>81</b>

3.17	Room temperature PL spectra of ZnO grown at different temperatures.	82
3.18	(a) Room temperature normalized PL spectra of ZnO deposited at different concentrations, (b) Room temperature PL spectra (Black dots), Gaussian fitting curves (Green) and summation of Gaussian Creve (red line) of ZnO film grown at 200 mM concentration.	83
3.19	(a) PL spectra of ZnO deposited at 90°C temperature. The “■” shows experimental data. Solid green and red lines are Gaussian fitting of individual peaks and sum of all peaks, respectively. (b) Schematic band diagram of ZnO nanostructure for ZN3.	84
3.20	RT Raman spectra of ZnO nanostructures synthesized at different temperature.	85
3.21	RT Raman spectra of concentration dependent ZnO nanostructure films.	86

#### **CHAPTER - 4**

<b>Figure No.</b>	<b>Figure Caption</b>	<b>Page No.</b>
4.1	Field Emission Scanning Electron Microscopy (FESEM) of (a) ZnO and (b) Sr-doped ZnO thin films.	100
4.2	(a-f). TEM and HRTEM images of $Zn_{1-x}Sr_xO$ ( $0.0 \leq x \leq 0.08$ ) of (a-b) $x=0$ , (c-d) $x=0.04$ and (e-f) $x=0.08$ respectively.	101
4.3	Elemental mapping of 8% Sr doped ZnO nanorod, (a) Zn, (b) O and (c) Sr. Inset of (a) shows Selected Area Electron Diffraction (SAED) of ZnO nano-rod.	102
4.4	XRD patterns of (a) undoped ZnO, (b) $Sr_{0.02}ZnO$ , (c) $Sr_{0.04}ZnO$ , (d) $Sr_{0.06}ZnO$ , and (e) $Sr_{0.08}ZnO$ thin films.	103
4.5	The variation of ZnO lattice parameters, ‘a’ and ‘c’ as a function of Sr doping concentration. Inset of the figure shows corresponding change in lattice volume with Sr doping concentration.	103
4.6	Secondary Ion Mass Spectroscopy (SIMS) of $Zn_{1-x}Sr_xO$ ( $0.0 \leq x \leq 0.08$ ) nano-rods films with $x = 0, 0.02, 0.04, 0.08$ .	105

<b>4.7</b>	XPS spectra of the (a) O1s peak in undoped ZnO film, (b) O1s peak in Zn <sub>0.92</sub> Sr <sub>0.08</sub> O film (c) Zn2p peak in ZnO and Zn <sub>0.92</sub> Sr <sub>0.08</sub> O film and (d) Sr 3p peak in Zn <sub>0.92</sub> Sr <sub>0.08</sub> O film.	<b>106</b>
<b>4.8</b>	Room temperature Raman spectra of Zn <sub>1-x</sub> Sr <sub>x</sub> O (0.0 ≤ x ≤ 0.08) thin films. Inset shows the relative shift of E <sub>2</sub> <sup>high</sup> mode with respect to Sr concentration in the films.	<b>108</b>
<b>4.9</b>	(a) Room temperature PL spectra of un-doped ZnO thin films. The “■” shows experimental data and solid green and red lines are Gaussian fitting of individual peaks and sum of all peaks respectively, (b) Schematic band diagram for ZnO thin film.	<b>112</b>
<b>4.10</b>	Experimental data for room temperature PL spectra of Zn <sub>1-x</sub> Sr <sub>x</sub> O (0.0 ≤ x ≤ 0.08) thin films. Inset shows the change in relative intensity of E <sub>3</sub> (V <sub>Zn</sub> related peak) and E <sub>5</sub> (O <sub>in</sub> related peak) peak with Sr doping concentration in the films.	<b>113</b>
<b>4.11</b>	Represents the FESEM images of (a) ZnO: Ni 0%, (b) ZnO: Ni 5%, (c) ZnO: Ni 7.5%, (d) ZnO: Ni 10%, and (e) ZnO: Ni 12.5% (scale at 200 nm).	<b>116</b>
<b>4.12</b>	Shows the (a) Rietveld refined XRD patterns of (a-a) ZnO (a-b) ZnO: Ni 5% (a-c) ZnO: Ni 7.5% (a-d) ZnO: Ni 10% and (a-e) ZnO: Ni 12.5%, (b) Displays the shift in 2θ after Ni doping in the diffraction peak corresponds to (002) peak, (c) Displays the variation in lattice parameter “a” and “c” (in unit Å) of pure and Ni doped ZnO.	<b>118</b>
<b>4.13</b>	(a) Shows the change in the average bond length (in Å) and unit cell volume (in Å <sup>3</sup> ), (b) displays the corresponding change in micro-strain (ε) value, and (c) represents the change in the R (degree of distortion) with increasing the Ni concentration.	<b>119</b>
<b>4.14</b>	Ni doped ZnO nanostructures (a) Normalized XANES data at Zn K-edge, (b) k <sup>2</sup> -weighted χ(k) spectra at Zn K-edge, (c) Normalized XANES data at Ni K-edge, and (d) k <sup>2</sup> -weighted χ(k) spectra at Ni K-edge. The χ(k) data has been vertically shifted for clarity.	<b>121</b>
<b>4.15</b>	Fourier transform of k <sup>2</sup> -weighted of (a) Zn K-edge, (b) Ni K-edge, for Ni doped ZnO nanostructure. The symbol shows empirical data and solid lines are the best fitting data. The curves are vertically shifted for clarity.	<b>122</b>

<b>4.16</b>	Displays (a) RT Raman spectra of pure and Ni doped ZnO (b) The Raman shift in the $E_2^{\text{high}}$ peak. (c) Shows the Raman peak of the additional mode ( $AM_1$ ).	<b>123</b>
<b>4.17</b>	UV-Vis absorbance spectra of pure and Ni doped ZnO nanostructure. Inset figure shows the relative variation in bandgap between pure and Ni doped ZnO.	<b>126</b>
<b>4.18</b>	(a) Demonstrates the RT Photoluminescence spectra of $Zn_{1-x}Ni_xO$ ( $0 \leq x \leq 12.5$ ) and (b) Displays RT- PL spectra of Ni 5% doped ZnO. The red dots display experimental data, green lines Gaussian fitting and black line sum of all fitted peaks.	<b>127</b>
<b>4.19</b>	Shows Room temperature PL spectra of (a) ZnO (b) Ni 7.5% doped ZnO (c) Ni 10% doped ZnO (d) Ni 12.5% doped ZnO. The black dots shows experimental data, solid green and red lines are Gaussian fitting of individual peaks and sum of all peaks, respectively ( $\uparrow$ arrow indicate the presence of $E_{10}$ peak in ZnO samples).	<b>128</b>

## **CHAPTER – 5**

<b>Figure No.</b>	<b>Figure Caption</b>	<b>Page No.</b>
<b>5.1</b>	(a) M-H plot at 80 K showing the hysteresis loop for pure and Ni doped ZnO nano structure and (b) Shows the M-H plot of Ni 5% doped ZnO at 80 K, 150 K and 300 K and inset shows M-H plot of ZnO at 300 K.	<b>145</b>
<b>5.2</b>	Shows Field emission of pure and Ni doped ZnO. (a) Applied electrical field as a function of emission current density, (b) Fowler-Nordheim (F-N) plot.	<b>147</b>
<b>5.3</b>	Shows the schematic (a) Electronic structure of transition metal at a substitution site in a wurtzite structure, (b) Splitting of impurity state under the influence of crystal field of host ZnO, energy band diagram of (c) ZnO, (d) Ni doped ZnO ( $E_g$ : Energy gap, $E_f$ : Fermi level, $E_c$ : Energy of Conduction band, $E_v$ : Energy of Valance band, $\phi$ : work function).	<b>148</b>

<b>5.4</b>	Shows typical field emission current stability recorded at 5 $\mu$ A indicating stable field emission current of (a) pure ZnO, (b) Ni 5% doped ZnO, (c) Ni 7.5% doped ZnO, and (d) Ni 10% doped ZnO (inset of figures show field emission pattern taken during the long term current stability measurements of the emitter).	<b>150</b>
<b>5.5</b>	(a) Open aperture Z scan curves of the samples, (b) Normalized transmittance as a function of input intensity, (c) Variation of $\beta$ (left axis) and optical limiting threshold intensity (right axis) as function Ni doping (bottom axis) and bandgap (top axis), (d) Optical limiting curve for the samples and the dashed line shows the linear absorption regime. The solid line represents the theoretical fit.	<b>153</b>
<b>5.6</b>	Photograph of the sensor device and micrograph of the sensing film surface. Inset shows a high magnification of the highly porous sensing film surface.	<b>157</b>
<b>5.7</b>	Dynamic responses of sensors: (a) ZO, (b) Sr8ZO, (c) Ni10ZO, (d) Ni5ZO.	<b>159</b>
<b>5.8</b>	Dynamic responses of sensors (a) ZO and (b) Sr8ZO, to 200 ppm of CO at 200°C.	<b>159</b>
<b>5.9</b>	Sensor responses (a) 1% CO <sub>2</sub> (b) 200 ppm CO, (c) 10% O <sub>2</sub> at different temperatures.	<b>160</b>
<b>5.10</b>	(a) Dynamic response towards different CO concentrations and (b) calibration curve at 250°C related to Ni5ZO sensor.	<b>162</b>
<b>5.11</b>	(a) Dynamic response towards different CO <sub>2</sub> concentrations and (b) calibration curve at 250°C related to Sr4ZO sensor. (c) Comparison of the response of Sr4ZO sensor to CO and CO <sub>2</sub> , at different temperatures.	<b>162</b>
<b>5.12</b>	N <sub>2</sub> adsorption/desorption isotherms of pure and doped ZnO (inset show the corresponding pore size distribution curve).	<b>164</b>
<b>5.13</b>	Sensor response as a function of lattice distortion for Ni-doped ZnO.	<b>165</b>



## LIST OF TABLES

### CHAPTER – 1

Table No.	Table Caption	Page No.
1.1	Physical parameters of ZnO.	9
1.2	Summary of methods for obtaining zinc oxide nanostructure.	12

### CHAPTER - 3

Table No.	Table Caption	Page No.
3.1	The value of average crystallite size and strain ( $\epsilon$ ) for the ZnO nano structures grown at different concentration obtained by Scherer's method and Williamson-Hall method.	70
3.2	The value of crystallite size and strain ( $\epsilon$ ) for the ZnO nano structures grown at different deposition temperature obtained by two methods: Scherer's equation and Williamson-Hall method.	75
3.3	Phonon mode frequencies (in units of $\text{cm}^{-1}$ ) of wurtzite ZnO films deposited at different temperatures (ZN1-ZN6).	87
3.4	Summary the Phonon mode frequencies (in units of $\text{cm}^{-1}$ ) of wurtzite ZnO films deposited at different concentrations.	88

### CHAPTER - 4

Table No.	Table Caption	Page No.
4.1	Refined structural parameters for $\text{Zn}_{1-x}\text{Sr}_x\text{O}$ ( $0.0 \leq x \leq 0.08$ ) thin film.	104
4.2	Atomic percentage of Zinc, Oxygen and Strontium measured by XPS.	107
4.3	Phonon mode frequencies (in units of $\text{cm}^{-1}$ ) of wurtzite $\text{Zn}_{1-x}\text{Sr}_x\text{O}$ ( $0.0 \leq x \leq 0.08$ ) thin films.	109
4.4	The peak position and relative peak intensity of deconvoluted PL spectra of $\text{Zn}_{1-x}\text{Sr}_x\text{O}$ ( $0.0 \leq x \leq 0.08$ ) thin films. Peak position (nm) and relative intensity (%) have the errors $\pm 1$ .	114
4.5	EDAX analysis of Ni-doped ZnO samples.	116

<b>4.6</b>	Refined structural parameters for $\text{Zn}_{1-x}\text{Ni}_x\text{O}$ ( $0.0 \leq x \leq 0.125$ ) thin film. (Error in $10^{-4}$ order in refined parameters).	<b>118</b>
<b>4.7</b>	From the Zn K-edge EXAFS data fitting, we have obtained variation of CN (co-ordination number), R (bond distance) and $\sigma^2$ (Debye-Waller factor). The amplitude reduction factor ( $S_0^2$ ) and $\Delta E$ were obtained from pure ZnO fitting $1.05 \pm 0.08$ and $1.9 \pm 0.5$ , respectively and kept fixed for all the samples. The numbers in parentheses indicate the uncertainty in the last digit.	<b>122</b>
<b>4.8</b>	Structural parameters CN (co-ordination number), R (bond distance) and $\sigma^2$ (Debye-Waller factor) obtained from Ni K-edge EXAFS data fitting. Similar to Zn K-edge, the amplitude reduction factor ( $S_0^2$ ) and $\Delta E$ were obtained from pure NiO fitting $1.01 \pm 0.06$ and $1.8 \pm 0.6$ , respectively and kept fixed for all the samples. The numbers in parentheses indicate the uncertainty in the last digit.	<b>122</b>
<b>4.9</b>	Phonon mode frequencies of wurtzite $\text{Zn}_{1-x}\text{Ni}_x\text{O}$ ( $0 \leq x \leq 0.125$ ) nanostructure (in units of $\text{cm}^{-1}$ ).	<b>124</b>
<b>4.10</b>	The peak position and relative peak intensity of deconvoluted PL spectra of Ni doped ZnO sample. Peak position (nm) and relative intensity (%) have the errors $\pm 1$ .	<b>127</b>

**CHAPTER – 5**

<b>Table No.</b>	<b>Table Caption</b>	<b>Page No.</b>
<b>5.1</b>	Comparison of field emission characteristics of pure and Ni doped ZnO nanostructures.	<b>147</b>
<b>5.2</b>	Comparison of field emission characteristics of the pure and doped ZnO nanostructure with the present work.	<b>151</b>
<b>5.3</b>	Experimentally calculated values of $E_g$ , $\beta$ , and limiting threshold.	<b>153</b>
<b>5.4</b>	Comparison of ZnO nanorods-based CO sensors.	<b>163</b>
<b>5.5</b>	Surface area values for the synthesized samples.	<b>164</b>

## NOMENCLATURE

### A

A Ampere

Ag Silver

Al Aluminium

Au Gold

### B

BET Brunauer-Emmett-Teller

BMP Bound magnetic polaron

### C

C Carbon

Cr Chromium

Cu Copper

CB Conduction band

CBD Chemical bath deposition

CVD Chemical vapour deposition

### D

D Donor

DI Deionized water

DMS Dilute magnetic semiconductor

### E

EDX Energy dispersive x-ray

EXAFS Extended x-ray absorption fine structure

$E_g$  Energy gap

### F

FESEM Field emission scanning electron microscopy

FTO Fluorine doped tin oxide

FE Field emission

$F_L$  Fermi level

### G

GaN Gallium nitride

### I

ITO Indium tin oxide

### M

M Molarity

**N**

**N<sub>2</sub>** Nitrogen  
**Ni** Nickel

**O**

**O<sub>2</sub>** Oxygen  
**OPV** Organic photovoltaic

**P**

**PC** Personal computer  
**PET** poly (ethylene terephthalate)  
**PL** Photoluminescence

**R**

**RT** Room temperature

**S**

**SEM** Scanning electron microscopy  
**SIMS** Secondary ion mass spectrometry  
**Sr** Strontium

**T**

**TEM** Transmission electron microscopy  
**Ti** Titanium  
**TiO<sub>2</sub>** Titanium dioxide

**U**

**UV** Ultraviolet

**V**

**VB** Valence band

**W**

**W** Watt

**X**

**XPS** X-Ray photoelectron spectroscopy  
**XRD** X-Ray diffraction  
**XANES** X-ray Absorption Near Edge Structure

**Z**

**ZnO** Zinc oxide

*Physical Constants and Conversion Factors*

<b>Avogadro's number</b>	$N_A = 6.02 \times 10^{23}$ molecules/mole
<b>Boltzmann's constant</b>	$k = 1.38 \times 10^{-23}$ J/K, $8.62 \times 10^{-5}$ eV/K
<b>Electronic charge (magnitude)</b>	$q = 1.6 \times 10^{-19}$ C
<b>Electronic rest mass</b>	$m_e = 9.11 \times 10^{-31}$ kg
<b>Planck's constant</b>	$h = 6.63 \times 10^{-34}$ J.s, $4.14 \times 10^{-15}$ eV.s
<b>Speed of light</b>	$c = 3 \times 10^8$ m/s, $3 \times 10^{10}$ cm/s

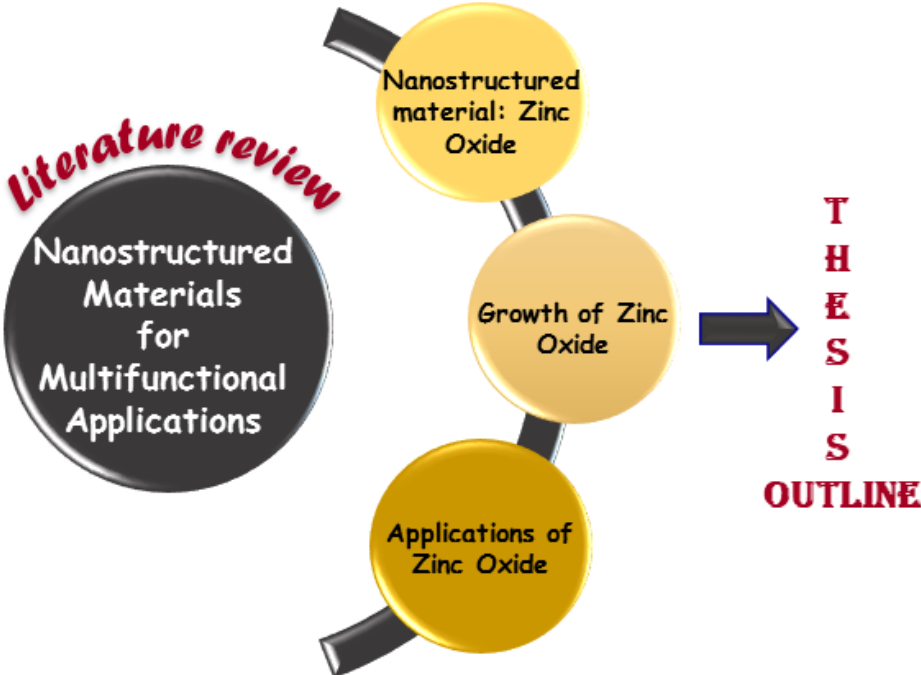
**Prefixes:**

1 Å (angstrom) = $10^{-10}$ m	milli-, m- = $10^{-3}$
1 μm (micron) = $10^{-6}$ m	micro-, μ- = $10^{-6}$
1 nm (nano) = $10^{-9}$ m	nano-, n- = $10^{-9}$
2.54 cm = 1 in.	pico-, p- = $10^{-12}$
1 eV = $1.6 \times 10^{-19}$ J	kilo-, k- = $10^3$
	mega-, M- = $10^6$



# CHAPTER 1

## Introduction to Nanostructured Materials





# 1

---

## Introduction to Nanostructured Materials

*In this chapter, a brief literature review on the current research on nanostructured materials is presented. It covers the topics related to inorganic nanomaterials including the design, properties, and applications associated with them. Also, the material(s) which are concerned to this thesis are highlighted. This section summarizes the controlled growth of Zinc Oxide (ZnO) nanostructures including the challenges and puzzles associated with its design, fabrication, and performance. Additionally, a brief description of the processing technique adopted in this thesis is highlighted which is based on wet chemical routes. Finally, it covers a precise overview of the diverse applications of nanostructured materials where prime focus is devoted to zinc oxide based multifunctional applications.*

## 1.1. Background and Motivation

### 1.1.1. Overview of Nanostructured materials

In the last few decades nanoscience and nanotechnology are one of the most important branches of science. The term “Nano” in science, engineering, and technology is regularly used and defined as the size of the matter about 1 to 100 nm. The idea and concept of “Nano” came into the picture in late 1959, which is firstly presented by the Nobel laureate physicist Richard Feynman’s on his famous talk “There’s Plenty of Room at the Bottom” at an American Physical Society meeting in California Institute of Technology. Since then applications of nanotechnology in its commercial version of cosmetics, food products, and electronics have been extensively delved in. These applications are limited to the bulk use of nanomaterials. Being a special class of matter, “*Nanomaterials*” with the constituents having nanometer range dimensions are regarded as the materials of 21<sup>st</sup> century taking into consideration its property combination and design uniqueness that are limits of the conventional bulk materials and monolithic. “Nature is a master chemist with incredible talent” stated in an article titled “Nano sandwiches” in Chemistry in Britain (1998) [1] mentioned that researchers are learning from nature to master the use of nanomaterials. Following this quest of learning, scientists stemmed into introducing various types of nanostructures for developing a new and advanced generation of materials.

Centuries have passed since the scientists are endeavouring to understand the field of inorganic semiconductor physics through rigorous experiments and theoretical approaches [2, 3]. Among the various semiconducting materials, wide bandgap inorganic metal oxides emerge as an essential class of materials which are acknowledged to cover the science of the upcoming materials research [4]. Over the decades, rapid and advanced progress have been made in the field of metal oxides, followed by the perpetual discovery of various new and intriguing form of nanostructured metal oxides (Figure 1.1) such as nanoparticles, nanoribbons, nanoflakes, nanotubes, nanosheets, nanoflowers, nanowires, nanorods, *etc.* [5-10].

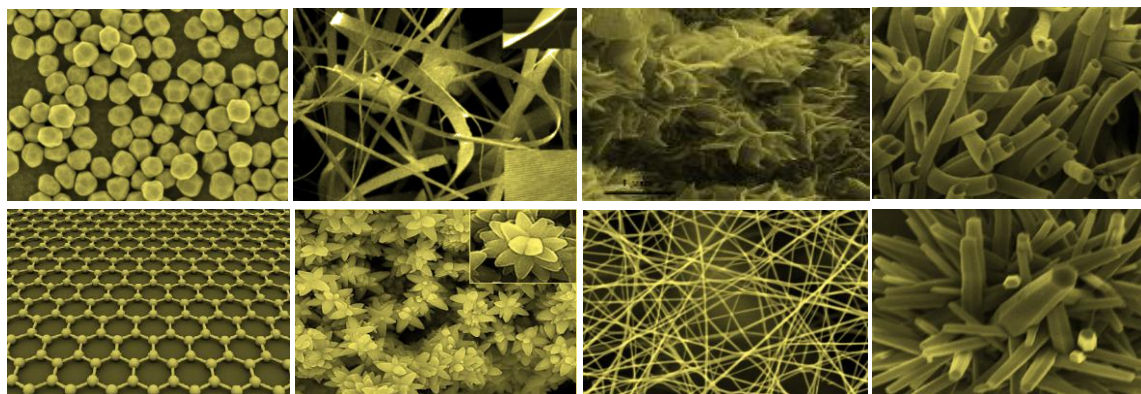


**Figure 1.1.** Types of nanostructures materials by size: 0D (zero dimensional), 1D (one dimensional), and 2D (two dimensional) [5-10].

Molecular and atomic level manipulation of the individual components building a nanomaterial is considered as one of the most tactical aspects of the growth of nanostructures and their varied application fields [11, 12]. The understanding of the importance of this class of nanomaterials comes by the fact that they are non-toxic, degradable and biocompatible compounds making their possible field of application very diverse ranging from electronic devices to protective garments and aerospace.

### 1.1.2. Zinc oxide (ZnO): The Material of Interest

**Literature Survey:** Research on ZnO is going on for many decades with interest following a roller-coaster pattern. ZnO has rich literature as it is not new in the field of inorganic semiconductors. Research on different configurations to design ZnO nanostructures are carried out way back in time in the early 1900s [13-20]. The first description of ZnO structure is reported in the year 1935 by C. W. Bunn [13] where the lattice parameters of ZnO are studied. Similarly, a detailed optical study of ZnO is done by Mollwo [15] in the year 1954, whereas Damen *et al.* [16] have done the Raman scattering studies for vibrational properties in 1966. The renewed interest in ZnO is fuelled and fanned by its prospects in optoelectronics applications owing to its direct wide band gap of 3.4 eV at room temperature which can be effectively modulated to 2.8–4.5 eV by doping. Additionally, it has large exciton energy of 60 MeV and efficient radiative recombination. The strong exciton binding energy, which is much larger than that of GaN (25 meV), and the thermal energy at room temperature (25 meV) can ensure an efficient exciton emission at room temperature under low excitation energy. As a consequence, ZnO is recognized as a promising photonic material in the blue-UV region. ZnO is also established to show

unique optical properties, such as optical absorption, transmission, reflection, photoluminescence and so on. Because of these two promising properties, ZnO has been highlighted as a strong candidate in the field of optoelectronics, such as UV sensors, photodiodes, light emitting diodes (LEDs), solar cells, *etc.* From the applied materials ground, various interfaces/contacts of ZnO are explored. The surface barrier study was done by C. A. Mead [17] in 1965. In parallel, the demonstration of LEDs by I. T. Drapak [18] was done in 1968. Furthermore, the growth of ZnO by chemical-vapour transport is reported by Galli and Coker [19] in 1970. Minami *et al.* [20] demonstrated the metal-insulator semiconductor structure in 1974. A year later, the *n-p* junction (ZnO/ZnTe) is accomplished in 1975 by Tsurkan *et al.* [21]. From the similar ground, Al/Au ohmic contacts were reported in 1978 by L. J. Brillson [22]. Very high quality whiskers and platelets, the nomenclature that gave way to the nanostructure, of late, have been prepared early on and used to deduce much of the principal properties of this material (ZnO), particularly the optical properties. The field is also powered by theoretical predictions and perhaps experimental confirmation of ferromagnetism at room temperature for potential spintronics applications during the 1980s. Of paramount importance is the transparency of ZnO to visible light that is in part responsible for exploring this material for applications in transparent ohmic contacts for light emitters based on GaN, solar cells that have been gaining considerable interest, transparent thin-film transistors, and nanostructures that can be used to extract light from LEDs such as those based on GaN. Furthermore, highly piezoelectric nature of ZnO and its favourable electromechanical coupling coefficient also emerge as an attractive alternative for devices such as surface acoustic waves during the 1990s till date. A few groups have reported the *n*-type and *p*-type ZnO by doping with different elements such as aluminium, gallium, indium, nitrogen, phosphorus (P), arsenic, and antimony (Sb) [23-38]. Zhang *et al.* [39] ascribed *n*-type doping for ZnO by native defects and provide an idea to achieve it. Similarly, Hapiuk *et al.* [40] have studied *p*-doping in ZnO sodalite by state-of-the-art calculations, and proposed that endohedral doping of cage-like structures was a promising method for achievement of *p*-doping in ZnO, even up to degenerate levels and O, F, Cl, Br, Te, and I were good possible candidates. Nitrogen is considered as a good candidate to obtain *p*-type ZnO. However, the solubility of nitrogen in ZnO is low, resulting in the low hole concentration. Some groups have reported co-doping method for obtaining the

*p*-type ZnO. Yamamoto *et al.* [41] also proposed a co-doping approach to obtain low resistivity *p*-type ZnO (which can increase acceptor solubility and make acceptor levels shallower). Based on the work of Yamamoto *et al.*, many groups have carried out co-doping using different dopants, such as Al-Ga with Nitrogen [42], N-Ag [43], N-P [44], P-In [45], N-Zr [46], N-B [47], Fe-N [48] and N-Mg [49] to obtain *p*-type ZnO, theoretically and experimentally. Successful *p*-type doping for ZnO nanostructures will greatly enhance their future applications in nanoscale electronics and optoelectronics [50]. Similarly, the magnetic behaviour of ZnO is one of the most controversial topic of debate till now, whether ZnO is ferromagnetic or not or it is intrinsic or extrinsic property and what is its Curie temperature ( $T_C$ )? The answers to these doubts have opened the novel use of ZnO in the field of spintronics [51-54]. The idea of diluted magnetic semiconductors (DMS) was first predicted by Dielt *et al.* [54] with the *p*-type wide band gap semiconductor GaN and Mn doped ZnO. Similarly Sato *et al.* [55, 56] by theoretical calculation, based on local density approximation shows ferromagnetic ordering with  $T_C$  above room temperature for *n*-type ZnO with doping of V, Cr, Co, Fe and Ni. Apart from the prediction of Dielt *et al.* and Sato *et al.* with results of last few decades which have displayed that doping of transition metal (TM) elements such as Cu, Ni, Co, Fe, Mn, *etc.* in a wide-gap semiconductor provides not only possible ferromagnetism properties but also tuning of optical properties as well in a single material [57-60].

Compiling all the pioneering research works on ZnO nanostructures, the magical genius of this material arises from its unique and remarkable properties which are listed below:

- It has a wide direct bandgap (3.37 eV at 300 K) and thus is receiving renewed attention for device applications as it has comparable bandgap (3.4 eV at 300 K) to GaN. It also has a larger exciton binding energy. The high exciton binding energy of 60 meV (which is larger than the thermal energy at room temperature) leads to excitonic emission at room temperature and above. In this regard, ZnO is considered as a promising photonic material for UV/blue devices such as short wavelength light emitting diodes and laser diodes in optoelectronics.
- ZnO is a semiconducting as well as piezoelectric material. It shows a high degree of surface "activity" in terms of interacting via ad- and chemi-sorption with the surrounding ambient. It is known as key technological material and leads to

potential applications in field emission displays, gas sensors, nano-resonators, and nano-cantilevers, *etc.*

- ZnO naturally forms a wide variety of nanostructures using a range of growth techniques, including nanorods, nanotubes, nanoflakes, nanowires, nanobelts, nanoflower, *etc.* These structures in many cases display a degree of crystal perfection, which is far better than that of thin films, even on lattice mismatched surfaces. In combination with above properties, this wide range of high crystal perfections nano-morphologies open more potential applications.
- *P*-type ZnO is predicted to display spin polarized carrier behaviour when doped with magnetic impurities and as such is a promising material for spintronics applications.
- ZnO is bio-safe and biocompatible, and it can be directly used for biomedical applications without coating.

***Crystal Structure:*** Zinc oxide is an II-VI compound semiconductor. It can crystallize in a variety of crystal structures including wurtzite, zincblende and rock salt as presented in Figure 1.2.

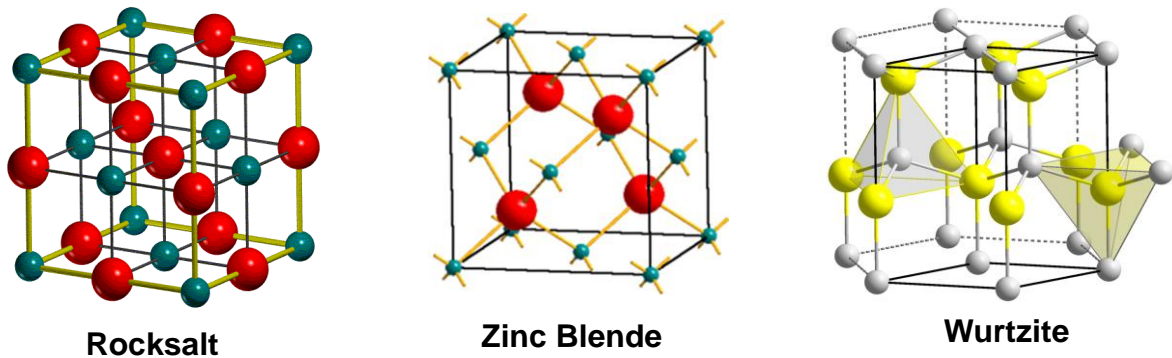


**Figure 1.2.** Stick and ball representation of the ZnO crystal structures, cubic rocksalt, cubic zinc blende and hexagonal Wurtzite (O= red and yellow ball, Zn= white and dark green ball) [61].

In general, ZnO has a stable hexagonal wurtzite structure at optimum pressure and temperature. In an ideal wurtzite crystal, the structure is composed of two interconnecting hexagonal close-packed (hcp) sub-lattice in a hexagonal lattice, each of which consisted of one of the  $\text{Zn}^{2+}$  and  $\text{O}^{2-}$  atom along the threefold *c*-axis involving  $sp^3$  covalent bonding where each anion is surrounded by four cations at the corners of a tetrahedron. A schematic representation of the wurtzite ZnO structure is shown in Figure 1.2. The lattice parameters,  $a_0 = 0.32495$  nm and  $c_0 = 0.52069$  nm, in the ratio of  $c_0/a_0 = 1.602$ , which is

close to the ideal value of 1.633 expected for the hcp unit cell, and it belongs to the space group of  $P6_3mc$ . In addition to intrinsic material properties, the lattice parameters are affected by extrinsic properties such as the free electron concentration (via the deformation potential of the conduction band minimum), the concentration of impurities with different ionic radii which can replace the host atom, substrate-induced strain, and temperature. The Zn-O bond length is 1.992 Å in the direction parallel to the  $c$ -axis of the hexagonal unit cell and 1.973 Å in the other three directions of the tetrahedral arrangement.

**Table 1.1.** Physical parameters of ZnO [50, 62-64].

Property	Value
Molecular formula	ZnO
Molar mass	81.4084 g/mol
Appearance	Amorphous white or yellowish white powder.
Odour	Odourless
Stable phase at 300 K	Wurtzite
Density	5.606 g/cm <sup>3</sup>
Melting point	1975 °C
Boiling point	2360 °C
Solubility in water	0.16 mg/100 mL
Thermal conductivity	0.6, 1-1.2
Refractive index	2.0041
Lattice Constants	$a_0 = 3.2469 \text{ \AA}$ , $c_0 = 5.2069 \text{ \AA}$ , $c_0/a_0=1.602$
Relative Dielectric Constant	8.66
Energy Gap	3.374 eV, Direct
Intrinsic Carrier Concentration	$< 10^6 /\text{cc}$
Exciton Binding Energy	60 meV
Electron effective mass	0.24
Electron mobility (at 300 K) for low n-type conductivity	200 cm <sup>2</sup> /V-s.
Hole Effective mass	0.59
Hole mobility (at 300 K) for low p type conductivity	5-50 cm <sup>2</sup> /V-s

Moreover, Table 1.1 displays some of the basic physical parameters for ZnO. It should be noted that there still exists uncertainty in some of these values. For example, the values for thermal conductivity show some spread in values, and this may be a result of the influence of defects such as dislocations, similar to the case for GaN. The values for carrier mobility will undoubtedly increase as more control is gained over compensation and defects in the material. Availability of few reports of  $p$ -type ZnO and therefore the hole mobility and effective mass are still in debate.

Zinc oxide is considered as an *n*-type semiconductor with a direct wide bandgap of 3.4 eV with a considerable fraction of ionic bonding. Many particular features of ZnO are determined by the fact that, among the elements of the VI-group, the ionization energy of oxygen is the highest, which leads to a strongest interaction between the Zn (*3d*) and O (*2p*) orbitals [65]. This accounts for an anomalously wide band gap of ZnO, compared to its relative ZnS,  $E_g = 3.7$  eV (theoretically, the band gap width should increase in the series of chalcogenides  $\text{ZnTe} \rightarrow \text{ZnSe} \rightarrow \text{ZnS} \rightarrow \text{ZnO}$  [66]). The cause for the natural *n*-type nature of ZnO is due to the sensitiveness of ZnO lattice constants to the presence of structural point defects (vacancies and interstitials) and extended defects (threading/planar dislocations) that are commonly found in ZnO resulting in a non-stoichiometric compound  $\text{Zn}_{1+d}\text{O}$  with an excess Zn. These excess Zn atoms tend to function as donor interstitials that give its natural *n*-type conductivity. In ionic form, the excess zinc exists as  $\text{Zn}^+$  interstitials that are mobile, and they tend to occupy special interstitial sites. These special sites offer passage routes for Zn interstitials to migrate within the ZnO wurtzite structure easily. ZnO also transparent to visible light but strongly absorbs ultra violet light below 365 nm. This combination of optical and semiconductor properties make ZnO a contender for new generations of devices [67].

## 1.2. Synthesis/Growth of ZnO nanostructures

As mentioned above, ZnO is a versatile, functional material, so the preparation of this material is very significant. Over the last forty years, different processing techniques are successfully developed and utilized for the synthesis of ZnO. Associated with these techniques, there is a range of structures of nanometric ZnO, which means that ZnO can be classified among new materials with potential applications in many fields of nanotechnology. ZnO can occur in 1D, 2D, and 3D structures as elaborated in Figure 1.1. One-dimensional structures make up the largest group, including nanorods, needles, helixes, springs, ribbons, tubes, belts, wires and combs. ZnO can also be obtained in 2D structures, such as nanoplate/nanosheet and nanopellets. Examples of 3D structures of ZnO include flower, dandelion, snowflakes, *etc.* [68 - 106] ZnO provides one of the greatest assortments of varied particle structures among all known materials. The zinc oxide occurs in a very rich variety of structures and offers a wide range of properties. The variety of methods for ZnO production, such as vapour deposition, precipitation in water solution, hydrothermal synthesis, the sol-gel process, precipitation from microemulsions

and mechanochemical processes, makes it possible to obtain products with particles differing in shape, size and spatial structure. These common methods adopted for the synthesis of ZnO are summarized in Table 1.2.

**Table 1.2.** Summary of methods for obtaining zinc oxide nanostructure.

Methods	Precursors	Synthesis condition	Properties and application	Ref.
<b>Mechano-chemical process</b>	ZnCl <sub>2</sub> , Na <sub>2</sub> CO <sub>3</sub> , NaCl	Calcination: 2 h, 600 °C.	hexagonal structure; particles diameter: 21–25 nm	71
		400–800°C	hexagonal structure; particles diameter: 18–35 nm	72
		400°C	regular shape of particles; diameter ~27 nm, BET: 47 m <sup>2</sup> /g	73
		0.5 h		
		300–450°C	particles diameter: 27–56 nm	74
			particles diameter: ~51 nm, BET: 23 m <sup>2</sup> /g	75
<b>Precipitation process</b>	Zn(CH <sub>3</sub> COO) <sub>2</sub> , and KOH as a water solutions	temperature: 20–80°C; drying: 120°C	particles diameter: 160–500 nm, BET: 4–16 m <sup>2</sup> /g	76
	Zn(CH <sub>3</sub> COO) <sub>2</sub> , (NH <sub>4</sub> ) <sub>2</sub> CO <sub>3</sub> , PEG10000 as a water solutions	drying: 12 h, 100°C; calcination: 3 h, 450°C	zincite structure; spherical particles ( <i>D</i> ~ 30 nm); application: as a photocatalyst in photocatalysis degradation	77
	Zn(NO <sub>3</sub> ) <sub>2</sub>	calcination: 2 h, 600°C; aging: 240 h, 320°C	wurtzite structure; particles diameter: 50 nm; application: as a gas sensor	78
	Zn(NO <sub>3</sub> ) <sub>2</sub> , NaOH	synthesis: 2 h; drying: 2 h, 100°C	particles of spherical size of around 40 nm	79
	ZnSO <sub>4</sub> , NH <sub>4</sub> HCO <sub>3</sub> , ethanol	drying: overnight, 100°C; calcination: 300–500°C	wurtzite structure; crystallite size 9–20 nm; particle size <i>D</i> : ~12 nm, BET: 30–74 m <sup>2</sup> /g	80

	Zn(CH <sub>3</sub> COO) <sub>2</sub> , NH <sub>3</sub> aq.	precipitation temperature: 85 °C;  drying: 10 h, 60 °C	hexagonal structure, shape of rods, flower-like particles: <i>L</i> : 150 nm, <i>D</i> : 200 nm	81
	ZnSO <sub>4</sub> , NH <sub>4</sub> OH, NH <sub>4</sub> HCO <sub>3</sub>	reaction: 30 min, 60 °C; drying: 12 h, 100 °C; calcination: 2 h, 400 °C	hexagonal structure, flake-like morphology ( <i>D</i> : 0.1–1 μm, <i>L</i> : 60 nm)	82
	micro sized ZnO powder, NH <sub>4</sub> HCO <sub>3</sub>	reaction: ~2 h, 25 °C; drying: 80 °C;  calcination: 1 h, 350 °C	hexagonal wurtzite structure; flower-like and rod-like shape ( <i>D</i> : 15–25 nm, <i>BET</i> : 50–70 m <sup>2</sup> /g)	83
	Zn(CH <sub>3</sub> COO) <sub>2</sub> , NaOH	reaction: 30 min, 75 °C; drying: overnight, room temperature	hexagonal structure; flower shape ( <i>L</i> : >800 nm); application: antimicrobial activity	84
<b>Precipitation in the presence of surfactants</b>	ZnCl <sub>2</sub> , NH <sub>4</sub> OH, CTAB	aging: 96 h, ambient temperature,  calcination: 2 h, 500 °C	zincite structure; particles diameter: 54–60 nm, <i>BET</i> = ~17 m <sup>2</sup> /g	85
	Zn(NO <sub>3</sub> ) <sub>2</sub> , NaOH, SDS, TEA (triethanolamin e)	precipitation: 50–55 min, 101 °C	wurtzite structure, the shape of rod-like ( <i>L</i> : 3.6 μm, <i>D</i> : 400– 500 nm) shape of nut-like and rice-like, size: 1.2–1.5 μm	86
<b>Sol-gel</b>	Zn(CH <sub>3</sub> COO) <sub>2</sub> , oxalic acid, ethanol and methanol	reaction temperature: 60 °C;  drying: 24 h, 80 °C; calcination: 500 °C	zincite structure; aggregate particles: ~100 nm; shape of rod; particles <i>L</i> : ~500 nm, <i>D</i> : ~100 nm; <i>BET</i> : 53 m <sup>2</sup> /g; application: decontamination of sarin (neuro-toxic agent)	87
	Zn(CH <sub>3</sub> COO) <sub>2</sub> , oxalic acid	reaction: 50 °C, 60 min; dried of gel: 80 °C, 20 h;	hexagonal wurtzite structure; uniform, spherically shaped of particles	88

	(C <sub>2</sub> H <sub>2</sub> O <sub>4</sub> ), ethanol	calcination: under flowing air for 4 h at 650 °C		
	Zinc 2-ethylhexanoate, TMAH ((CH <sub>3</sub> ) <sub>4</sub> NOH), ethanol and 2-propanol	reaction: room temperature; drying: 60 °C	cylinder-shaped crystallites, <i>D</i> : 25–30 nm; <i>L</i> : 35–45 nm	89
	Zn(CH <sub>3</sub> COO) <sub>2</sub> , diethanolamine, ethanol	reaction: room temperature; annealed of sol: 2 h, 500 °C	hexagonal wurtzite structure; particles: nanotubes of 70 nm	90
<b>Solvothermal hydrothermal and microwave techniques</b>	ZnCl <sub>2</sub> , NaOH	reaction: 5–10 h, 100–220 °C in a Teflon-lined autoclave	particles morphology: bullet-like (100–200 nm), rod-like (100–200 nm), sheet (50–200 nm), polyhedron (200–400 nm), crushed stone-like (50–200 nm)	91
	Zn(CH <sub>3</sub> COO) <sub>2</sub> , NaOH, HMTA (hexamethylene tetramine)	reaction: 5–10 h, 100–200 °C; HMTA concentration: 0–200 ppm	spherical shape; particles diameter: 55–110 nm	92
	Zn(CH <sub>3</sub> COO) <sub>2</sub> , Zn(NO <sub>3</sub> ) <sub>2</sub> , LiOH, KOH, NH <sub>4</sub> OH	reaction: 10–48 h, 120–250 °C	hexagonal (wurtzite) structure, size of micro crystallites: 100 nm–20 μm	93
	Zn(CH <sub>3</sub> COO) <sub>2</sub> , NH <sub>3</sub> , zinc 2-ethylhexanoate, TMAH, ethanol, 2-propanol	time of autoclaving: 15 min, 2–72 h; final pH: 7–10	particles with irregular ends and holes; aggregates consist particles of 20–60 nm, <i>BET</i> : 0.49–6.02 m <sup>2</sup> /g	94
	trimethylamine N-oxide, 4-picoline N-oxide, HCl, toluene, ethylenediamine (EDA), N,N,N',N'-tetramethylethylenediamine (TMEDA)	reaction: 24–100 h, 180 °C	wurtzite structure; particles morphology: nanorods (40–185 nm), nanoparticles (24–60 nm)	95

<b>Emulsion</b>	Zn(NO <sub>3</sub> ) <sub>2</sub> , surfactant (ABS, Tween-80 and 40, C <sub>21</sub> H <sub>38</sub> BrN)	reaction: 25 °C, pH~8; drying: 24 h, 80 °C; calcination: 2 h, 600 °C	grain size: cationic surfactants (40–50 nm), nonionic surfactants (20–50 nm), anionic surfactants (~20 nm)	96
	Zn(C <sub>17</sub> H <sub>33</sub> COO) <sub>2</sub> , NaOH, decane, water, ethanol	reaction: 2 h, room temperature or 90 °C	particles morphology: irregular particles aggregates (2–10 μm); needle-shaped ( <i>L</i> : 200–600 nm, <i>T</i> : 90–150 nm); nearly spherical and hexagonal ( <i>D</i> : 100–230 nm); spherical and pseudo spherical aggregates ( <i>D</i> : 150 nm)	97
	Zn(CH <sub>3</sub> COO) <sub>2</sub> , heptane, Span-80, NH <sub>4</sub> OH	reaction: 1 h; aging: 2.5 h; drying: in rotary evaporator; calcination: 2 h, 700–1000 °C	hexagonal structure; spherical shape; particles diameter: 0.05–0.15 μm	98
	Zn(CH <sub>3</sub> COO) <sub>2</sub> , NaOH and KOH, cyclohexane, non-ionic surfactants	reaction: ambient temperature; drying: 24 h, 120 °C	hexagonal structure; particles morphology: solids (164–955 nm, <i>BET</i> : 8 m <sup>2</sup> /g), ellipsoids (459–2670 nm, <i>BET</i> : 10.6 m <sup>2</sup> /g), rods (396–825 nm, <i>BET</i> : 12 m <sup>2</sup> /g), flakes (220–712 nm, <i>BET</i> : 20 m <sup>2</sup> /g); crystallites size: 32–77 nm; application: as a photocatalyst	78
<b>Micro-emulsion</b>	Zn(NO <sub>3</sub> ) <sub>2</sub> , NaOH, heptane, hexane, Triton X-100, PEG400	reaction: 15 h, 140 °C; drying: 60 °C	hexagonal (wurtzite) structure; particles morphology: needle ( <i>L</i> : 150–200 nm, <i>D</i> : ~55 nm), Nano columns ( <i>L</i> : 80–100 nm, <i>D</i> : 50–80 nm), spherical (~45 nm)	99
	Zn(NO <sub>3</sub> ) <sub>2</sub> , oxalic acid, isooctane, benzene, ethanol, diethyl ether, chloroform, acetone, methanol, Aerosol OT	reaction: 1 h; calcination: 3 h, 300 °C	equivalent spherical diameter: 11.7–12.9 nm, <i>BET</i> : 82–91 m <sup>2</sup> /g; grain size: 11–13 μm	100
	Zn(CH <sub>3</sub> COO) <sub>2</sub> , Aerosol OT,	reaction: 24 h, 60–70 °C;	hexagonal wurtzite structure, spherical shape (15–24 nm),	101

	glycerol, C <sub>20</sub> H <sub>37</sub> NaO <sub>7</sub> S, n-heptane, NaOH, methanol, chloroform	drying: 1 h, 100 °C; calcination: 3 h, 300–500 °C	rods shape ( <i>L</i> : 66–72 nm, <i>D</i> : 21–28 nm)	
	ZnCl <sub>2</sub> , Zn(CH <sub>3</sub> COO) <sub>2</sub> , heptane, BTME (1,2-trimethoxysilyl) ethane, TMOS(tetramethoxysilane), methanol, Aerosol OT, NaOH	reaction: 2–3 h, room temperature or 40 °C; drying: under vacuum overnight; calcinations: 24 h, 700 °C	hexagonal structure, uniformly dispersed small particles, size of particles ~10 nm	102
<b>Other methods</b>	Zn(CH <sub>3</sub> COO) <sub>2</sub>	thermal decomposition: 350–800 °C	uniform size of particles 20–30 nm	103
	Zn(NO <sub>3</sub> ) <sub>2</sub> , deionized water, HMT (hexamethylene tetramine)	ultrasonic irradiation: 30 min, 80 °C; drying: 2 h, 60 °C	hexagonal wurtzite structure, nanorods and nanowire shape ( <i>L</i> : ~1 μm, <i>D</i> : ~160 nm); application: electronic and optoelectronic devices	104
	micron scale zinc metal powder	feed rate: 1 g/min; plasma power: 1 kW; O <sub>2</sub> flow rate: 2.5 l pm; N <sub>2</sub> flow rate: 12.5 l pm; reaction: 900 °C	nanowires shape ( <i>L</i> : 1–30 μm, <i>D</i> : 5–50 nm) application: as hydro- desulfurization catalyst	105
	diethyl zinc (DEZ), oxygen	helium as a carrier gas	wurtzite structure; average particle size: 9 nm	106

Very recently, a notable amount of global attention draws in the direction of conventional bottom-up approaches that has led an increased patent number. Therefore, keeping that in mind, within the scope of this thesis, a conventional and comprehensive bottom-up approach using wet chemical method is adopted to synthesize diverse nanostructures of ZnO to understand the growth mechanism and their integration in multifunctional applications. The adopted technique is aimed towards providing the direct implementation of the developed products for multifunctional applications.

### 1.3. Application of Zinc Oxide [2-5, 50]

For the past few decades researchers have continued to understand how the physical properties are affected by shrinking the dimension of bulk ZnO to the nanoscale range for exceeding state-of-the-art solid state electronic devices and developed the novel applications of ZnO nanostructures. A broad range of applications of ZnO nanostructures in different fields of science have been explored due to its unique electrical, optical and mechanical properties. Starting from the wide band gap of ZnO makes it able to form clusters consisting of ZnO nanocrystals and ZnO nanorods. Many fine optical devices are fabricated based on the free-exciton binding energy in ZnO because of its large exciton binding energy that makes it eligible to persist at room temperature and even higher temperatures too.



*Figure 1.3. Unique properties and diverse applications of ZnO nanostructures.*

Since ZnO crystals and thin films exhibit second- and third-order non-linear optical behaviour, it also opens its potential applications in non-linear optical devices.

The electrical, optical, magnetic, and chemical properties of ZnO can be very well tuned by making permutation and combination of the two basic structural characteristics they possess, *i.e.*, as cations with mixed valence states, and as anions with deficiencies (vacancies). Based on these ideas, the diverse applications of ZnO nanostructures are represented in the form of a chart in Figure 1.3.

#### **1.4. Scope and Goals of Thesis**

The main aspiration of this thesis is to synthesize ZnO nanostructures which are functional in its unique way contributing to the diverse fields of applications. The preliminary idea is to prepare ZnO nanostructure first and systematically study its property modification. The prepared ZnO nanostructures are then implemented in diverse applications including, optical, sensing, magnetic, and field emission studies.

##### **1.4.1. Thesis objectives**

The precise objectives of the research work plans are categorized as follows:

1. Controlled growth of ZnO nanostructures using the simple and economical wet chemical approach.
2. To understand the growth mechanism of the nanostructures.
3. Effect of doping on ZnO nanostructures and to study their physico-chemical, structural, optical and magnetic properties.
4. To implement the prepared un-doped/doped ZnO nanostructures for multifunctional applications.

##### **1.4.2. Thesis outline**

With reference to the selected objectives, and examining all the information gained from the literature review, the controlled growth of ZnO nanostructures is executed. The growth of ZnO nanostructures is conducted by simple and an economical wet chemical route followed by proper investigations. In conjunction with ZnO nanostructures, the effect of doping on ZnO is also explored and followed by systematic material characterizations to understand the physical properties. The pure and doped ZnO nanostructures are then successfully realized in multifunctional applications including, two photon absorption, sensors, magnetism, and field emission studies.

In this thesis, all the above stated works have been presented in the form of six chapters circumscribed between the introduction chapter (Chapter 1) and a conclusion chapter (Chapter 6). The chapter contents are summarized as follows:

**Chapter 1**, entitled, “Introduction to the nanostructured materials projects a literature review concerning inorganic nanostructures where prime focus is given on metal oxides mainly zinc oxide (ZnO).

**Chapter 2**, entitled “Experimental techniques” provides the details of the experimental setup and the processing techniques used for the controlled growth of ZnO nanostructures. A brief review of the various analytical characterization tools are also summarized. Further, the preparation of substrates used for the desired application is also described.

**Chapter 3**, entitled “Controlled growth of zinc oxide (ZnO) nanostructures” present the synthetic routes to prepare nanostructured ZnO. This work provides an in-depth analysis regarding the optimization of the controlling variable *i.e.* the pH, concentration, time and temperature for preparing diverse structures of ZnO for instance, nanorods, nanoflowers, nanoneedles and nanotubes via a simple wet chemical approach. Subsequently, the material property variance of the prepared nanostructured ZnO is investigated for structural, optical and morphological properties. A detailed understanding of the growth mechanism of ZnO nanostructures is also highlighted in this chapter.

**Chapter 4**, entitled “Effect of doping on zinc oxide (ZnO) nanostructures” presents the effect of strontium (Sr) doping in ZnO and study of its structural, optical and morphological properties. In an effort to check the magnetic application of ZnO nanostructures, nickel (Ni) doping is carried out. In this work, the origin of room temperature ferromagnetism in Ni doped ZnO is systematically investigated through physical, optical and magnetic properties.

**Chapter 5**, entitled “Multifunctional applications of zinc oxide (ZnO) nanostructures” demonstrates the effect of Ni doping in ZnO nanostructures for, two photon absorption, field emission and magnetic applications. Performance of field emission and two photon absorption in Ni-doped ZnO is investigated in details. The effect of Sr- and Ni-doped ZnO for the gas sensing performance, especially for CO and CO<sub>2</sub> are also included in this

chapter. The origin of room temperature ferromagnetism in Ni-doped ZnO is investigated in this chapter.

**Chapter 6**, entitled “The conclusion and scope for future work” summarize the overall concluding remarks drawn from the thesis by justifying its title and proposed objectives. This chapter also highlights the probable scope of outspreading this work in the near future.

## References

- [1] Oriakhi C. (1998), Nano sandwiches, Chemistry in Britain, Chem. Soc., London, *Royaue-Uni*, 34, 59-62.
- [2] Morris P. R. (1990), A history of the world semiconductor industry, IET, pp. 11–25 (ISBN 0-86341-227-0).
- [3] Yacobi B.G. (2003), Semiconductor materials: An introduction to basic principles, Springer, pp. 1–3, (ISBN 0-306-47361-5).
- [4] Nicollian E. H., Brews J. R. (1982), Metal oxide semiconductor physics and technology, Wiley, ISBN 0471085006, 9780471085003.
- [5] Ploschner M. Cizmar T., Mazilu M., Falco A. Di, Dholakia K. (2012), Bidirectional optical sorting of gold nanoparticles, *Nano Lett.* 12, 1923-1927.
- [6] Li J., Chen X., Qiao Z., He M., Li H. (2001), Large-scale synthesis of single-crystalline  $\beta$ -Ga<sub>2</sub>O<sub>3</sub> nanoribbons, nanosheets and nanowires, *J. Phys.: Condens. Matter.* 13, 1937-1941.
- [7] Chen C.-C., Chen C.-F., Lee I.-H., Lin C.-L. (2005), Fabrication of high surface area graphitic nanoflakes on carbon nanotubes templates, *Diamond Relat. Mater.* 14, 1897-1900.
- [8] Movafaghi S., Wang, W., Metzger, A., Williams D. D., Williams J. D., Kota A. K. (2016) Tunable superomniphobic surfaces for sorting droplets by surface tension, *Lab. Chip.* 16, 3204.
- [9] Yao Y.-F., Shen C.-H., Chen W.-F. *et al.* (2014) Void structures in regularly patterned ZnO nanorods grown with the hydrothermal method, *J. Nanomater.* doi.org/10.1155/2014/756401.
- [10] Li Y. *et al.* (2012) One-dimensional metal oxide nanotubes, nanowires, nanoribbons, and nanorods: Synthesis, characterizations, properties and applications, *Crit. Rev. Solid State Mater. Sci.* 37, 1-74.
- [11] Ray S. S., Okamoto M. (2003), Polymer/layer silicate nanocomposites: a review from preparation to processing, *Prog. Polym. Sci.* 28, 1539-1641.
- [12] Jordan J., Jacob K. I., Tannenbaum R., Sharaf M. A., Jasiuk I. (2005), Experimental trends in polymer nanocomposites: A review, *Mater. Sci. Eng. A* 393, 1-11.

- 
- [13] Bunn C. W. (1935), The lattice-dimensions of zinc oxide, *Proc. Phys. Soc. London*, 47, 835.
- [14] Heller R. B., McGannon J., Weber A. H. (1950), Precision determination of the lattice constants of zinc oxide, *J. Appl. Phys.* 21, 1283-1284.
- [15] Mollwo E. (1954), Dispersion, absorption and thermal emission of zinc-oxide crystals, *Z. Angew. Phys.* 6, 257-260.
- [16] Damen T. C., Porto S. P. S., Tell B. (1966), Raman effect in zinc oxide, *Phys. Rev.* 142, 570-574
- [17] Mead C. A. (1965), Surface barriers on ZnSe and ZnO, *Phys. Lett.* 18, 218.
- [18] Drapak I. T. (1968), Visible luminescence of a ZnO-Cu<sub>2</sub>O heterojunction, *Semiconductors*, 2, 624.
- [19] Gali G., Coker J. E. (1970), Epitaxial ZnO on sapphire, *Appl. Phys. Lett.* 16, 439-441.
- [20] Minami T., Tanigawa M., Yamanishi M., Kawamura T. (1974), Observation of ultraviolet-luminescence from the ZnO MIS diodes, *Jpn. J. Appl. Phys.* 13, 1475.
- [21] Tsurkan et al. (1975), ZnO /ZnSe n-p junctions, *Semiconductors* 6, 1183-1185.
- [22] Brillson L. J. (1978), Chemical reaction and charge redistribution at metal-semiconductor interfaces, *J. Vac. Sci. Technol.* 15, 1378-1383.
- [23] Kim H.-K., Han S.-H., Seong T.-Y., and Choi W.-K. (2000), Low-resistance Ti/Au ohmic contacts to Al-doped ZnO layers, *Appl. Phys. Lett.* 77, 1647-1649.
- [24] Yu X., Mat J., Ji F., Wang Y., Zhang X., and Ma H. (2005), Influence of annealing on the properties of ZnO: Ga films prepared by radio frequency magnetron sputtering, *Thin Solid Films*, 483, 296-300.
- [25] Kumar B., Gong H., and Akkipeddi R., J. (2005), A study of conduction in the transition zone between homologous and ZnO-rich regions in the In<sub>2</sub>O<sub>3</sub> -ZnO system, *Appl. Phys. Lett.* 97, 063706.
- [26] Ip K., Heo Y. W., Baik K. H., Norton D. P., Pearton S. J., and Ren F. (2004), Carrier concentration dependence of Ti/Al/Pt/Au contact resistance on n-type ZnO, *Appl. Phys. Lett.* 84, 544-546.
- [27] Hu G. X., Kumar B., Gong H., Chor E. F., and Wu P. (2006), Transparent indium zinc oxide ohmic contact to phosphor-doped n-type zinc oxide, *Appl. Phys. Lett.* 88, 101901.

- [28] Minegishi K., Koiwai Y., Kikuchi Y., Yano K., Kasuga M., Shimizu A. (1997), Growth of p-type Zinc Oxide films by chemical vapor deposition, *Jpn. J. Appl. Phys.*, 36, L 1453-L 1455.
- [29] Aoki T., Shimizu Y., Miyake A., Nakamura A., Nakanishi Y., Hatanaka Y. (2002), p-type ZnO layer formation by excimer laser doping, *Phys. Status Solidi B*, 229, 911-914.
- [30] Hwang D.-K., Kim H.-S., Lim J.-H., Oh J.-Y., Yang J.-H., Park S.-J., Kim K.-K., Look D. C., Park Y. S. (2005), Study of the photoluminescence of phosphorus-doped p-type ZnO thin films grown by radio-frequency magnetron sputtering, *Appl. Phys. Lett.* 86, 151917.
- [31] Kim K.-K., Kim H.-S., Hwang D.-K., Lim J.-H., Park S.-J. (2003), Realization of p-type ZnO thin films via phosphorus doping and thermal activation of the dopant, *Appl. Phys. Lett.* 83, 63-65.
- [32] Jang S., Chen J.-J., Kang B. S., Ren F., Norton D. P., Pearton S. J., Lopata J., Hobson W. S. (2005), Formation of p - n homojunctions in n - ZnO bulk single crystals by diffusion from a Zn<sub>3</sub>P<sub>2</sub> source, *Appl. Phys. Lett.*, 87, 222113.
- [33] Hu G. X., Gong H., Chor E. F., Wu P. (2006), ZnO homojunctions grown by cosputtering ZnO and Zn<sub>3</sub>P<sub>2</sub> targets, *Appl. Phys. Lett.* 89, 021112.
- [34] Yu Z. G., Wu P., Gong H. (2006), Control of p - and n -type conductivities in P doped ZnO thin films by using radiofrequency sputtering, *Appl. Phys. Lett.* 88, 132114.
- [35] Yu Z. G., Gong H., Wu P. (2005), Dopant Sources Choice for Formation of p-Type ZnO: Phosphorus Compound Sources, *Chem. Mater.* 17, 852-855.
- [36] Xiu F. X., Yang Z., Mandalapu L. J., Liu J. L. (2006), Donor and acceptor competitions in phosphorus-doped ZnO, *Appl. Phys. Lett.* 88, 152116.
- [37] Ryu Y. R., Lee T. S., White H. W. (2003), Properties of arsenic-doped p -type ZnO grown by hybrid beam deposition, *Appl. Phys. Lett.* 83, 87-89.
- [38] Xiu F. X., Yang Z., Mandalapu L. J., Zhao D. T., Liu J. L., Beyermann W. P. (2005), High-mobility Sb-doped p-type ZnO by molecular-beam epitaxy, *Appl. Phys. Lett.*, 87, 152101.
- [39] Zhang S. B., Wei S. -H., Zunger A. (2001), Intrinsic n-type versus p-type doping asymmetry and the defect physics of ZnO, *Phys. Rev. B*, 63, 075205.

- [40] Hapiuk D., Marques M. A. L., Melinon P, Flores-Livas José A, Botti S, Masenelli B. (2012), p Doping in Expanded Phases of ZnO: An Ab Initio Study, *Phys. Rev. Lett.* 108, 115903.
- [41] Yamamoto T., Katayama-Yoshida H. (2000), Unipolarity of ZnO with a wide-band gap and its solution using codoping method, *J. Cryst. Growth*, 214/215, 552-555.
- [42] Duan X. M., Stampfl C., Bilek M. M. M., McKenzie D. R. (2009), Co-doping of aluminum and gallium with nitrogen in ZnO: a comparative first-principles investigation, *Phys. Rev. B*, 79, 235208.
- [43] Ying Z. C., Jing W., Lei B. Y. (2010) First-principles investigation of N–Ag co-doping effect on electronic properties in p-type ZnO, *Chin. Phys. B* 19, 047101.
- [44] Tian R.-Y., Zhao Y. -J. (2009), The origin of p-type conduction in (P, N) codoped ZnO, *J. Appl. Phys.* 106, 043707.
- [45] Hong et al. (2009), Formation mechanism and properties of In, P codoped p-type ZnO thin film, *Chin. J. Lumin.*, 30, 12.
- [46] Kim H., Cepler A., Osofsky M. S., Auyeung R. C. Y., Piqué A. (2007), Fabrication of Zr-N codoped p-type ZnO thin films by pulsed laser deposition, *Appl. Phys. Lett.* 90, 203508.
- [47] Sui Y. R., Yao B., Hua Z., et al. (2009), Fabrication and properties of B-N codoped p-type ZnO thin films, *J Phys D: Appl. Phys.* 42, 065101.
- [48] Deng B., Guo Z., Sun H. (2010), Theoretical study of Fe-doped p-type ZnO, *Appl. Phys. Lett.* 96, 172106.
- [49] Chen L., Xiong Z., Wan Q., Li D. (2010), Realization of p-type ZnO by (nN, Mg) codoping from first-principles, *Opt. Mater.* 32, 1216-1222.
- [50] Wang Z. L. (2004), Zinc oxide nanostructures: growth, properties and applications, *J. Phys.: Condens. Matter.* 16, R829- R858.
- [51] Wolf S. A., Awschalom D. D., Buhrman R. A. et al. (2001), Spintronics: A spin-based electronics vision for the future. *Science*, 294, 1488–1495.
- [52] Pearton, S. J., Abernathy, C. R., Overberg, M. E. et al. (2003), Wide band gap ferromagnetic semiconductors and oxides, *J. Appl. Phys.* 93, 1–13.
- [53] Sarma S. D. (2001), Spintronics: A new class of device based on electron spin, rather than on charge, may yield the next generation of microelectronics, *Am. Sci.* 89, 516–523.

- [54] Dielt T., Ohno H., Matsukura F., Cibert J., Ferrand D. (2000), Zener model description of ferromagnetism in Zinc-blende magnetic semiconductors, *Science* 287, 1019–1022.
- [55] Sato, K.; Katayama-Yoshida, H. (2000), Material design for transparent ferromagnets with ZnO-based magnetic semiconductors, *Jpn. J. Appl. Phys.* 39, L555–L558.
- [56] Sato, K.; Katayama-Yoshida, H. (2001), Material design of GaN-based ferromagnetic diluted magnetic semiconductors, *Jpn. J. Appl. Phys.* 40, L485–L487.
- [57] Samanta, K.; Bhattacharya, P.; Katiyar, R. S. (2016), Optical properties of  $Zn_{1-x}Co_xO$  thin films grown on  $Al_2O_3(0001)$  substrates, *Appl. Phys. Lett.* 87, 101903-101903.
- [58] Panigrahy, B.; Aslam, M.; Bahadur, D. (2012), Effect of Fe doping concentration on optical and magnetic properties of ZnO nanorods, *Nanotechnology* 23, 115601.
- [59] Sans, J. A.; Sánchez-Royo, J. F.; Segura, A.; Tobias, G.; Canadel, E. (2009), Chemical effects on the optical band-gap of heavily doped ZnO:M<sub>III</sub> (M = Al, Ga, In): An investigation by means of photoelectron spectroscopy, optical measurements under pressure, and band structure calculations, *Phys. Rev. B: Condens. Matter Mater. Phys.* 79, 195105.
- [60] Kumar, S.; Mukherjee, S.; Singh, R. K.; Chatterjee, S.; Ghosh, A. K. (2011), Structural and optical properties of sol-gel derived nanocrystalline Fe-doped ZnO, *J. Appl. Phys.* 110, 103508.
- [61] Espitia P. J. P., Soares N. de F. F., Coimbra J. S. dos R. et al. (2012), Zinc oxide nanoparticles: Synthesis, antimicrobial activity, and food packaging applications, *Food Bioprocess Technol.* 5, 1447-1464.
- [62] Fan Z., Lu J. G. (2005), Zinc oxide nanostructures: synthesis and properties, *J. Nanosci. Nanotechnol.* 5, 1561-1573.
- [63] Porter, F. C. (1991), *Zinc oxide Handbook: Properties, Processing, and Use in Design*, 1 ed. CRC Press.
- [64] Subramanyam T. K., Naidu B. S., Uthanna S. (2000), Physical properties of zinc oxide films prepared by dc reactive magnetron sputtering at different sputtering pressures, *Cryst. Res. Technol.* 35, 1193-1202.

- [65] Ellmer K., Klein A., Rech B. (2008), *Transparent conductive zinc oxide*, Springer-Verlag, Berlin, pp. 1-233 (ISBN 978-3-540-73612-7)
- [66] Wei S. H., Zunger A. (1998), Calculated natural band offsets of all II–VI and III–V semiconductors: Chemical trends and the role of cation d orbitals, *Appl. Phys. Lett.* 72, 2011-2013.
- [67] Janotti A., Van de Walle C. G., (2009), Fundamentals of zinc oxide as a semiconductor, *Rep. Prog. Phys.* 72, 126501.
- [68] Wang Z. L. (2004), Nanostructures of zinc oxide, 7, 26-33.
- [69] Lao J. Y., Wen J. G., Ren Z. F. (2002), Hierarchical ZnO nanostructures, *Nano Lett.* 2, 1287–1291.
- [70] Tian Z. R. et al. (2003), Complex and oriented ZnO nanostructures, *Nat. Mater.* 2, 821-826.
- [71] Ao et al. (2006), Mechanochemical synthesis of zinc oxide nanocrystalline, *Powder Technol.* 168, 148-151.
- [72] Stanković et al. (2011), Controlled mechanochemically assisted synthesis of ZnO nanopowders in the presence of oxalic acid, *J. Mater. Sci.* 46, 3716–3724.
- [73] Tsuzuki T., McCormick P. G. (2001), ZnO nanoparticles synthesized by mechanochemical processing, *Scr. Mater.* 44, 1731-1734.
- [74] Moballegh et al. (2007), ZnO nanoparticles obtained by mechanochemical technique and optical properties, *Surf. Sci.*, 601, 2850-2854.
- [75] Aghababazadeh et al. (2006), ZnO nanoparticles synthesized by mechanochemical processing, *J. Phys. Chem. Solids*, 26, 312-314.
- [76] Kołodziejczak-Radzimska A., Jesionowski T., Krysztalkiewicz A. (2010), Obtaining zinc oxide from aqueous solutions of KOH and  $Zn(CH_3COO)_2$ , *Physicochem. Probl. Miner. Process.* 44, 93-102.
- [77] Hong et al. (2006), Synthesis and surface modification of ZnO nanoparticles, *Chem. Eng. J.* 119, 71-81.
- [78] Xu et al. (2000), Grain size control and gas sensing properties of ZnO gas sensor, *Sens. Actuators B Chem.* 66, 277-279.
- [79] Lanje et al. (2013), Low temperature dielectric studies of zinc oxide (ZnO) nanoparticles prepared by precipitation method, *Adv. Powder Technol.*, 24, 331-335.

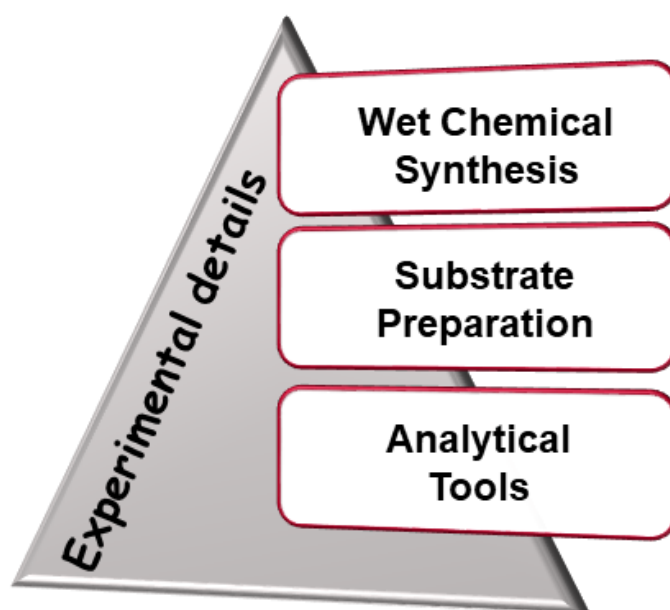
- [80] Wang et al. (2010), Preparation of ZnO nanoparticles using the direct precipitation method in a membrane dispersion micro-structured reactor, *Powder Technol.* 202, 130-136.
- [81] Jia et al. (2012), Evidence of the formation mechanism of ZnO in aqueous solution, *Mater. Lett.* 82, 99-101.
- [82] Cao et al. (2009), Synthesis and UV shielding properties of zinc oxide ultrafine particles modified with silica and trimethyl siloxane, *Colloids Surf. A Physicochem. Eng. Asp.* 340, 161-167.
- [83] Khoshhesab Z. M., Sarfaraz M., Houshyar Z. (2012), Influence of urea on precipitation of zinc oxide nanostructures through chemical precipitation in ammonium hydrogencarbonate solution, *Synth. React. Inorg. Met. Org. Nano Met. Chem.*, 42, 1363-1368.
- [84] Kumar et al. (2013), Synthesis and characterization of flower shaped zinc oxide nanostructures and its antimicrobial activity, *Spectrochim. Acta Part A Mol. Biomol. Spectrosc.* 104, 171-174.
- [85] Wang et al. (2002), Preparation of nanocrystalline metal oxide powders with the surfactant-mediated method, *Inorg. Chem. Commun.* 5, 751-755.
- [86] Li et al. (2005), Growth of well-defined ZnO microparticles with additives from aqueous solution, *J. Solid State Chem.* 178, 855-860.
- [87] Mahato et al. (2009), Nanocrystalline zinc oxide for the decontamination of sarin, *J. Hazard. Mater.* 165, 928-932.
- [88] Benhebal et al. (2013), Photocatalytic degradation of phenol and benzoic acid using zinc oxide powders prepared by sol-gel process, *Alex. Eng. J.* 52, 517-523.
- [89] Ristić et al. (2005), Sol-gel synthesis and characterization of nanocrystalline ZnO powders, *J. Alloy. Compd.* 39, L1-L4.
- [90] Yue et al. (2013), Synthesis of zinc oxide nanotubes within ultrathin anodic aluminum oxide membrane by sol-gel method, *Mater. Lett.* 98, 246-249.
- [91] Chen D., Jiao X., Cheng G. (2000), Hydrothermal synthesis of zinc oxide powders with different morphologies, *Solid State Commun.* 113, 363-366.
- [92] Ismail et al. (2005), Application of statistical design to optimize the preparation of ZnO nanoparticles via hydrothermal technique, *Mater. Lett.* 59, 1924-1928.

- [93] Dem'Yanets L. N., Li L. E., Uvarova T. G. (2006), Zinc oxide: Hydrothermal growth of nano- and bulk crystals and their luminescent properties, *J. Mater. Sci.* 41, 1439-1444.
- [94] Musić et al. (2005), Precipitation of ZnO particles and their properties, *Mater. Lett.* 59, 2388-2393.
- [95] Chen et al. (2003), Preparation and characterization of nanocrystalline zinc oxide by a novel solvothermal oxidation route, *J. Cryst. Growth*, 252, 184-189.
- [96] Zhang et al. (2010), Ionic liquid-controlled synthesis of ZnO microspheres, *J. Mater. Chem.*, 20, 9798-9804.
- [97] Schneider et al. (2010), Synthesis, characterization, defect chemistry, and FET properties of microwave-derived nanoscaled zinc oxide, *Chem. Mater.* 22, 2203-2212.
- [98] Hu X. L., Zhu Y. J., Wang S. W. (2004), Sonochemical and microwave-assisted synthesis of linked single-crystalline ZnO rods, *Mater. Chem. Phys.* 88, 421-426.
- [99] Vorobyova S. A., Lesnikovich A. I., Mushinski, V. V. (2004), Interphase synthesis and characterization of zinc oxide, *Mater. Lett.* 58, 863-866.
- [100] Lu C. H., Yeh C. H. (1997), Emulsion precipitation of submicron zinc oxide powder, *Mater. Lett.* 33, 129-132.
- [101] Kołodziejczak-Radzimska A., Markiewicz E., Jesionowski T. (2012), Structural characterization of ZnO particles obtained by the emulsion precipitation method, *J. Nanomater.* doi:10.1155/2012/656353
- [102] Li et al. (2009), Synthesis and morphology control of ZnO nanostructures in microemulsions, *J. Colloid Interface Sci.* 333, 465-473.
- [103] Singhai et al. (1997), Synthesis of ZnO nanoparticles for varistor application using Zn-substituted aerosol on microemulsion, *Mater. Res. Bull.* 32, 239-247.
- [104] Yildirim, Ö. A., Durucan C. (2010), Synthesis of zinc oxide nanoparticles elaborated by microemulsion method, *J. Alloy. Compd.* 506, 944-949.
- [105] Moleski R., Leontidis E., Krumeich F. (2006), Controlled production of ZnO nanoparticles from zinc glycerolate in a sol-gel silica matrix, *J. Colloid Interface Sci.* 302, 246-253.
- [106] Zhao et al. (1998), Acetate-derived ZnO ultrafine particles synthesized by spray pyrolysis, *Powder Technol.* 100, 20-23.



# CHAPTER 2

## Experimental Techniques





# 2

---

## Experimental Techniques

*This chapter elaborates the experimental methods employed to synthesize, characterize and fabricate the ZnO nanostructured powder/film and the prototype devices that are described in this thesis. Firstly, a brief description of the wet chemical route that is employed for preparing ZnO nanostructures is presented. Secondly, the substrate preparation procedures are presented. Finally, a brief review of the various analytical tools including their principle of operations for material characterizations are summarized.*

## 2.1. Wet Chemical Synthesis: Chemical Bath Deposition

This section is focussed on the details of the wet chemical synthetic technique which is used in this thesis. There are primarily three approaches falls into chemical based technique at low temperature, *i.e.*, the hydrothermal, chemical bath deposition (CBD) and electrochemical deposition. In this thesis, the chemical bath deposition (CBD) technique is used [1, 2]. Chemical bath deposition involves a variety of routes for producing functional oxide films and coatings at relatively low temperature by immersing a substrate in a liquid solution. The major advantage of CBD is that it requires only containers with a solution and mounting devices to hold the substrates. However one of the disadvantages of this technique is the wastage of solution after every single deposition. In contrary, CBD has many advantages such as, the yields are adherent, stable, and uniform with good reproducibility.

**Theory:** This technique enables to control the thickness of film and chemical composition by simply playing with the deposition parameters such as pH of the solution, concentration, temperature, and time. The merit of this technique relies on its inexpensiveness and also to coat large areas with high reproducibility. Basically, the deposition/growth of thin film is governed by chemical reactions from aqueous solutions [1]. Thus, by appropriately controlling the growth parameters, very precise composition of thin films can be achieved. In this method, the films are grown on a rigid (solid) substrate after immersing it into the dilute solutions containing one or more metal salts. The schematic diagram of chemical bath deposition technique is presented in Figure 2.1.

By means of this technique the metal oxide films will be deposited on substrates by following four major steps:

- Establishing an equilibrium state between the complexing agent and water
- Creation of metal-complex species
- Hydrolysis of the metal basis
- Construction of solid film on the substrate

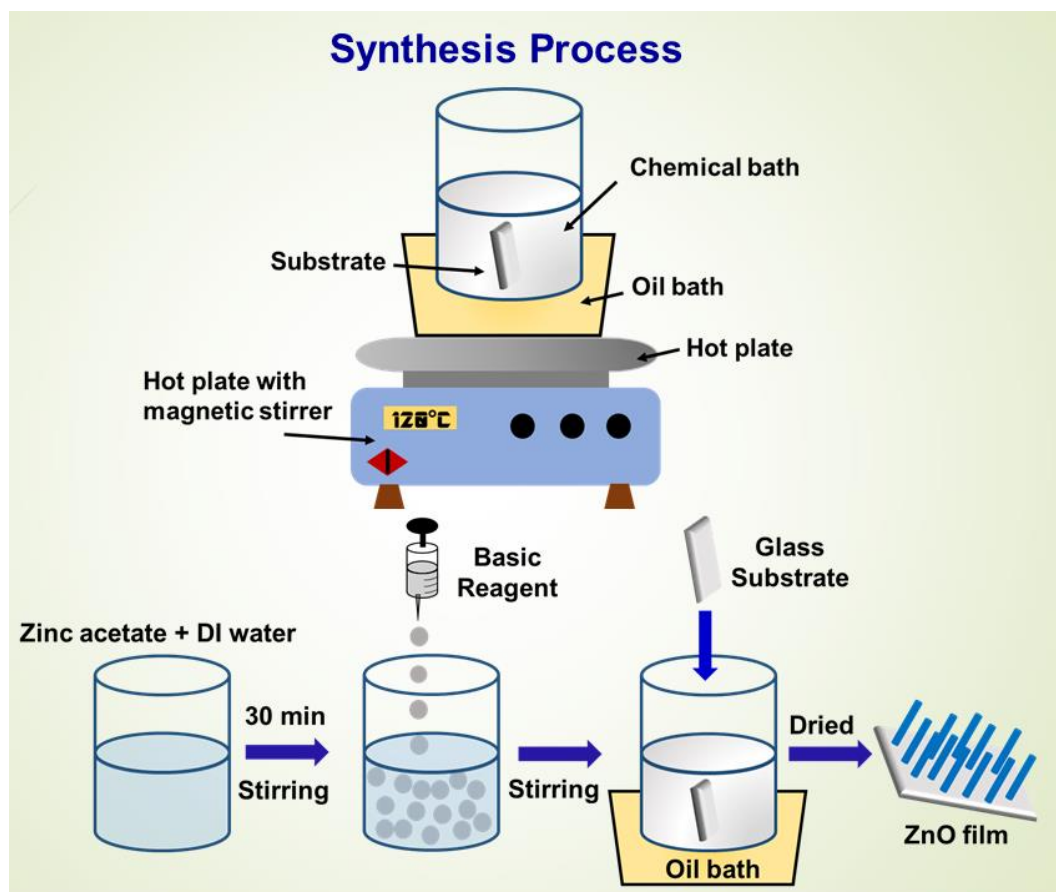


Figure 2.1. Schematic diagram of chemical bath deposition.

There is a critical requirement for the deposition of films, *i.e.*, when the value of solubility product is less than that of the ionic product, or else it will form a precipitate. During the reaction, the metal ions are complexed by an appropriate complexing agent that steadily releases metal ions. The rate of formation of metal hydroxides are controlled by the creation of metal-complex ions that finally led to solid film formation. Therefore, it is necessary for the metal ion to be complexed to prevent precipitation of metal hydroxide. The fundamental principle of CBD is to control the chemical reaction in order to get the desired film deposition by precipitation. For thin film deposition by CBD, three different possible processes described as follows:

**Ion by ion:** It is the simplest process where the condensation of ions takes place at the reacting surface to form a film.

**Cluster by cluster:** In this process, as an outcome of the homogeneous reaction, the colloidal particles are formed in the solution. These particles get absorbed on the surface of the substrate in order to form thin films.

**Mixed:** Normally, both the above stated procedures possibly interact with one another leading to film formation where the colloidal particles are contained within the growing layers. Here, based on the level of homogeneous and heterogeneous nucleation, the predominance of one route over the other is governed.

**Factors Influencing the Deposition Process:** The following factors influence the formation of a thin film by CBD

- Bath temperature
- Nature and concentration of the precursors
- Nature and concentration of the complexing agent
- pH of the solution
- Deposition time
- Nature of the substrate

**Bath Temperature:** A key factor that affects the reaction rate is the bath temperature. The As the temperature increases, dissociation of the complex increases. The kinetic energy of the molecule also increases leading to the greater interaction between the ions. This results in more increase or decrease in the film thickness depending on the extent of super saturation of the solution.

**Nature and concentration of the precursors:** Nature of the precursors influence the composition of the product. The growth kinetics also depends on the nature of the precursors. For example, when metal sulphate is used to deposit the metal Selenide film, the rate of deposition decreases and the thickness increases. Here the  $\text{SO}_4^{2-}$  ions obtained from the metal sulphate reduce the concentration of selenide ions. The deposition rate and terminal thickness initially increase with an increase in the ionic concentration of precursors. However, at higher concentrations, the precipitation becomes very fast leading to decrease in film thickness.

**Nature and concentration of complexing agent:** Nature of the complexing agent has great influence on the final products. For example, when EDTA is used as a complexing agent for FeS<sub>2</sub> thin film preparation, it was found that marcasite and other phases were formed rather than pyrite FeS<sub>2</sub>, while ammonia and EDTA were used this could be avoided to a great extent. Generally in a reaction, metal ion concentration decreases with the increase of complexing ion concentration. As a consequence, the rate of reaction and hence the precipitation are reduced leading to a large terminal thickness of the film.

**pH of the solution:** When the pH of the reaction bath increases, the metal complex usually becomes more stable reducing the availability of free metal ions. This will decrease the reaction rate resulting in a higher thickness of the film.

**Deposition time:** In general, the growth of good quality thin films proceeds at a slower rate. The CBD method is suitable for producing uniform thickness films.

**Nature of substrates:** It plays an important role in the reaction kinetics and adhesion of the deposited films. Hence, cleaning of the substrate surface is the first step in the thin film deposition. Higher deposition rates and thicknesses are observed for those substrates whose lattice parameters were well matched with those of the deposited material.

## 2.2. Substrate preparation procedure

For desired growth of a material or a prototype device in the field of nanotechnology, the prime requirement is the choice of substrates. The frequently used substrates in thin film processing are glass, quartz, silicon wafer, indium tin oxide (ITO) coated glass, Fluorine doped tin oxide (FTO) coated glass and mica. These substrates when purchased, are prone to impurities and some of the common sources of impurities are dust from the environment, oil, and grease from the hands and the dust while cutting the substrates for desired applications.

In the experimental works presented in this thesis, three types of substrates were used for instance glass, FTO coated glass and transparent polyester films. The glass substrates (2.54 cm × 2.54 cm) were purchased from *Microlife, JSGW, India*.

Initially, the substrates were cut into desired dimensions as required for the various characterizations with the help of a diamond cutter and a desktop electrical substrate cutting system (High Speed Diamond Cut-off Saw with Vise- SYJ- 40-LD). Normally,

the microscopic glass substrates were made in the dimension of 2.54 cm × 2.54 cm for optical measurements like UV-Vis, XRD and PL studies. The same glass substrates were cutted into minor pieces of 1 cm × 1 cm for XPS, FESEM. Finally, for the sensing device fabrication and electrical measurements, a planar configuration based on Alumina substrate 0.6 cm × 0.3 cm with Pt inter-digitized electrode and Pt electrode located on the back was constructed. The devices for electrical and sensing test were prepared by printing films of 10 μm thickness of nanorods dispersed in water.

**Substrate cleaning:** Two types of substrate cleaning processes were often practiced, wet cleaning and dry cleaning. In the present case, wet cleaning of the substrates were preferred.

**Wet cleaning:** After cutting the substrates into desired sizes, the substrates were first mechanically cleaned with organic solvents that include acetone (Merck, Germany), ethanol (Merck, Germany) and propanol (Merck, Germany) followed by rinsing with deionized water. The substrates were then cleaned ultrasonically by immersing in propanol and sonicated for 30 minutes at 40 °C. The substrates are then dried in an oven at a temperature of 50 °C.

## 2.3. Analytical characterization tools

### 2.3.1. X-ray Diffraction

Diffraction is one of the dominant tools to probe inside the materials to get information about the spatial arrangements of atoms conceived by Max von Laue in the year 1912 [3]. X-ray diffraction (XRD) belongs to a class of non-destructive analytical tool for phase identification of crystalline material. Laue and his co-workers have performed the first experiment with single crystals of copper sulfate and zinc sulfite where they discovered that crystalline substances acts as three dimensional diffraction gratings for X-ray wavelengths similar to the spacing of planes in a crystal lattice. After four years in 1916, the first powder diffraction pattern is produced by Debye and Scherrer [4]. XRD is often used to determine structural properties such as lattice parameters, strain, grain size, phase composition, orientation and thermal expansion.

**Theory:** The wavelength of X-rays is comparable to the interatomic distances in crystals and molecules. This permits X-rays to be diffracted from a crystalline specimen by irradiating on it according to Bragg's law:

$$2d \sin \theta = n\lambda \quad (2.1)$$

where,  $d$  is the interplanar spacing,  $\lambda$  is the wavelength of X-rays, and  $\theta$  is the glancing angle.

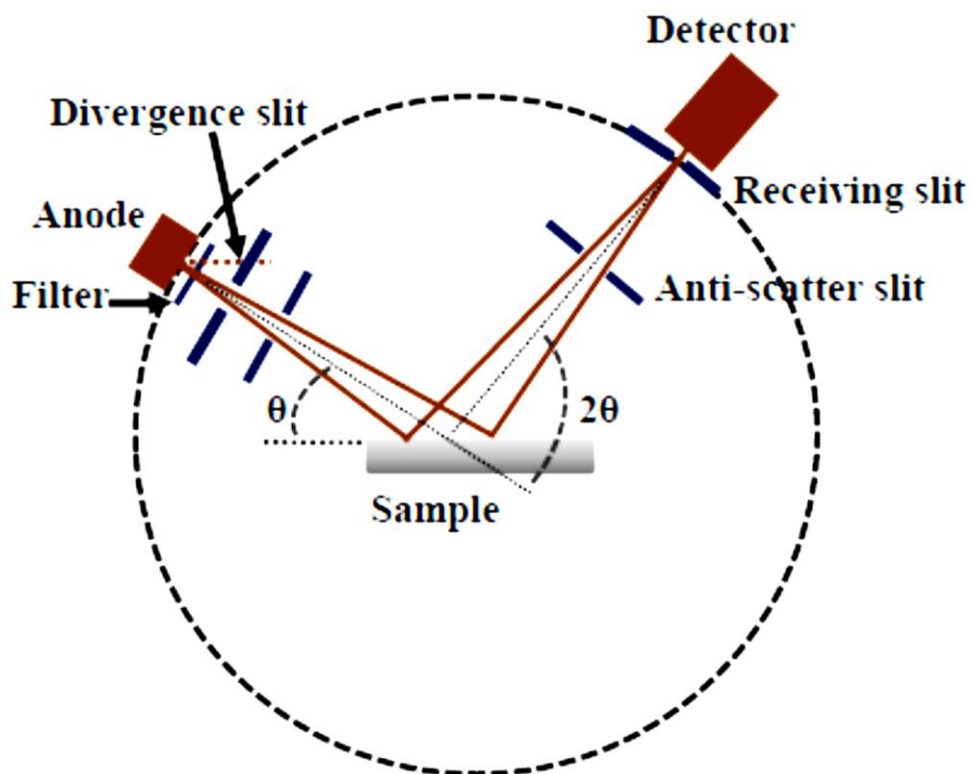


**Figure 2.2.** Scheme of different components of an XRD. The dotted circles represent the goniometer where the sample is placed in the centre. A divergent source of x-rays is focused on the flat plate sample which then diffracted and collected by the detector. The diffraction pattern is recorded by rotating both the source and the detector at an angle  $\theta$ , while the sample is kept fixed.

The method which is employed in XRD measurement is to measure the scattered intensity of an X-ray beam incident on a sample (Figure 2.2). The intensity of the diffracted beam is then measured as a function of the diffraction angle ( $2\theta$ ), the wavelength and the specimen's orientation. The experimentally obtained diffraction pattern of a specimen contains information about the Bragg's scattering angle ( $2\theta$ ), which is the unique signature of the material. The diffraction pattern of a material, as obtained experimentally, are compared with standard powder diffraction files published by the international center for diffraction data (ICDD) and thus the actual composition of the material can be deduced. ICDD which is formerly known as the joint committee on

powder diffraction standards (JCPDS) is the organization that maintains the diffraction database of organic and inorganic materials.

XRD measurements of the samples were performed using X-ray diffractometer (Bruker D8 Advance, Germany). The filtered copper  $K_{\alpha}$  (Cu  $K_{\alpha}$ ) radiation with a wavelength of 1.5406 Å was used for recording the diffraction pattern in the  $2\theta$  range of 10-80°. Standard corundum or silicon sample is often used for instrumental broadening corrections and Fullprof software is used for X-ray profile analysis.

### 2.3.2. X-ray Absorption Spectroscopy

X-ray absorption spectroscopy (XAS) is a widely used technique for determining the local geometric and/or electronic structure of matter. The experiment is usually performed at synchrotron radiation sources, which provide intense and tunable X-ray beams. Wilhelm Conrad Röntgen (March 28, 1845 – February 10, 1923) detected absorption of X-rays by matter, and he discovered X-rays (November 8, 1895) [5, 6]. The X-ray absorption spectrum is typically divided into two regimes: X-ray absorption near-edge spectroscopy (XANES) and extended X-ray absorption fine-structure spectroscopy (EXAFS). EXAFS began over ten years later than Röntgen X-ray discovery.

**Theory:** X-rays are light with energies ranging from approx. 500 eV to 500 keV, or wavelengths from approx. 25 to 0.25Å. At this energy regime, light is absorbed by all matter through the photo-electric effect.

When discussing X-ray absorption, we are primarily concerned with the absorption coefficient,  $\mu$  which gives the probability that X-rays will be absorbed according to Beer's Law:

$$I = I_0 e^{-\mu t} \quad (2.2)$$

where  $I_0$  is the X-ray intensity incident on a sample,  $t$  is the sample thickness, and  $I$  is the intensity transmitted through the sample.

XANES is strongly sensitive to formal oxidation state and coordination chemistry (e.g., octahedral, tetrahedral coordination) of the absorbing atom, while the EXAFS is used to determine the distances, coordination number, and species of the neighbours of the absorbing atom.

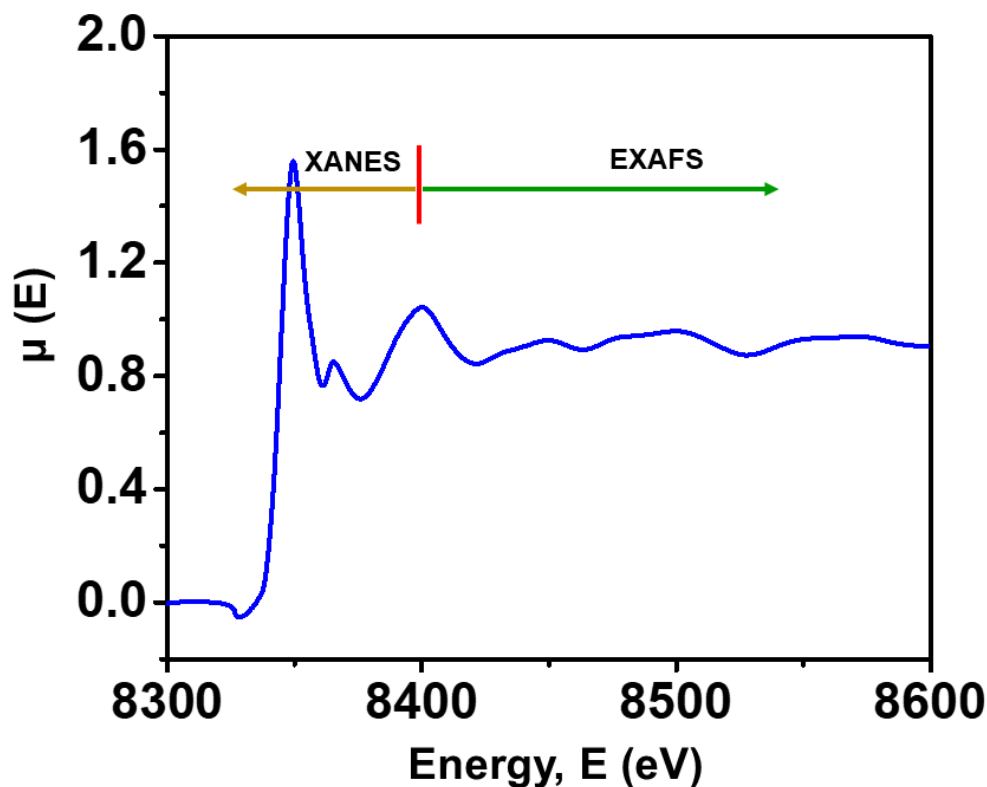


Figure 2.3. XAFS spectrum with EXAFS and XANES regions.

XAFS can be measured either in transmission or fluorescence geometries. We can measure the energy dependence of the absorption coefficient  $\mu(E)$  either in transmission as:

$$\mu(E) = \log \left( \frac{I_0}{I} \right) \quad (2.3)$$

or in X-ray fluorescence (or Auger emission) as

$$\mu(E) \propto \log \left( \frac{I_f}{I_0} \right) \quad (2.4)$$

where,  $I_f$  is the monitored intensity of a fluorescence line (or, again, electron emission) associated with the absorption process. For the EXAFS, we are interested in the oscillations well above the absorption edge, and define the EXAFS fine-structure function  $\chi(E)$ , as

$$\chi(E) = \frac{\mu(E) - \mu_0(E)}{\Delta\mu_0(E)} \quad (2.5)$$

where,  $\mu(E)$  is the measured absorption coefficient,  $\mu_0(E)$  is a smooth background function representing the absorption of an isolated atom, and  $\mu_0$  is the measured jump in the absorption  $\mu(E)$  at the threshold energy  $E_0$  EXAFS Equation,

$$\chi(k) = \sum_j \frac{N_j f_j(k) e^{-2k^2 \sigma_j^2}}{k R_j^2} \sin[2k R_j + \delta_j(k)] \quad (2.6)$$

where,  $f(k)$  and  $\delta(k)$  are scattering properties of the atoms neighbouring the excited atom,  $N$  is the number of neighbouring atoms,  $R$  is the distance to the neighbouring atom, and  $\sigma^2$  is the disorder in the neighbour distance. Though somewhat complicated, the EXAFS equation allows us to determine  $N$ ,  $R$ , and  $\sigma^2$  knowing the scattering amplitude  $f(k)$  and phase-shift  $\delta(k)$ . Furthermore, since these scattering factors depend on the  $Z$  of the neighbouring atom, EXAFS is also sensitive to the atomic species of the neighbouring atom.

In this work, XAS measurement, which includes both extended EXAFS and XANES measurements of Zn and Ni K-edges, are carried out at the beamline-9 at the Indus-2 synchrotron source. This beamline operates in the energy range of 4–25 keV and offers a typical resolution ( $\Delta E/E$ ) of  $10^{-4}$  at 10 keV photon energy. The beamline optics mainly consist of an Rh/Pt-coated collimating meridional cylindrical mirror and Si (111) double crystal monochromator (DCM). For horizontal beam focus, the second crystals were design as sagittal cylindrical and another Rh/Pt-coated bendable post mirror used for vertical focus. The 300 mm long 3 ionization chambers are used for data collection at the experimental hutch. In the first ionization chamber, the gas pressure with a mixture of gases was kept to the desired  $\sim 10$ -20% absorption, whereas in the second ionization chamber was 70–90% absorption to obtain better signal-to-noise ratio. For the present work, Zn and Ni K-edges XANES and EXAFS measurements were done in the transmission mode and the DCM energy was calibrated using standard Zn and Ni foils, respectively, before the third ionization chamber.

For the analysis of the EXAFS data, the energy dependent absorption coefficient  $\mu(E)$  has been converted to the energy dependent absorption function  $\chi(E)$  and then to the wave number dependent absorption coefficient  $\chi(k)$ . Finally  $k^2$  weighted  $\chi(k)$  spectra were Fourier transformed in  $R$  space to generate the  $\chi(R)$  versus  $R$  spectra in terms of the real distance from the center of the absorbing atoms. The analysis of the EXAFS data have

been carried out following the standard procedures using the IFEFFIT software package, [7, 8] which includes Fourier transform (FT) to derive the  $\chi(R)$  versus  $R$  plots from the absorption spectra using ATHENA software [9], generation of the theoretical EXAFS spectra starting from an assumed crystallographic structure using ARTEMIS software and finally fitting of  $\chi(R)$  versus  $R$  experimental data with the theoretical ones using the FEFF 6.0 code.[10] EXAFS data best fit were obtained to minimize  $R_{factor}$  in the above process and defined by the below formula:

$$R_{factor} = \sum \frac{[\text{Im}(\chi_{dat}(r_i) - \chi_{th}(r_i))]^2 + [\text{Re}(\chi_{dat}(r_i) - \chi_{th}(r_i))]^2}{[\text{Im}(\chi_{dat}(r_i))]^2 + [\text{Re}(\chi_{dat}(r_i))]^2} \quad (2.7)$$

where  $\chi_{dat}$  and  $\chi_{th}$  refer to the experimental and theoretical  $\chi(R)$  values respectively and *Im* and *Re* refer to the imaginary and real parts of the respective quantities.

### 2.3.3. X-ray Photoelectron Spectroscopy

X-ray photoelectron spectroscopy (XPS), is an extensively used technique for analyses of surface properties, developed by the noble laureate Kai Siegbahn in the 1960s [7]. XPS measurements are utilized for detecting the elemental constituents of a sample surface, the empirical formula of materials, any contamination on the sample surface, and electronic state of the elements.

**Theory:** XPS involves the photo-ionization and examination of the kinetic energy distribution of the emitted electrons. In XPS, soft X-rays of energy 100 – 2500 eV is usually used to study the core levels of the sample surface under ultra-high vacuum. Normally, when the sample is illuminated with X-rays of sufficient energy, it results in the excitation of electrons in the bound states leading to ionization and emission of the core electrons (Figure 2.4). The ejected photoelectrons are then collected with the help of a hemispherical electron analyzer which measures their kinetic energy. Based on the concept of the photoelectric effect, the electron analyzer produces an energy spectrum of the ejected photoelectrons versus binding energy according to the relation based on Ernest Rutherford [11]:

$$E_B = h\nu - (E_k + \Phi) \quad (2.8)$$

where,  $E_B$  is the binding energy of the photoelectrons,  $h\nu$  is the photon energy,  $E_k$  is the kinetic energy of the emitted photoelectrons and  $\Phi$  is the work function of the spectrometer.

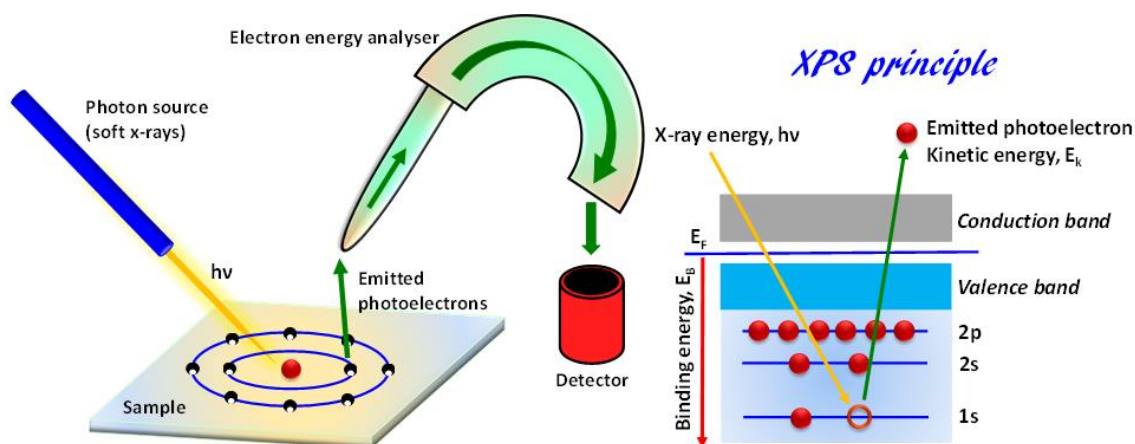


**Figure 2.4.** Schematic of the x-ray photoelectron spectroscopy showing its basic components.

The XPS data of the thin films are recorded with an angle integrated photoemission spectroscopy (AIPES) beam line at Indus-1 synchrotron radiation source (RRCAT Indore), which is equipped with a  $MgK_{\alpha}$  X-ray source (1253.6 eV) and a hemispherical electron analyser. The pressure inside the ion-pumped analysis reactor is sustained at  $1.0 \times 10^{-9}$  mbar throughout the data procurement. The shifting in the binding energy values as a result of surface charging effects is rectified using the C1s peak with a binding energy value of 285 eV taken as the standard reference. The accuracy of the binding energy values is within  $\pm 0.2$  eV.

### 2.3.4. Raman spectroscopy

Raman spectroscopy is based on the Raman Effect which is discovered in 1928 by C. V. Raman and K. S. Krishnan [12, 13]. It states that “when a monochromatic beam of light is scattered from a medium, the scattered radiation exhibit a change of wavelength.” This effect is specific to the molecule which causes it and can be used for spectroscopic analysis.

**Theory:** At the molecular level, radiation can interact with matter by absorption or scattering process. The scattering process can occur either by elastically or in-elastically. The elastic process is termed as the *Rayleigh scattering*, and the inelastic process is termed as the *Raman scattering*. *Raman Effect* arises when electric field vector of the incident photon interacts with electric dipole of the molecule. Raman spectroscopy is a form of vibrational spectroscopy. In quantum mechanical terms, the scattering can be regarded as exciting the system to a ‘virtual’ state. The system exchanges energy with the

incident photon and subsequently decays to a vibrational energy level above or below that of the initial state. In other words, incident and scattered photon exhibit a frequency shift corresponding to the energy difference which is termed as *Raman shift*. The scattered photon frequency either up- or down-shifted relative to that of the incident photon. The downshifted and upshifted components are termed as *Stokes* and *Anti-Stokes* lines respectively (Figure 2.5). Raman spectrum is a plot of the detected number of photons versus Raman shift from the incident laser frequency.

Classically, the interaction of light with the molecule can be pictured as the perturbation of the molecule's electric field. This interaction induces a dipole moment which is proportional to electric field strength and the molecular polarizability  $\alpha$ . A molecular vibration is Raman active only if there is a modulation of the molecular polarizability by the vibration [14].

$$\left(\frac{\partial\alpha}{\partial Q}\right) \neq 0 \quad (2.9)$$

where  $\alpha$  is the molecular polarizability which is a measure how an electron cloud around a molecule can be distorted,  $Q$  stands for the normal coordinate of vibration.

Similar to FTIR, Raman spectroscopy is a form of vibrational spectroscopy. Unlike IR spectroscopy, the interaction of radiation with matter is quite different in Raman spectroscopy. The IR-band arises due to change in the dipole moment of the molecule upon interaction with the incident radiation. The interaction is possible only when radiation fields' electric vector oscillates at the same frequency as the dipole moment. For IR active mode, the net change in permanent dipole moment must be modulated by normal vibration.

$$(\partial\mu/\partial Q)\neq 0 \quad (3.0)$$

where  $\mu$  is the dipole moment of the molecule.

Some of the Raman active modes are forbidden in IR, and other vibrations may be observed by both the techniques at significantly different intensities; therefore, Raman and IR spectroscopy gives a complementary image of molecular vibration. In 1928, the first-ever Raman 'instrument' was constructed which used monochromatized sunlight as a light source and human eye as a detector. The modern instrument typically consists of

a laser, Notch filter, a few lenses, and detector. The laser is used as a light source due to its high monochromaticity and high beam fluxes.

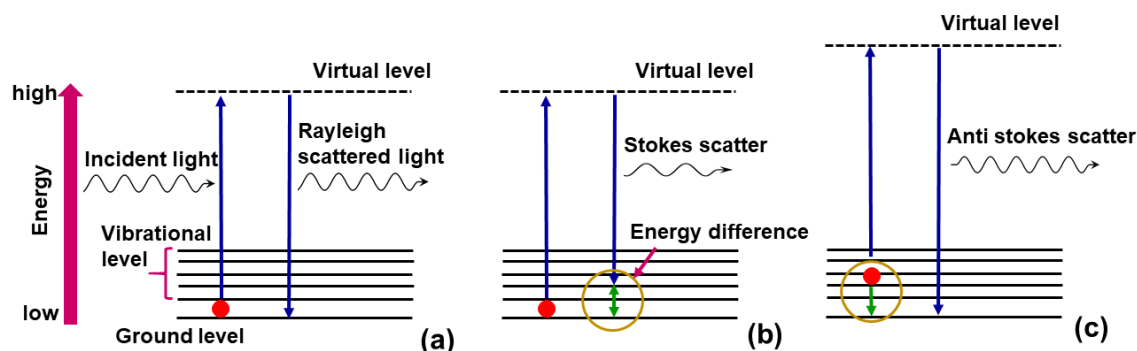


**Figure 2.5.** Raman transitional scheme (a) An electron is excited from ground state and falls back to the original position (b) An electron is excited from the ground state and falls to a vibrational level (c) An electron is excited from a vibrational level and falls to the ground level.

When monochromatic light is irradiated on a sample, the inelastically scattered light contains a spectrum of a wavelength longer and shorter than the excitation wavelength, which corresponds to the molecular vibration modes or crystal phonons. These bands are specific to molecular vibrations since the sample contains different materials having different vibrational modes. *Raman Effect* is very weak process (typically Stokes lines are  $\sim 10^5$  times weaker than the Rayleigh scattered components). Therefore, intense light sources and low noise detectors are used [15]. To remove elastically scattered a portion of the light from the sample, Raman spectrometer uses Notch filter which allows only the Raman scattered radiation to reach the detector.

Most Raman spectrometer is coupled with an optical microscope which is capable of giving conventional images along with Raman spectra from a particular spot on the sample. The microscope is capable of focusing the laser beam to a small spot ( $\sim 1$  micron) on the sample. Scattered light from the sample again passes back through the microscope optics into the spectrometer, detected by Charge Coupled Detectors (CCD) and a computer is used for data acquisition and curve fitting. CCD detectors are employed due to their low dark current, high quantum efficiency, and multichannel capability.

Raman scattering measurements of the samples are carried out using a Labram-HR 800 spectrometer with excitation radiation (wavelength of 488 nm) from an argon ion laser at spectra with a resolution of  $1 \text{ cm}^{-1}$ .

### 2.3.5. UV-Visible spectroscopy

Ultraviolet-Visible (UV-Vis) spectra refer to absorption or reflection spectroscopy in UV-Vis spectral region. When irradiated, molecules in a specimen absorb light in the ultraviolet and visible part of the electromagnetic spectrum and undergoes electronic transitions which give rise to UV-Vis spectra. Nowadays, UV-Vis spectroscopy becomes a reliable analytical tool for the qualitative and quantitative analyses of samples. The absorption or reflectance in the visible range directly affects the perceived color of the chemicals involved [16].

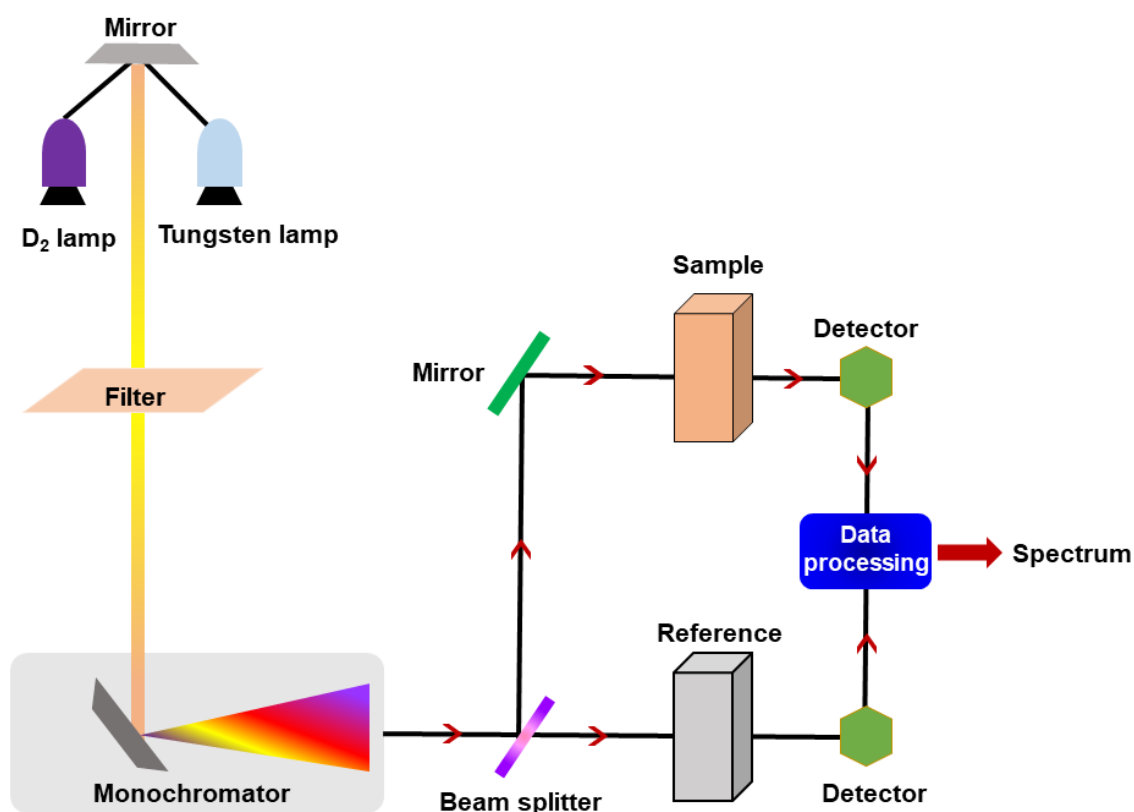


*Figure 2.6. Schematic diagram of UV-Visible spectrophotometer.*

**Theory:** When sample molecules are irradiated with UV or visible light having an energy equivalent to the possible electronic transition within the molecule, the electrons in the molecule absorb some of the light energy and are promoted to a higher energy orbital, which is characteristic of the atom. UV-Vis spectroscopy provides information about the dispersion and homogeneity of the solution which is calculated from the absorbance of a sample. The absorbance is proportional to the number of molecules absorbed in the spectrometer light beam. An optical spectrometer records both the degree of absorption

(i.e., intensity) and absorption peak for each wavelength. The resulting spectrum is a graph of absorbance versus wavelength. The wavelengths of the absorption peaks represent the types of bonds present in a given molecule and are valuable in determining the electronic transition in a molecule.

Essential parts of this photo-spectrometer are a light source, a diffraction grating in a monochromator, a detector and a sample holder (Figure 2.6). The light source consists of two lamps: Tungsten filament for visible region (300-2500 nm) and deuterium arc lamp (190-400 nm) or Xenon arc lamp (160-2000 nm) for UV region. Light emitting diodes (LEDs) may be used as a source of visible light. The detectors employed are typically photomultiplier tube, a photodiode or charged coupled devices. Single photodiode detectors and photomultiplier tubes are used with scanning monochromator, which filters the different wavelengths of light, such that light of single wavelength reaches the detector at one time. The scanning monochromator allows the diffraction grating to “step through” each wavelength so that its intensity may be measured as a function of wavelength. The output of the detector is a plot of intensity versus wavelength which contains information about the sample. In this work, Agilent Cary-60 is used for UV-Vis spectrophotometer. The optical bandgap is determined by the diffuse reflectance spectroscopy mode.

### **2.3.6. Photoluminescence spectroscopy**

Photoluminescence (PL) spectroscopy is a very efficient and important technique for the investigation of optoelectronic properties of materials [17]. This technique encompasses the measurement of the emitted photons as a result of optical excitation. The energy distribution of the photons is later examined to compute the properties of materials which include defect species/concentrations, probable stimulated emission, *etc.* It is widely recognized as a useful tool for understanding and elucidating the physics that is accompanied by radiative recombination. PL is convenient in computing optical emission efficacies, composition, impurity content, *etc.*

**Theory:** The schematic representation of PL spectrometer is shown in Figure 2.7. When the light of adequate energy falls on a material, photons get absorbed by creating excitations. These excited carriers when relaxes to the lower energy states often accompanied by the emission of photons. However, only the photon energy which is equal

to or higher than the band-gap of the material, the absorption can happen in materials as suggested from the above mentioned UV-Vis absorption. Therefore, choice of different excitation sources to do the measurements should be made according to the materials with different electronic band structure or absorptions. The PL peak positions, therefore, provide detailed information on the discrete electronic states.

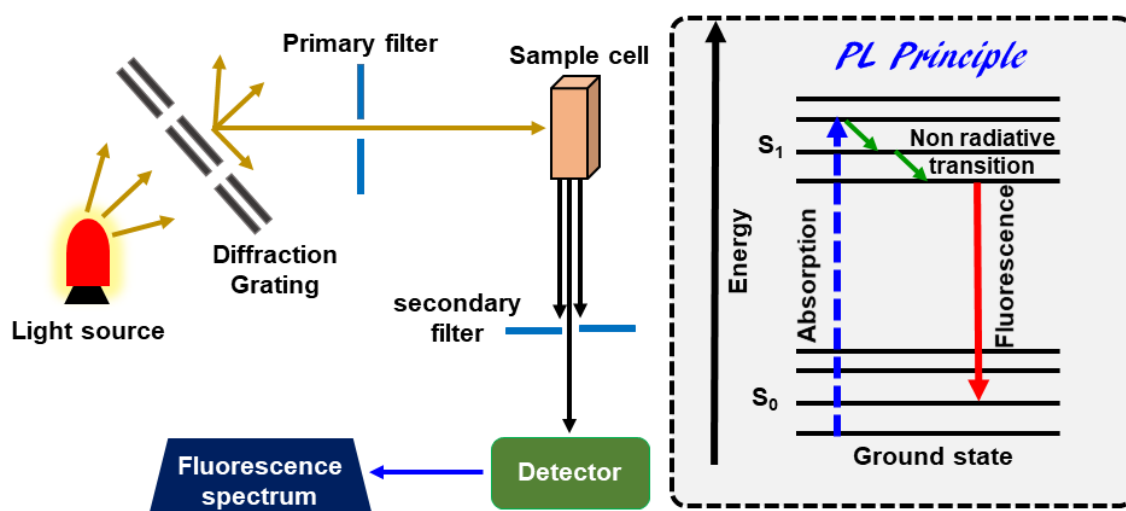


Figure 2.7. Schematic diagram of Photoluminescence spectrometer.

Room temperature fluorescence spectroscopic measurement is conducted using a spectrofluorometer having a Xe lamp source (excitation wavelength of 325 nm), Horiba Jobin Yuon fluorolog-3.

### 2.3.7. Field Emission Scanning Electron Microscopy

A scanning electron microscope (SEM) uses a beam of electrons to image samples in a raster scan pattern. SEM is one of the most heavily used microscopic instruments in research areas today because of its extremely high magnification, larger depth of focus, higher resolution and ease of sample observation [18].

**Theory:** SEM uses a beam of electrons to image the samples. A precise selection of electron energies over a desired range makes it possible to produce an image with high resolution. An SEM consists of the following components: (i) an electron gun, (ii) electromagnetic lens system, (iii) detectors and (iv) a stage or sample holder. The electron gun provides an intense beam of high energy electrons. There are two type of guns, which are Thermionic gun and Field emission gun. The thermionic gun uses a heated filament

to overcome the work function of the filament material, such that the electron can escape from the material itself. While the field emission gun uses a large electrical potential gradient across the filament to pull out the electrons. The electron beam follows a vertical path through the column of the microscope. It passes through the electromagnetic lenses which focus and direct the beam down towards the sample.

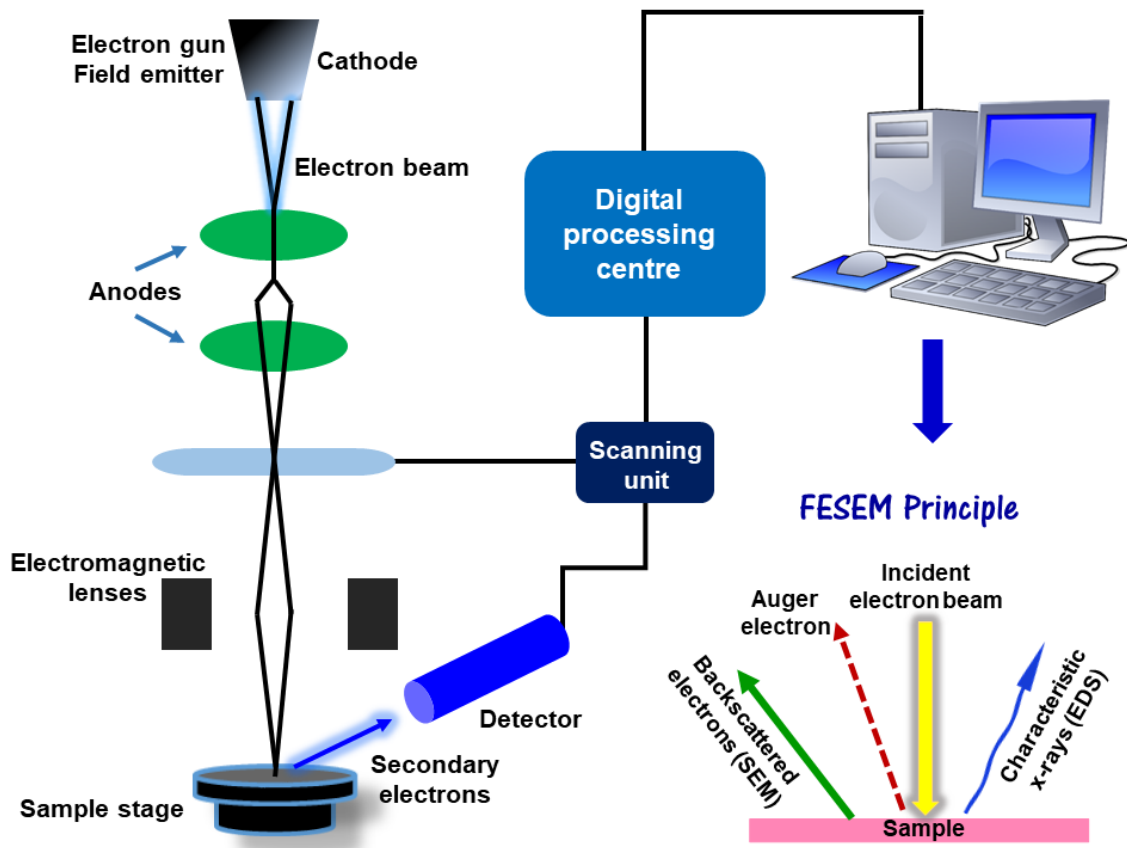


*Figure 2.8. Schematic representation of electron-sample interaction in an SEM.*

The high energy electrons upon interaction with the samples undergo either inelastic scattering with the atomic electrons or elastic scattering with the atomic nucleus. As a result of electron sample interaction backscattered electrons (BSEs), secondary electrons (SEs), and characteristics X-rays are produced. Several detectors are employed to detect these BSE electrons, SE electrons (Everhart-Thornely detector) and X-rays. The SE produces a most detailed image of the surface of an object, while BSE image can provide atomic number contrast in addition to topographic contrast. X-ray detectors give information on the composition of a substance (Figure 2.8).

The stage holds the sample on small stainless steel screws called ‘stub’ (size approx.: 8 x 8 mm). The stage can be placed at different angles and can be rotated to make different images at different orientations. A modern electron microscope uses field emission technology for ultra-high resolution  $\sim 0.5$  nm, magnification  $\sim \times 1,000,000$  of electron imaging, which is far better than compared to conventional scanning electron microscopes. The combination of higher magnification, greater resolution, larger depth of field, compositional information and user-friendliness of the apparatus and general simplicity of the image interpretation makes the SEM as one of the most heavily used instruments for research purposes.

Sample preparation is relatively easy in SEM. A thin metallic film of gold-palladium about 2 nm thickness is sputter coated on the samples and viewed under the SEM. The surface morphology of ZnO films is observed by field emission scanning electron microscopy (FESEM, Supra 55 Zeiss, UK). The system is also equipped with EDS analyzer (Oxford Instruments, UK), which is used for compositional analysis ZnO films.

### 2.3.8. Transmission Electron Microscopy

A transmission electron microscope (TEM) is a very potent tool for material characterization on the microscopic scale. A TEM provides information about the microstructural, crystal structure and micro-chemical state with a high spatial resolution from each of the microscopic phases individually [19].

**Theory:** TEM uses a high energy electron beam to ‘see through’ the specimen. The electrons beam interaction (Figure 2.9) with the sample gives the following results:

- A part of the high energy electron beam get transmitted, and part of it scattered while passing through the specimen.
- Transmitted electrons suffer no interaction and no loss of energy in the specimen which carries information about the structure of the sample. Elastically scattered electrons get diffracted from their original path while passing through the specimen, without loss of energy and transmitted through the remaining portion of the specimen.
- All incident electrons which are scattered by some atomic spacing will be scattered by the same angle and will follow the Bragg’s law. This diffracted beam carries the

information about the orientation, atomic arrangements, and phases present in the area being examined.

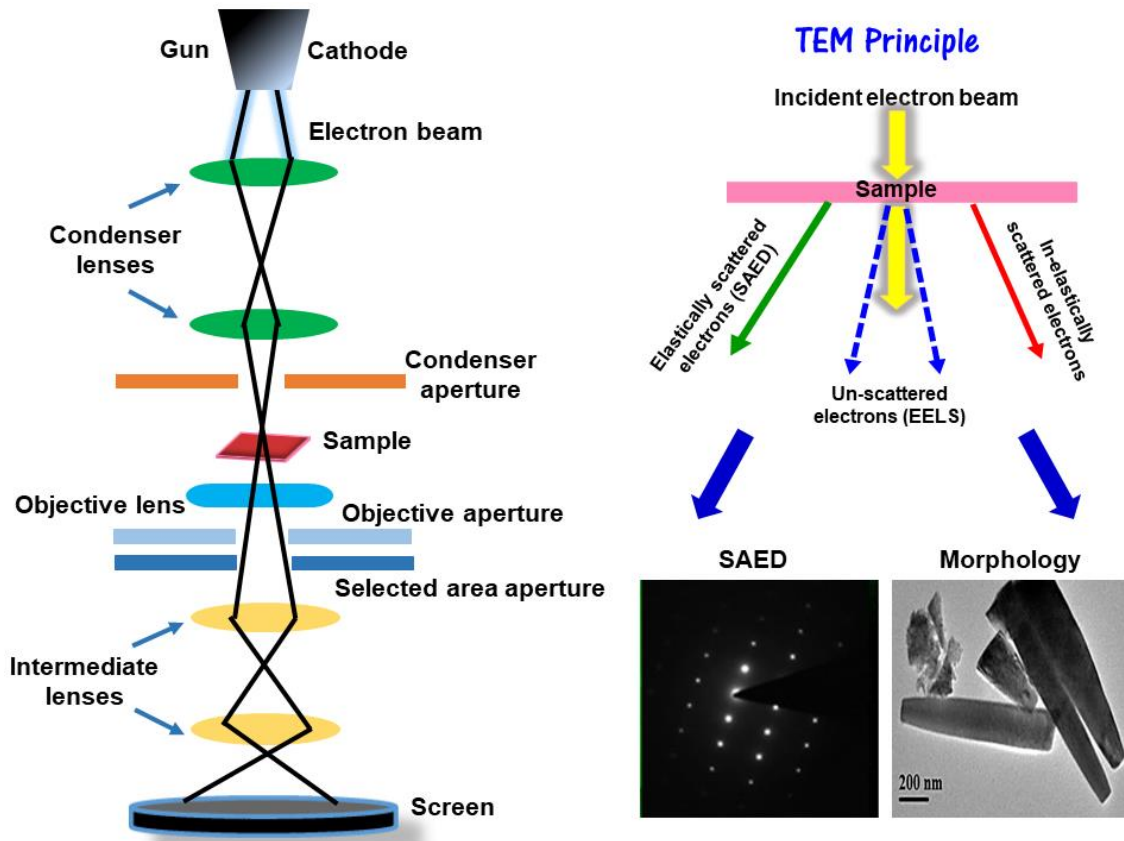


*Figure 2.9. Schematic representation of electron-sample interaction in a TEM.*

- The transmitted beam gives a bright field image of the specimen. A dark field image is formed when one of the diffracted beams is selected by using a selected area diffraction aperture.
- The incident electrons also inelastically interact with the specimen, then lose their energy due to this interaction and transmitted through the rest of the specimen. The loss of energy due to the inelastic scattering of electrons (Electron Energy Loss Spectroscopy or EELS) can be measured. This information can be used to determine elemental composition, chemical bonding and valence and conduction band electronic properties.

Similar to SEM, a modern TEM is composed of filament, an objective lens system, magnification system, a specimen stage and data recording and chemical analysis system.

Sample preparation in a TEM is essential because the sample has to be thin enough to pass the electron beam through it.

JEOL JEM-2100 and JEOL 3010 with UHR pole piece which is a computer-controlled high-resolution transmission electron microscope (HRTEM) are used to characterize the samples in our research work. The samples are prepared by sonicating the glass substrate with as-grown ZnOs present on the surface. The sonication process is carried out for 30 minutes in propanol. It results scrapping away of the ZnO nanostructures from the substrate and dispersion in the propanol. This solution is cast on to copper TEM grid using a micropipette and allowed to dry for another 30-60 minutes inside a heating furnace, such that only ZnO samples are left behind. The ZnO samples are examined using TEM in the bright field as well as dark field imaging modes. Modern high-resolution transmission electron microscopy (HRTEM) is the ultimate tool for imaging at the atomic scale and has excellent analytical performance. HRTEM images are analyzed using ImageJ software, which is a public domain Java-based image processing program developed at the National Institutes of Health, USA.

### **2.3.9. Secondary Ion Mass Spectrometry**

Secondary ion mass spectrometry (SIMS) is based on the observation of secondary ions (charged particles) that are ejected from a sample surface when bombarded by a primary ion beam [20]. SIMS is a powerful imaging technique providing chemical information with high spatial resolution ( $< 50$  nm). Besides the advantages of being label-free and having molecular specificity, which is also obtained with any other mass spectrometric imaging techniques, SIMS provides chemical information potentially at submicron spatial resolution. In addition, it is versatile and capable of ionizing chemical species from almost all kinds of materials.

*Theory:* The chemical ejection and ionization process of SIMS is shown in Figure 2.10. In brief, a focused ion beam, typically with energy in the range of 5 keV to 40 keV, impacts the sample surface resulting in the ejection of secondary species (positive, negative, and neutral), the charged portion of which can be extracted and mass analysed. The mass analysers can be time-of-flight (ToF), ion trap, and magnetic sector; however, the most commonly used analyser for biological analysis is the ToF due to its capability to rapidly carry out parallel mass detection with good mass resolution and mass range.

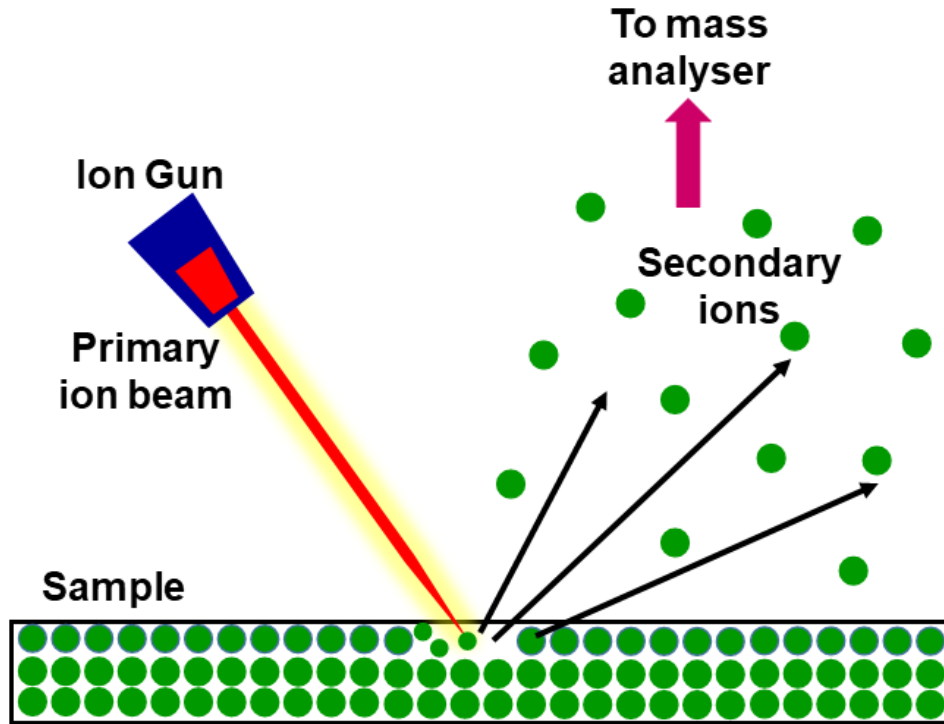


Figure 2.10. Ion ejection process in SIMS.

Secondary ion mass spectrometry (SIMS) was performed on the Sr doped ZnO films in the Hidden Analytical SIMS Workstation (Primary ion  $O^{2+}$ , Energy 5keV, Beam Current 400 nA). The measurement was performed in the presence of electron flood gun (500 eV) to avoid charging at a base pressure of  $8 \times 10^{-10}$  mbar and operating pressure  $8 \times 10^{-8}$  mbar. The intensity of the sputtered element depends on many factors like sputtering yield, ionization probability of the individual elements, *etc.* and the elemental intensity ratio for a simple compound can be expressed as,

$$\frac{C_A}{C_B} = K \frac{I_A}{I_B} \quad (3.1)$$

Where, the proportionality constant  $k$  is the relative sensitivity factor (RSF) for compositional analysis,  $I_A$  and  $I_B$  are the intensity of  $A$  and  $B$  element respectively, and  $C_A$  and  $C_B$  are the surface concentration of  $A$  and  $B$  element, respectively, in the compound. In case of the Sr doped ZnO films, as the neighbor of the element (Sr or Zn) is similar and same experimental environment is maintained for all the films, the RSF value is considered to be identical for all samples.

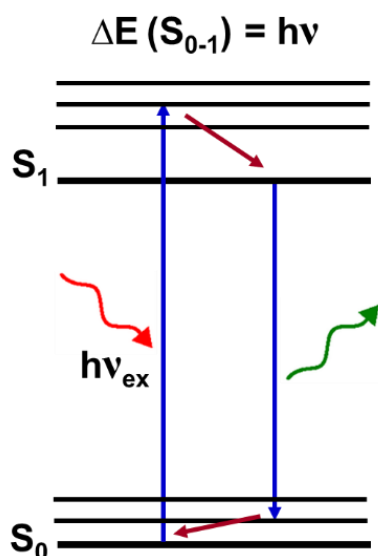
### 2.3.10. Two photon Absorption

Two photon absorption (TPA) is one of the most basic radiation-matter interaction mechanisms. It is a very important tool in laser spectroscopy as it makes possible the transition between two states that cannot be connected by electric-dipole interaction [21].

**Theory:** Two-photon absorption (TPA) is the absorption of two photons of identical or different frequencies in order to excite a molecule from one state (usually the ground state) to a higher energy electronic state (Figure 2.11). The energy difference between the involved lower and upper states of the molecule is equal to the sum of the photon energies of the two photons. Two-photon absorption is a second-order process, several orders of magnitude weaker than linear absorption at low light intensities. It differs from linear absorption in that the atomic transition rate due to TPA depends on the square of the light intensity. Thus it is a nonlinear optical process, and can dominate over linear absorption at high intensities. Two-photon absorption (TPA) is a third order nonlinear optical phenomenon in which a molecule absorbs two photons at the same time. The transition energy for this process is equal to the sum of the energies of the two photons absorbed. The probability that a molecule undergoes two-photon absorption depends on the square of the intensity of the incident light if the two photons are from the same beam (in the case of two incident beams, the transition probability depends on the product of the beams intensities). This intensity dependence is at the origin of the interest in two-photon absorbing materials for use in microscopy and microfabrication applications.

Open aperture Z-scan which measures the total transmittance as a function of incident laser intensity was employed to study the off-resonant third-order nonlinear optical properties of the Ni doped ZnO nanorods. The Z-scan of the samples at the peak on-axis intensity of 360 MW/cm<sup>2</sup>. As the bandgap of all ZnO is (3.3 eV) well above the single photon energy of 532 nm, it is reasonable to assume that a two photon process occurs in the samples. Expectedly, the Z-scan peak-shape response indicates the TPA for the samples. To derive the TPA coefficient ( $\beta$ ) of the samples, we have measured the intensity-dependent normalized transmittance, where the input intensity was tuned from 10 to 360 MW/cm<sup>2</sup>.

### One-photon absorption



### Two-photon absorption

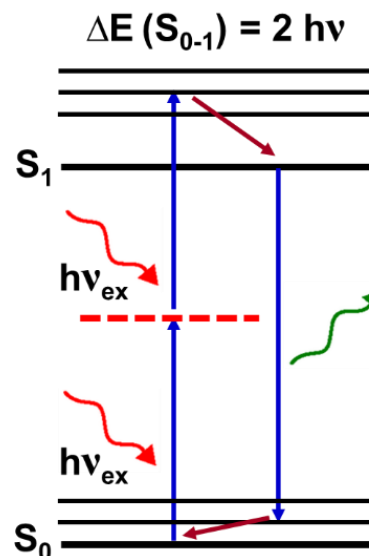


Figure 2.11. Illustration of single photon absorption (left) and two photon absorption (right) for a sample.

#### 2.3.11. Field electron emission

The theory of electron emission from metals under the influence of strong electric fields has been applied in field electron and ion microscopy. Adsorption and desorption from surfaces, metal, and semiconductor interface studies have been performed by Gomer, Dyke and Dolan, Swanson and Bell and Gadzuk and Plummer [22].

Although field emission was first observed by R.W. Wood in 1897, theoretical predictions of the current voltage characteristics were not particularly successful, since field emission was viewed as a classical process in which electrons were thermally activated and traversed a field reduced potential barrier. A satisfactory theoretical explanation of field emission had to wait for the advent of quantum mechanics. Using Schrödinger's wave theory, Fowler and Nordheim satisfactorily explained field emission as the quantum mechanical tunneling of electrons from the metal into vacuum under the influence of the applied electric field. The now commonly referred to Fowler-Nordheim (F-N) equation, describes the relation between the emission current density  $J$ , the surface work function, and the applied electric field strength  $F$ .

**Theory:** Field emission for electrons to escape from a metal surface, they need to have sufficient energy to overcome the potential barrier across the metal-vacuum interface. This quantity is called the work function and corresponds to the potential difference

between the Fermi level ( $E_F$ ) of the metal and the field free vacuum ( $E_v$ ). The work function is a surface property of the material and depends on the electronic structure and orientation of the crystal plane. It differs for different crystallographic orientations of the same material. For example, crystalline Mo has reported work functions of 4.36 eV for the (112) face to 4.95 eV for the (110) crystallographic orientation. The work function plays a dominant role in determining electron emission characteristics of metals.

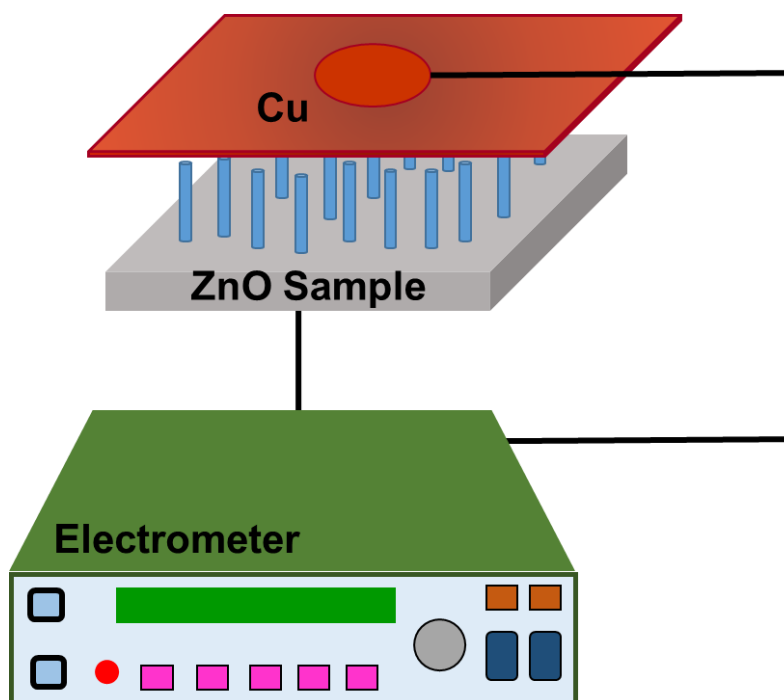


*Figure 2.12. Schematic of field emission set up.*

Field emission investigations were carried out in a planar diode configuration in all-metal ultrahigh vacuum (UHV) chambers, which were evacuated to a base pressure of  $\sim 1 \times 10^{-8}$  mbar. A typical diode configuration consisted of a phosphor-coated semi-transparent indium tin oxide glass disc (a circular disc having a diameter of  $\sim 50$  mm), which acted as an anode. A Ni-doped ZnO nanostructure sprinkled onto a piece of UHV-compatible conducting carbon tape pasted on a copper rod holder (diameter  $\sim 5$  mm) served as the cathode. The emission current was measured by a Keithley electrometer (6514) by sweeping a DC voltage applied to the cathode in steps of 40 V (0–40 kV, Spellman, U.S.) (Figure 2.12). The stability of the field emission current was investigated using a computer-controlled data acquisition system with a sampling interval of 10 seconds. Special care was taken to avoid any leakage

current using shielded cables and proper grounding. Field emission images were recorded using a digital camera (Canon SX150 IS).

### 2.3.12. Gas sensing experiment

Gas sensing is a process that detects the presence of harmful gases in an area, often as part of a safety system. This type of equipment is used to detect a gas leak or other emissions and can interface with a control system so a process can be automatically shut down. A gas detector can sound an alarm to operators in the area where the leak is occurring, giving them the opportunity to leave. This type of device is important because many gases can be harmful to organic life, such as humans or animals. Gas detectors can be used to detect combustible, flammable and toxic gases, and oxygen depletion. This type of device is used widely in industry and can be found in locations, such as on oil rigs, to monitor manufacture processes and emerging technologies such as photovoltaic. They may be used in firefighting.

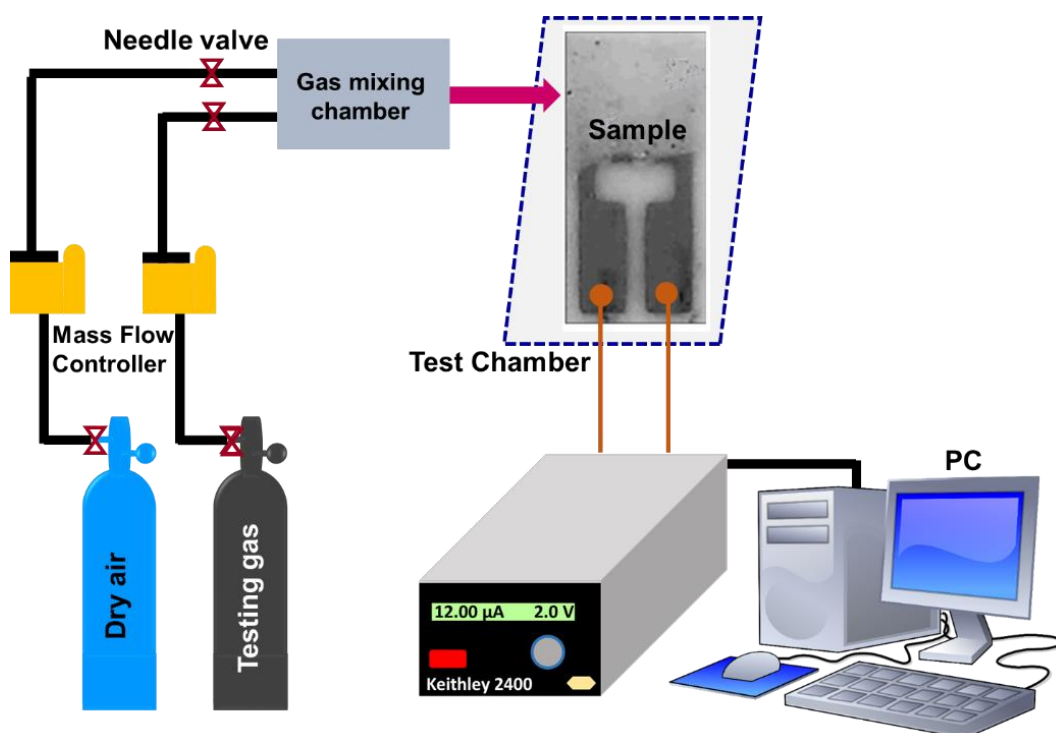


*Figure 2.13. Schematic of the gas sensing setup used for the detection of various gases.*

Sensing tests were carried on resistive sensors having a planar configuration and based on alumina substrates ( $6\text{ mm} \times 3\text{ mm}$ ) with Pt interdigitated electrodes and a Pt heater located on the back. The devices for electrical and sensing tests were prepared by printing films ( $\sim 10$

µm thick) of the nanorods dispersed in water. A pictorial representation of the sensing setup with the device is shown in Figure 2.13.

The sensors were then introduced in a Teflon test chamber for the sensing tests. The electrical measurements were carried out over the temperature range from RT to 350 °C under a synthetic dry air (20% O<sub>2</sub>–80% N<sub>2</sub>) stream of 100 sccm by collecting the electrical resistance of the sensitive films. An Agilent 34970A multimeter data acquisition unit was used for this purpose, while an Agilent E3632A dual-channel power supplier instrument was employed to bias the built-in heater of the device. Sensing tests were performed by injecting pulses of the analytic from certified bottles. The concentration of the target gas was varied by using mass flow controllers. The gas response is defined as the ratio  $R_{\text{air}}/R_{\text{gas}}$ , where  $R_{\text{air}}$  is the electrical resistance of the sensor in dry air and  $R_{\text{gas}}$  the resistance at different target gas concentrations.

## References

- [1] Guire M. R. D., Bauermann L. P., Parikh H., Bill J. (2013), Chemical bath deposition. Chapter 14, Springer, London, pp 1-801, ISBN 978-3-211-99310-1.
- [2] Hodes G. (2002), Chemical solution deposition of semiconductor films, Marcel Dekker, Inc. New York, pp 1-379, ISBN 0-8247-0851-2.
- [3] Dinnebier R. E., Billinge S. J. L. (Eds.) (2008), Powder Diffraction: Theory and Practice, RSC Publishing, Cambridge, UK, pp 1-582, ISBN 978-0-85404-231-9.
- [4] Cullity B. D., Stock S. R. (2001), Elements of X-Ray Diffraction, 3<sup>rd</sup> edition, Prentice Hall, Inc., New Jersey, pp 1-531, ISBN 9789332535169.
- [5] Bunker G. (2010), Introduction to XAFS: A practical guide to x-ray absorption fine structure spectroscopy, Cambridge University Press, pp 1-260, ISBN 9780511809194.
- [6] Gaur A., Shivastava B. D., Nigam H. L. (2013), X-ray absorption fine structure (XAFS) spectroscopy-A review, Proc, Indian Natn. Sci. Acad. 79, 921-966.
- [7] Konigsberger D. C., R. Prince, (1988) R.X-Ray Absorption: Principles, Applications, Techniques of EXAFS, SEXAFS and XANES, Wiley: New York, ISBN: 978-0-471-87547-5.
- [8] Kelly S. D., Hesterberg D., Ravel B., (2008), In Methods of Soil Analysis Part 5: Mineralogical Methods, Ulery, A.L, Drees, L. R., Eds.; Soil Science Society of America: Madison, WI, Chapter 14; pp 367–464, ISBN: 978-0-89118-846-9.
- [9] Ravel B., Newville M., (2005), Athena, Artemis, Hephaestus: Data Analysis for X-ray Absorption Spectroscopy using IFEFFIT. J. Synchrotron Radiat. 12, 537–541.
- [10] Zabinsky S. I., Rehr J. J., Ankudinov A., Albers R. C., Eller M. J., (1995), Multiple Scattering Calculations of X-Ray-Absorption Spectra. Phys. Rev. B: Condens. Matter Mater. Phys. 52, 2995–3009.
- [11] Hollander J. M., Jolly W. L. (1970), X-Ray photoelectron spectroscopy, Acc. Chem. Res. 3, 193-200.
- [12] Watt J. F. (1994), X-Ray photoelectron spectroscopy, Vacuum 45, 653-671.
- [13] Raman, C. V., Krishnan, K. S. (1928), A new type of secondary radiation, Nature 121, 501.
- [14] Smith E., Dent G. (2005), Modern Raman Spectroscopy: A Practical Approach (John Wiley & Sons Ltd. pp 1-225, ISBN 0-471-49668-5.

- 
- [15] Schrader B. (Ed.) (1995), *Infrared and Raman Spectroscopy*, VCH Publishers, New York, pp 1-787, ISBN 3-527-26446-9.
- [16] Britton G. (1995), *UV/Visible Spectroscopy*, ChemInform, Wiley, 10.1002/chin.199532313.
- [17] Ronda C. R. (2007), *Luminescence: From Theory to Applications*, Wiley, pp 1-276, ISBN: 978-3-527-31402-7
- [18] Vernon-Parry K. D. (2000), *Scanning electron microscopy: An introduction*, III-Vs Review, 13, 40-44.
- [19] Williams D. B., Carter C. B. (1996), *The Transmission Microscope*, Springer, pp 1-275, ISBN 978-0-387-76501-3.
- [20] Gross J. H. (2011), *Mass Spectrometry – A Textbook (2nd ed.)* Springer Verlag, Heidelberg.
- [21] Pèrez-Arjona I., de Valcárcel G. J., Roldán E. (2003), Two-photon absorption, *Revista Mexicana De Física*, 49, 91–100.
- [22] Gadzuk J. W., Plummer E. W. (1973), Field emission energy distribution. *Rev. Mod. Phys.* 44, 487.



## CHAPTER 3

### Controlled Growth of Zinc Oxide (ZnO) Nanostructures



- **Amit K. Rana**, Yogendra Kumar, Niharika Saxena, Rajasree Das, Somaditya Sen, Parasharam M. Shirage. *AIP Advances* 5(9), 097118, 2015.
- Yogendra Kumar, **Amit K. Rana\***, Prateek Bhojane, Manojit Pusty, Vivas Bagwe, Somaditya Sen, Parasharam M. Shirage. *Materials Research Express* 2(10), 105017, 2015. \*(equal contribution)



# 3

---

---

## Controlled Growth of Zinc Oxide (ZnO) Nanostructures

*In the pursuit of synergic activity, metal oxides are inspiring the world of nanotechnology through their unique properties. ZnO is positioned as one of the most widely studied material due to its multiple functionalities and its unique physical and chemical properties. It is well documented in the literature and also discussed in chapter one, that how the material properties are strongly dependent on the shape and size or morphology of the material at the nanoscale. Hence it is of prime importance to study and control the morphology of this ZnO material by varying different growth parameters such as time, temperature, concentration, precursors, capping molecule, and solvents [1-5].*

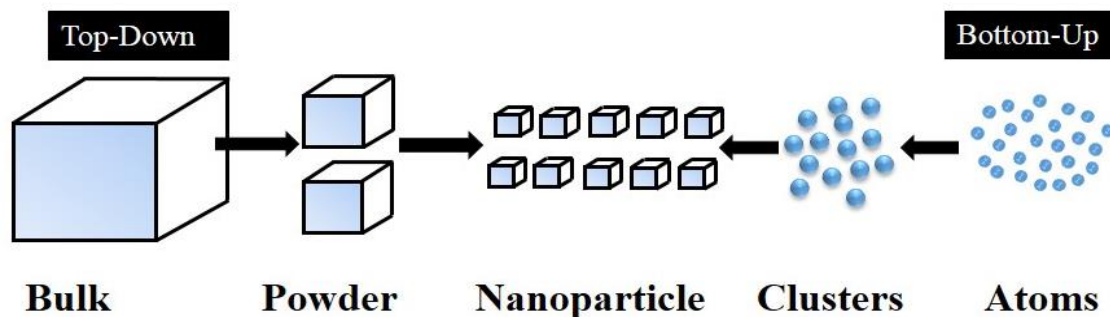


**Figure 3.1.** Techniques for synthesis of nanomaterial: top-down and bottom-up approach.

Basically, for synthesis and controlling the size of nanomaterials, there are two approaches “Top-down” and “Bottom-up”. As shown in Figure 3.1, in case of “Top-down” approach, the nanostructures are synthesized by etching out crystal planes (removing crystal planes) which are already present on the bulk substrate. This approach can thus be viewed as an approach where the building blocks are removed from the bulk to form the nanostructure. However, this technique needs high power to decrease the size of the particles physically. Unlike the top down approaches, the bottom up approaches are typically driven by thermodynamic aspects and make use of much weaker forces like chemical bonding, the intermolecular attraction for nanomaterial synthesis. This involves with assembling of the nanoparticles from fundamental building blocks of matter: atoms and molecules, *etc.* This technique is also classified into two broad groups: gas phase methods and wet chemical methods, depending on the medium at which nanoparticles form. Keeping in view of the excellent properties with the extensive use of ZnO, different types of synthesis techniques formulated over the past decades. Concerned with ZnO nanostructure, although different vapour-phase processes, fabrication methods, such as vapour–liquid–solid epitaxial (VLSE) growth, metal–organic chemical vapour deposition (MOCVD), and thermal evaporation have been developed [6, 7]. In the wet chemical process; hydrothermal methods, precipitation methods, electrochemical deposition, sol-gel deposition, *etc.* have been widely used [8, 9]. These processes need sophisticated equipment, for instance, high temperatures and vacuum, adequate atmospheric control, harmful chemical, multistep process, *etc.*, which make them very hard and complicated to grow ZnO nanostructure in large-scale for commercial application. Another problem associated with nanostructured ZnO is the growth mechanism, and growth habit of ZnO nanostructure because of different growth processes. However, the previous and recent

reports on growth process explain the growth mechanism, but from the literature survey, we did not find any conclusion on the accurate understanding of the growth process for preparing diverse nanostructures of ZnO [10-18].

Recently, low-temperature wet chemical methods have received more attention and already have been commonly used to grow ZnO nanostructures. There are mainly three common approaches in chemical growth at low temperature, *i.e.*, the hydrothermal, chemical bath deposition (CBD) and electrochemical deposition. In present work CBD method is employed to grow the ZnO nanostructures. One of the major advantages of this process is that the growth temperature can be as low as 60°C without any need of autoclave and sophisticated instrument. Materials growth at such low temperature, makes easier to use much cheaper substrates like flexible plastic films, glasses and a possibility to use *p*-type polymer (act as a *p*-type substrate when producing *p-n* junctions from ZnO nanorods since the ZnO nanorods are *n*-type).

In this chapter, we have focused on the synthesis technique in particular, the chemical bath deposition and fine tuned its parameters such as temperature, time, concentration and pH to synthesize ZnO nanostructures. We have demonstrated how these parameters affect the growth process and morphology of ZnO, and the obtained morphology affects the structural and optical properties.

### 3.1. Materials and Method

**Materials:** Zinc acetate dehydrate ( $\text{Zn}(\text{CH}_3\text{COO})_2 \cdot 2\text{H}_2\text{O}$ ) or Zinc nitrate hexahydrate ( $\text{Zn}(\text{NO}_3)_2 \cdot 6\text{H}_2\text{O}$ ) (Alfa Aesar), aqueous ammonia (Merck), deionized water as a solvent, pH paper (Merck), Glass substrates (Borolab).

**Synthesis Procedure:** Highly crystalline single phase ZnO nanostructures such as nanoflowers, nanorods, nanotubes, nanoneedles, nanoflakes *etc.* on the glass as well as flexible transparent substrates were prepared by employing a most simple and inexpensive technique called chemical bath deposition. 100 mM solution was prepared by zinc acetate in a 150 ml glass beaker containing 100 ml deionized water as a solvent. After 30 min. of continuous stirring for uniform mixing and complete dissolution, the appropriate quantity of aqueous ammonia was added drop wise to maintain a pH ~12 of the solution. Then a well cleaned glass or flexible transparent substrates were dipped vertically, and the solution was heated at desired temperature for a certain time interval with the help of silicon oil bath temperature and time controlled magnetic stirrer. After

completion of the reaction, the ZnO deposited glass substrates were taken out from the solution and cleaned with deionized water several times and then dried overnight in the air. Additionally, the powder samples were also filtered out with the help of a filter paper and dried overnight. The dried films and powders were annealed in air at an appropriated temperature to get the pure phase of ZnO nanostructures. To understand the growth mechanism of ZnO more clearly, the parameters of the reaction were controlled such as time, temperature, concentration and pH. Three series of experiments were conducted.

- First, the variation of pH from ~ 9 to 12 was carried out by keeping the time, temperature and concentration constant at 120 min, 90°C and 100 mM, respectively.
- Second, the variation of concentrations from 50-250 mM was carried out by keeping the time (90 min.), temperature (120°C) and pH (~12) constant at 90 min, 120 °C and ~12, respectively.
- Third, the variation of time from 30 - 120 min. and temperatures from 70°C to 120°C was carried out keeping the concentration and pH constant at 100 mM and ~12, respectively.

## 3.2. Results and Discussion

### 3.2.1. Effect of pH

***X-Ray Diffraction and Scanning Electron Microscope:*** The phase formation and surface morphology of the ZnO nanostructures were investigated by X-ray diffraction and scanning electron microscope. Figure 3.2 shows the XRD pattern of ZnO nanostructures grown at different pH conditions. All the major peaks of XRD represent the hexagonal phase of wurtzite ZnO (space group P6<sub>3</sub>mc). However very low intensity peak near  $2\theta \sim 32.4^\circ$ , was observed which might be due to the contribution from CuK <sub>$\beta$</sub>  radiation.

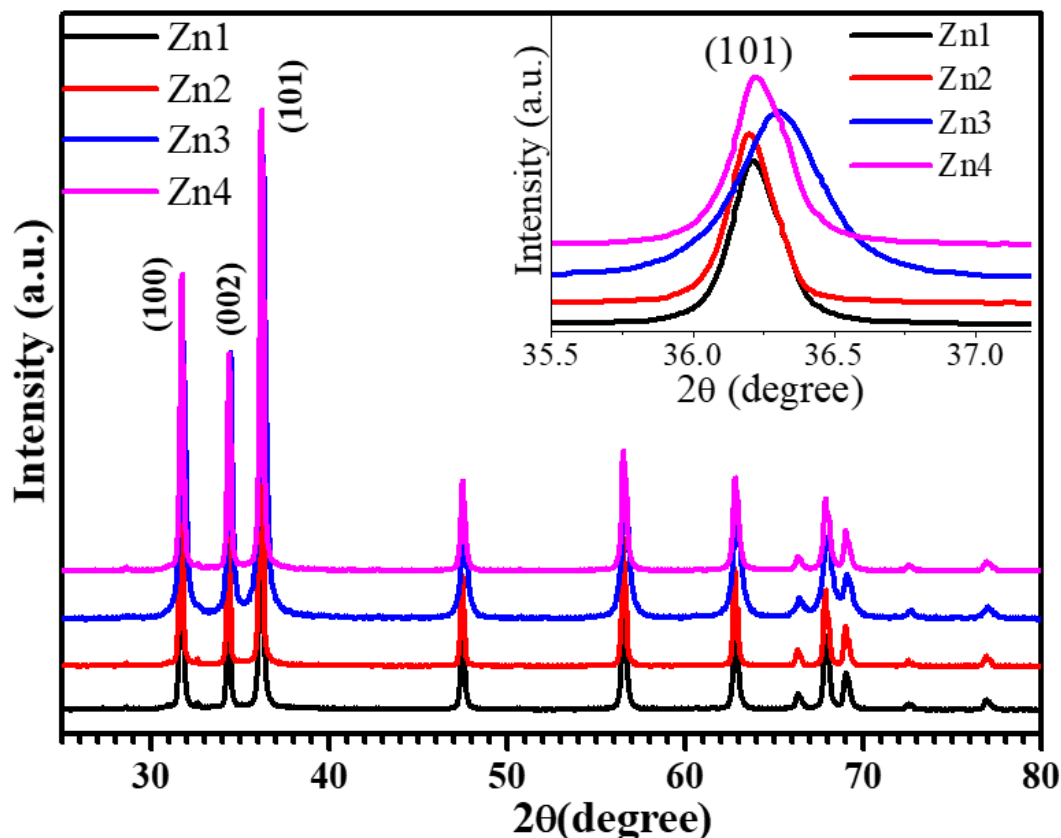


**Figure 3.2.** Represent the XRD pattern of the ZnO nanostructure of different pH (a) Zn1 (pH=9), (b) Zn2 (pH=10), (c) Zn3 (pH=11), and (d) Zn4 (pH=12).

Surface morphologies of all the samples were examined by SEM. Figure 3.3 shows the SEM micrographs of all the samples. The ZnO nanostructures were taken at different magnification (5 KX and 10 KX). At low pH ~ 9 (Figure 3.3(a), 3.3(a1)) thick micro-rod of average diameter more than 1  $\mu\text{m}$  were observed where layered growth was evidenced. As the solution pH reaches 10, these layers were separated from the micro-rod and form individual nanorods and also form fans or bouquets like structure (Figure 3.3(b), 3.3(b1)). However, a further increase in pH (~11), the growth of nanorods with an average thickness of about 200 nm were observed in the form of nanoflowers like structure (Figure 3.3(c), 3.3(c1)). Finally at pH ~ 12 thickness of nanostructure transform to form a tapered needles nanoflower (Figure 3.3(d), 3.3(d1)). At pH ~ 12 of the deposition of ZnO on glass substrates was observed indicating that pH 12 is favourable for thin film growth.

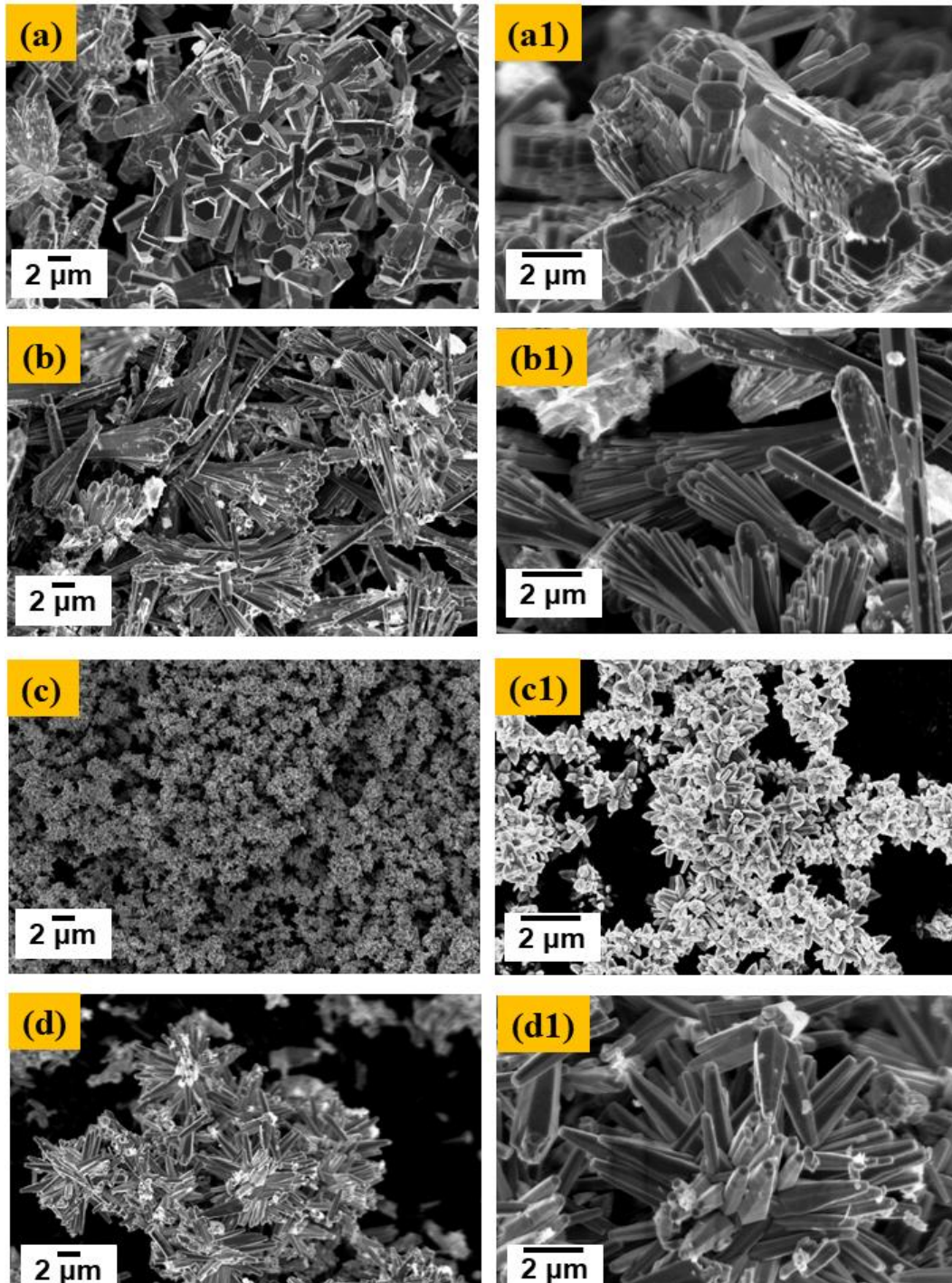


**Figure 3.3.** SEM images of ZnO nanostructure at different pH (a, a1) pH-9, (b, b1) pH-10, (c, c1) pH-11, and (d, d1) pH-12.

### 3.2.2. Effect of Concentration

**X-Ray Diffraction:** Phase purity and crystal structure of ZnO thin films are successfully examined by XRD measurement. Figure 3.4 shows the XRD pattern of ZnO nanostructures deposited on glass substrates with different concentrations *i.e.* (a) 50 mM,

(b) 100 mM, (c) 150 mM, (d) 200 mM, and (e) 250 mM at constant pH, temperature and time. All the major peaks in the range of  $2\theta \sim 25-80^\circ$  are indexed to hexagonal phase wurtzite ZnO, which are in agreement with JCPDS card number 80-0075 suggesting the phase purity of the films. However, the comparably less intense peak near  $2\theta = 31.03^\circ$  is observed, which may be related to the impurity phase of  $\text{Zn}(\text{OH})_2$ .

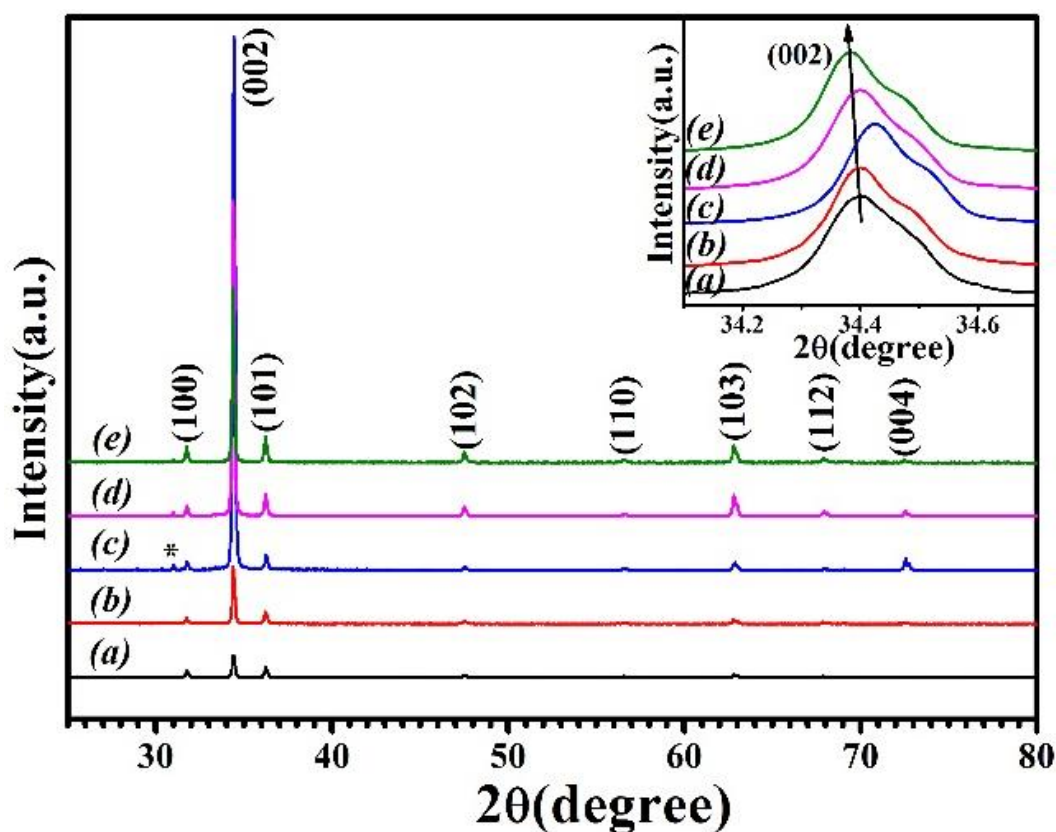


**Figure 3.4.** XRD patterns of ZnO nanostructure synthesis at different concentrations, (a) 50 mM (b) 100 mM (c) 150 mM (d) 200 mM (e) 250 mM, inset of figure shows the relative position of (002) peak (\*related to  $\text{Zn}(\text{OH})_2$  phase).

It is evidenced from Figure 3.4, that the strong directional growth in all the films along  $c$ -axis, *i.e.* (002) plane, which is unusual compared to other ZnO nanostructures that confirmed the highly oriented growth of ZnO nanostructures along the vertical direction [19]. Inset of Figure 3.4 shows the negligible variation in peak position with the variation in concentration; this indicates that the lattice parameters are not changed significantly by changing the concentration. Furthermore, the XRD analysis is performed by Rietveld refinement [20] (Figure 3.5(a)) using Fullprof [21] software and the values of the refined lattice parameters obtained from Rietveld fitting are shown in Figure 3.5(b).

The variation in lattice parameters with concentration shows non-systematic or negligible variation. There might be two probable reasons for the non-systematic change in lattice parameters with concentration; first is due to the change in the structure of ZnO and second is due to internal compressive micro strain [22]. Size determination and effect of strain developed in the nano structure grown on glass substrates were analyzed using Scherer's formula [23] and Williamson-Hall [24] plot using uniform deformation model (UDM) expressed as:

$$D = \frac{K\lambda}{\beta_D \cos\theta} \quad (3.1)$$

$$\beta_{hkl} = \frac{K\lambda}{D \cos\theta} + 4\varepsilon \tan\theta \quad (3.2)$$

where,  $D$  = crystalline size,  $K$  = shape factor (0.9),  $\lambda$  = wavelength of  $\text{Cu}(k_\alpha)$  radiation and  $\beta_{hkl}$  is full width half maxima of a corresponding peak and “ $\varepsilon$ ” is induced strain value.

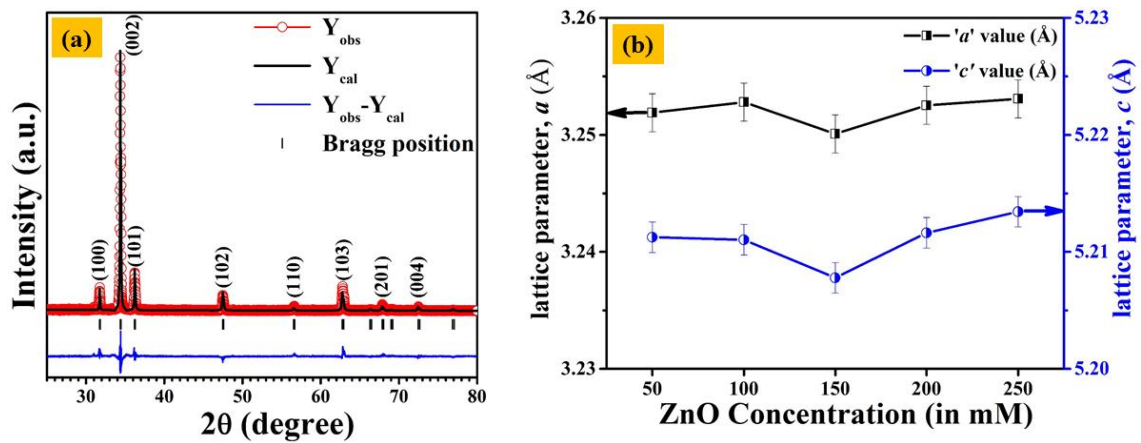


**Figure 3.5.** (a) Rietveld refinement of ZnO film deposited at a concentration of 250 mM, (b) The lattice parameter variation in ZnO films at different concentrations.

**Table 3.1.** The value of crystallite size and strain ( $\varepsilon$ ) for the ZnO nano structures grown at different concentration obtained by Scherer's equation and Williamson-Hall method.

Sample	Scherer's method D (nm)	Williamson- Hall method Uniform Deformation Model (UDM)	
		D (nm)	Strain ( $\varepsilon$ ) x $10^{-3}$
50 mM	45.71	46.32	1.92
100 mM	46.20	46.98	2.40
150 mM	47.25	48.17	2.69
200 mM	48.36	49.35	2.80
250 mM	49.50	50.60	2.97

The parameters obtained by using Scherer's and Williamson-Hall formula are listed in Table 3.1. It is observed that the increase in concentration led to increase in crystallite size that consequently increases the strain.

**Scanning Electron Microscopy and Transmission Electron Microscopy:** The variation of the surface morphology with solute concentration for the deposition of ZnO nanostructures is studied by SEM and is represented in Figure 3.6.

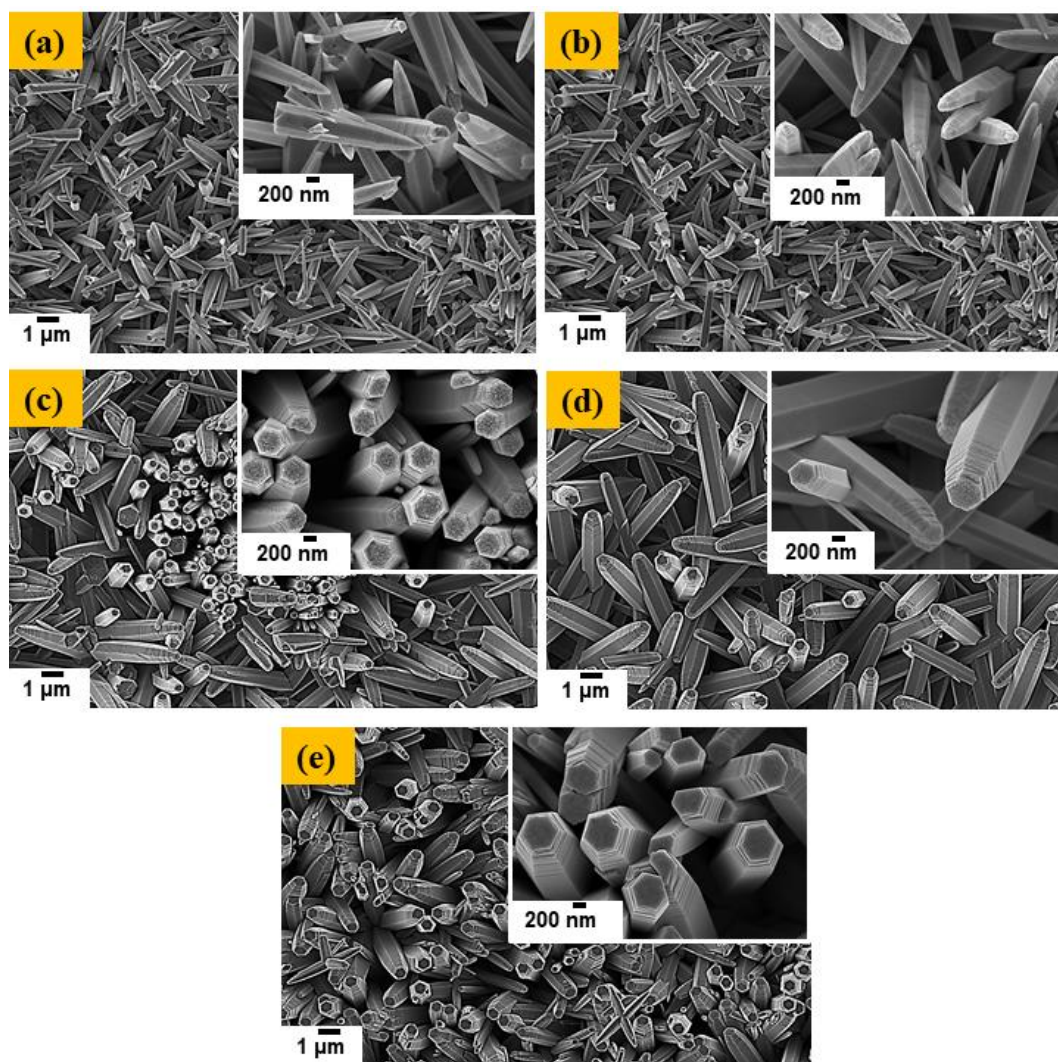


**Figure 3.6.** SEM images of ZnO deposited on glass substrates at different concentrations of (a) 50 mM, (b) 100 mM, (c) 150 mM, (d) 200 mM, and (e) 250 mM.

It shows that the surface consists of nano-needles, tapered nano-rods and nano-rod-like microstructures with an average length of 3  $\mu\text{m}$  to 7  $\mu\text{m}$  and an average diameter of 100 nm to 600 nm. All the samples are composed of nano-needles or nano-rod like

structures. With the increase in the concentration, an increase in the diameter of the nano-needles/rods is found ( $\sim 150$  nm,  $\sim 200$  nm,  $\sim 450$  nm,  $\sim 600$  nm and  $\sim 650$  nm for 50 mM, 100 mM, 150 mM, 200 mM and 250 mM, respectively). ZnO deposited at lower concentration (50 mM) showed tower (needle) shape nanostructure (Figure 3.6(a)). Higher concentration produces micron-size diameter with densely packed *c*-axis aligned ZnO rods, as shown in Figure 3.6(e). As the solute concentration of ZnO is increased, due to the high nucleation growth, nano-needles start the stacking of flat tips to form a stable tapered rod structure and subsequently with further increase in the concentration, the diameter of the tapered rods increases to give a flat tip-like nano-rod structure with a larger diameter.

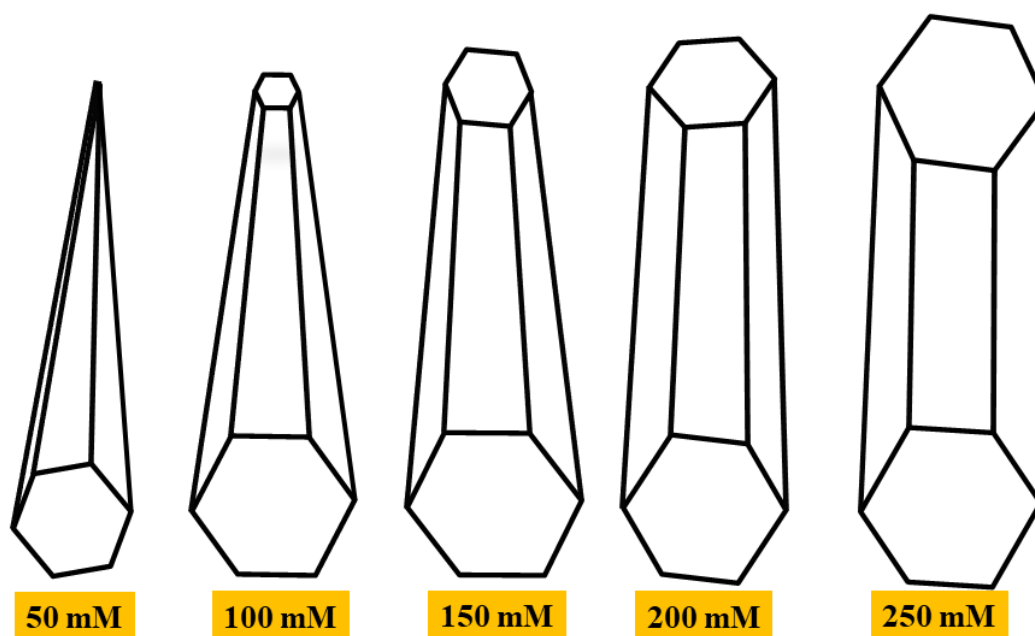


**Figure 3.7.** The schematic diagram represents the effect of concentration on the growth process of the ZnO nanostructures.

Based on the SEM morphologies of ZnO nanostructures, a pictorial representation of the transformation of nano-needles to nano-rods with variation in concentration is constructed and presented in Figure 3.7. It is clear from the schematic and the FESEM images that lower concentration results in needles and higher concentration results in rods.

The internal structure of the ZnO nanostructures is examined using TEM and high resolution TEM and is represented in Figure 3.8. Figure 3.8(a) shows the TEM image of one of the ZnO nano-rods synthesized at 100 mM concentration. It shows a ZnO nano-

rod with a diameter of  $\sim 200$  nm. Also, the corresponding SAED pattern (inset of Figure 3.8(a)) confirms that the nano-rod has a single-crystalline wurtzite structure grown along the  $c$ -axis. HRTEM image (Figure 3.8(b)) indicates clear lattice fringes with  $d$ -spacing of 0.26 nm, corresponding to the (002) lattice plane of hexagonal ZnO. It is worth mentioning that adopting the present synthetic route using chemical bath deposition results in the formation of nanostructured ZnO oriented along  $c$ -axis which is very useful in optoelectronic device fabrication as an electron transport material.

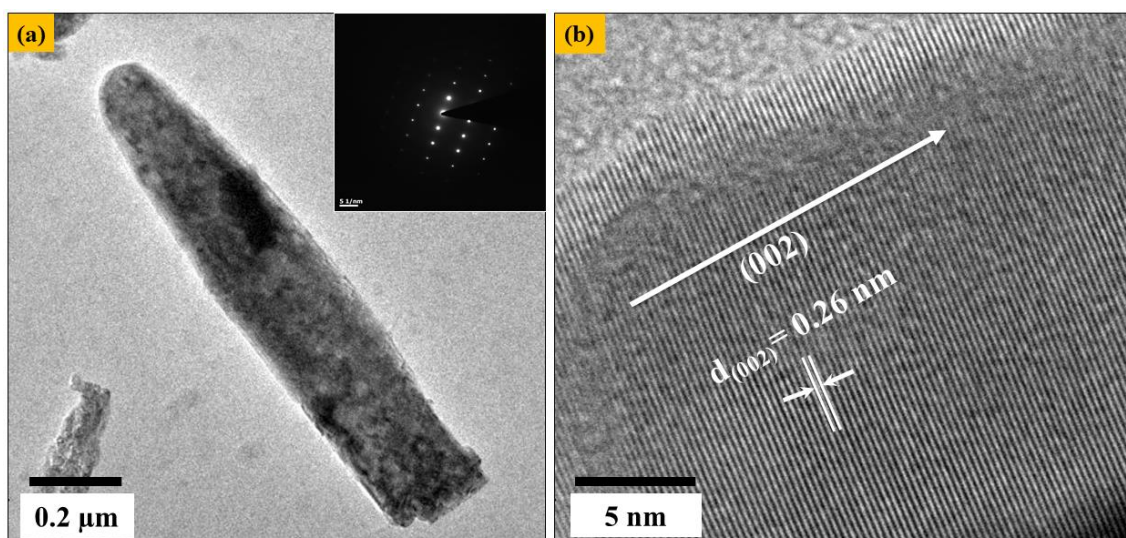


**Figure 3.8.** (a) Typical cross sectional TEM image of a single ZnO nanorod inset of the figure shows selected area electron diffraction (SAED) pattern of the nano-rod structure, (b) The HRTEM image of nano-rod (arrow indicates the growth direction of the nano-rod).

### 3.2.3. Effect of Temperature and Time

**X-Ray Diffraction:** Figure 3.9(a) shows the XRD pattern of ZnO nanostructure deposited on glass substrate at different deposition temperatures keeping deposition time constant at 120 min. All major peaks ( $2\theta \sim 30^\circ$  to  $60^\circ$ ) can be assigned to the pure hexagonal phase of wurtzite-type ZnO structure with space group  $P6_3mc$ . We also observed highly crystalline and pure phase of ZnO at very low synthesis temperature. The film grown below  $120^\circ\text{C}$  shows a more preferred orientation along (002) planes in comparison to powder samples where (101) planes have the strongest peak intensity [25]. However, the ZnO thin films grown at  $120^\circ\text{C}$ , shows a reduced relative intensity of the (002) reflection while the disappearance of (00 $l$ ) plane is might be due to the change in structure [26]. Figure 3.9(b) shows that the (002) peaks shift slightly towards the higher diffraction angle

until growth temperature of 110°C (ZN1 to ZN5) while for growth at 120°C (ZN6) the peak shifts to the lower diffraction angle.

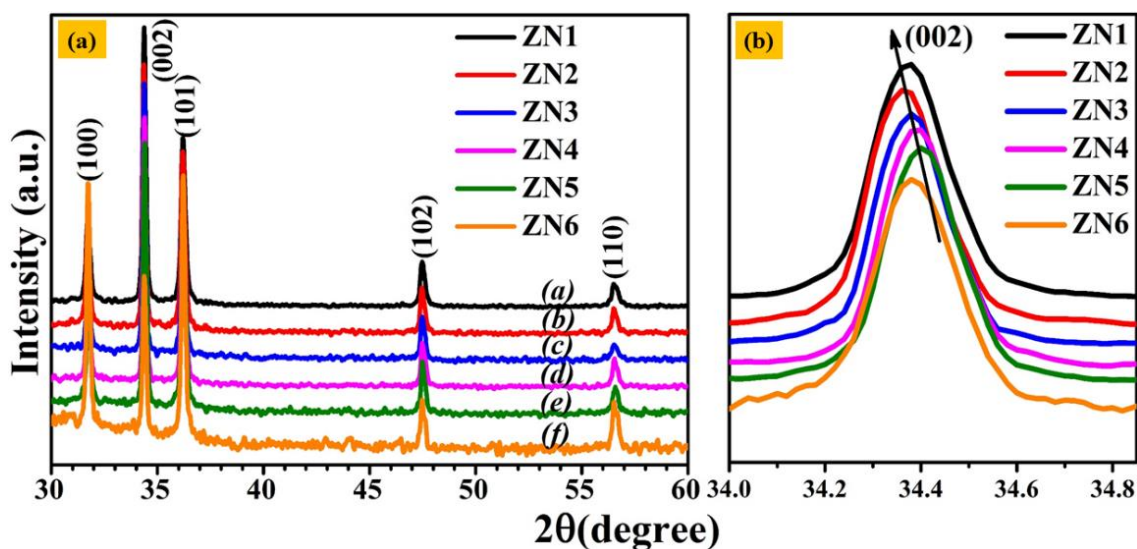


**Figure 3.9.** (a) XRD patterns of ZnO grown at different temperature (a) ZN1 (70°C), (b) ZN2 (80°C), (c) ZN3 (90°C), (d) ZN4 (100°C), (e) ZN5 (110°C), and (f) ZN6 (120°C) nanostructures, (b) shows the relative shift in (002) peak position.

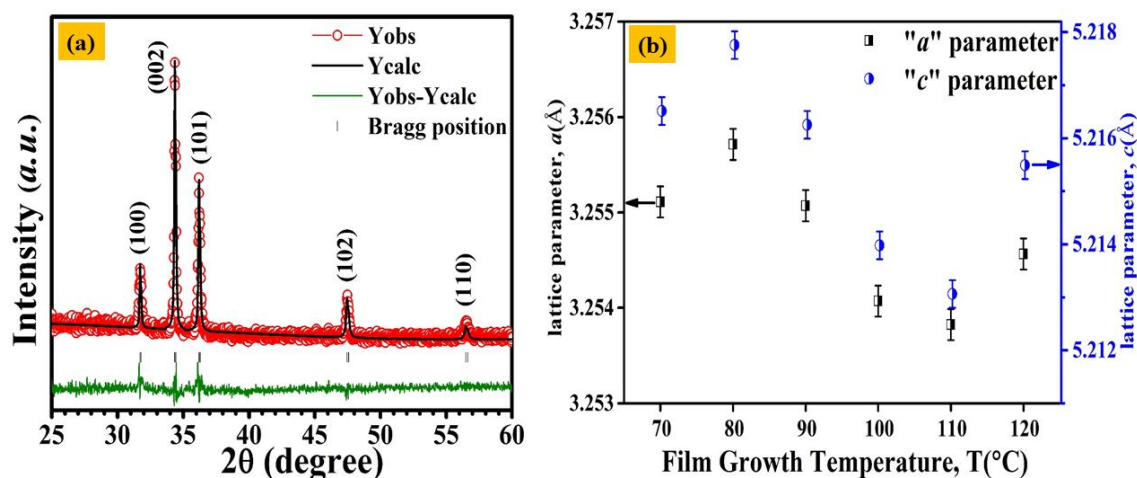


**Figure 3.10.** (a) Rietveld refinement of ZnO film deposited at 90°C with a deposition time of 120 min. (b) The effect of deposition temperature on lattice parameter of ZnO.

This trend is further verified by Rietveld refinement data (Figure 3.10(a)), where the lattice constant decreases until the growth temperature is 110°C followed by an increase in temperature at 120°C (Figure 3.10(b)).

There might be two possible reasons for the non-systematic change in lattice parameter with growth temperature in pure ZnO; (1) due to the change in the morphology

of ZnO nanostructure, (2) due to internal micro strain or defect. Effect of strain developed in the nanostructure grown on glass substrates were analyzed using Williamson-Hall formula (Table 3.2). Comparing Figure 3.10(b) and Table 3.2, it is clear that decrease in lattice parameter has a strong correlation with the increase in strain in the nanostructures or vice versa.

**Table 3.2.** The value of crystallite size and strain ( $\epsilon$ ) for the ZnO nano structures grown at different deposition temperature obtained by two methods: Scherer's equation and Williamson-Hall method.

Sample Name	Scherer's method D (nm)	Williamson- Hall method Uniform Deformation Model (UDM)	
		D (nm)	Strain ( $\epsilon$ ) $\times 10^{-3}$
ZN1	33.21	84.51	1.53
ZN2	37.32	73.72	0.97
ZN3	36.72	107.44	1.72
ZN4	36.93	197.18	2.18
ZN5	36.03	206.86	2.33
ZN6	35.80	55.66	1.57

**Scanning Electron Microscopy:** As it is previously discussed and explained how the morphology and structure of ZnO nanostructure is not solely dependent on the preparation technique but also on other external conditions such as pH value, solution concentration, reaction temperature, and time, *etc.* which play a vital role in wet chemical method [27].

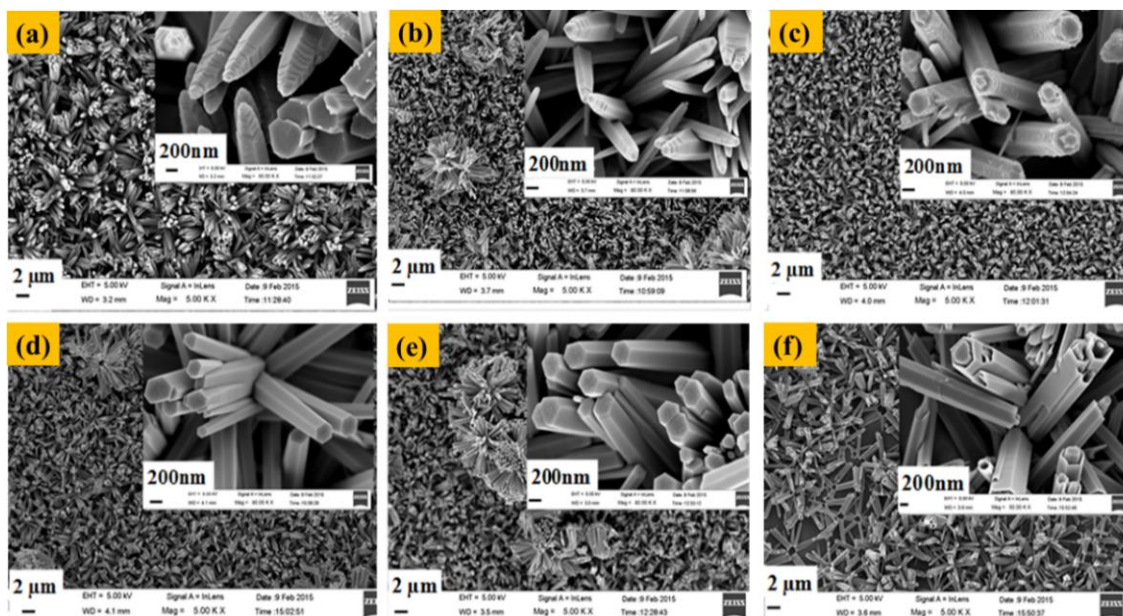
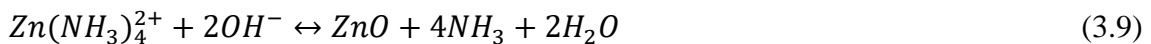


**Figure. 3.11.** FESEM images ZnO nanostructures (a) 70°C -ZN1, (b) 80°C -ZN2, (c) 90°C -ZN3, (d) 100°C -ZN4, (e) 110°C -ZN5, and (f) 120°C -ZN6 for deposition time of 120 min.

Figure 3.11 shows SEM images of ZnO films (scale at 2  $\mu\text{m}$ ) deposited at different temperatures (70-120°C) and inset of the Figure shows a magnified image of the same sample (scale at 200 nm). Comparing the nanostructure size from Figure 3.11, it can be noted that nanorods formed at 70°C (Figure 3.11(a)) are bigger than the structures at 80°C (Figure 3.11(b)). Due to the fast nucleation process at a higher temperature, bigger rods are divided/branched into smaller rods, with a decrease of average size from 323 nm (ZN1) to 206 nm (ZN3). Afterward, due to the layer formation, the size of rods again increases. The average diameters of rod samples from ZN1 to ZN6 are 323 nm, 210 nm, 206 nm, 228 nm, 271 nm and 339 nm, respectively.

### 3.3. Growth Mechanism

The growth mechanism responsible for the growth of ZnO nanomaterial is  $\text{Zn(OH)}_4^{2-}$  or  $\text{Zn(NH}_3)_4^{2+}$  as the growth units, [28, 29] in high pH solution, following the reactions from (3.3)-(3.9).



The chemistry of the reaction during growth in the solution is discussed by Zainelabdin *et al.* [30]. However the growth mechanism of different ZnO nanostructures (nano-rods, nano-flower, nano-needle, nanotube, nano-particles etc.) formation is still not clear yet. The important parameters which are responsible for the growth of ZnO nanostructures such as growth temperature, time, pH, and concentration play a crucial role in shape and size control of the nanostructure. For a better understanding, schematic (Figure 3.12) of the idealized and proposed formation mechanism of ZnO nanostructure is drawn based on the observed nano structure in FESEM.

ZnO consists of an interesting structure with both metastable polar and stable non-polar face [29]. Zinc-terminate (001) and oxygen-terminate (00 $\bar{1}$ ) are two polar faces (along *c*-axis) while the other non-polar faces are (010) and (110) (parallel to *c*-axis), so

the growth along the  $(00l)$  direction is fastest with respect to other faces (Figure 3.12(a)) [31]. The relative velocity of crystal growth along the different plane is well studied by Wen-Jun Li *et al.* [32], *i.e.*,  $V(001) > V(01\bar{1}) > V(010) > V(011) > V(00\bar{1})$ . The most common plausible mechanism known for the growth of ZnO nano wires and tubes are either screw dislocation along the axial direction or layer by layer. Figure 3.11 (a), (b), (c) and (f) shows that screw dislocation mechanism (as indicated in Schematic diagram Figure 3.12 (b), (c) and (e)) may be most possible as a hexagonal top with screw like structure can be easily realized.

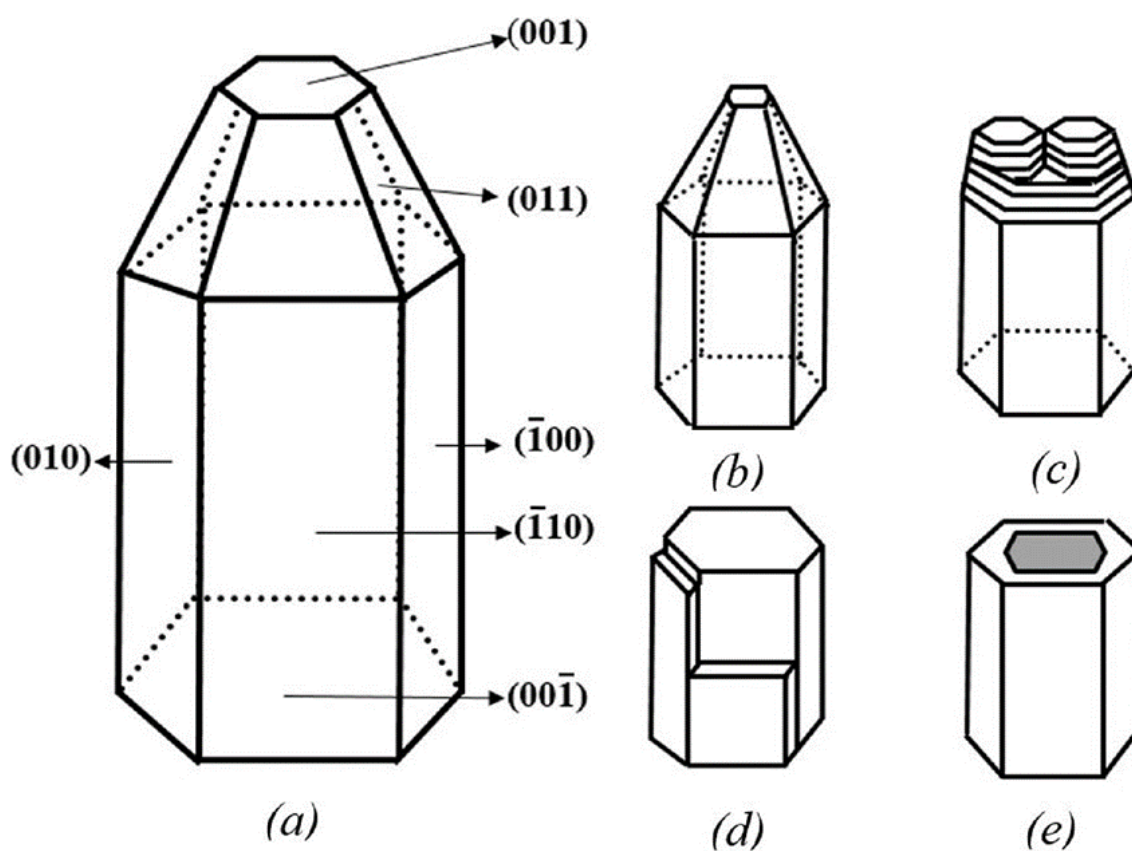


**Figure 3.12.** Schematic diagram (a) shows idealized growth process of nano-rod with tapered tip. Schematic diagram of growth of (b) Nano-needle, (c) Splitting of nano-rod into small nano-rods, (d) layer formation along  $c$ -axis, and (e) Nanotube.

In Figure 3.11 (d) and (e), no clear hint of screw dislocation can be found. In Fig. 3.11 (d) and (e), layer by layer mechanism may be responsible (as indicated in Fig. 3.12(d)) along with screw dislocation and mechanism is under debate. Firstly, nano-needle like structure appears at low temperature and low deposition time along  $(00l)$  direction and form a tapered shape nano-needle on top. With the increase in reaction

temperature further, the structure reduces their surface energies and tapered shape changes to flat top and gradually hexagonal rods starts appearing (Figure 3.11 (c), (d) and (e)). It is also seen that there are not many active sites around the ZnO nuclei at the low reaction temperature. Therefore, the formed nuclei with limited growth rate can get attached along the preferential direction to form nano-flower like structure. It is well known that crystal plane, whose growth rate is slow, easily appears and whose growth rate is fast easily disappears. So, the (00l) plane easily dissolve with respect to another non-polar face at a higher temperature (120°C) resulting in the formation of the nanotube (Fig. 3.12(e)).

Furthermore, for a detailed analysis of the plausible mechanism of ZnO nanostructures, the experiments were performed at fixed deposition temperatures (at 70°C and 120°C) and varied the deposition time at an interval of 30 min. and depositions were carried out at 30 min., 60 min., 90 min. and 120 min. respectively. Figure 3.13 shows the SEM images of films deposited at 70°C for 30 min -120 min in (a-d) and 120°C for 30 min. -120 min. from (e-h). It noticeably visible that the rods and tubes synthesized at different temperature and time evidenced screw dislocation mechanism (Figure 3.14(a-c)) as reported by Yang *et al.*, Jin *et al.* and Bierman *et al.* [13,14,33]. Also one cannot rule out layer by layer deposition in these rods and tubes as from the side view of the rods and tubes one can obviously realize the layer like structure (Figure 3.14(d-e)).

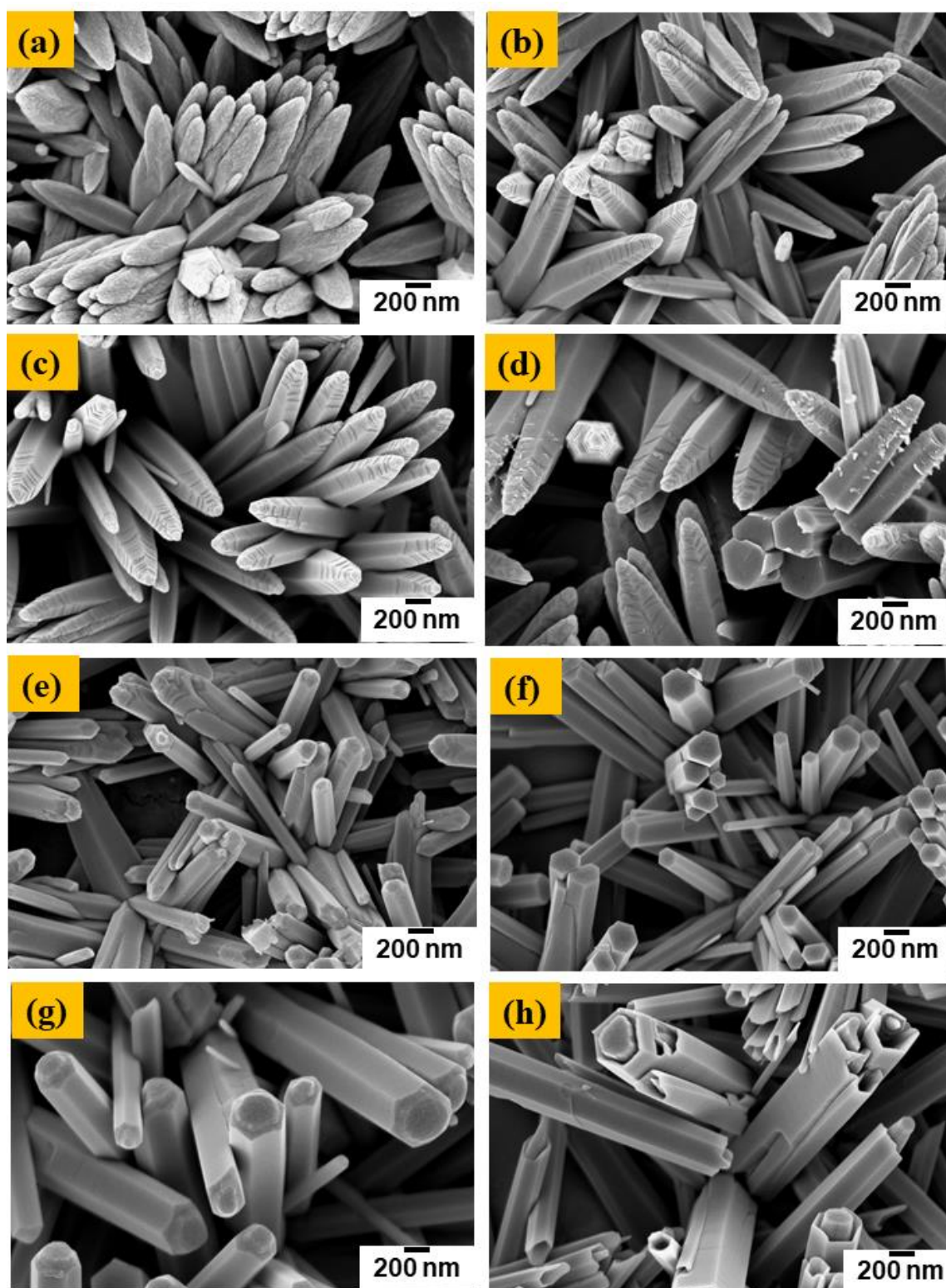


**Figure 3.13.** ZnO film deposited at 70°C with deposition time (a) 30 min, (b) 60 min, (c) 90 min, (d) 120 min, and 120°C with deposition time (e) 30 min, (b) 60 min, (c) 90 min, and (d) 120 min.

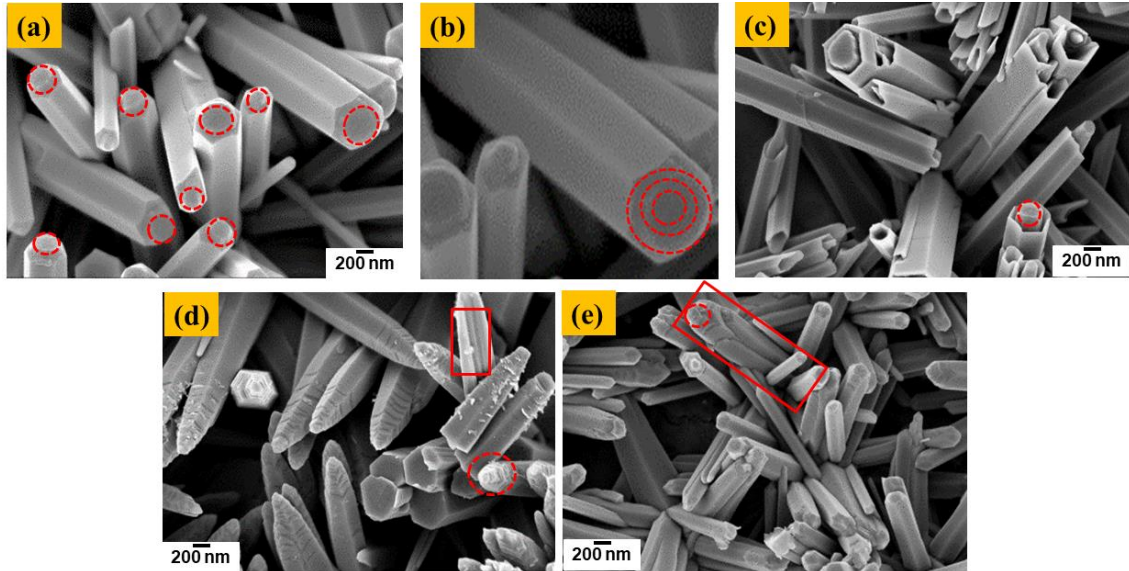


**Figure 3.14.** FESEM images of nanostructures (a) Formation of the needle like structure at 70°C for 120 min and (b) rod like structure at 120°C for 30 min (c) tubes at 120°C for 120 min. The SEM indicates the screw dislocation nucleation mechanism as marked in at the central part of the rods and tubes.

### 3.4. Effect of Morphology on Optical Properties of ZnO

**UV-Visible Spectroscopy:** The effect of morphology on the intrinsic optical properties of the pure ZnO is studied at room temperature (RT) by UV-Vis spectroscopic analysis. Figure 3.15 shows the UV-Visible spectra of ZnO. It is visible that the band gap is varying from 3.11 eV to 3.19 eV as the deposition temperature increase. The band gap was determined from Tauc plot (using Kubelka-Munk method [34]):

$$F(R_{\infty}) h\nu = A (h\nu - E_g)^n \quad (3.10)$$

where,  $F(R_{\infty})$  is the Kubelka-Munk function,  $A$  is a constant,  $E_g$  is the band gap value and  $n$  is an unit less parameter with a value 2 or 1/2 for indirect or direct band gap semiconductors, respectively [35]. Inset (a) of Figure 3.15 shows a typical example of the Tauc plot for the ZN1 sample. From the inset (b) of Figure 3.15, displays the variation of band gap with growth temperature, it is very clear that the band gap is smaller ( $\sim 3.11$  eV) in needles ZN1, intermediate in rods ( $\sim 3.14$  eV) (ZN2-ZN5) and highest in tubes ( $\sim 3.19$  eV) ZN6. From band-gap studies it is distinctly visible that the synthesis temperature plays a vital role, which tunes the band-gap and it is expected to realize these nanostructures for device realization, where the synthetic controlling parameters using chemical bath method can be easily tuned.

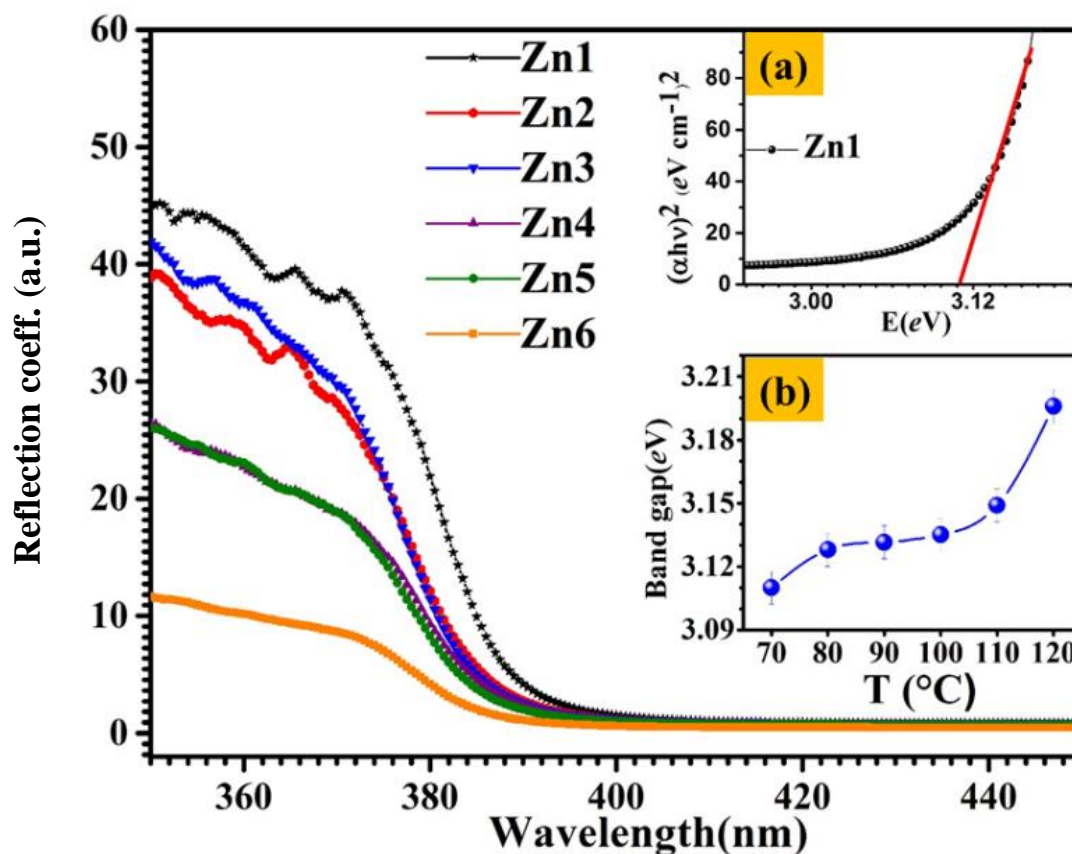


**Figure 3.15.** Room temperature UV-Vis reflection spectra of ZnO nanostructures. Inset image shows (a) Tauc plot of Zn1 and (b) Variation in bandgap with synthesis temperature.

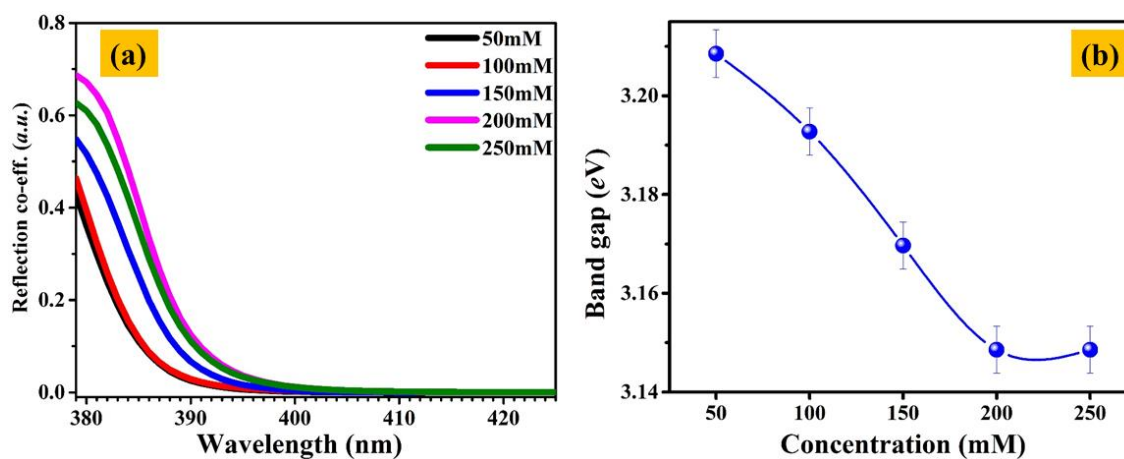


**Figure 3.16.** (a) Room temperature UV-Vis reflection spectra measured on ZnO nanostructures films deposited on the glass substrates at different concentrations, (b) Shows the variation on the band gap of ZnO nanostructures with concentration.

Similarly the effect of solute concentration on the band gap of ZnO also investigated as shown in Figure 3.16. It is noticeable that the band gap varies from 3.20 eV to 3.14 eV

as the concentration increases, which is due to the change in morphology of ZnO nanostructures from nano-needles to nano-rods and also the size of the nanostructure. This result indicates that the optical properties like the band gap of ZnO strongly depend on the morphology and the size of the nanostructures.

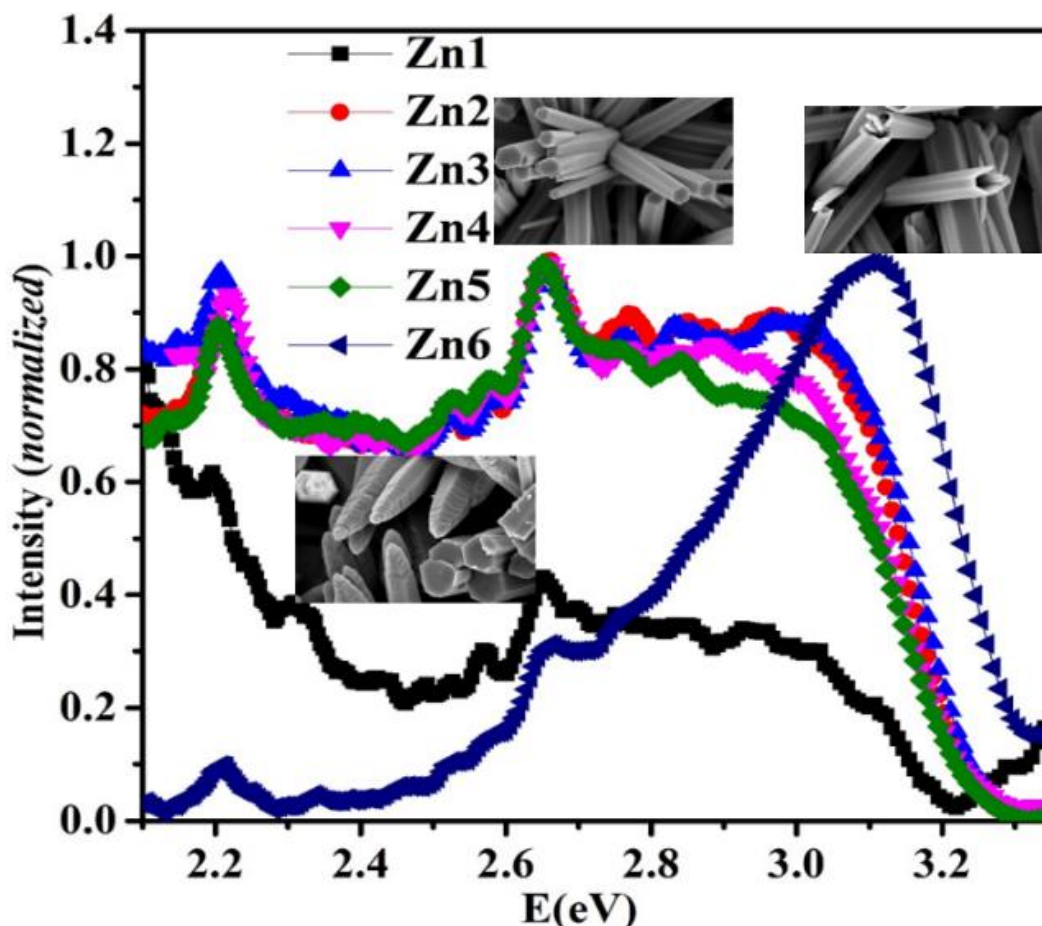
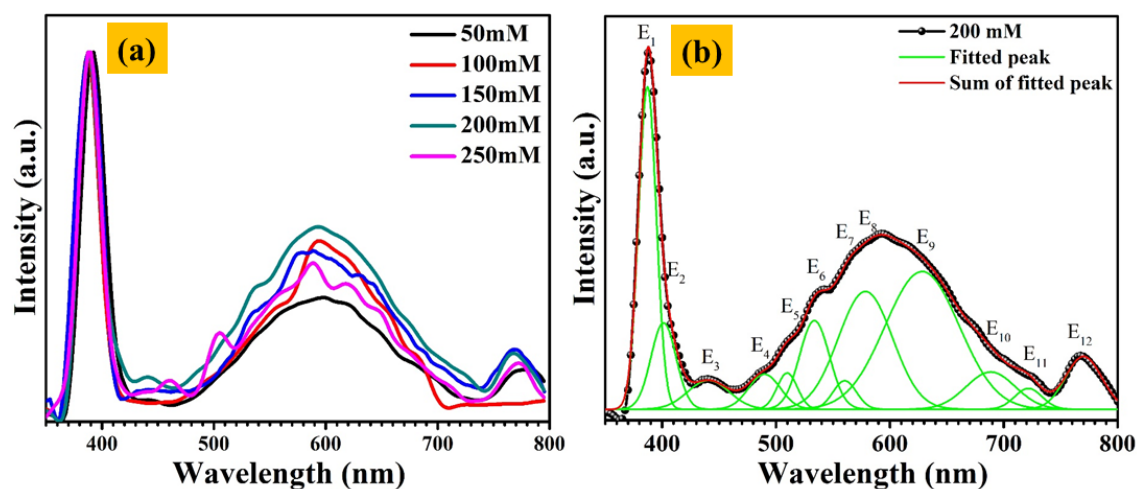


Figure 3.17. Room temperature PL spectra of ZnO grown at different temperatures.

**Photoluminescence spectroscopy (PL):** In contrast to the UV-Vis spectra, room temperature (RT) photoluminescence (PL) spectra of ZnO nanostructures are sensitive to the preparation procedure. PL studies reveal comprehensive information about the nature of light emission and the fundamental material properties. It is an effective method to investigate the presence of defects in the semiconductors. Two emission bands in the PL spectrum of ZnO are observed, one is in the UV range associated with excitonic recombination or band-edge emission, and another is in the broad visible range, which originates from the electron-hole recombination at a deep level, caused by oxygen vacancy or zinc interstitial defects *etc.* [36].

Figure 3.17 shows RT-PL emission of ZnO as temperature dependent measured by exciting at 325 nm over a broad range from 3.3 to 2.1 eV (330 to 590 nm). With the increase in growth temperature of ZnO films, near band edge peak position shifts toward higher energy side, irrespective of defect which is responsible for PL. The existence of Zn interstitials ( $Zn_{in}$ ), Oxygen vacancies ( $V_O$ ), Zn vacancies ( $V_{Zn}$ ), Oxygen interstitials ( $O_{in}$ ), Antisite oxygen ( $O_{Zn}$ ) has been reported as possible defects in PL previously [36].



**Figure 3.18.** (a) Room temperature normalized PL spectra of ZnO films deposited at different concentrations, (b) Room temperature PL spectra (Black dots), Gaussian fitting curves (Green) and summation of Gaussian curves (red line) of ZnO film grown at 200 mM concentration.

Similarly, Figure 3.18 displays the room temperature PL of ZnO nanostructure synthesized at a different concentration with an excited wavelength of 325 nm. The emission band is composed of a weak UV band at around 3.12 eV, a weak blue band at around 2.66 eV and a strong orange band at around 2.20 eV. The UV emission band must be explained by a near band-edge transition of wide band gap ZnO nanorods, namely the free excitons recombination through an exciton–exciton collision process [37]. Similarly, an orange band is also observed and it is attributed to the intrinsic defect in ZnO as  $O_{in}$  [38, 39] suggesting oxygen excessive in the sample. We can conclude that the ZnO nanorods have a strong ability to absorb oxygen to form oxygen interstitials defects on the surface. In the case of the weak blue emission, the exact mechanism is not yet clear [40]. It may also relate to the surface defects in the present condition. From Figure 3.17 and 3.18, it is clear that the PL spectra strongly depends on the morphology of the ZnO nanostructures as can be seen that for needles (ZN1) intensity is low at higher energy

levels. For rods it is almost flat with higher intensities, expecting certain emissions and overlap for ZN2-ZN5. For nanotubes (ZN6) the intensity is higher at a higher energy level and then decreases. For ZnO rods (ZN2-ZN5) the yellow and green light emission is prominent from PL spectra while for ZnO nano-tubes (ZN6) violet light is prominent. It indicates that the synthesis temperature is one of the important factors to control the surface morphology which ultimately controls the optical properties. So this study presents an important message to the basic and applied science that to tune the optical properties, the control over synthesis temperature in wet chemical bath method is very important.

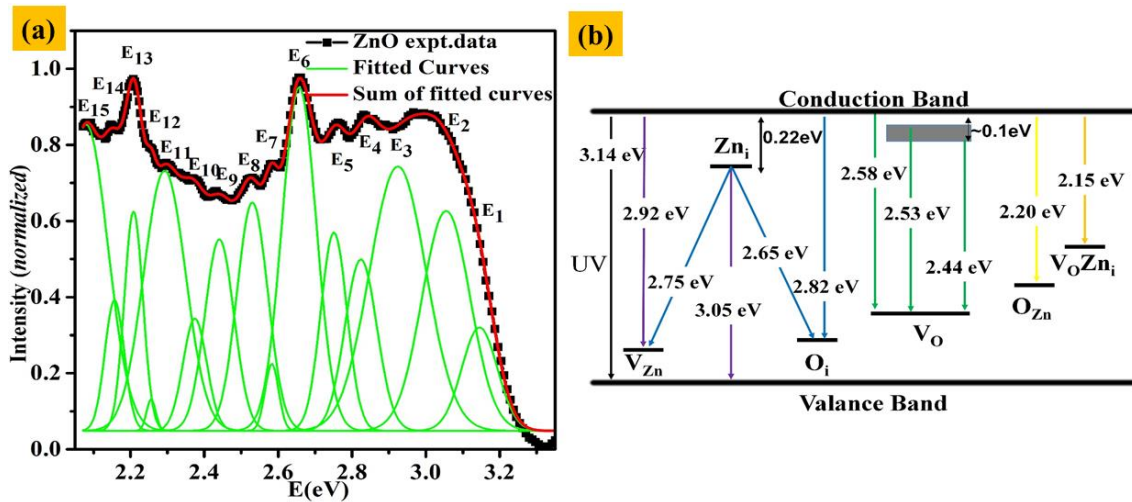


**Figure 3.19.** (a) PL spectra of ZnO deposited at 90°C temperature. The “■” shows experimental data. Solid green and red lines are Gaussian fitting of individual peaks and sum of all peaks, respectively. (b) Schematic band diagram of ZnO nanostructure for ZN3.

Figure 3.19(a) shows the typical PL spectra of ZnO nanorods grown at 90°C measured at room temperature (excited at 325 nm), which is deconvoluted into 15 well-resolved peaks. The “■” shows experimental data, solid green and red lines are Gaussian fitting of individual peaks and sum of all peaks, respectively. Figure 3.19(b) shows the schematic band diagram. First peak  $E_1$  at 3.14 eV correspond to UV region and it is related to near band emission present in ZnO films.  $E_2$  at 3.05 eV and  $E_3$  at 2.92 eV is considered to appear from the shallow donor  $Zn_i$  to valance band (VB) and conduction band to shallow acceptor  $V_{Zn}$ , respectively. Both these transitions are responsible for violet-blue emissions. A broad blue peak  $E_4$  at 2.82 eV in between conduction band (CB) to  $O_{in}$  level and small peak  $E_5$  (2.75 eV) in between  $Zn_{in}$  and  $V_{Zn}$ , these both peaks are known to originate due to the recombination of an electron-hole pair. Another intense blue peak at

$E_6$  (2.65 eV) was attributed to electron transition from  $Zn_{in}$  to  $O_{in}$  acceptor level. The origin of green emission in ZnO is one of the most controversial issues. Liu *et al.* [41] ascribed to  $Zn_i$  and  $O_i$ . According to Vanheusden *et al.* [42], it is related to  $V_O$ . Figure 3.19 (a) shows three prominent peaks  $E_7$ ,  $E_8$  and  $E_9$  at 2.58, 2.53 and 2.44 eV, respectively. Calculation based on full potential linear muffin-tin orbital method explained that the position of oxygen vacancies ( $V_O$ ) level is located at approximately 2.46 eV below the CB [43]. So these three emissions are attributed to CB or deep level or trap-state oxygen singly charged  $V_O$  defect state. Very strong yellow luminescence peak observed at 2.20 eV ( $E_{13}$ ) and orange luminescence at 2.15 eV ( $E_{14}$ ) below the conduction band, these defects are originated due to antisite oxygen ( $O_{Zn}$ ) defect state and complex of  $V_O Zn_i$  cluster, *i.e.*, combination of two point defect  $V_O$  and  $Zn_i$ , respectively [44].

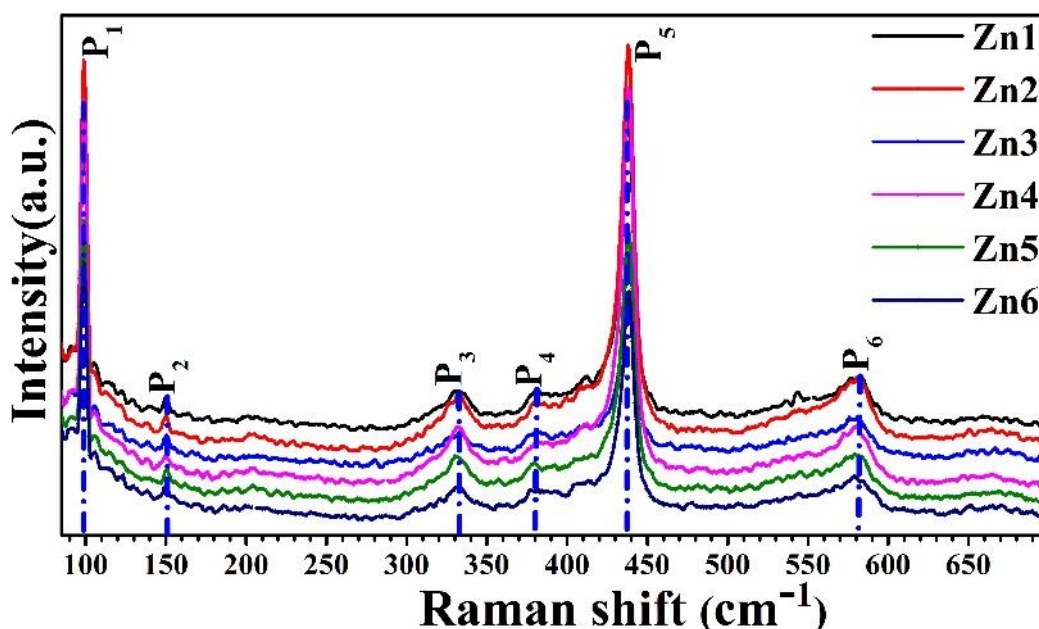


Figure 3.20. RT Raman spectra of ZnO nanostructures synthesized at a different temperature.

**Raman spectroscopy:** The optical phonon properties of the ZnO nanostructures prepared at different temperature and concentration have been investigated by Raman spectroscopy, and the results are presented in Figures 3.20 and 3.21. ZnO has a wurtzite structure that belongs to the space group  $C_{6v}^4$  with two unit formulas per primitive cell, with all atoms occupying  $C_{3v}$  sites. The group theory predicts the existence of the following optical modes at the  $\Gamma$  point of the Brillouin zone:  $\Gamma = A_1 + 2B_1 + E_1 + 2E_2$ . ZnO has 12 branches consists of polar modes ( $A_1$  and  $E_1$ ), two non-polar modes ( $2E_2$ ) and two silent ( $2B_1$ ) Raman modes [45, 46].

Among these,  $A_1$  and  $E_1$  polar modes are divided into transverse optical ( $TO$ ) and longitudinal optical ( $LO$ ) phonons due to the long-range electrostatic forces [47, 48]. It is well understood that the electrostatic forces dominate the anisotropy of in the short-range forces, the  $TO$ - $LO$  splitting is larger than the  $A_1$ - $E_1$  splitting, whereas,  $E_2$  is divided into  $E_2^{low}$  and  $E_2^{high}$  active modes.

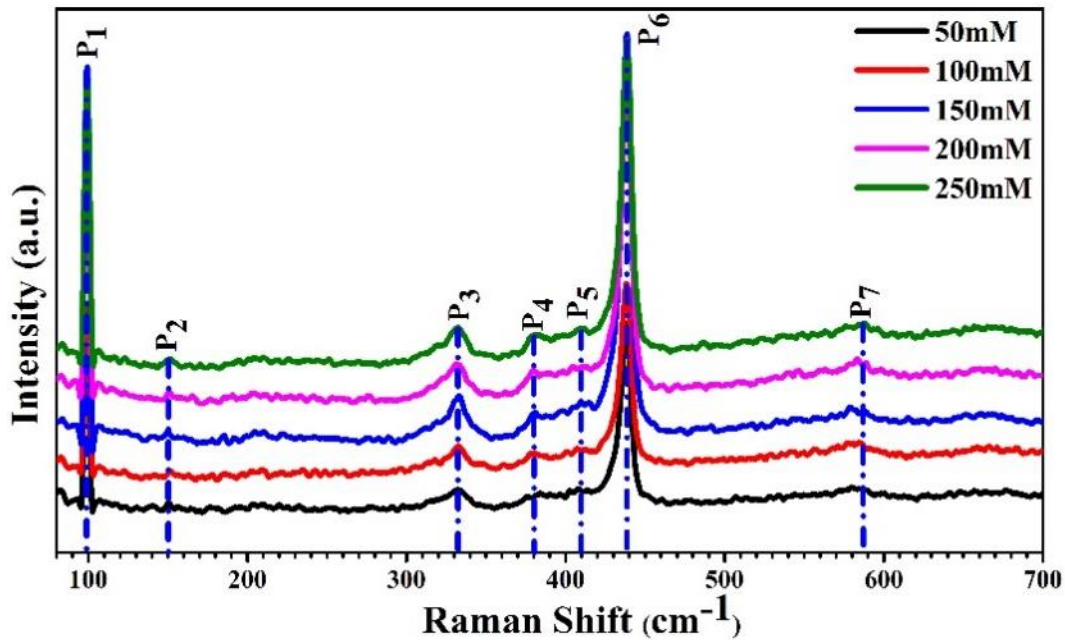


Figure 3.21. RT Raman spectra of concentration dependent ZnO nanostructure films.

The  $A_1$  and  $E_1$  branches are both infrared and Raman active, the two non-polar  $E_2$  branches are Raman active only, and the  $B_1$  branches are inactive. The atoms move parallel and perpendicular to the  $c$ -axis, for the lattice vibrations with  $A_1$  and  $E_1$  symmetries, respectively. The low-frequency  $E_2$  mode ( $E_2^{low}$ ) is related with the vibration of the heavy Zn sub-lattice, while the high-frequency  $E_2$  mode ( $E_2^{high}$ ) comprises simply the oxygen atoms. According to theory, the scarring peaks at  $\sim 438$ ,  $381$  and  $583$   $\text{cm}^{-1}$ , correspond to the fundamental optical modes of  $E_2$ ,  $A_1(TO)$ , and  $A_1(LO)$ , respectively and they have been attributed to the intrinsic defects, such as oxygen vacancy and interstitial zinc. All these active Raman modes are very well assigned in the literature [49]. Decremps *et al.* [50] reported six phonon frequencies,  $E_2^{low}$ ,  $E_2^{high}$ ,  $A_1(TO)$ ,  $E_1(TO)$ ,  $A_1(LO)$  and  $E_1(LO)$ , at  $\Gamma$ -point using Raman spectroscopy (at 99, 439, 382, 414, 574 and 580  $\text{cm}^{-1}$ ) and *ab initio* calculations (at 92, 449, 397, 426, 559 and 577  $\text{cm}^{-1}$ ) at ambient condition. Whereas, Serrano *et al.* [51] reported phonon frequency of two  $B_1$  modes also

along with the other six modes at 91, 261, 391, 409, 440, 552, 560 and 556  $\text{cm}^{-1}$ . The spectrum of all ZnO nano structure grown at different temperature and concentration are similar (Figure 3.20 and 3.21).

**Table 3.3.** Phonon mode frequencies (in units of  $\text{cm}^{-1}$ ) of wurtzite ZnO films deposited at different temperatures (ZN1-ZN6).

Peak	The position of the vibration bands ( $\text{cm}^{-1}$ )						Phonon mode
	ZN1	ZN2	ZN3	ZN4	ZN5	ZN6	
P <sub>1</sub>	98.7	98.7	98.7	98.7	98.7	99.7	$E_2^{low}$
P <sub>2</sub>	149.9	149.9	150.5	150.5	150.5	149.9	$2E_2^{low}$
P <sub>3</sub>	330.1	333.1	333.1	332.5	329	331.8	$E_2^{high} - E_2^{low}$
P <sub>4</sub>	380.8	380.2	380.8	381.4	379.6	382.1	$A_1(TO)$
P <sub>5</sub>	438.1	438.1	438.1	438.1	438.1	438.1	$E_2^{high}$
P <sub>6</sub>	583.3	581.5	580.9	580.3	579.1	579.1	$LO (A_1 + E_1)$

Table 3.3 and 3.4 summarize the Phonon mode frequencies (in units of  $\text{cm}^{-1}$ ) of wurtzite ZnO nano structures deposited at different temperatures and concentration. By comparing the obtained modes of ZnO from table 3.4 with literature, one can assign the peak at around 98  $\text{cm}^{-1}$  (P<sub>1</sub>) to  $E_2^{low}$  mode. There is a secondary phonon mode presented at 150  $\text{cm}^{-1}$ , which is assigned as  $2E_2^{low}$  [52]. The small peak  $\sim 330 \text{ cm}^{-1}$  (P<sub>3</sub>) is assigned to  $E_2^{high} - E_2^{low}$  (multi-phonon process) and is known to be a second order vibration mode arising from zone-boundary phonons [53]. Another small peak, P<sub>4</sub> is observed at  $\sim 380 \text{ cm}^{-1}$  is assigned to  $A_1(TO)$  mode. P<sub>5</sub> around 438.1  $\text{cm}^{-1}$  is assigned to  $E_2^{high}$  which is the characteristics of wurtzite structure and good crystallinity. Wide peak at around 580  $\text{cm}^{-1}$  (P<sub>6</sub>) is assigned to the combination of  $A_1$  and  $E_1$  longitudinal optical mode, ( $LO (A_1 + E_1)$ ) mode. A red shift in P<sub>6</sub> can be explained on the basis of possible mechanisms; (1) spatial confinement within the nano-rods/nano-tubes boundaries; (2) Phonon localization by the defects such as oxygen deficiency, zinc excess, surface impurities, *etc.* The broadening of the spectra and strong red shifts of  $LO$  modes are reported due to the optical phonon confinement. As the crystalline size of ZnO nanostructures is around 100 nm (Table 3.2), so phonon confinement might be responsible for the observed P<sub>6</sub> peak shift.

A similar type of result is observed in case of concentration dependent ZnO thin films (Table 3.4). However, additional peaks are observed at 411.2 and 587.3  $\text{cm}^{-1}$ , which are assigned to  $E_1(TO)$  and  $E_1(LO)$ , respectively. This  $E_1$  mode is related to the existence of defects corresponding to interstitial Zn, oxygen vacancies, or their complex and indicates that the prepared ZnO nano-rods have good optical features.

**Table 3.4.** Summary of the Phonon mode frequencies (in units of  $\text{cm}^{-1}$ ) of wurtzite ZnO films deposited at different concentrations.

Peak	The positions of the vibrations bands ( $\text{cm}^{-1}$ )					Assignment
	ZnO (50mM)	ZnO (100mM)	ZnO (150mM)	ZnO (200mM)	ZnO (250mM)	
1	98.6	99.1	99.4	99.4	99.4	$E_2^{\text{low}}$
2	150.3	151.6	150.4	151.6	151.6	$2E_2^{\text{low}}$
3	332.4	333.5	332.6	333.4	333.6	$E_2^{\text{high}} - E_2^{\text{low}}$
4	382.8	380.4	381.0	381.0	382.2	$A_1(\text{TO})$
5	411.2	411.2	411.3	412.5	411.9	$E_1(\text{TO})$
6	438.6	438.2	438.6	438.4	438.7	$E_2^{\text{high}}$
7	581.3	581.3	580	584.8	587.3	$E_1(\text{LO})$

### 3.5. Summary

Here, we have explored the well-ordered and controlled growth of ZnO nanostructures by fine tuning the pH, solute concentration, time and temperature using the wet chemical method. The structural, optical and morphological properties of the as-grown ZnO nanostructures are investigated in detail. The prime focus is given on tuning the morphology of ZnO nanostructures which can directly influence the structural and optical properties suitable for different applications. The growth of ZnO nanostructures in the form of nano-flowers, nano-needles, nano-rods and nano-tubes are realized by monitoring the pH, concentration, time and temperature. Variation of pH from 9-12 shows that at a pH of  $\sim 12$ , it is possible to get ZnO film on glass substrates with micro-rods morphology. Similarly, changing the concentration from 50 mM to 250 mM, the ZnO nanostructures are tuned from nano-needles to nano-flowers to nano-rods. In addition, the change in time and temperature plays an important role in realizing robust ZnO nanostructures. At lower deposition time and temperature (30 min.,  $70^\circ\text{C}$ ) nano-needles/flowers are formed. As the time and temperature increases (60-90 min.,  $80-110^\circ\text{C}$ ) nano-rods/flowers are formed. From the similar account, a further increase in time and temperature (90-120 min.,  $120^\circ\text{C}$ ), the ZnO nanostructures are transformed from nano-rods to nano-tubes. The possible growth mechanism is explained. Furthermore, the influence of the different morphologies of ZnO from needles to rods to tubes directly affects the structural and optical properties. The XRD analysis shows the high crystallinity of the films oriented along  $c$ -axis. Moreover, the Rietveld refinement data are determined for different growth conditions where with variation in concentration the lattice constant remain almost unaltered. But, with the change in temperature, the lattice constants first decrease until

growth temperature is 110°C and then increase to 120°C. The optical properties of ZnO nanostructures are analyzed from UV-Visible and PL spectroscopy. It is found that at a lower concentration the optical bandgap increases and vice versa. Whereas at lower a temperature the optical bandgap decreases. The PL analyses reveal the presence of defect states in ZnO which will greatly benefit its application in optoelectronics. Raman spectroscopy studies support the defects formation related to Zn and O as conclude from PL spectroscopy.

**References**

- [1] Wang Z. L. 2004, Zinc oxide nanostructures: growth, properties and applications, *J. Phys.: Condens. Matter*, 16, R829.
- [2] Baruah S., Dutta J. (2009), pH-dependent growth of zinc oxide nanorods, *J. Cryst. Growth*, 311, 2549-2554.
- [3] Amin *et al.* (2011), Influence of pH, Precursor Concentration, Growth Time, and Temperature on the Morphology of ZnO Nanostructures Grown by the Hydrothermal Method, *J. Nanomater.* 2011, 269692.
- [4] Khoza P. B., Moloto M. J., Sikhwivhilu L. M. (2012), The Effect of Solvents, Acetone, Water, and Ethanol, on the Morphological and Optical Properties of ZnO Nanoparticles Prepared by Microwave, *J. Nanotechnol.* DOI: 10.1155/2012/195106.
- [5] Pimentel *et al.* (2015), Effect of solvents on ZnO nanostructures synthesized by solvothermal method assisted by microwave radiation: a photocatalytic study, *J. Mater. Sci.* 50, 5777–5787.
- [6] Gomez J. L., Tigli O. (2013), Zinc oxide nanostructures: from growth to application, *J. Mater Sci.* 48, 612–624.
- [7] Wang *et al.* (2003), Ultraviolet lasing of ZnO whiskers prepared by catalyst-free thermal evaporation, *Chem. Phys. Lett.* 377, 329-332.
- [8] Radzimska A. K. and Jesionowski T. (2014) Zinc Oxide-From Synthesis to Application: A Review, *Materials*, 7, 2833-2881.
- [9] Znaidi L. (2010), Sol-gel-deposited ZnO thin films: A review, *Mater. Sci. Eng. B*, 174, 18-30.
- [10] Li *et al.* (1999), Growth mechanism and growth habit of oxide crystals, *J. Cryst. Growth*, 203, 186-196.
- [11] Eriko Ohshima *et al.* (2004), Growth of the 2-in-size bulk ZnO single crystals by the hydrothermal method, *J. Cryst. Growth*, 260, 166-170.
- [12] Sufang Zhang *et al.* (2011), Growth habit control of ZnO single crystals in molten hydrous alkali solutions, *J. Cryst. Growth*, 336, 56-59.
- [13] Yang H. J., He S. Y., Tuan H. Y. (2014), Simultaneous axial screw dislocation-mediated growth and radial layer-by-layer deposition for controlled synthesis of asymmetric axial ZnO nanospindles, *Nanoscale*, 6, 9034-9042.

- 
- [14] Jin S., Bierman M. J., Morin S. A. (2010), A New Twist on Nanowire Formation: Screw-Dislocation Driven Growth of Nanowires and Nanotubes, *J. Phys. Chem. Lett.* 1, 1472-1480.
- [15] Ouerfelli et al. (2006), Properties of ZnO thin films deposited by chemical bath deposition and post annealed, *J. Phys. D: Appl. Phys.* 39, 1954-1959.
- [16] Khallaf *et al.* (2009), Investigation of chemical bath deposition of ZnO thin films using six different complexing agents, *J. Phys. D: Appl. Phys.* 42, 135304.
- [17] Govender *et al.* (2004), Understanding the factors that govern the deposition and morphology of thin films of ZnO from aqueous solution, *J. Mater. Chem.* 14, 2575-2591.
- [18] Baruah S., Dutta J. (2009), Hydrothermal growth of ZnO nanostructures, *Sci. Technol. Adv. Mater.* 10, 013001.
- [19] Li *et al.* (1999), Growth mechanism and growth habit of oxide crystals, *J. Cryst. Growth*, 203, 186-196.
- [20] Pola-Albores *et al.* (2011), Microstructural study of ZnO nanostructures by rietveld analysis, *J. Nanomater.*, DOI: 10.1155/2011/643126.
- [21] Rodríguez-Carvajal J. (1993), Recent advances in magnetic structure determination by neutron powder diffraction, *Physica B*, 192, 55-69.
- [22] Cao J., Wu J. (2011), Strain effects in low-dimensional transition metal oxides, *Mater. Sci. And Eng. R*, 71, 35-52.
- [23] Taylor A., Sinclair H. (1945), On the determination of lattice parameters by the debye-scherrer method, *Proc. Phys. Soc.* 57, 126-135.
- [24] Williamson G. K., Hall W. H. (1953), X-Ray line broadening from fcc aluminum and wolfram, *Acta Metallurgica*, 1, 22-31.
- [25] Wang *et al.*, (2006), Raman scattering and high temperature ferromagnetism of Mn-doped ZnO nanoparticles, *Appl. Phys. Lett.* 88, 252502.
- [26] Xu *et al.* (2008), Growth and spectral analysis of ZnO nanotubes, *J. App. Phys.* 103, 094303.
- [27] Dong *et al.* (2013), Controllable synthesis of ZnO nanostructures on the Si substrate by a hydrothermal route, *Nanoscale Res. Lett.* 8, 378.

- [28] Cho S., Jung S. H., Lee K. H. (2008), Morphology-Controlled Growth of ZnO Nanostructures Using Microwave Irradiation: from Basic to Complex Structures, *J. Phys. Chem. C* 112, 12769-12776.
- [29] Fang *et al.* (2006), Synthesis of ultrathin ZnO nanofibers aligned on a zinc substrate, *Small*, 2, 612-615.
- [30] Zainelabdin *et al.* (2010), Deposition of well-aligned ZnO nanorods at 50 °C on metal, semiconducting polymer, and copper oxides substrates and their structural and optical properties, *Cryst. Growth Des.* 10, 3250-3256.
- [31] Zhao *et al.* (2010), Complex ZnO nanotree arrays with tunable top, stem and branch structures, *Nanoscale*, 2, 1674-1683.
- [32] Li *et al.* (1999), Growth mechanism and growth habit of oxide crystals, *J. Cryst. Growth* 203, 186-196.
- [33] Bierman M. J., Lau Y. K., Kvit A. V., Schmitt A. L., Jin S. (2008), Dislocation-Driven Nanowire Growth and Eshelby Twist, *Science*, 320, 1060-1063.
- [34] Kubelka P., Munk F. (1931), An article on optics of paint layers, *Z. Tech. Phys. (Leipzig)*, 12, 593–601.
- [35] Urbach F. (1953), The long-wavelength edge of photographic sensitivity and of the electronic absorption of solids, *Phys. Rev.* 92, 1324.
- [36] Zeng *et al.* (2006), Violet photoluminescence from shell layer of Zn/ZnO core-shell nanoparticles induced by laser ablation, *Appl. Phys. Lett.* 88, 171910.
- [37] Kong *et al.* (2001), Ultraviolet-emitting ZnO nanowires synthesized by a physical vapor deposition approach, *Appl. Phys. Lett.* 78, 407-409.
- [38] Pierce B. J., Hengehold R. L., (1976), Depth resolved cathodoluminescence of ion implanted layers in zinc oxide, *J. Appl. Phys.* 47, 644-651.
- [39] Studenikinm S. A., Golegu N., Cocivera M., (1998), Fabrication of green and orange photoluminescent, undoped ZnO films using spray pyrolysis, *J. Appl. Phys.* 84, 2287-2294.
- [40] Dai *et al.* (2003), Growth and luminescence characterization of large-scale zinc oxide nanowires, *J. Phys.: Condens. Matter.* 15, 2221-2226.
- [41] Liu M., Kitai A. H., Mascher P. (1992), Point defects and luminescence centres in zinc oxide and zinc oxide doped with manganese, *J. Lumin.* 54, 35-42.

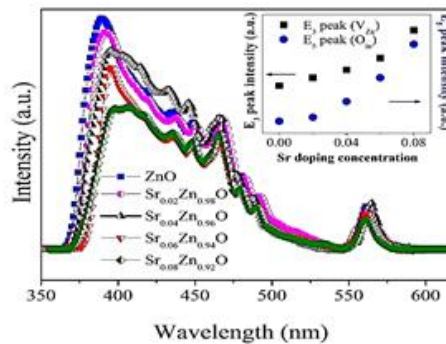
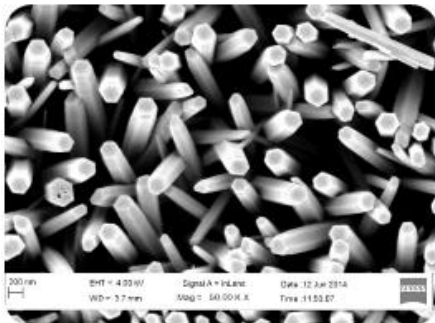
- [42] Vanheusden *et al.* (1996), Correlation between photoluminescence and oxygen vacancies in ZnO phosphors, *Appl. Phys. Lett.* 68, 403-405.
- [43] Erhart P., Albe K., Klein A. (2006), First-principles study of intrinsic point defects in ZnO: Role of band structure, volume relaxation, and finite-size effects, *Phys. Rev. B*, 73, 205203.
- [44] Behera D., Acharya B. S. (2008), Nano-star formation in Al-doped ZnO thin film deposited by dip-dry method and its characterization using atomic force microscopy, electron probe microscopy, photoluminescence and laser Raman spectroscopy, *J. Lumin.* 128, 1577-1586.
- [45] Arguello C. A., Rousseau D. L., and Porto S. P. S, (1969), First-order raman effect in wurtzite-type crystals, *Phys. Rev.* 181, 1351-1363.
- [46] Ashkenov N. *et al.*, (2006), Infrared dielectric functions and phonon modes of high-quality ZnO films, *J. Appl. Phys.* 93, 126-133.
- [47] Singh S. and Chakrabarti P., (2013), Comparison of the structural and optical properties of ZnO thin film deposited by three different method for optoelectronics application, *Superlattice. Microst.* 64, 283-293.
- [48] Rajalakshmi M., Arora A. K., Bendre B. S., and Mahamuni S. (2000), Optical phonon confinement in zinc oxide nanoparticles, *Journal of Applied Physics*, 87, 2445-2448.
- [49] Ashkenov *et al.* (2006), Infrared dielectric functions and phonon modes of high-quality ZnO films, *Journal of Applied Physics*, 93, 126-133.
- [50] Decremps, *et al.* (2002), High-pressure Raman spectroscopy study of wurtzite ZnO, *Phys. Rev. B*, 65, 092101.
- [51] Serrano *et al.* (2004), Pressure dependence of the lattice dynamics of ZnO: An ab initio approach, *Phys. Rev. B* 69, 094306.
- [52] Pimentel, *et al.*, (2014), Synthesis of long ZnO nanorods under microwave irradiation or conventional heating, *J. Phys. Chem. C* 118, 14629-14639.
- [53] Chen, *et al.* (2006), Photoluminescence and Raman behaviours of ZnO nanostructures with different morphologies, *Journal of Crystal Growth*, 289, 55-58.



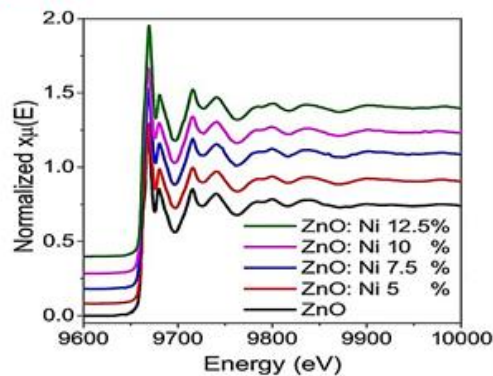
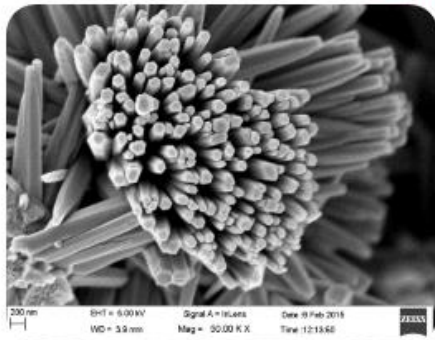
# CHAPTER 4

## Effect of Doping on Zinc Oxide Nanostructures

### $Zn_{1-x}Sr_xO$



### $Zn_{1-x}Ni_xO$



- **Amit K. Rana, Rajasree Das, Yogendra Kumar, Somaditya Sen, Parasharam M. Shirage, *Applied Surface Science* 379, 23 – 32, 2016.**
- **Amit K. Rana, Yogendra Kumar, Parasmani Rajput, Shambhu Nath Jha, Dibyendu Bhattacharyya, Parasharam M. Shirage, *ACS Applied Materials and Interfaces* 9(8), 7691 – 7700, 2017.**



# 4

---

## Effect of Doping on Zinc Oxide (ZnO) Nanostructures

*Unique physical and chemical properties of zinc oxide make it a multifunctional material and also it emerges as the most striking semiconductors in the category of 1D and 2D nanomaterials with numerous morphologies, which is already discussed in chapter 1 and 3. Due to its significant physical and chemical properties, it is a potential candidate for various applications such as photo electronic devices, nanosensors, nanogenerators, electronic devices, dye sensitized solar cells, spintronics, detection of metal ions, photocatalysis, etc.*

For particular applications, certain properties are needed which directly link with the internal and external properties of the material. The properties of a material depend upon numerous parameters such as morphology, internal defects, impurity/doping, *etc.* Morphological effects of pure ZnO have its limitations, which will constrain its application in some technologies. However, an impurity or doping in the semiconductor plays a major role to control its internal and external properties. Doping or impurity modifies the electrical and optical properties dramatically. Various dopants such as  $\text{Al}^{3+}$ ,  $\text{Cu}^{2+}$ ,  $\text{Ga}^{3+}$ ,  $\text{Ag}^{1+}$ ,  $\text{In}^{3+}$ ,  $\text{Sn}^{4+}$ ,  $\text{Sb}^{5+}$ ,  $\text{Fe}^{2+}$ ,  $\text{Fe}^{3+}$ ,  $\text{F}^{-}$ ,  $\text{Co}^{2+}$ ,  $\text{N}^{3-}$ ,  $\text{Ni}^{2+}$ , *etc.* [1, 2] have been used to study and manipulate properties of ZnO, and there is no doubt that these doping investigations are very important to understand the physical properties of ZnO thin films by facilitating their practical applications in industry. It has been observed that the efficiency of the dopant also has its merit and demerit as it depends on the electronegativity and ionic radius of the dopant.

As already discussed, ZnO is a promising candidate for the various applications. Therefore, to apply the prepared ZnO nanostructures for novel applications, here we have studied the effect of doping on the property variance of ZnO nanostructures in detail. To study the doping effect, we have chosen two elements strontium (Sr) and nickel (Ni), where both belong to different groups *i.e.* 2<sup>nd</sup> and 10<sup>th</sup>, respectively. Sr is alkaline earth *s*-block element with large ionic radii of 0.118 nm which is paramagnetic, while Ni is *d*-block transition element with ionic radii of 0.69 nm which is ferromagnetic.

The prime objective of this chapter is to study the effect of doping on ZnO nanostructures and investigate their structural, morphological and optical properties. The chapter is divided into two sections:

- (A) Effect of Strontium (Sr) doping on ZnO nanostructures.
- (B) Effect of Nickel (Ni) doping on ZnO nanostructures.

These two sections present a wet chemical approach for the preparation of doped ZnO nanostructures. The detailed investigations of their material properties and their possible fields of applications are discussed in each of the respective sections.

#### 4 (A). Effect of Strontium (Sr) doping on ZnO nanostructures

Regarding Sr-doped ZnO thin films, to the best of our knowledge, there are still very few related results reported till to date [3-6].  $Zn_{1-x}Sr_xO$  shows promising feature to fabricate transparent electrodes in solar cells, love wave filter applications, micro-electromechanical systems (MEMS), and ultrasonic oscillators [7]. Water *et al.* reported the thermal treatment of Sr doped ZnO thin film in a reducing atmosphere which modifies the optical and electrical properties of the films [5]. Vijayan *et al.* showed enhancement of the band gap and high gas sensitivity in the Sr doped ZnO films, deposited with a chemical bath deposition technique [6]. Pachoumi *et al.* [3] also used sol-gel method for deposition of Sr doped ZnO thin films and studied the electrical conductivity of the samples. Similarly, L. Xu *et al.* [8] and Yousefi *et al.* [9] used sol-gel method for growth of Sr doped ZnO nanostructures to study the optical and structural properties that showed the enhanced visible-light photocatalysis activity of Sr doped ZnO nanoparticles. These studies are prime importance to the alkaline earth element, especially those with large cationic radius, which is projected to influence both the varistor properties and microstructure greatly. However, despite all these findings, an experimental study on defects and optical properties of ZnO is somewhat limited, particularly on  $Zn_{1-x}Sr_xO$  compound. Complete understanding regarding defect driven luminescence and phonon vibrational modes are necessary to develop high quality optoelectronic devices. So, Sr doped ZnO thin film is a very interesting field to explore as it is one of the least studied materials, which is important for technological applications.

##### 4(A).1. Materials and Method

**Materials:** Zinc nitrate hexahydrate ( $Zn(NO_3)_2 \cdot 6H_2O$ ; Alfa Aesar), strontium nitrate ( $Sr(NO_3)_2$ ; Sigma Aldrich), aqueous ammonia ( $NH_3$ ; Merck), deionized water as a solvent, pH paper (Merck), flexible substrates (polyester film; Borolab), *etc.*

**Method:** The  $Zn_{1-x}Sr_xO$  ( $0.0 \leq x \leq 0.08$ ) films were prepared on flexible transparent substrate using wet chemical process from aqueous solution of high purity nitrates (100 mM concentration). An aqueous solutions of Zn nitrate hexahydrate ( $Zn(NO_3)_2 \cdot 6H_2O$ ) and strontium nitrate ( $Sr(NO_3)_2$ ) were prepared in deionized water and stirrer for 30 min. Then aqueous  $NH_3$  was added under constant stirring. A white precipitate was initially observed, which subsequently dissolved back in solution upon further addition of aqueous  $NH_3$ . The pH of the solution was maintained at  $\sim 12$ . After the pH was maintained for 30

min., carefully cleaned transparent substrates were dipped vertically and the solution was heated at 90°C for ~ 60 min. Finally, thin layers of material are coated on the substrates, which were then removed from the solution, washed with deionized water and dried in air for overnight. All the transparent films were annealed at 100°C for 2 h to get pure phase films.

## 4(A).2. Results and Discussion

### 4(A).2.1. Morphological properties

**Scanning electron microscopy:** Figure 4.1 shows the typical SEM image of (a) un-doped and (b) 8% Sr doped ZnO on transparent sheets. The surface morphology of all the films shows rods like structures. The average diameter of the rods are ~100 nm for pure ZnO and almost double for the Sr-doped ZnO (~200 nm). The increase in diameter of the rods may be related to the Sr-doping effect, as the Sr doping might enhance reaction process in the solution [10]. The length of the rods is in the range of few micrometers.

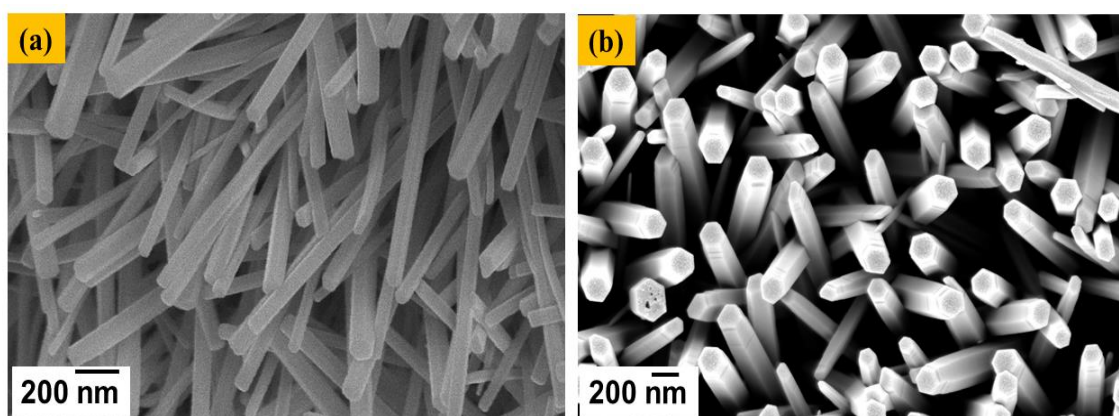


**Figure 4.1.** Field Emission Scanning Electron Microscopy (FESEM) of (a) ZnO and (b) Sr-doped ZnO thin films.

**Transmission Electron Microscopy:** The structures and size of ZnO nanorods are characterized by TEM and selected area electron diffraction (SAED). Fig. 4.2 (a–f) represents the TEM and HRTEM images of  $\text{Zn}_{1-x}\text{Sr}_x\text{O}$  ( $0.0 \leq x \leq 0.08$ ). The HRTEM images of the un-doped and Sr-doped ZnO confirm the formation of rod like structure with diameter altering from ~150-250 nm. All the images show extended well developed lattice fringes throughout the highly crystalline ZnO nanorods, with a lattice spacing of about 0.26 nm in case of pure ZnO, which corresponds to the interplanar spacing of (002) plane.

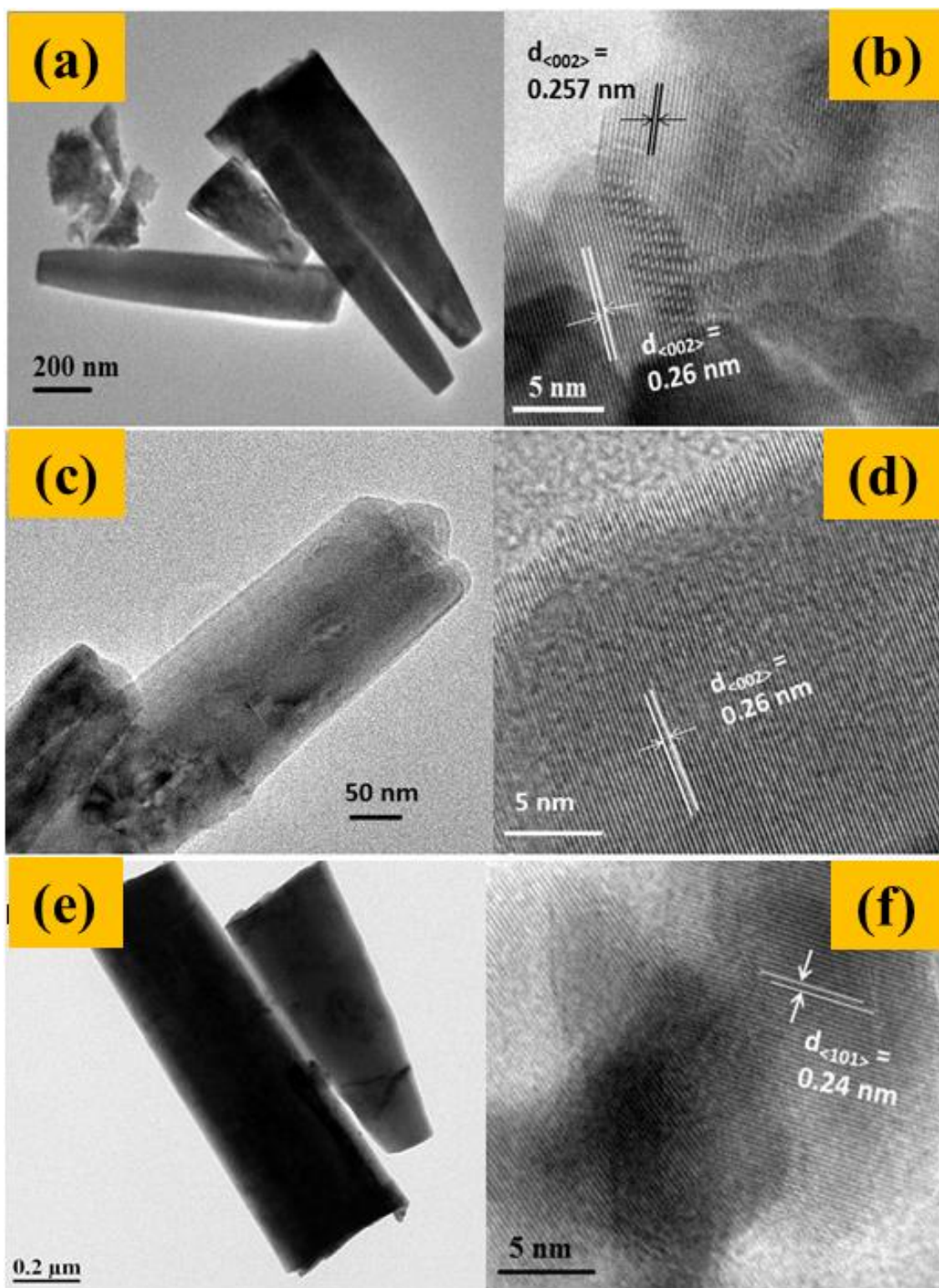


**Figure 4.2.** (a-f) TEM and HRTEM images of  $\text{Zn}_{1-x}\text{Sr}_x\text{O}$  ( $0.0 \leq x \leq 0.08$ ) of (a-b)  $x=0$ , (c-d)  $x=0.04$  and (e-f)  $x=0.08$  respectively.

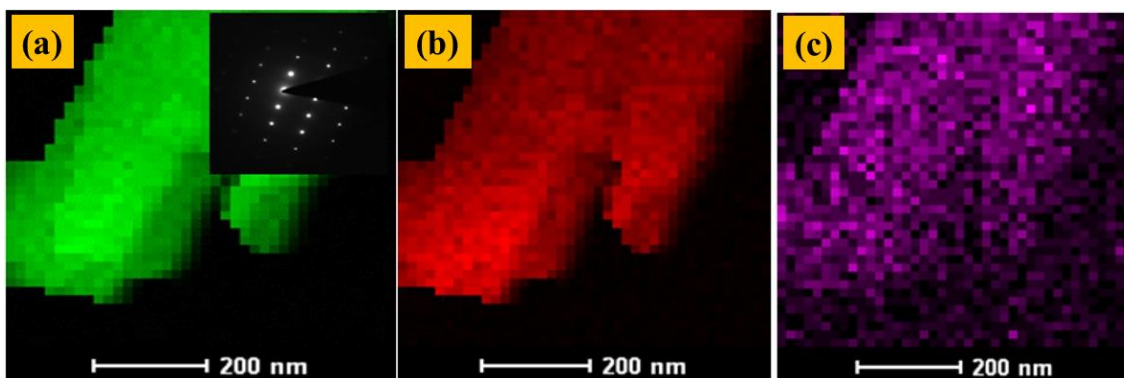


**Figure 4.3.** Elemental mapping of 8% Sr doped ZnO nanorod, (a) Zn, (b) O and (c) Sr. Inset of (a) shows Selective Area Electron Diffraction (SAED) of ZnO nano-rod.

Whereas, the fringes of Sr doped samples shows lattice spacing of about 0.24 nm which corresponds to the (101) reflection planes of ZnO hexagonal structure for 8% Sr doping. SAED pattern of ZnO nano-rod suggests single crystalline nature of the nano-rods (inset of Fig. 4.3(a)). To confirm the doping of the Sr in ZnO, the elemental color mapping TEM was carried out on 8% Sr doped ZnO. Figure 4.3 shows TEM image of  $\text{Zn}_{0.92}\text{Sr}_{0.08}\text{O}$  nano-rods selected for elemental color mapping. Figure 4.3(a)–(c) represents an elemental color mapping of Zn, Sr and O respectively. Elemental mapping using TEM confirms the homogeneous distribution of Sr in the 8% Sr doped ZnO nano-rods.

#### 4(A).2.2. Structural properties

**X-Ray diffraction:** XRD patterns of  $\text{Zn}_{1-x}\text{Sr}_x\text{O}$  ( $0.0 \leq x \leq 0.08$ ) thin films are shown in Figure 4.4. The peak position of the films reveals that all peaks are associated with the characteristic peaks of the hexagonal wurtzite structure with space group  $P6_3mc$ . No trace of impurity is found in the  $\text{Zn}_{1-x}\text{Sr}_x\text{O}$  ( $0.0 \leq x \leq 0.08$ ) films, indicating the growth of high purity films. Rietveld refinement is carried out to obtain detailed information of the crystal structure and lattice parameter of the  $\text{Zn}_{1-x}\text{Sr}_x\text{O}$  ( $0.0 \leq x \leq 0.08$ ) films.

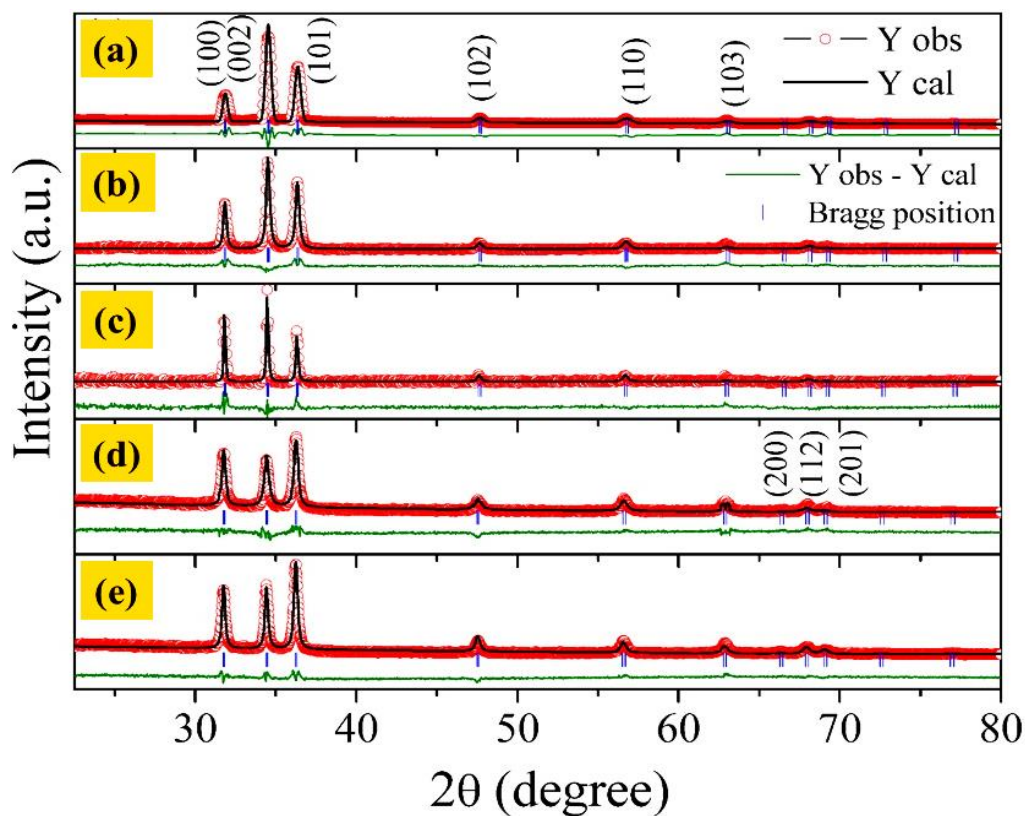


**Figure 4.4.** XRD patterns of (a) undoped ZnO, (b)  $\text{Sr}_{0.02}\text{ZnO}$ , (c)  $\text{Sr}_{0.04}\text{ZnO}$ , (d)  $\text{Sr}_{0.06}\text{ZnO}$  and (e)  $\text{Sr}_{0.08}\text{ZnO}$  thin films.

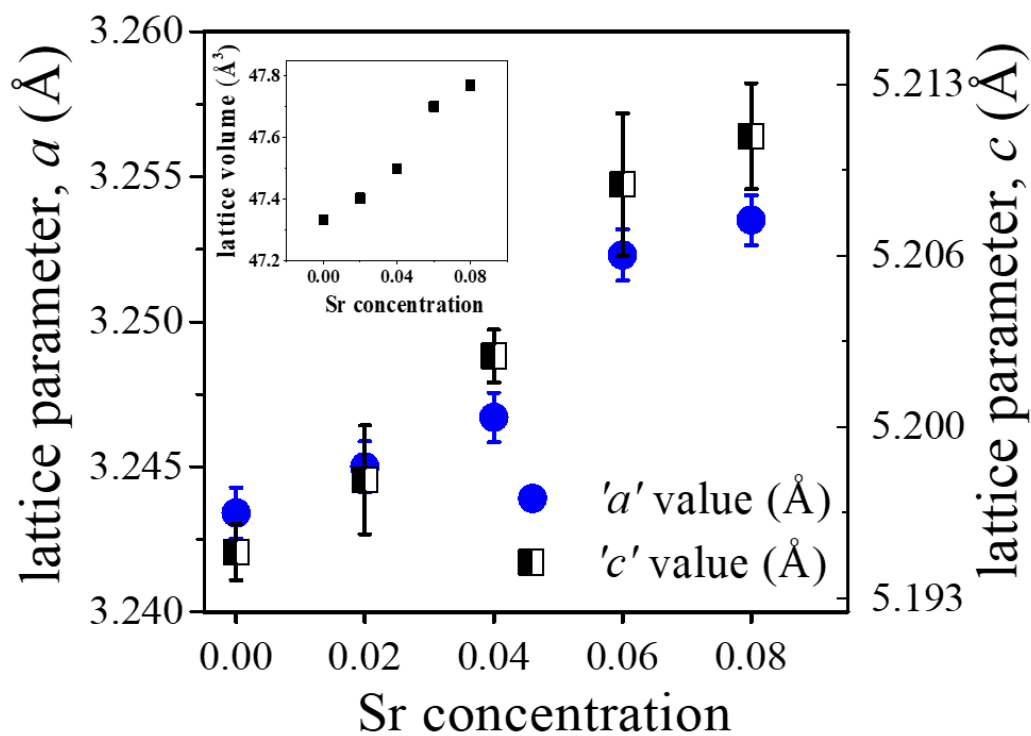


**Figure 4.5.** The variation of ZnO lattice parameters, 'a' and 'c' as a function of Sr doping concentration. Inset of the figure shows corresponding change in lattice volume with Sr doping concentration.

**Table 4.1.** Refined structural parameters for  $Zn_{1-x}Sr_xO$  ( $0.0 \leq x \leq 0.08$ ) thin film.

Sample	Lattice parameter (Å)	Atoms	Positions			Occ. Ratio (Zn/O)	Volume (Å <sup>3</sup> )	
			X	Y	Z			
ZnO	$a=3.243(4\pm 2)$	Zn	2a	0	0	$0.855(5\pm 3)$	0.503	47.33(2±2)
	$c=5.195(2\pm 1)$	O	2b	0.3333	0.6667	$0.880(0\pm 2)$		
$Zn_{0.98}Sr_{0.02}O$	$a=3.245(0\pm 2)$	Zn/Sr	2a	0	0	$0.395(0\pm 1)$	0.417	47.40(2±6)
	$c=5.198(0\pm 2)$	O	2b	0.3333	0.6667	$0.350(0\pm 3)$		
$Zn_{0.96}Sr_{0.04}O$	$a=3.246(7\pm 5)$	Zn/Sr	2a	0	0	$0.855(5\pm 3)$	0.485	47.49(8±2)
	$c=5.202(7\pm 1)$	O	2b	0.3333	0.6667	$0.880(0\pm 2)$		
$Zn_{0.94}Sr_{0.06}O$	$a=3.252(3\pm 4)$	Zn/Sr	2a	0	0	$0.869(0\pm 3)$	0.464	47.71(9±1)
	$c=5.209(2\pm 3)$	O	2b	0.3333	0.6667	$0.785(0\pm 4)$		
$Zn_{0.92}Sr_{0.08}O$	$a=3.253(5\pm 2)$	Zn/Sr	2a	0.3333	0.6667	0	0.409	47.77(0±2)
	$c=5.211(0\pm 3)$	O	2b	0.3333	0.6667	$0.502(0\pm 1)$		

Table 4.1 summarizes the parameters obtained from Rietveld refinement. Increase in doping concentration shows peak shift towards lower theta, which is due to the addition of higher radii  $Sr^{2+}$  (0.118 nm) ion in the lattice, replacing  $Zn^{2+}$  (0.074 nm). Figure 4.5 shows an increase in the lattice parameters ('a' and 'c') with doping concentration which follows the Vegards Law. The existence of zinc and oxygen related defects are a well-known factor; our analysis shows a good agreement with it too. Table 4.1 shows that the ratio of Zn/O occupancy is less than 1 in ZnO lattice structure and Sr doping decreases this ratio further, which supports the mechanism of defect formation by doping [11].

**Secondary ion mass spectroscopy (SIMS):** SIMS is one of the most reliable analytical techniques to determine elemental concentrations in the compound [12]. Figure 4.6 shows that SIMS intensity signals of Sr in all the doped films remain almost constant over the entire period of sputtering time, indicating homogeneity in composition throughout the films. A careful observation of the data shows that the change in  $C_{Sr}/RSF_{Sr}$  (concentration of Sr / relative sensitivity factor of Sr) ratio is very systematic with an increase in doping concentration in the films which confirms the successful doping of Sr in the ZnO matrix further.

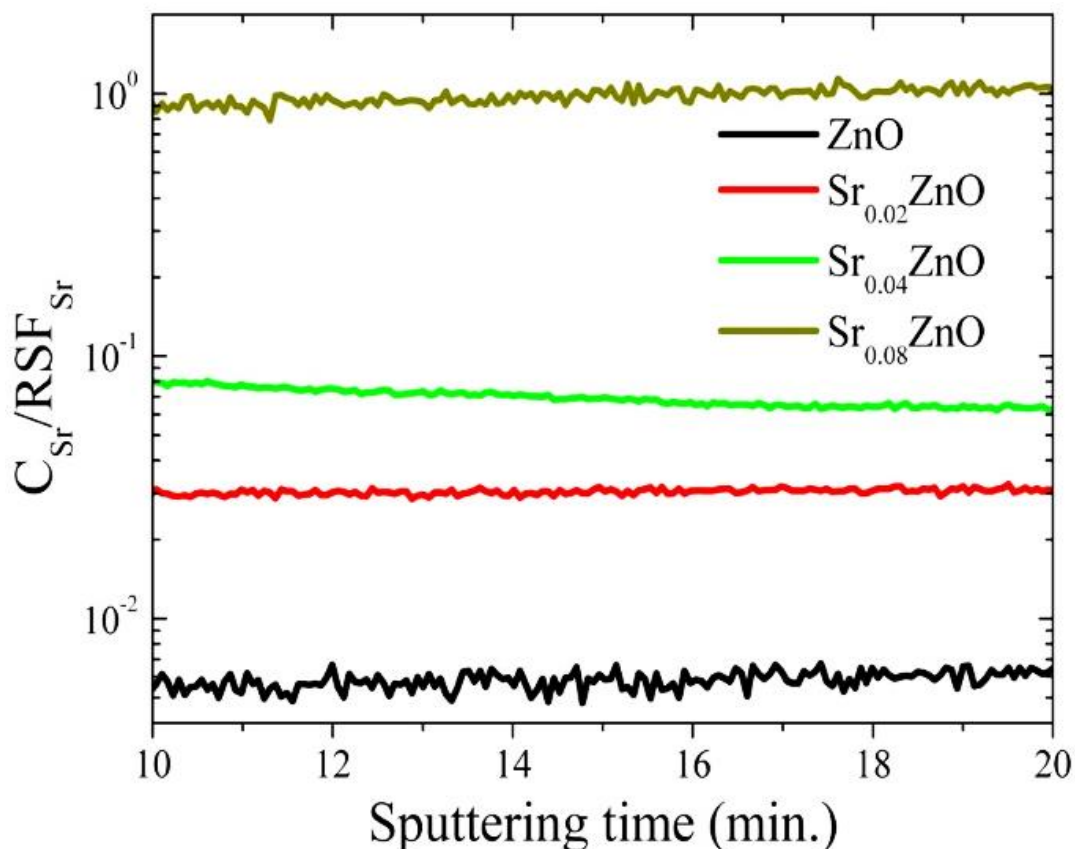


**Figure 4.6.** Secondary Ion Mass Spectroscopy (SIMS) of  $\text{Zn}_{1-x}\text{Sr}_x\text{O}$  ( $0.0 \leq x \leq 0.08$ ) films with  $x = 0, 0.02, 0.04, 0.08$ .

**X-Ray photoelectron spectroscopy (XPS):** Figure 4.7(a) and (b) shows high-resolution XPS spectra of asymmetric O1s core peak fitted with two Gaussian components, of pure ZnO and with  $x = 0.08$  ( $\text{Zn}_{1-x}\text{Sr}_x\text{O}$ ) thin films, respectively. Lower binding energy (LBE) peak at 529.3 and 529.6 eV for  $x = 0$  and  $x = 0.08$ , respectively, arises from  $\text{O}^{2-}$  ions in a normal ZnO wurtzite lattice structure which forms Zn-O bond [13]. Whereas, higher binding energy (HBE) peak at 531.4 and 531.3 eV for  $x = 0$  and  $x = 0.08$ , respectively, are attributed to Zn-OH bond due to the hydroxyl group [14], or other radicals on the film surface such as CO or  $\text{CO}_2$ , etc. [4].

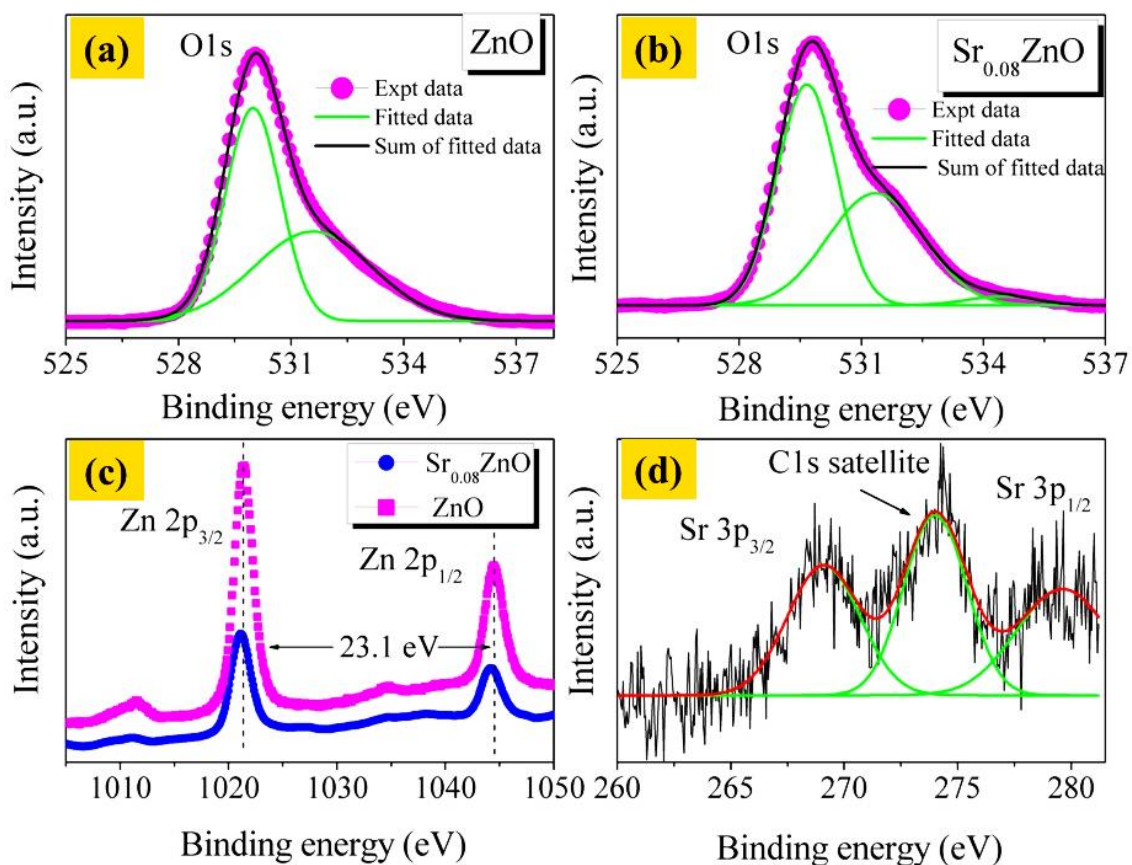


**Figure 4.7.** XPS spectra of the (a) O1s peak in undoped ZnO film, (b) O1s peak in Zn<sub>0.92</sub>Sr<sub>0.08</sub>O film (c) Zn 2p peak in ZnO and Zn<sub>0.92</sub>Sr<sub>0.08</sub>O film and (d) Sr 3p peak in Zn<sub>0.92</sub>Sr<sub>0.08</sub>O film.

However, some contribution to this HBE peak of the O1s spectrum can also be related to the presence of oxygen deficiency within the ZnO matrix [15, 16]. In our case the changes in the intensity ratio of the LBE and HBE oxygen peak with Sr doping is worth noticing. As mentioned before, Zn/O occupancy decreases slightly (Table 4.1) in the doped thin films indicating a large concentration of oxygen and Zn vacancies. Therefore, increase in the HBE peak intensity in the  $x = 0.08$  film can be explained as, in the Sr doped films more O1s electrons are loosely bonded to lattice compared to the pure ZnO film.

The oxidation state of Zn can be determined by analyzing the Zn 2p spectra of the films, shown in Figure 4.7(c). Both the films possess characteristic doublet peak of Zn 2p<sub>3/2</sub> and Zn 2p<sub>1/2</sub> at 1021.5 and 1044.6 eV for ZnO and at 1021.2 and 1044.2 eV for Zn<sub>0.92</sub>Sr<sub>0.08</sub>O, respectively, along with their corresponding satellite peaks. The obtained binding energy (BE) difference between Zn 2p<sub>3/2</sub> and 2p<sub>1/2</sub> (23.1 and 23.0 eV for un-doped and doped films, respectively) peaks are in good agreement with the reported value for

Zn<sup>2+</sup> oxidation state [17, 18]. Figure 4.7(d) shows high-resolution XPS spectra of Sr 3p region of the Sr<sub>0.08</sub>ZnO thin film. It reveals two distinct peaks at 269.3 and 279.4 eV correspond to Sr 3p<sub>3/2</sub> and 3p<sub>1/2</sub> states, respectively, [19, 20] having a BE difference of 10.1 eV. BE separation of the doublet 3p peaks for the Sr-O bond is 10.1 eV whereas, for metallic Sr it is 10.4 eV [21]. The second peak at 274.1 eV in Figure 4.7(d) is the shake up or satellite peak of C1s. The chemical composition of the film is calculated according to the formula as follows [22]:

$$X(\%) = \frac{A_X/S_X}{\sum_{i=1}^N A_X/S_i} \quad (4.1)$$

where  $A_X$  ( $A_i$ ) and  $S_X$  ( $S_i$ ) indicated the peak area and sensitivity factor of elements,  $x(i)$  and  $N$  is total the number elements. The results of the chemical composition, based on the intensities of the O, Zn and Sr lines are given in Table 4.2. XPS spectra of the Sr 3p region suggest successful incorporation of Sr in ZnO matrix replacing Zn and that Sr is in 2<sup>+</sup> oxidation state in the doped films. The actual doping of Sr is less than the nominal doping (*i.e.*, in 8 % Sr doped samples only 5 % Sr is being doped, as per our XPS data analysis).

**Table 4.2.** Atomic percentage of Zinc, Oxygen and Strontium measured by XPS.

Sample	Atomic % concentration		
	Zn	O	Sr
ZnO	52.97	48.03	0
Zn <sub>0.92</sub> Sr <sub>0.08</sub> O	50.26	44.63	5.11

**Raman spectroscopy:** The group theory analysis of wurtzite ZnO structure (the total number of atoms per unit cell is  $s = 4$ , space group P6<sub>3</sub>mc, at the Brillouin zone center ( $q = 0$ )) shows that phonon dispersion of ZnO has 12 branches consists of polar modes ( $A_1$  and  $E_1$ ), two non-polar modes ( $2E_2$ ) and two silent ( $2B_1$ ) Raman modes [23]. Among these,  $A_1$  and  $E_1$  polar modes are divided into two active phonon modes (transverse optical (TO) and longitudinal optical (LO)), and  $E_2$  is divided into  $E_2^{low}$  and  $E_2^{high}$  active modes and the  $B_1$  branches are Raman inactive modes.



ZnO is situated at 575 ( $A_1$ ) and 587 ( $E_1$ )  $\text{cm}^{-1}$ . Defect states in ZnO ( $V_{\text{O}}$ ,  $Zn_{\text{in}}$  or free carriers) contributes to the LO mode intensity of  $E_1$  symmetry [25]. Mn and Co-doped ZnO shows significant change in  $E_1(\text{LO})$  mode due to the modification in intrinsic host lattice defects with doping [27, 26]. Whereas, Bundesmann *et al.* [27] and Kaschner *et al.* [28] have observed a peak at 583 and 582  $\text{cm}^{-1}$  respectively, only in the doped films and assigned it as additional peak (APs) due to the defects. All the samples shows a broad Raman scattering peak centered around 582  $\text{cm}^{-1}$ , as a consequence this peak can be assigned to the combination of both LO vibrational modes of ZnO. An insignificant shift is demonstrated in the observed peak positions compared to the reported values as the phonon mode frequencies varies depending on the size, morphology and preparation techniques of the samples [16].

**Table 4.3.** Phonon mode frequencies (in units of  $\text{cm}^{-1}$ ) of wurtzite  $Zn_{1-x}Sr_xO$  ( $0.0 \leq x \leq 0.08$ ) thin films.

Peak no.	The position of the vibration bands ( $\text{cm}^{-1}$ )					Assignment
	ZnO	$Zn_{0.98}Sr_{0.02}O$	$Zn_{0.96}Sr_{0.04}O$	$Zn_{0.94}Sr_{0.06}O$	$Zn_{0.92}Sr_{0.08}O$	
1	99.5	99.4	99.4	99.5	99.7	$E_2^{\text{low}}$
2	-	277	277.3	277.8	278	Defects due to $Sr^{2+}$ doping
3	332.9	331.5	332.3	333.1	333.9	$(E_2^{\text{high}} - E_2^{\text{low}})$
4	382.5	382.1	380.9	380.8	380.9	$A_1$ (TO)
5	438.2	438.8	438.9	439.3	438.9	$E_2^{\text{high}}$
6	582.1	582.5	579.9	582.4	581.3	LO ( $A_1 + E_1$ )
7	-	663.1	664.8	663.4	665.7	Defects due to $Sr^{2+}$ doping

Apart from these five major peaks, doped samples show two more small intensity peaks (P2  $\sim 277$  and P7  $\sim 663$   $\text{cm}^{-1}$ ). The origin of these two peaks is not very clear yet as the earlier reports claims the various reason for the occurrence of these peaks. Kaschner *et al.* [28] correlated phonon vibration modes at 275  $\text{cm}^{-1}$  with N incorporation in ZnO structure, claiming that intensity of this peak increases linearly with N doping concentration. Meanwhile, Bundesmann *et al.* [27] observed similar peak (277  $\text{cm}^{-1}$ ) in Fe, Sb, Al, Ga, and Li doped ZnO films and reported it as a result of lattice defects. Following these literatures, APs at 277  $\text{cm}^{-1}$  in Sr doped ZnO film, which is more prominent in the  $x = 0.08$  doped film, can be assigned to the defects created in the ZnO matrix due to doping. Last broad peak at 663  $\text{cm}^{-1}$  is also a reason for major debate. Serrano *et al.* [29] showed using the two-phonon density of states calculation that intrinsic mode of ZnO at 650  $\text{cm}^{-1}$  arises from two phonon process TA + LO. While, Wang *et al.*

[30] observed a peak at  $663\text{ cm}^{-1}$  in Mn doped ZnO nanoparticles and reported it due to the combined effect of  $A_1(\text{LO}) + E_2^{\text{high}}$  and existence of  $\text{Zn}_2\text{MnO}_4$  precipitates. Meanwhile, Yang *et al.* [31] assigned this peak (at  $660\text{ cm}^{-1}$ ) to  $\text{V}_\text{O}$  related intrinsic mode of ZnO. In present case, Raman spectra of pure ZnO does not have any peak in this region, however low intensity peak at  $663\text{ cm}^{-1}$  was observed in case of the Sr doped ZnO and can be assigned to merely because of the presence of  $\text{Sr}^{2+}$  in ZnO lattice.

#### 4(A).2.3. Optical properties

**Photoluminescence spectroscopy:** PL spectra of ZnO are investigated theoretically and experimentally by many research groups to some extent to understand the complex defect physics of ZnO structure. In ZnO, shallow Zn interstitials ( $\text{Zn}_{\text{in}}$ ) and Oxygen vacancy ( $\text{V}_\text{O}$ ) are responsible for the main visible emission, as in Zn-rich or O-rich conditions,  $\text{Zn}_{\text{in}}$  and  $\text{V}_\text{O}$  have low formation enthalpies [32]. Whereas, the existence of other intrinsic point defects and complexes such as Zn vacancy ( $\text{V}_{\text{Zn}}$ ), oxygen interstitials ( $\text{O}_{\text{in}}$ ), antisite oxygen ( $\text{O}_{\text{Zn}}$ ), a complex of  $\text{V}_\text{O}$  and  $\text{Zn}_{\text{in}}$  ( $\text{V}_\text{O}\text{Zn}_{\text{in}}$ ) and complex of  $\text{V}_{\text{Zn}}$  and  $\text{Zn}_{\text{in}}$  ( $\text{V}_{\text{Zn}}\text{Zn}_{\text{in}}$ ) in ZnO are also reported previously. Van Dijken proposed that intensity of these defect emissions, especially exciton emission, strongly depends on the size of ZnO nanostructures [33]. This observation makes it more sensible about the different emission peaks and related defects observed by different research groups such as, Behera and Acharya [34] observed six different defect states consisting of emission from conduction band and/or defect donor sites to valence band and/or deep acceptor defects sites. Ghosh *et al.* [8] showed existence of seven emission peak in doped ZnO nanowires. Theoretical analysis carried out by Xu *et al.* [35] showed seven different defect states in ZnO, whereas, Zhang *et al.* [14] observed only five donor and acceptor type defect levels by local density approximation (LDA) theorem. Figure 4.9(a) represents room temperature (RT) normalized PL spectrum, and Gaussian fitted curves of ZnO thin film and Figure 4.9(b) shows the schematic band diagram of all the emissions assembled from the PL data. The typical wide emission spectrum of ZnO extending from near band edge (NBE) to green emission can be well resolved into 10 peaks at 378 (3.29 eV), 388 (3.21 eV), 404 (3.07 eV), 436 (2.85 eV), 450 (2.76 eV), 467 (2.66 eV), 480 (2.59 eV), 489 (2.54 eV), 499 (2.49 eV) and 562 nm (2.20 eV). Existence of all these well resolved peaks are related to the defects level in ZnO film.

The first peak ( $E_1$ ) located in the UV region (378 nm) corresponds to the NBE in ZnO film, arises due to the free exciton (FX) recombination process via exciton–exciton collision [36]. Second emission peak ( $E_2$ ) located at 388 nm with an energy difference of 77 meV with  $E_1$  is reported to be attributed to the first longitudinal optical (LO) phonon replica of FX [37]. The emission peak  $E_3$  at 404 nm, originates from the singly ionized  $V_{Zn}$  [18]. Whereas, the violet emission peak at 436 nm ( $E_4$ ) is originated due to electron transition between valence band maxima (VBM) and shallow donor level of the  $Zn_{in}$  [18, 19]. Low intensity peak at 450 nm ( $E_5$ ) and 467 nm ( $E_6$ ) are reported due to the carrier transition from exciton level to the  $O_{in}$  level and  $Zn_{in}$  to acceptor  $V_{Zn}$ , respectively [12]. Another low intensity blue peak at 480 nm ( $E_7$ ), which might be originated from the conduction band minima to the  $V_O$  [38].

Green emission or deep band emission (DBE) region in the ZnO films need special attention as various interpretations can be found regarding the origin of PL band here. Børseth *et al.* [39] reported the energy value of the optical signal of  $V_O$  and  $V_{Zn}$  based on the data of annealing of samples in a different atmosphere. Following the analysis and results reported by Leiter *et al.* [40] and Børseth *et al.* green emission peak  $E_8$ , at 489 nm can be attributed to the  $V_O$  defects. Similarly, green emission peak  $E_9$  situated at 499 nm may be correlated to the defects result of deep level or trap-state emission [41]. Lin *et al.* [42] theoretically showed that green emissions with a peak at 2.38 eV could be assigned to the antisite oxygen ( $O_{Zn}$ ). Yellow luminescence band peak  $E_{10}$  at 564 nm is identified as dopant defect in wet chemical process grown ZnO [21] or even the interstitial oxygen ( $O_{in}$ ) vacancy defect [23]. As in our case, structural measurements detect no trace of elemental impurity in the films;  $E_{10}$  is attributed to the electronics transition from the bottom of the conduction band to  $O_{in}$ , which is close to the reported value (573 nm) by Liu *et al.* [43].

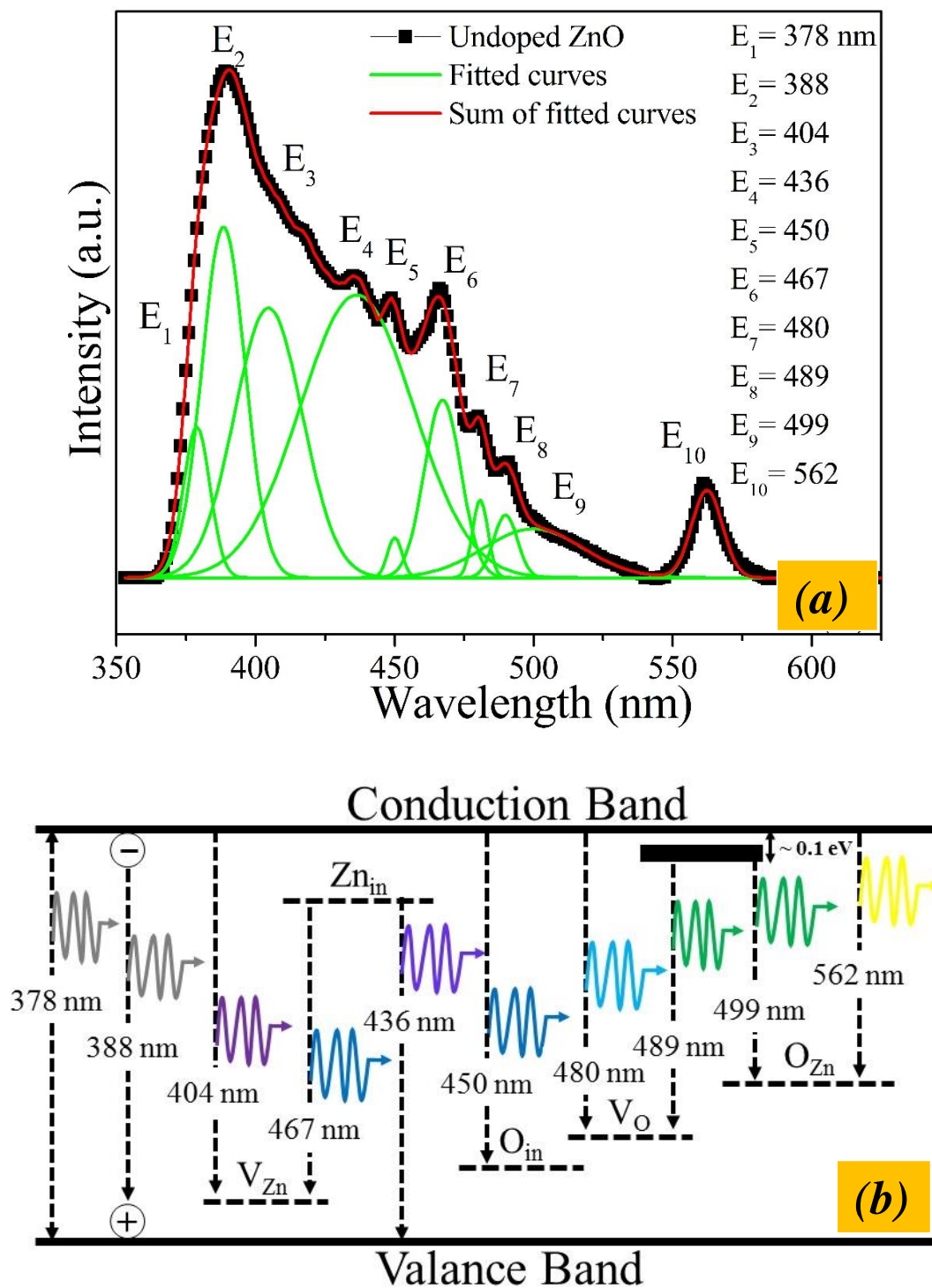


**Figure 4.9** (a) Room temperature PL spectra of undoped ZnO thin films. The “■” shows experimental data and solid green and red lines are Gaussian fitting of individual peaks and sum of all peaks, respectively (b) Schematic band diagram for ZnO thin film.

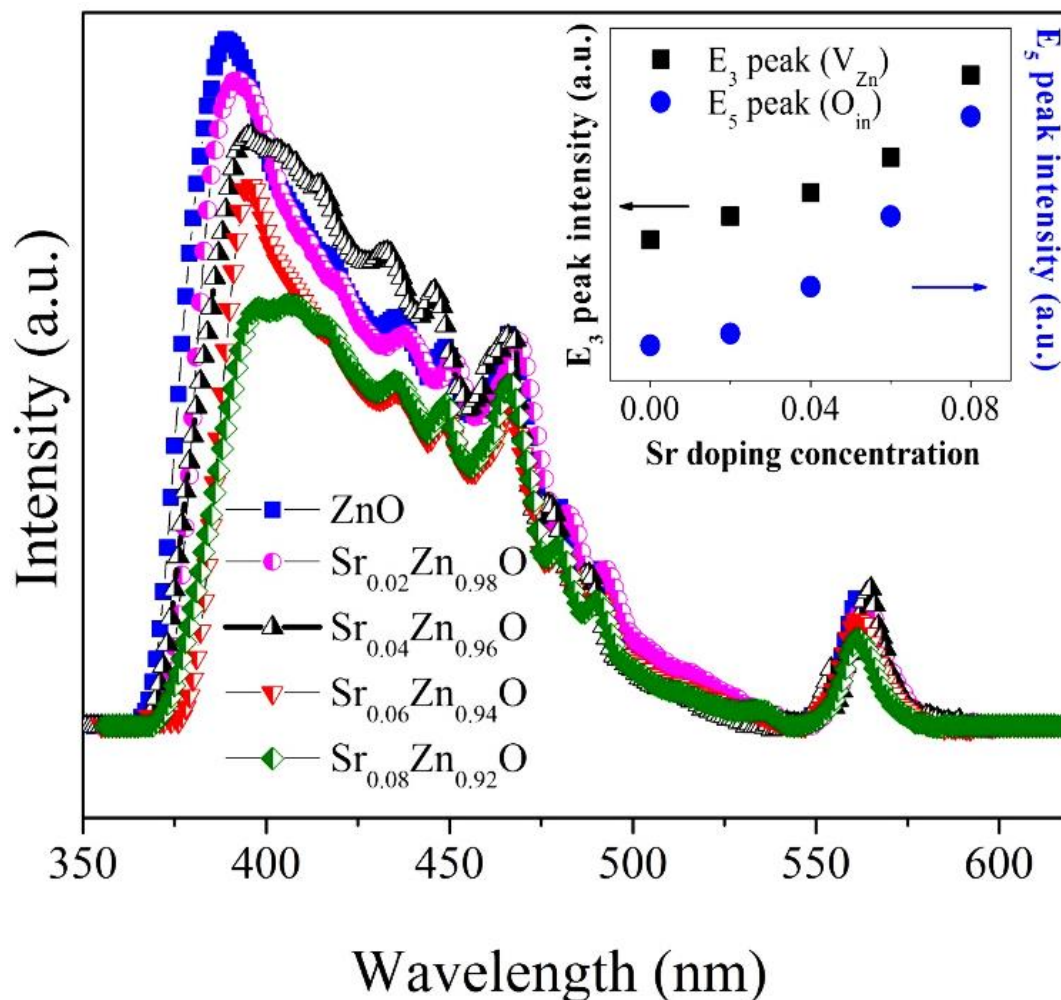


**Figure 4.10.** Experimental data for room temperature PL spectra of  $\text{Zn}_{1-x}\text{Sr}_x\text{O}$  ( $0.0 \leq x \leq 0.08$ ) thin films. Inset shows the change in relative intensity of  $E_3$  ( $V_{\text{Zn}}$  related peak) and  $E_5$  ( $O_{\text{in}}$  related peak) peak with Sr doping concentration in the films.

Figure 4.10 shows a clear change of the PL peak positions with a doping concentration of alkaline metal ion Sr in ZnO film. Table 4.4 shows deconvolution of PL spectra of intrinsic and Sr doped films. Inset of Figure 4.10 shows a noticeable increase in the relative intensity of  $V_{\text{Zn}}$  ( $E_3$  and  $E_6$ ) and  $O_{\text{in}}$  ( $E_5$ ) related peak is observed with doping indicating that doping of Sr replaces Zn and creates more defects in the matrix. Lin *et al.* [24] also mentioned similar phenomenon in their finding. However, it is worth to mention here that with an increase in Sr doping emission intensity of valance band maxima (VBM) to  $\text{Zn}_{\text{in}}$  ( $E_4$ ) decreases consistently. Therefore, it is evident that relative intensity of this violet-blue luminescence peak decreases sharply due to incorporation of different Sr-defects such as Sr substitution ( $\text{Sr}_{\text{Zn}}$ ) and/or Sr interstitials ( $\text{Sr}_{\text{in}}$ ) defects in the lattice. Green emission peak intensity ( $E_8$  and  $E_{10}$ ) remains same in all samples as all

are annealed in an air atmosphere. This observation is inconsistent with the previous report on ZnO NPs, which shows that the incorporation of alkali metal ions increase the green band emission and yellow band emissions of ZnO [23]. Whereas, a very small decrease in E<sub>9</sub> peak intensity is noticed. All the above mentioned changes in the PL spectrum further confirm Sr substitution in ZnO films, which can be safely concluded from the SIMS experiment too.

**Table 4.4.** The peak position and relative peak intensity of deconvoluted PL spectra of Zn<sub>1-x</sub>Sr<sub>x</sub>O (0.0 ≤ x ≤ 0.08) thin films. Peak position (nm) and relative intensity (%) have the errors ±1.

Peak No	ZnO		Zn <sub>0.98</sub> Sr <sub>0.02</sub> O		Zn <sub>0.96</sub> Sr <sub>0.04</sub> O		Zn <sub>0.94</sub> Sr <sub>0.06</sub> O		Zn <sub>0.92</sub> Sr <sub>0.08</sub> O	
	Peak Position (nm)	Rel. int. (%)	Peak Position (nm)	Rel. int. (%)	Peak Position (nm)	Rel. int. (%)	Peak Position (nm)	Rel. int. (%)	Peak Position (nm)	Rel. int. (%)
1	378	43	383	60	392	58	382	59	394	62
2	388	100	392	100	405	100	391	100	406	100
3	404	77	408	79	417	81	418	80	417	91
4	436	81	439	84	439	58	436	36	436	39
5	450	11	452	13	452	27	451	21	449	58
6	467	51	469	56	468	82	469	46	466	71
7	480	22	483	23	483	25	480	23	480	23
8	489	18	492	19	492	19	490	17	490	16
9	499	14	501	16	500	11	500	11	535	9
10	562	25	564	26	564	29	562	26	562	23

#### 4 (B). Effect of Nickel (Ni) doping on ZnO nanostructures

As compared to Sr doping, a huge number of study are already carried out on Ni doped ZnO nanostructures. This is because of its ionic radii, *i.e.*, Ni (0.69 Å), ferromagnetic nature with its unique chemical stability in the zinc site that makes it as one of the most effective doping element to improve and tune the structural, optical, magnetic and electrical properties of ZnO. There are several reports which display that Ni ions create an energy level at the bottom of the conduction band, which help to provide electrons to the conduction band easily [44]. Because of this it shows the diverse properties and applications for instances, Ni doped ZnO stands for its application in the dilute magnetic semiconductor at room temperature [45-47] however some disputes are attached with its room temperature magnetic properties which have been reported by many research groups [48-50]. Along with this, Ni doped ZnO nanorods have enhanced gas-sensing performance and gas sensitivity which is found to depend on the Ni concentration in ZnO films [51]. It also shows the good photocatalysis and field emitter application [52, 53].

Nanowire arrays of Ni doped ZnO show the enhancement in the photo sensing properties as compared to pure ZnO [54]. However, there are very fewer studies on the internal structure in case of Ni doped ZnO. Here in this section of chapter we minutely studied the effect of Ni doping on ZnO and investigated how the Ni ions affect its internal and external properties especially on the magnetic origin in ZnO. This will help us to manipulate its properties according to the specified application.

#### 4(B).1. Materials and method

**Materials:** Zinc nitrate hexahydrate ( $\text{Zn}(\text{NO}_3)_2 \cdot 6\text{H}_2\text{O}$ ) (Alfa Aesar), Nickel nitrate hexahydrate (Alfa Aesar), aqueous ammonia ( $\text{NH}_3$ ) (Merck), deionized water as a solvent, pH paper (Merck), flexible substrates (polyester film) (Borolab).

**Method:**  $\text{Zn}_{1-x}\text{Ni}_x\text{O}$  ( $0 \leq x \leq 0.125$ ) samples synthesized by simple wet chemical process have been named as ZnO, ZnO: Ni5%, ZnO: Ni7.5%, ZnO: Ni10%, ZnO: Ni12.5% for different Ni-concentration  $x = 0\%$ ,  $5\%$ ,  $7.5\%$ ,  $10\%$ , and  $12.5\%$ , respectively. We have used appropriate amounts of analytical grade metal nitrates, *i.e.*, Zinc nitrates hexahydrate, Nickel nitrate hexahydrate, (100 mM: Alfa Aesar chemicals) powders which were thoroughly mixed and dissolved in deionized water with stirred for 30 min. Subsequently ammonia was added and the pH of the solutions was maintained at  $\sim 11$ . Then the solutions were heated at  $85^\circ\text{C}$  for 2 h and solutions were filtered using Whatman's filter paper and washed several times with deionized water. Subsequent to overnight drying pure and Ni doped ZnO samples were collected and annealed at  $150^\circ\text{C}$  for 2 h to obtain phase pure samples.

#### 4(B).2. Results and discussion

##### 4(B).2.1. Morphological properties

**Scanning electron microscopy:** The surface morphology of the nanostructure has been observed by FESEM. Figure 4.11 displays the SEM image (magnification at 50 KX) of pure and Ni doped ZnO nanostructure. In the case of ZnO, nanorods are being observed and the highest Ni-doped ZnO samples (12.5% Ni doped ZnO) displays nano-flakes like structure along with nanorods. It is visible from Figure 4.11 that Ni doping increases the size of ZnO nanostructures. In the case of pure ZnO, there is rod like morphology with an average diameter of 100 nm and a length of 2  $\mu\text{m}$ , whereas with 5%, 7.5%, and 10% Ni doping, the diameters changes to  $\sim 150$ ,  $\sim 200$ , and  $\sim 300$  nm, respectively. However,

in the case of 10% and higher doping concentration of Ni, flakes like morphology also co-exist along with the rods. This suggests that Ni is replacing Zn in ZnO and altering its morphology. From the EDXS (Energy Dispersive X-ray Spectra) of all samples, the percentages of Ni and ZnO in the samples are estimated and shown in Table 4.5.

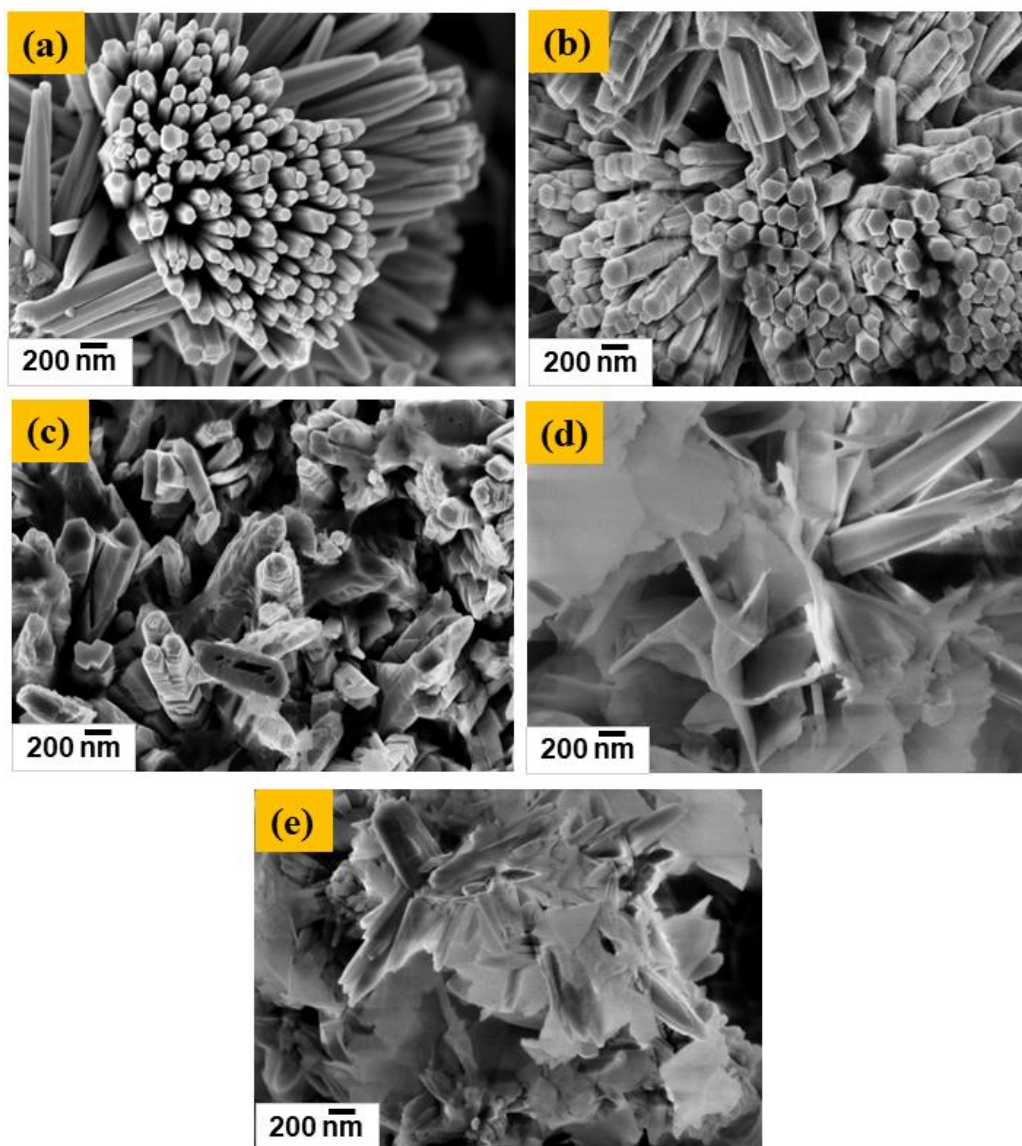


**Figure 4.11.** Represents the FESEM images of (a) ZnO: Ni 0%, (b) ZnO: Ni 5%, (c) ZnO: Ni 7.5%, (d) ZnO: Ni 10%, and (e) ZnO: Ni 12.5% (scale at 200 nm).

**Table 4.5.** EDAX analysis of Ni-doped ZnO samples.

Element	ZnO:Ni0%	ZnO:Ni5%	ZnO:Ni7.5%	ZnO:Ni10%	ZnO:Ni12.5%
Ni	0	4.85( $\pm$ 0.05)	7.25( $\pm$ 0.03)	9.63( $\pm$ 0.01)	12.24( $\pm$ 0.04)
ZnO	100	95.15( $\pm$ 0.05)	92.75( $\pm$ 0.03)	90.37( $\pm$ 0.01)	87.76( $\pm$ 0.04)

#### 4(B).2.2. Structural properties

**X-Ray diffraction:** The Rietveld-refined XRD patterns of Ni doped ZnO are represented in Figure 4.12(a). All peaks resemble the standard Bragg positions for the hexagonal phase of wurtzite ZnO (space group  $P6_3mc$ ), which have been indicated by the upright lines at the bottom of the XRD patterns. Ni doping does not lead to the occurrence of an additional peak or the vanishing of a peak related to the hexagonal wurtzite pure ZnO structure in XRD pattern and confirms that the samples are phase pure without any change in their wurtzite phase. There is no trace of impurity related to NiO, and any binary phases of zinc/nickel are observed up to 12.5% Ni doping. However, the probability of the existence of the minute phase or small cluster cannot be completely ruled out, considering the detection limit of XRD technique.

It has been noticed from Figure 4.12(a) that all samples showed strong directional growth along the (002) plane, indicating that the growth along the  $c$ -axis is more preferred as compared to the other axes. This might be due to the nucleation of rod like morphology of the samples, which is most common in ZnO.

However, with an increase in Ni concentration, there is a signature of growth along the (100) and (101) directions also, which gives the hint of alteration in morphology or orientation and incorporation of Ni into the ZnO lattice [55]. Due to the comparable ionic size of  $Ni^{2+}$  (0.55 Å) and  $Zn^{2+}$  (0.60 Å), Ni ions replace  $Zn^{2+}$  ions easily in the ZnO lattice, without distorting the crystal structure significantly. However, vigilant investigation of the peak location of samples shows that the (002) peak is shifted toward the lower two theta values up to 10% Ni doping, and in higher doping concentrations, the peak is slightly rearranged to higher two theta values, as shown in Figure 4.12(b). From the Rietveld refinement, the full detail of the lattice parameter and crystal structure of Ni doped ZnO samples are provided in Table 4.6. It shows that the Zn/O occupancy ratio is less than 1; moreover with Ni doping, it decreases. Therefore this supports that the defect formations mechanism is due to doping [35]. The lattice parameters computed from the Rietveld refinements are presented in Figure 4.12(c) with respect to Ni doping. Figure 4.12(c) provides evidence of an abrupt escalation in lattice parameter because of Ni doping followed by a gradual increase up to 10% doping. A very slight decline in  $a$  and  $c$  lattice constants can be evidenced in higher Ni doping (12.5%). The above results, which are

similar to the previous observations, [56, 57] where defects are generated by Ni<sup>2+</sup> ions and manifest successful incorporation of Ni<sup>2+</sup> at the Zn<sup>2+</sup> sites of the ZnO lattice.

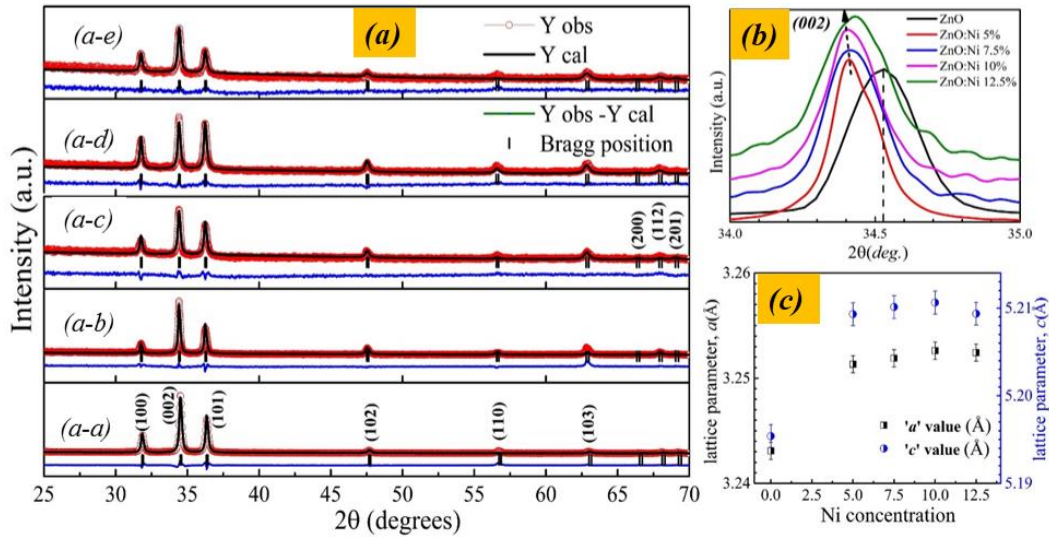


**Figure 4.12.** Shows the (a) Rietveld refined XRD patterns of (a-a) ZnO, (a-b) ZnO: Ni 5%, (a-c) ZnO: Ni 7.5%, (a-d) ZnO: Ni 10%, and (a-e) ZnO: Ni 12.5%. (b) Displays the shift in  $2\theta$  after Ni doping in the diffraction peak corresponds to (002) peak, (c) Displays the variation in lattice parameter “a” and “c” (in unit Å) of pure and Ni doped ZnO.

**Table 4.6.** Refined structural parameters for Zn<sub>1-x</sub>Ni<sub>x</sub>O (0.0 ≤ x ≤ 0.125) thin film. (Error in 10<sup>-4</sup> order in refined parameters).

Sample	Lattice parameters (Å)	Atoms	Positions			Occ. Ratio (Zn/O)
			X	Y	Z	
ZnO	a = 3.2430 ± 0.0002 c = 5.1953 ± 0.0001	Zn O	2a 2b	0 0.3333	0 0.6667	0.9938 0.3473
ZnO: Ni 5%	a = 3.2513 ± 0.0002 c = 5.2093 ± 0.0003	Zn/Ni O	2a 2b	0 0.3333	0 0.6667	0.4953 0.4458
ZnO: Ni 7.5%	a = 3.2518 ± 0.0001 c = 5.2101 ± 0.0004	Zn/Ni O	2a 2b	0 0.3333	0 0.6667	0.1570 0.5779
ZnO: Ni 10%	a = 3.2526 ± 0.0003 c = 5.2106 ± 0.0002	Zn/Ni O	2a 2b	0 0.3333	0 0.6667	0.1515 0.5745
ZnO: Ni 12.5%	a = 3.2524 ± 0.0002 c = 5.2093 ± 0.0003	Zn/Ni O	2a 2b	0.3333 0.3333	0.6667 0.6667	0 0.5968

Unit cell volumes (V) for a hexagonal structure and average bond lengths (L) of Zn-O have been calculated using eq. 4.2 and 4.3, as shown in Figure 4.13(a).

$$V = 0.866 \times a^2 \times c \quad (4.2)$$

$$L = \sqrt{\frac{a^2}{3} + (0.5 - u_p)^2 c^2} \quad (4.3)$$

where  $u_p$  is the positional parameter, defined as the bond length parallel to the  $c$ -axis, along with the  $c$ -axis [58] (given by  $u_p = \frac{a^2}{3c^2} + 0.25$ ).

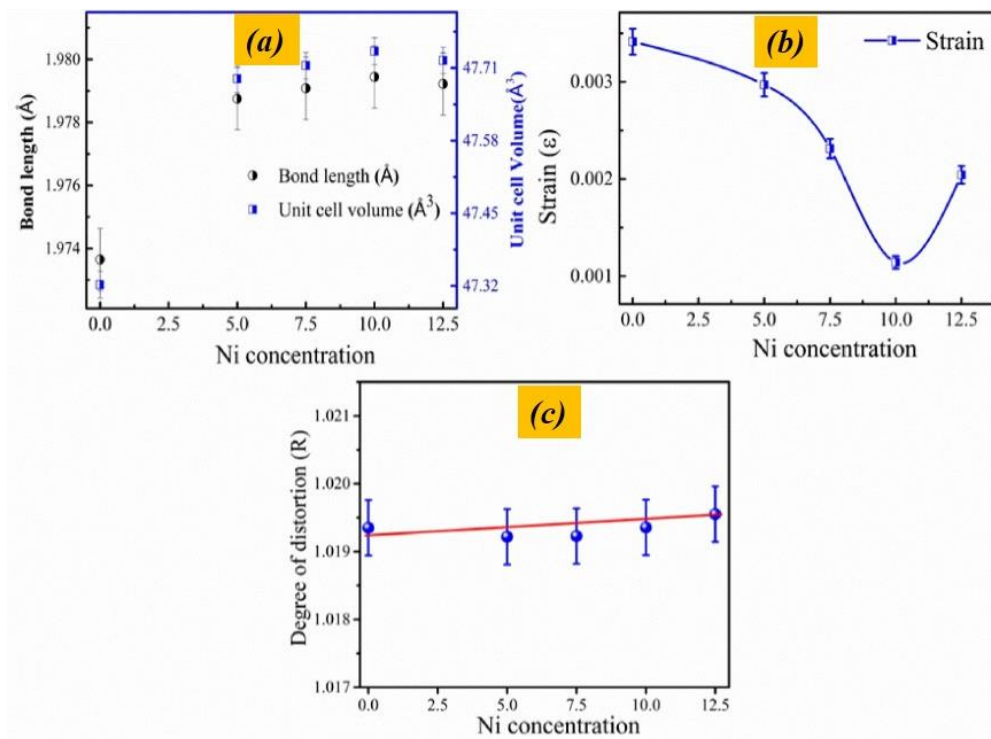


**Figure 4.13.** (a) Shows the change in the average bond length (in Å) and unit cell volume (in Å<sup>3</sup>), (b) displays the corresponding change in micro Strain (ε) value, and (c) represents the change in the R (degree of distortion) with increasing the Ni concentration.

Figure 4.13(b) displays the uniform tensile micro strain, which is also one of the reasons for the shift of the Bragg's peak toward the lower  $2\theta$  value up to 10% Ni doping concentration, and it is observed that higher Ni doping creates a uniform compressive strain with an increase in the  $2\theta$  value. The lattice strain in the crystal structure is calculated by Williamson-Hall methods. It is apparently visible that the increase in lattice parameter has a strong correlation with the decrease in strain in the nanostructures or vice versa. Similar results have been described by Kumar *et al.* [59], in the case of Co-doped ZnO and Dakhel *et al.* [60] for Gd-doped ZnO, where such change in lattice parameter with a change in strain value has been recognized with the creation of oxygen-related defects such as oxygen vacancies. Thus, from XRD results, we conclude that Ni<sup>2+</sup> ions get successfully incorporated in the host structure and produce oxygen vacancies in the sample. Beside this variation in lattice parameters also illustrates the distortion in crystal

structure because of Ni<sup>2+</sup> ions doping into the ZnO crystal lattice. The degree of distortion shown in Figure 4.13(c) is calculated by the following relation:

$$R = \frac{2a(2/3)^{1/2}}{c} \quad (4.4)$$

where  $R = 1$  gives the ideal wurtzite structure, [61] here  $a$  and  $c$  are lattice constants computed from the Rietveld refinement [62].

**X-Ray Absorption Near Edge Structure (XANES) and Extended X-Ray Absorption Fine Structure (EXAFS):** Figure 4.14 (a and c) represents normalized XANES spectra and Figure 4.14 (b and d) shows  $k^2$  - weighted  $\chi(k)$  EXAFS spectra of Ni-doped ZnO nanostructure at Zn and Ni K- edges. One may note that there is a variation of white line intensity (denoted as peak A) and intensity of peak B for Ni doped ZnO nanostructure. There is a huge drop in the intensity of peaks A and B of Zn K-edge XANES, whereas a very small change occurs at peak C of Ni-edge XANES, which mainly arises due to the variation of charge-transfer [63] upon Ni<sup>2+</sup> doping in ZnO nanocrystal. The variation in the white line intensity suggests that there is a large variation in the number of vacancies/holes due to Ni doping. For a detailed analysis of local structure, Figure 4.15 (a, b) shows Fourier transform (FT) of EXAFS spectra of samples. The  $k$ -range of 2.5-10 and 2.5-9 Å<sup>-1</sup> were used for FT of Zn and Ni EXAFS data, respectively. For Zn K-edge EXAFS fitting, the structure is assumed as pure ZnO wurtzite, where Zn is coordinated with four O atoms (Zn-O) at a 1.98 Å distance in the first shell and second next near-neighbour Zn is bounded by 12 Zn atoms (Zn-Zn) at a 3.21 Å distance. The fittings were performed in phase uncorrected R-space range of 1 - 3.21 Å. Similarly, the Ni K-edge data were fitted, assuming that Zn atoms are replaced by Ni atoms in the wurtzite structure. During fitting of the data, coordination numbers of the different shells, Debye–Waller factor (DWF) ( $\sigma^2$ ) and bond distance (R) were fitted as free parameters, whereas the non-structural parameter  $E_0$  was fixed. Figure 4.15 (panels a, b) also shows the best-fit curves and best-fit values of the parameters listed in Table 4.7 and Table 4.8.

Results of the Zn K-edge EXAFS fitting reveal that the Zn-O bond distance is slightly reduced on Ni doping, while no change in Zn-Zn bond distance is observed. Ni K-edge fitting however shows decrease in both Ni-O and Ni-Ni/Zn bond distances with rise in Ni substitution concentration. Although the ionic radii of Zn<sup>2+</sup> and Ni<sup>2+</sup> are almost the same (0.60 and 0.55 Å, respectively), the change in bond lengths are insignificant in

this case. Nonetheless, there is a systematic increase in the Debye-Waller factor ( $\sigma^2$ ) (DWF) values for both Zn-O and Zn-Zn paths, which indicate an increase in local disorder in the ZnO lattice near the host sites due to Ni doping. DWF values of Ni-O and Ni-Ni/Zn paths however do not show any change. Similar increase in Debye-Waller factors at the site of the Zn atom have also been detected by us in the case of Co- and Fe-doped ZnO nanocrystalline samples also [64, 65]. It is evident that there is systematic decrease in coordination numbers (CNs) of Zn-O, Zn-Zn, and Ni/Zn-Zn, whereas no variation in CN of Ni-O. This confirms that with Ni doping, the number of holes/vacancies were increased in Ni-doped ZnO nanocrystals as it has been observed from XANES also.

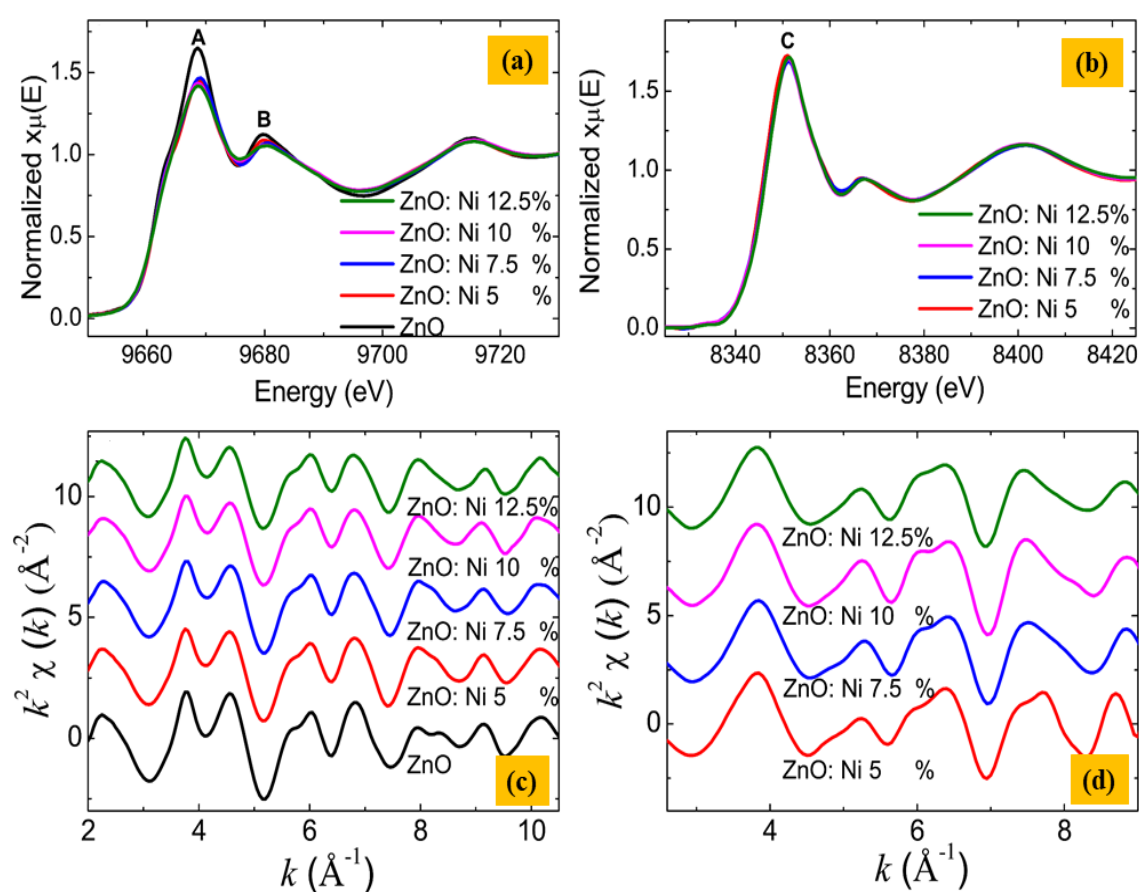


**Figure 4.14.** Ni doped ZnO nanostructures (a) Normalized XANES data at Zn K-edge, (b)  $k^2$ - weighted  $\chi(k)$  spectra at Zn K-edge, (c) Normalized XANES data at Ni K-edge, (d)  $k^2$ - weighted  $\chi(k)$  spectra at Ni K-edge. The  $\chi(k)$  data has been vertically shifted for clarity.

**Table 4.7.** From the Zn K-edge EXAFS data fitting, we have obtained a variation of CN (co-ordination number),  $R$  (bond distance) and  $\sigma^2$  (Debye-Waller factor). The amplitude reduction factor ( $S_0^2$ ) and  $\Delta E$  were obtained from pure ZnO fitting  $1.05 \pm 0.08$  and  $1.9 \pm 0.5$ , respectively and kept fixed for all the samples. The numbers in parentheses indicate the uncertainty in the last digit.

Sample	$CN_{Zn-O}$	$R_{Zn-O}(\text{\AA})$	$\sigma^2_{Zn-O}(\text{\AA}^2)$	$CN_{Zn-Zn}$	$R_{Zn-Zn}(\text{\AA})$	$\sigma^2_{Zn-Zn}(\text{\AA}^2)$
ZnO	3.7(3)	1.952(2)	0.0040(3)	11.8(3)	3.211(3)	0.0088(2)
ZnO:Ni5%	3.3(2)	1.952(3)	0.0055(2)	11.5(2)	3.211(5)	0.0091(3)
ZnO:Ni7.5%	3.3(2)	1.949(2)	0.0056(2)	11.4(2)	3.208(6)	0.0094(2)
ZnO:Ni10%	3.0(3)	1.943(3)	0.0056(2)	11.3(3)	3.209(5)	0.0095(2)
ZnO:Ni12.5%	2.8(2)	1.942(2)	0.0062(3)	10.9(2)	3.209(6)	0.0108(2)

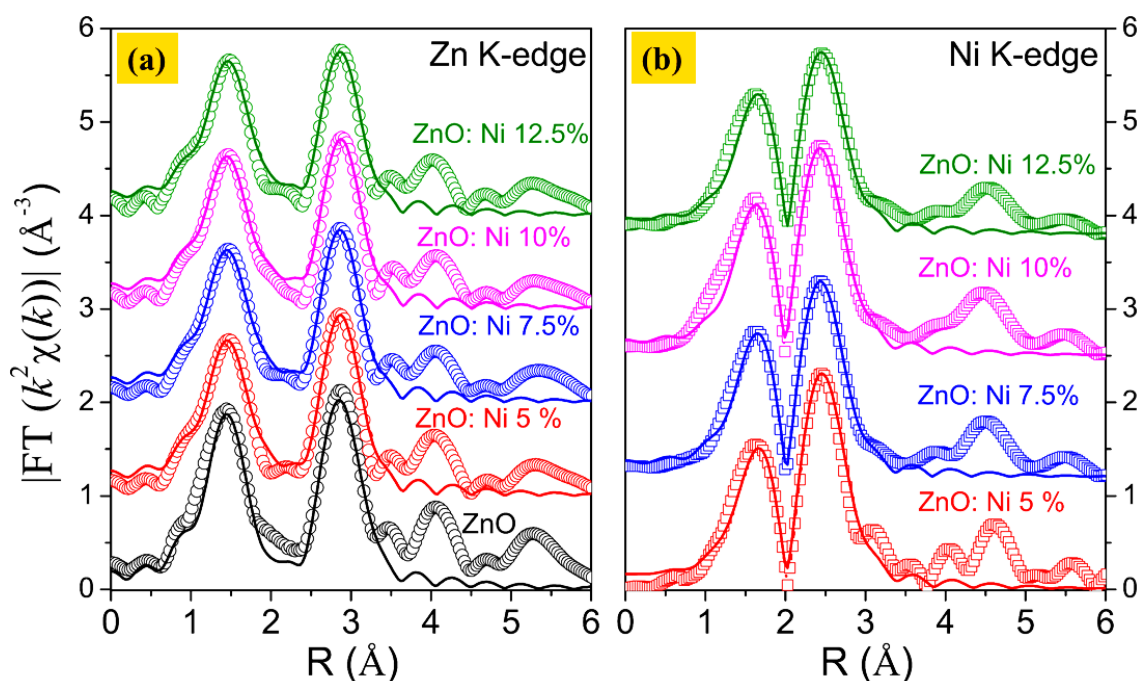


**Figure 4.15.** Fourier transform of  $k^2$ -weighted of (a) Zn K-edge, (b) Ni K-edge, for Ni doped ZnO nanostructure. The symbol shows empirical data and solid lines are the best fitting data. The curves are vertically shifted for clarity.

**Table 4.8.** Structural parameters CN (co-ordination number),  $R$  (bond distance) and  $\sigma^2$  (Debye-Waller factor) obtained from Ni K-edge EXAFS data fitting. Similar to Zn K-edge, the amplitude reduction factor ( $S_0^2$ ) and  $\Delta E$  were obtained from pure NiO fitting  $1.01 \pm 0.06$  and  $1.8 \pm 0.6$ , respectively and kept fixed for all the samples. The numbers in parentheses indicate the uncertainty in the last digit.

Sample	$CN_{Ni-O}$	$R_{Ni-O}(\text{\AA})$	$\sigma^2_{Ni-O}(\text{\AA}^2)$	$CN_{Ni-Ni/Zn}$	$R_{Ni-Ni/Zn}(\text{\AA})$	$\sigma^2_{Ni-Ni/Zn}(\text{\AA}^2)$
Ni 5%	3.9(3)	2.111(4)	0.0030(2)	10.7(3)	2.944(3)	0.0082(3)
Ni 7.5%	3.8(2)	2.106(6)	0.0030(3)	10.5(2)	2.932(4)	0.0087(3)
Ni 10%	3.9(2)	2.092(4)	0.0030(2)	10.6(3)	2.936(3)	0.0084(3)
Ni 12.5%	3.9(2)	2.094(3)	0.0030(2)	9.9(2)	2.937(6)	0.0094(2)

**Raman spectroscopy:** Raman spectroscopy is very sensitive and one of the powerful techniques for studying the change in local structure, defect state, and disorder in the ZnO host lattice because of incorporation of transition metal ions [66]. Besides this, the technique is used to study crystalline quality of nanostructure. The  $\Gamma$ -point of the Brillouin zone, the complex illustration of optical phonons are represented by  $\Gamma_{\text{opt}} = A_1 + 2B_1 + E_1 + 2E_2$ , where  $E_1$  and  $A_1$  modes are polar and divided into longitudinal and transverse phonons and all are infrared and Raman actives.  $E_2$  modes are nonpolar and Raman active; however,  $B_1$  modes are silent or Raman inactive. With lattice vibrations of  $A_1$  and  $E_1$  modes, the atoms move parallel and perpendicular to the  $c$ -axis, respectively. Sharpest and strongest peaks at 99 and 438  $\text{cm}^{-1}$  presented in Figure 4.16(a) are allocated to the high- and low-frequency branch of  $E_2$  mode,  $E_2^{\text{low}}$  and  $E_2^{\text{high}}$ , respectively.  $E_2^{\text{low}}$  is due to the vibration of a heavy atom (*i.e.*, Zn), and  $E_2^{\text{high}}$  is due to the oxygen sublattice, which is the characteristic and most prominent peak of the wurtzite ZnO structure [67, 68]. The modes  $A_1(\text{TO})$  and  $E_1(\text{TO})$  show the polar lattice bond strength, [69] while  $A_1(\text{LO})$  and  $E_1(\text{LO})$  modes can be detected in the unpolarised Raman spectra under back-scattering geometry in bulk ZnO.

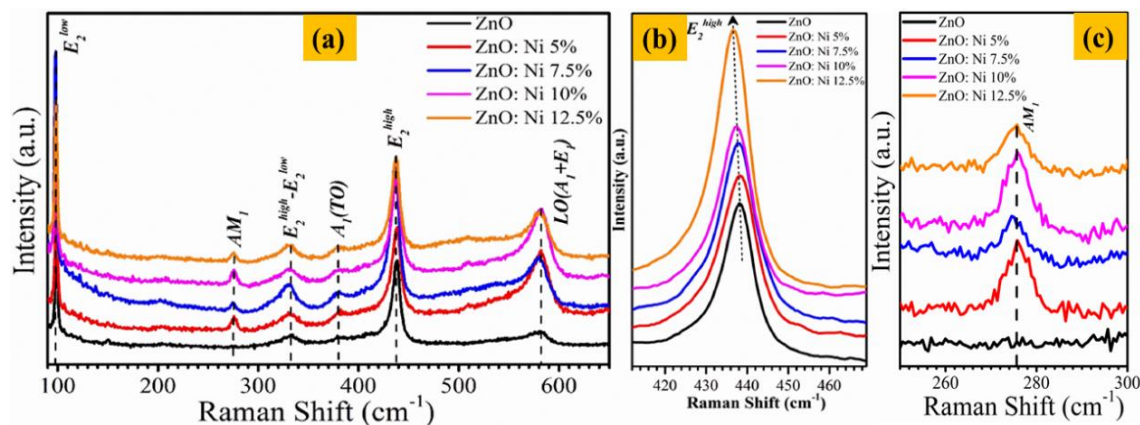


**Figure 4.16.** Displays (a) RT Raman spectra of pure and Ni doped ZnO (b) The Raman shift in the  $E_2^{\text{high}}$  peak. (c) Shows the Raman peak of the additional mode ( $AM_1$ ).

However, when the size of a crystal is in the nanometre level, first-order Raman scattering is relaxed (for selection rule with  $k=0$ ), and phonon scattering is not restricted to the centre of the Brillouin zone [70]. As a result of this, the ZnO nanostructure shows different Raman modes [ $E_2^{\text{low}}$ ,  $E_2^{\text{high}}$ ,  $A_1(\text{LO})$ ,  $A_1(\text{TO})$ ,  $E_1(\text{LO})$ , and  $E_1(\text{TO})$  modes]. RT Raman spectra, ranging from wavenumber 90 to 700  $\text{cm}^{-1}$ , is presented in Figure 4.16(a),

which shows all prominent peaks of wurtzite ZnO after Ni doping with an additional peak at  $276\text{ cm}^{-1}$  appearing in the Ni-doped sample only (Figure 4.16(c)). As the Ni content increases, some of the Raman modes become broad and highly intense without an appreciable shift in comparison to pure ZnO. This provides the hint that there is change a in local symmetry of the nanostructures due to the incorporation of the Ni atom in the host lattice, while the crystal structure remains the same.

**Table 4.9.** Phonon mode frequencies of wurtzite  $\text{Zn}_{1-x}\text{Ni}_x\text{O}$  ( $0 \leq x \leq 0.125$ ) nanostructure (in units of  $\text{cm}^{-1}$ ).

Vibration frequency ( $\text{cm}^{-1}$ )					Assignment
ZnO	ZnO:Ni 5%	ZnO:Ni 7.5%	ZnO:Ni 10%	ZnO:Ni 12.5%	
99	98	98	98	99	$E_2^{\text{low}}$
-	276	274	276	276	AM
333	331	331	330	333	$(E_2^{\text{high}} - E_2^{\text{low}})$
383	382	380	382	382	$A_1$ (TO)
439	439	437	437	436	$E_2^{\text{high}}$
580	581	581	582	583	LO ( $A_1 + E_1$ )

This fact is corroborated by from the EXAFS result also as discussed earlier. Table 4.9 summarizes the details of the peaks appearing in  $\text{Zn}_{1-x}\text{Ni}_x\text{O}$  ( $0 \leq x \leq 12.5$ ) samples. We have already discussed the origin of  $E_2^{\text{high}}$  and  $E_2^{\text{low}}$ , which are the representative peaks of the wurtzite structure. It is observed from Table 4.9 that with increased Ni-concentration, there is a very small redshift in the nonpolar mode  $E_2^{\text{high}}$  in contrast to pure ZnO. This result can be ascribed to the fact that  $\text{Ni}^{2+}$  substitution prompts the atomic structural irregularities in the periodic Zn atomic sublattice and interrupts its translational symmetry with increase in local alterations in the lattice. This disorder and local distortion interrupt the long-range order in ZnO and deteriorates the electric field related with a mode [71]. The peaks at  $333$  and  $383\text{ cm}^{-1}$  correspond to the  $E_2^{\text{high}} - E_2^{\text{low}}$  and  $A_1(\text{TO})$ , respectively, which are due to the multiphonon process and can be ascribed to the single crystalline nature of ZnO [50]. In comparison with earlier reports of ZnO, two LO modes are located at  $587\text{ cm}^{-1}$  ( $E_1$ ) and  $575\text{ cm}^{-1}$  ( $A_1$ ) [72, 73]. These LO modes arise due to defects such as  $V_{\text{O}}$  and  $\text{Zn}_{\text{in}}$  or free carriers present in ZnO nanostructure [74]. Transition metal (such as Fe and Mn) replacement in ZnO, shows significant modification in the  $E_1(\text{LO})$  mode because of variation in inherent host lattice defects [48, 52]. In present case, the Raman scattering peak is centred around  $580\text{ cm}^{-1}$  for pure ZnO and with Ni doping this peak becomes broad and slightly shifted to  $583\text{ cm}^{-1}$ . As a result, this peak can be allocated to the mixture of both LO ( $A_1$  and  $E_1$ ) vibrational modes of ZnO. Apart from

these five foremost peaks, we have observed an additional mode ( $AM_1$ ) only in doped samples at  $\sim 276 \text{ cm}^{-1}$ . So far the source of this peak is still unclear, as the previous literature ascertains dissimilar reasons for the existence of this peak. Kaschner *et al.* [75] reported this  $AM_1$  in Raman spectra at  $274 \text{ cm}^{-1}$  associated with nitrogen (N)-doping appealing with N substitution and the intensity of this peak growth and have assigned them as nitrogen-induced local vibration modes (LVMs). Similarly Wang *et al.* [76] have also reported this in N-doped ZnO sample. However, later, a group similarly investigated and found that these additional modes also appear in the Raman spectra of Fe-, Sb-, and Al-doped ZnO films and proposed inherent host lattice defects [52]. Also, Du *et al.* in (Co, Mn) codoped a ZnO film and correlated this peak with the oxygen vacancy and Zn interstitial [77]. Ye *et al.* [78] have proposed two plausible mechanisms to describe the source of this AM: LVMs (local vibrational modes) and DARS (disorder activated Raman scattering). The DARS is prompted by the collapse of the translation symmetry of the lattice caused by either impurities or defects due to variation in the growth condition or dopant nature. Therefore, it can be expected, AM in Ni-doped samples could arise because of both or either of the aforesaid two mechanisms. Thus, from Raman study, we can conclude that Ni doping in ZnO nanostructures leads to generate a disorder and lattice defects by troubling the long range ionic ordering in the host ZnO nanostructure.

#### 4(B).2.3. Optical properties

**UV-Visible spectroscopy:** Optical properties of the pure and Ni doped ZnO are studied by RT UV-vis absorption spectroscopy from the range 200-600 nm. Figure 4.17 shows the UV-vis absorption spectra of pure and Ni doped ZnO nano-structure and inset of the figure shows the band gap variation with increasing Ni concentration.

To calculate the band gap, we follow the standard procedure of extrapolating the vertical and linear part of the curve to cut the energy axis. The value of energy at the point where the extrapolated line cut  $x$ -axis is taken as band gap energy. The band gap is estimated by extrapolation of the linear portion of  $(\alpha h\nu)^2$  versus  $h\nu$  curve by using the Tauc plot relation:

$$\alpha h\nu = A (h\nu - E_g)^n \quad (4.5)$$

where  $\alpha$  is the absorption coefficient,  $h$  is plank constant,  $\nu$  is the frequency of the incident photon,  $A$  is a constant,  $E_g$  is the band gap value and  $n$  is the unit less parameter with value 2 and  $\frac{1}{2}$  for indirect and direct band gap semiconductor, respectively.

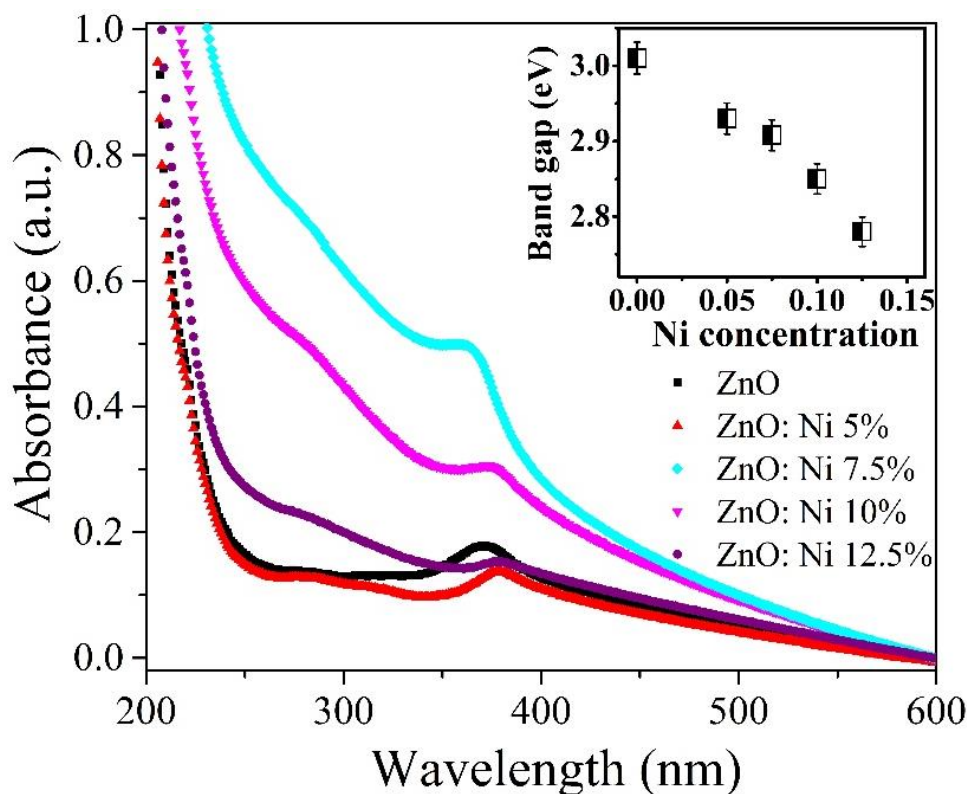


**Figure 4.17.** UV-Vis absorbance spectra of pure and Ni doped ZnO nano-structure. Inset figure shows the relative variation in band gap between pure and Ni doped ZnO.

Band gap observed for pure ZnO is 3.01 eV but with increasing Ni concentration in ZnO the band gap decreases from 2.93 to 2.78 eV, which is similar to the results of Das *et al.* [79]. They consider the reduction in the band edge is a definite hint of the interaction of Ni states with the host ZnO states. Deka *et al.* [80] explain by incorporation of Ni inside the ZnO lattice. This red shift in a band edge is due to the increased in *sp-d* exchange interaction between the ZnO band electrons and the localized *d*-electron associated with the Ni<sup>2+</sup> ions [81], this interaction may consider as the blossoming of magnetic phase.

**Photoluminescence spectroscopy:** Photoluminescence (PL) spectroscopy is one of the most sensitive non-destructive and very effective optical approaches to describe the existence of the intrinsic and extrinsic defects in a sample. It not only provides the information regarding energy state of defects and impurities at very low densities but also provides useful information regarding structural defects present in semiconductors, which play a crucial role in the growth of RT ferromagnetism (FM) ordering in ZnO-based dilute magnetic semiconductor (DMSs).

Figure 4.18(a) displays the RT PL spectra of  $Zn_{1-x}Ni_xO$  ( $0 \leq x \leq 0.125$ ) samples measured by exciting with a wavelength of 325 nm in the energy range from 350 to 600 nm. Detected broad PL spectra in the UV-visible region indicate the existence of multicomponent contributions, which is extracted with the fitting of multiple Gaussian peaks and shown in Figure 4.18(b). The characteristic wide-range emission spectrum of pure ZnO, ranging from near band edge (NBE) (380 nm) to yellow emission (600 nm), can be deconvoluted into ten peaks at 396, 412, 431, 437, 450, 467, 481, 492, 524, and 563 nm. Ni-doping in ZnO produces a shift and additional defect as compared to pure ZnO (Table 4.10).

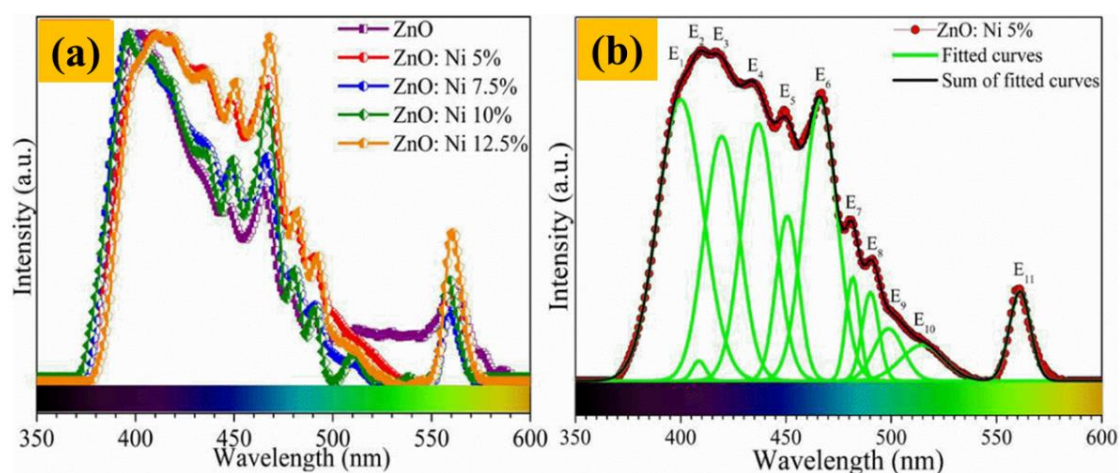


**Figure 4.18.** (a) Demonstrates the RT Photoluminescence spectra of  $Zn_{1-x}Ni_xO$  ( $0 \leq x \leq 12.5$ ) and (b) Displays RT-PL spectra of Ni 5% doped ZnO. The red dots display experimental data, green lines Gaussian fitting and black line sum of all fitted peaks.

**Table 4.10.** The peak position and relative peak intensity of deconvoluted PL spectra of Ni doped ZnO samples. Peak position (nm) and relative intensity (%) have the errors  $\pm 1$ .

Peak No.	ZnO		ZnO: Ni 5%		ZnO: Ni 7.5%		ZnO: Ni 10%		ZnO: Ni 12.5%	
	Peak Position (nm)	Rel. int. (%)								
1	396	61	399	100	390	39	381	4	397	76
2	412	100	408	2	401	51	394	40	411	100
3	431	47	419	67	420	100	408	3	423	52
4	437	5	436	57	437	18	417	100	433	53
5	450	37	450	29	450	30	436	10	440	15
6	467	31	466	73	466	45	450	25	450	95
7	481	6	481	11	481	7	466	35	468	90
8	492	3	490	1	490	9	481	6	483	21
9	524	79	498	12	505	7	490	5	492	16
10	563	13	514	12	543	0.6	511	2	504	19
11	-	-	561	14	560	9	559	9	561	30

The first peak ( $E_1$ ) at 396 nm is related to NBE, which arises due to the recombination of free exciton existing in the ZnO nanostructure [82]. Ni doping shows the red shift in NBE for Ni 5% doping; this red shift may be the feature of robust exchange interaction between  $sp$ -electrons and  $d$ -electrons of  $Ni^{2+}$  ions of the ZnO band [83]. The  $E_2$  peak at 401 nm is attributed to the first longitudinal optical phonon copy of free excitons, [84] while the origin of the rest of the peaks has been discussed in detail in our previous study [35, 85]. We also observed that there is a change in the relative intensity after Ni doping; it is due to the dependence of intensity on the concentration of electrons at a particular defect level. Ni doping creates a defect level near the conduction band, and the concentration of electrons increases at the conduction band. This might be one of the reasons for changing the relative intensity after doping.

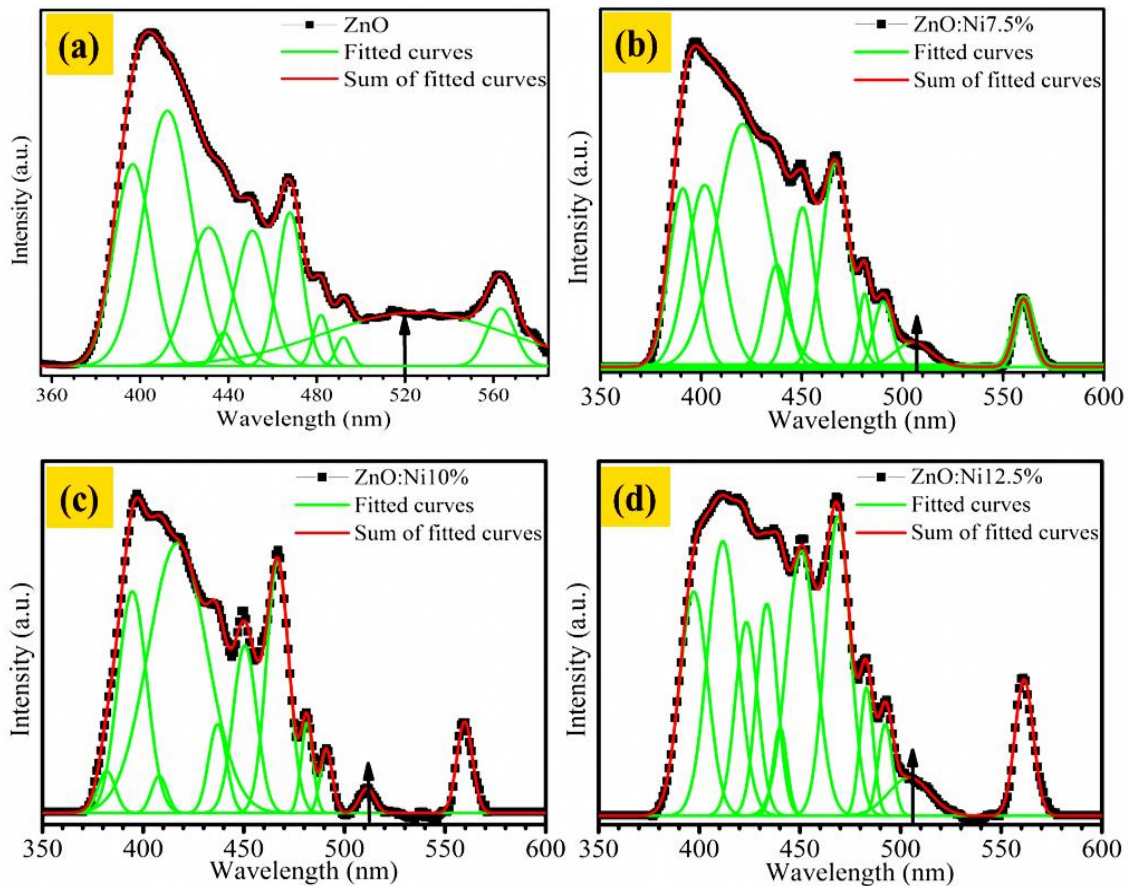


**Figure 4.19.** Shows Room temperature PL spectra of (a) ZnO (b) Ni 7.5% doped ZnO (c) Ni 10% doped ZnO (d) Ni 12.5% doped ZnO. The black dots show experimental data, solid green and red lines are Gaussian fitting of individual peaks and sum of all peaks, respectively ( $\uparrow$  arrow indicate the presence of an  $E_{10}$  peak in ZnO samples).

There is a broad and intense green emission peak  $E_{10}$  observed in all ZnO samples see Figure 4.19. The cause of this peak, considered as a green emission (504-524 nm), is due to the recombination of the photo-generated hole and the electron trapped by single ionized oxygen vacancies ( $V_{O^+}$ ), clearly indicating the presence of singly ionized oxygen vacancy states [62, 86]. However, oxygen vacancies, which are an important class of point defects in oxides and also known as colour centres (F centres), [87] show three different charge states, as  $F^{2+}$  (unoccupied),  $F^+$  (singly occupied), and  $F^0$  (doubly occupied), in the ZnO lattice. In this case,  $F^{2+}$  and  $F^0$  vacancies have spin zero ground states; hence, they do not induce FM in ZnO [88, 89]. However, in case of  $F^+$  vacancy, which is singly occupied, it can contribute in activate bound magnetic polarons (BMPs) and magnetic moment in DMSs [65]. These defects arising due to Ni doping in the ZnO nanostructure and they play a vital role in deciding the magnetic behaviour of the samples which has been discussed in next chapter.

### 4.3. Summary

In this chapter, the effect of doping on ZnO nanostructures has been investigated in detail. In the first section, the effect of Sr doping on ZnO in the form of  $Zn_{1-x}Sr_xO$  ( $0.0 \leq x \leq 0.08$ ) nano-rods thin films are successfully synthesized by a facile wet chemical process on the flexible transparent substrate and studied. SEM and TEM results show the formation of nano-rods with diameter  $\sim 100$ -250 nm depending on Sr doping concentration. TEM with SAED provided important information that nano-rods are highly single crystalline in nature and while HRTEM results suggest orientation of rods along (00 $l$ ) planes for 0-4% Sr doped samples which then deviate for higher doping levels. Elemental color mapping by TEM and SIMS data indicate that Sr is indeed doped in ZnO. The systematic variation of the Sr doping levels and Sr homogeneity in ZnO also confirmed and represented from SIMS experiment. Rietveld refinement of the XRD data shows all the films crystallizes into wurtzite structure, corresponds to the space group  $P6_3mc$ , with a systematic increase in the lattice parameters with Sr doping. Room temperature XPS analysis provide strong evidence regarding the creation of oxygen related defects in the doped films, while the valance state of Zn remains same in un-doped and doped films. This finding is further explained qualitatively based on the PL data. Oxygen vacancy concentration in all the films is almost same; while peak related to Zn vacancy ( $V_{Zn}$ ) and oxygen interstitial ( $O_{in}$ ) show an obvious enhancement. Raman spectra

of all the films shows characteristic phonon dispersion peak of wurtzite ZnO, while two additional peaks are observed in the doped films only, which provide the hints of doping dependent changes. These additional peaks around 277 and 663  $\text{cm}^{-1}$  are assigned to the intrinsic defects created in the ZnO matrix due to Sr doping. These optical observations may help to get further insight regarding the development of better ZnO based optoelectronic devices.

In the second section, Ni doped ZnO nanostructures have been successfully synthesized by simple wet chemical technique. Rietveld-refined XRD patterns indicate that up to 12.5% of Ni doping in ZnO samples have no secondary phase related to Ni or NiO and show the decrease in Zn/O occupancy ratio, which is associated with the defect induced due to Ni doping. The degree of distortion and lattice strain calculated from the Williamson-Hall method confirms the incorporation of Ni ions without a change in wurtzite structure of ZnO. SEM images demonstrate a modification of rod like morphology in pure ZnO to flakes like with Ni doping. XANES spectra confirm that Ni has +2 oxidation state in Ni doped ZnO nanocrystals. EXAFS analysis provides the hint of an increase in disorder systematically and decreases in coordination number near the host (Zn) sites in the samples due to Ni doping. Raman study validates the results obtained from XRD studies and suggests the doping of Ni ions without a change in the crystal structure of the ZnO lattice. Furthermore, Raman spectroscopy shows that with Ni doping there is shifting and broadening of the  $LO (A_1 + E_1)$  peak with an additional peak at 276  $\text{cm}^{-1}$ , which confirms the presence of an oxygen-related defect such as  $V_O$ . This is further confirmed by PL spectra, showing the peak at 524 nm associated with green emission, which corresponds to singly ionized oxygen vacancies ( $V_O^+$ ), which are known to generate the BMPs (accountable for ferromagnetisms) in the ZnO nanostructure.

The Sr- and Ni-doped ZnO nanostructures are later used in this thesis for multifunctional applications that include magnetic, optical and gas sensing applications.

**References**

- [1] Jin *et al.* (2001), High throughput fabrication of transition-metal-doped epitaxial ZnO thin films: A series of oxide-diluted magnetic semiconductors and their properties, *Appl. Phys. Lett.* 78, 3824.
- [2] Janotti A., Van de Walle C. G. (2009), Fundamentals of zinc oxide as a semiconductor, *Rep. Prog. Phys.* 72. 126501.
- [3] Pachoumi *et al.* (2013), Improved performance and stability of inverted organic solar cells with sol–gel processed, amorphous mixed metal oxide electron extraction layers comprising alkaline earth metals, *Adv. Energy Mater.* 3 1428-1436.
- [4] Water W., Wang S. F., Chen Y. P., Pu J. C. (2005), Calcium and strontium doped zno films for love wave sensor applications, *Integr. Ferroelectr.* 72, 13-22.
- [5] Water W., Yan Y. S. (2007), Characteristics of strontium-doped zno films on love wave filter applications, *Thin Solid Films* 515, 6992-6996.
- [6] Vijayan T.A., Chandramohan R., Valanarasu S., Thirumalai J., Subramanian S.P. (2008), Comparative investigation on nanocrystal structure, optical, and electrical properties of ZnO and Sr-doped ZnO thin films using chemical bath deposition method, *J. Mater. Sci.* 43, 1776-1782.
- [7] Chu S.Y., Chen T.Y., Water W., (2005), The effects of ZnO films on surface acoustic wave properties of modified lead titanate ceramic substrates, *IEEE Trans. Ultrason. Ferroelectr. Freq. Control*, 52, 2308-2313.
- [8] Xu L. *et al.* (2014), Optical and structural properties of Sr-doped ZnO thin films, *Mater. Chem. Phys.* 148, 720-726.
- [9] Yousefi R. *et al.* (2015), Enhanced visible-light photocatalytic activity of strontium-doped zinc oxide nanoparticles, *Materials Science in Semiconductor Processing*, 32, 152-159.
- [10] Udayabhaskar R., Karthikeyan B. (2014), Role of micro-strain and defects on band-gap, fluorescence in near white light emitting Sr doped ZnO nanorods, *J. Appl. Phys.* 116, 094310.
- [11] Stehr *et al.* (2014), Zinc-Vacancy–Donor Complex: A Crucial Compensating Acceptor in ZnO, *Phys. Rev. Appl.* 2, 021001.

- [12] Bracht H., Haller E. E., Clark-Phelps R. (1998), Silicon self-diffusion in isotope heterostructures, *Phys. Rev. Lett.* 81, 393-396.
- [13] Gu et al. (2006), Structure, optical, and magnetic properties of sputtered manganese and nitrogen-codoped ZnO films, *Appl. Phys. Lett.* 88, 082111.
- [14] Kotsis K., Staemmler V. (2006), Ab initio calculations of the O1s XPS spectra of ZnO and Zn oxo compounds, *Phys. Chem. Chem. Phys.* 8, 1490-1498.
- [15] Fan J. C. C., Goodenough J. B. (1977), X-ray photoemission spectroscopy studies of Sn-doped indium-oxide films, *J. Appl. Phys.* 48, 3524-3531.
- [16] Naeem et al. (2006), Effect of reducing atmosphere on the magnetism of  $Zn_{1-x}Co_xO$  ( $0 \leq x \leq 0.10$ ) nanoparticles, *Nanotechnology* 17, 2675-2680.
- [17] Ghosh S., Khan G. G., Varma S., Mandal K. (2012), Influence of Li-N and Li-F co-doping on defect-induced intrinsic ferromagnetic and photoluminescence properties of arrays of ZnO nanowires, *J. Appl. Phys.* 112, 043910.
- [18] Joshi *et al.* (2010), Valence band and core-level analysis of highly luminescent ZnO nanocrystals for designing ultrafast optical sensors, *Appl. Phys. Lett.* 96, 123102.
- [19] Franzen et al. (1977), XPS spectra and crystalline potentials in alkaline-earth chalcogenides and hydrides, *J. Electron Spectrosc. Relat. Phenom.* 11, 439-443.
- [20] Aika K. I., Aono K. (1991), Oxidative coupling of methane over  $SrCO_3$  and SrO, *J. Chem. Soc. Faraday Trans.* 87, 1273-1277.
- [21] Van Doveren H., Verhoeven J. A. T. H. (1980), XPS spectra of Ca, Sr, Ba and their oxides, *J. Electron Spectrosc. Relat. Phenom.* 21, 265-273.
- [22] Moulder J. F., Stickle W. F., Sobol P. E., Bombier K. D. (1992), *Handbook of X-ray Photoelectron Spectroscopy*, edited by Chastain J. (Perkin-Elmer, Eden Prairie, MN).
- [23] Arguello C. A., Rousseau D. L., Porto S. P. S. (1969), First-order raman effect in wurtzite-type crystals, *Phys. Rev.* 181, 1351-1363.
- [24] Damen T. C., Porto S. P. S., and Tell B. (1966), Raman effect in zinc oxide, *Phys. Rev.* 142, 570-574.
- [25] Pradhan *et al.* (2004), Structural and spectroscopic characteristics of ZnO and ZnO:  $Er^{3+}$  nanostructures, *J. Phys.: Condens. Matter.* 16, 7123-7129.

- [26] Alaria *et al.* (2006), Pure paramagnetic behaviour in Mn-doped ZnO semiconductors, *J. Appl. Phys.* 99, 08M118.
- [27] Bundesmann *et al.* (2003), Raman scattering in ZnO thin films doped with Fe, Sb, Al, Ga, and Li, *Appl. Phys. Lett.* 83, 1974-1976.
- [28] Kaschner *et al.* (2002), Nitrogen-related local vibrational modes in ZnO:N, *Appl. Phys. Lett.* 80, 1909-1911.
- [29] Serrano *et al.* (2004), Pressure dependence of the lattice dynamics of ZnO: An ab initio approach, *Phys. Rev. B* 69, 094306.
- [30] Wang *et al.* (2005), Raman study for E2 phonon of ZnO in  $Zn_{1-x}Mn_xO$  nanoparticles, *J. Appl. Phys.* 97, 086105.
- [31] Yang *et al.* (2005), In situ synthesis of Mn-doped ZnO multileg nanostructures and Mn-related Raman vibration, *J. Appl. Phys.* 97, 014308-014311.
- [32] Zhang S. B., Wei S. H., Zunger A. (2001), Intrinsic n-type versus p-type doping asymmetry and the defect physics of ZnO, *Phys. Rev. B* 63, 075205.
- [33] Dijken *et al.* (2000), The luminescence of nanocrystalline ZnO particles: the mechanism of the ultraviolet and visible emission, *J. Lumin.* 87, 454-456.
- [34] Behera D., Acharya B. S. (2008), Nano-star formation in Al-doped ZnO thin film deposited by dip-dry method and its characterization using atomic force microscopy, electron probe microscopy, photoluminescence and laser Raman spectroscopy, *J. Lumin.* 128, 1577-1586.
- [35] Xu *et al.* (2003), The electronic structure and spectral properties of ZnO and its defects, *Pan Nucl. Instrum. Methods Phys. Res. B* 199, 286-290.
- [36] Wu *et al.* (2010), Influence of nitrogen on the defects and magnetism of ZnO:N thin films, *J. Appl. Phys.* 108, 063530-063534.
- [37] W. Shan *et al.* (2005), Nature of room-temperature photoluminescence in ZnO, *Appl. Phys. Lett.* 86, 191911.
- [38] Rana *et al.* (2015), Studies on the control of ZnO nanostructures by wet chemical method and plausible mechanism, *AIP Adv.* 5, 097118.
- [39] Børseth *et al.* (2006), Identification of oxygen and zinc vacancy optical signals in ZnO, *Appl. Phys. Lett.* 89, 262112.
- [40] Leiter *et al.* (2003), Oxygen Vacancies in ZnO, *Phys. B*, 340, 201-204.

- [41] Hameed *et al.* (2013), Impact of alkaline metal ions  $Mg^{2+}$ ,  $Ca^{2+}$ ,  $Sr^{2+}$  and  $Ba^{2+}$  on the structural, optical, thermal and antibacterial properties of ZnO nanoparticles prepared by the co-precipitation method, *J. Mater. Chem. B*, 1, 5950-5962.
- [42] Lin B., Fu Z., Jia Y. (2001), Green luminescent center in undoped zinc oxide films deposited on silicon substrates, *Appl. Phys. Lett.* 79, 943-945.
- [43] Liu M., Kitai A. H., Mascher P. (1992), Point defects and luminescence centres in zinc oxide and zinc oxide doped with manganese, *J. Lumin.* 54, 35-42.
- [44] T. Al-Harbi, (2011), Hydrothermal synthesis and optical properties of Ni doped ZnO hexagonal nanodiscs, *J. Alloys Compd.* 509, 387-390.
- [45] Dietl T., Ohno, H., Matsukura, F., Cibert, J., Ferrand, D. (2000), Zener model description of ferromagnetism in zinc-blende magnetic semiconductors, *Science*, 287, 1019-1022.
- [46] Sato K., Yoshida H. K. (2000), Material design for transparent ferromagnets with ZnO-based magnetic semiconductors. *Jpn. J. Appl. Phys.* 2000, 39, L555-L558.
- [47] Dietl T. (2007), Origin of ferromagnetic response in diluted magnetic semiconductors and oxides, *J. Phys.: Condens. Matter.* 19, 165204.
- [48] Wakano T., Fujimura N., Morinaga Y., Abe N., Ashida A., Ito T. (2001), Magnetic and magneto-transport properties of ZnO:Ni films, *Physics E* 10, 260-264.
- [49] Yin Z., Chen N., Yang F., Song S., Chai C., Zhong J., Qian H., Ibrahim K. (2005), Structural, magnetic properties and photoemission study of Ni-doped ZnO, *Solid State Commun.* 135, 430-433.
- [50] Liu X. J., Zhu X. Y., Song C., Zeng F., Pan F. Intrinsic and extrinsic origins of room temperature ferromagnetism in Ni-doped ZnO films, *J. Phys. D: Appl. Phys.* 42, 035004.
- [51] Rambu A. P. *et al.* (2013), Study on Ni-doped ZnO films as gas sensors, *Appl. Surf. Sci.* 280, 598-604.
- [52] Zhao J. *et al.* (2011), Structure and photocatalytic activity of Ni-doped ZnO nanorods, *Materials Research Bulletin* 46, 1207-1210.
- [53] Chang Y. C., Chen L. J. (2007), ZnO Nanoneedles with enhanced and sharp ultraviolet cathodoluminescence peak, *J. Phys. Chem. C* 111, 1268-1272.

- [54] He J. H. *et al.* (2005), Large-scale Ni-doped ZnO nanowire arrays and electrical and optical properties, *J. Am. Chem. Soc.* 127, 16376-16377.
- [55] Rana *et al.* (2016), Growth of transparent  $Zn_{1-x}Sr_xO$  ( $0.0 \leq x \leq 0.08$ ) films by facile wet chemical method: effect of Sr doping on the structural, optical and sensing properties, *Appl. Surf. Sci.* 379, 23-32.
- [56] Das *et al.* (2013), Band gap tuning in ZnO through Ni doping via spray pyrolysis, *J. Phys. Chem. C* 117, 12745-12753.
- [57] Rana *et al.* (2015), Enhancement of two photon absorption with Ni doping in the dilute magnetic semiconductor ZnO crystalline nanorods, *Appl. Phys. Lett.* 107, 231907.
- [58] Kwak G., Jung S., Yong K. (2011), Multifunctional transparent ZnO nanorod films, *Nanotechnology*, 22, 115705.
- [59] Kumar *et al.* (2014), Structural, optical and magnetic properties of sol-gel derived ZnO: Co diluted magnetic semiconductor nanocrystals: an EXAFS study, *J. Mater. Chem. C* 2, 481-495.
- [60] Dakhel A. A., El-Hilo M. (2010), Ferromagnetic nanocrystalline Gd-doped ZnO powder synthesized by co-precipitation, *J. Appl. Phys.* 107, 123905.
- [61] Gaudon M., Toulemonde O., Demourgues A. (2007), Green coloration of Co-doped ZnO explained from structural refinement and bond considerations, *Inorg. Chem.* 46, 10996-11002.
- [62] Khorsand Zak *et al.* (2011), X-ray analysis of ZnO nanoparticles by williamson-hall and size-strain plot methods, *Solid State, Sci.*, 13, 251-256.
- [63] Singhal *et al.* (2010), Chemical synthesis and structural and magnetic properties of dispersible Cobalt-and Nickel-doped ZnO nanocrystals, *J. Phys. Chem. C* 114, 3422-3430.
- [64] Kumar *et al.* (2014), Structural, optical and magnetic properties of sol-gel derived ZnO: Co diluted magnetic semiconductor nanocrystals: an EXAFS study, *J. Mater. Chem. C* 2, 481-495.
- [65] Kumar *et al.* (2015), Insight into the origin of ferromagnetism in Fe-doped ZnO diluted magnetic semiconductor nanocrystals: an EXFAS study of local structure, *RSC Adv.* 5, 94658-94669.

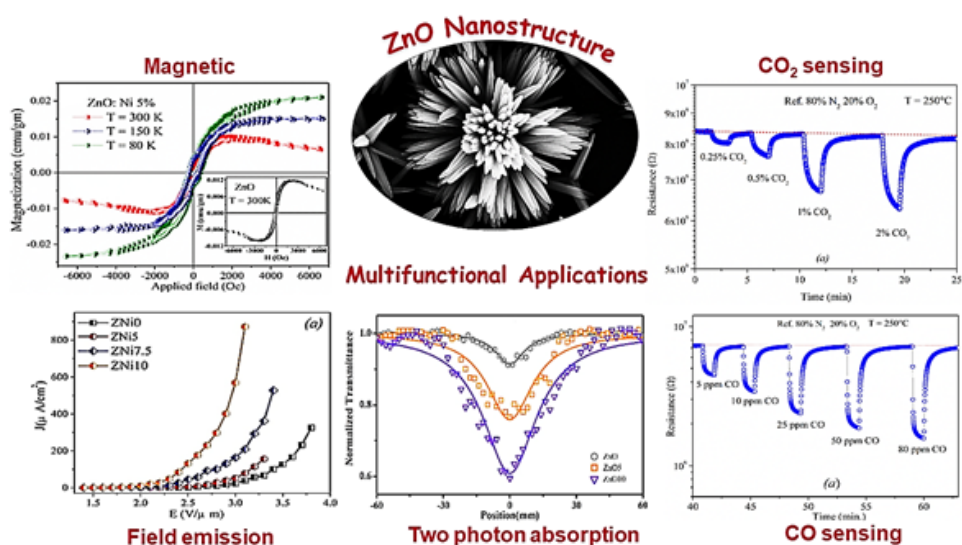
- [66] Arguello C. A., Rousseau D. L., Porto S. P. S. (1969), First-order raman effect in wurtzite-type crystals, *Phys. Rev.* 181, 1351-1363.
- [67] Duan *et al.* (2008), Magnetization and raman scattering studies of (Co, Mn) codoped ZnO nanoparticles, *J. Appl. Phys.* 104, 013909.
- [68] Singh S., Rao M. S. R. (2009), Optical and electrical resistivity studies of isovalent and aliovalent 3d transition metal ion doped ZnO, *Phys. Rev. B: Condens. Matter Mater. Phys.* 80, 045210.
- [69] Yang *et al.* (2005), In situ synthesis of Mn-Doped ZnO multileg nanostructures and Mn-related raman vibration, *J. Appl. Phys.* 97, 014308.
- [70] Wang *et al.* (2006), Raman scattering and high temperature ferromagnetism of Mn-doped ZnO nanoparticles, *Appl. Phys. Lett.* 88, 252502.
- [71] Bundesmann *et al.* (2003), Raman scattering in ZnO thin films doped with Fe, Sb, Al, Ga, and Li, *Appl. Phys. Lett.* 83, 1974-1976.
- [72] Pradhan *et al.* (2004), Structural and spectroscopic characteristics of ZnO and ZnO: Er<sup>3+</sup> nanostructures, *J. Phys.: Condens. Matter.* 16, 7123-7129.
- [73] Das *et al.* (2015), Photoluminescence and raman studies for the confirmation of oxygen vacancies to induce ferromagnetism in Fe doped Mn: ZnO compound, *J. Magn. Mater.* 382, 111-116.
- [74] Phan *et al.* (2007), Electron spin resonance and raman studies of Mn-doped ZnO ceramics, *J. Appl. Phys.* 101, 09H103.
- [75] Kaschner *et al.* (2002), Nitrogen-related local vibrational modes in ZnO:N, *Appl. Phys. Lett.* 80, 1909-1911.
- [76] Wang *et al.* (2001), Nitrogen doped ZnO film grown by the plasma-assisted metal-organic chemical vapour deposition, *J. Cryst. Growth* 226, 123-129.
- [77] Du *et al.* (2006), Raman spectroscopy of (Mn, Co)-codoped ZnO films, *J. Appl. Phys.* 99, 123515.
- [78] Ye *et al.* (2006), Raman study of lattice dynamic behaviours in phosphorus-doped ZnO films, *Appl. Phys. Lett.* 88, 101905.
- [79] Das S. C. *et al.* (2013), Band gap tuning in ZnO through Ni doping via spray pyrolysis, *J. Phys. Chem. C* 2013, 117, 12745-12753.
- [80] Deka S., Joy P. A. (2005), Direct observation of Ni metal impurities in lightly doped ferromagnetic polycrystalline (ZnNi)O, *Chem. Mater.* 17, 6507-6510.

- 
- [81] Kim K. J., Park Y. R. (2002), Spectroscopic ellipsometry study of optical transitions in  $Zn_{1-x}Co_xO$  alloys, *Appl. Phys. Lett.* 81, 1420.
- [82] Wu *et al.* (2010), Influence of Nitrogen on the defects and magnetism of ZnO:N thin films, *J. Appl. Phys.* 108, 063530.
- [83] Kim K. J., Park Y. R. (2002), Spectroscopic ellipsometry study of optical transitions in  $Zn_{1-x}Co_xO$  alloys, *Appl. Phys. Lett.* 81, 1420-1422.
- [84] Meng *et al.* (2010), Temperature behaviour of electron-acceptor transitions and oxygen vacancy recombinations in ZnO thin films, *J. Appl. Phys.* 107, 023501.
- [85] Shan *et al.* (2005), Aging effect and origin of deep-level emission in ZnO thin film deposited by pulsed laser deposition, *Appl. Phys. Lett.* 86, 221910.
- [86] Kaftelen *et al.* (2012), EPR and photoluminescence spectroscopy studies on the defect structure of ZnO nanocrystals, *Phys. Rev. B* 86, 014113.
- [87] Henderson B., Wertz J. E. (1968), Defects in the alkaline earth oxides, *Adv. Phys.* 17, 749-855.
- [88] Pan *et al.* (2006), Observation and manipulation of paramagnetic oxygen vacancies in Co-doped  $TiO_2$  nanocrystals. *Appl. Phys. Lett.* 89, 082510.
- [89] Coey J. M., Venkatesan M., Fitzgerald C. B. (2005), Donor impurity band exchange in dilute ferromagnetic oxides, *Nat. Mater.* 4, 173.



# CHAPTER 5

## Multifunctional Applications of Zinc Oxide (ZnO) Nanostructures



- **Amit K. Rana, Yogendra Kumar, Arjunan M. S., KV Adarsh, Somaditya Sen, Parasharam M. Shirage, *Applied Physics Letters* 107(23), 231907, 2015.**
- **Amit K. Rana, Prashant Bankar, Yogendra Kumar, Mahendra A. More, Dattatray J. Late, Parasharam M. Shirage, *RSC Advances* 6(106), 104318–104324, 2016.**
- **Parasharam M. Shirage, Amit K. Rana, Yogendra Kumar, Somaditya Sen, SG Leonardi, G Neri, *RSC Advances* 6(86), 82733 – 82742, 2016.**



---

## Multifunctional Applications of Zinc Oxide (ZnO) Nanostructures

*The fate and pre-conceptualized nature of ZnO nanostructures took a novel turn after it has been realized in multifunctional applications. Out of many application fields as briefly discussed in the preceding chapters, ZnO nanostructures have gained increasing attention particularly in magnetic, optoelectronic and sensing applications [1, 2]. Within the scope of this thesis, it has been realized that addition of specific nanomaterials into ZnO nanostructures exhibit multifunctional, high performance characteristics beyond what traditional bulk ZnO possess. The reinforcing nanoscale material used in ZnO nanostructures varies depending on the desired application. In most instances, the nanomaterials that are incorporated in ZnO nanostructures are metals, metal oxides, carbon nano allotropes, polymers, etc. The combination of the characteristics of the distinct constituents of materials in ZnO nanostructures thus plays a major role, which results in improvement in structural, optical and morphological properties.*

As investigated in chapter 4 about the effect of transition metal (Ni) and Sr doping in ZnO nanostructures, it is of utmost interest to explore their direct realization in multifunctional applications. In this chapter, we explore the possible application of ZnO in the field of spintronics, which is next generation semiconductor known as dilute magnetic semiconductor, in which dilute magnetic impurity is doped into the host lattice. There are several reports on the possible application of ZnO in the field of spintronics [3]. Here we use un-doped and Ni doped ZnO sample DMS and see how the Ni doping will affect the magnetic nature of ZnO. Another application of ZnO we are showing is in the area of Field emission (FE), it's because ZnO emerges as one of the most promising materials for FE devices [4, 5] and show different morphology and variable optical and electronic properties which will help to enhance the field emission properties of ZnO. Again, here we investigate the effect of Ni doping on the field emission properties of ZnO. It is because we observed that there is an alteration in the morphology of ZnO nanostructure and optical properties after Ni doping. There are several reports which displays that Ni ions create an energy level at the bottom of the conduction band, which help to provide electrons to the conduction band easily and this helps to enhance the field emission properties [6]. Furthermore, we also observed Ni doping also create or enhance the defect in the ZnO lattice and our synthesis approach also very simple which will encourage us to study the two-photon absorption (TPA). Finally, the gas sensing performance of Sr and Ni doped ZnO towards the hazards gas CO and CO<sub>2</sub> are performed. It's because very few papers regarding Ni doped ZnO sensors are reported in the literature whereas, to the best of our knowledge, only one paper deals with sensing properties of Sr-ZnO sensors. Therefore, we decided to evaluate the sensing capability of ZnO nanorods doped with different loading of Sr and Ni synthesized by a simple wet chemical method.

## **5.1. Multifunctional Applications**

### **5.1.1. Dilute magnetic semiconductor application**

One of the next generation semiconductors is known as dilute magnetic semiconductors (DMSs), where there is a small fraction of the nonmagnetic site (*i.e.*, the host cations are replaced by magnetic ions). DMSs have drawn much attention to the scientific community because of their promising technological applications in the emerging field of spin electronic devices (*i.e.*, in spintronic devices), such as non-volatile memory [7], spin light

emitting diode [8], spin-based quantum computers, spin field effect transistors, logic devices [9], *etc.* These spintronic devices are multifunctional devices with superior efficiency, lower power consumption and higher speed. The elementary requirement from the application point of view is the Curie temperature ( $T_C$ ) of DMS material i.e. 300 K or beyond. Recently researchers are focusing on metal-oxide-based DMSs, such as ZnO, TiO<sub>2</sub>, CeO<sub>2</sub>, SnO<sub>2</sub>, *etc.* ZnO has been widely studied as a host material for DMS due to its theoretical prediction to attain room temperature (RT) DMS [10]. The idea of DMS with dilute doping of magnetic elements in a host semiconductor to create the RT magnetic semiconductor was first predicted by Dielt *et al.* [4] on the *p*-type wide band gap semiconductor GaN and Mn doped ZnO. Similarly Sato *et al.* [11, 12] by theoretically calculation, based on local density approximation shows ferromagnetic ordering with  $T_C$  above room temperature for *n*-type ZnO with doping of V, Cr, Co, Fe and Ni. Above predication of Dielt *et al.* and Sato *et al.* and results of last few decades have displayed that doping of transition metal (TM) elements such as Cu, Ni, Co, Fe, Mn, *etc.* in a wide-gap semiconductors provides a conceivable means of tuning of both optical properties as well as ferromagnetism (FM) properties of a single material [13-16]. Recently, RT-FM was detected in un-doped semiconductors besides nonmagnetic element doped in semiconductors. For example, Schwartz *et al.* [17] have detected strong ferromagnetic behaviour with  $T_C$  above 350 K in Ni doped ZnO films. Meanwhile Cong *et al.* [18] detected ferromagnetism with  $T_C$  above 335 K in Zn<sub>1-x</sub>Ni<sub>x</sub>O ( $x=0.03$ ) nanoparticles while Wakano *et al.* [19] have noticed ferromagnetism at a very low temperature of 2 K and super-paramagnetic at 30 K for Ni (with 25%) doped ZnO. However, Ueda *et al.* [20] have reported that Co-doped ZnO films exhibit FM above RT, though Ni-, Cr- and Mn-doped ZnO films do not display any indication of ferromagnetic behaviour. Yin *et al.* have also verified that there is no ferromagnetism observed in Ni doped ZnO films [21]. These results unveil the FM nature at RT in Ni doped ZnO, which is still an open controversial issue, whether FM in Ni doped ZnO is an inherent or extrinsic property.

To ascertain the origin of ferromagnetism ordering in Ni doped ZnO DMS nanostructures, Ni doped ZnO films are grown by the wet chemical method and studied its structural, optical and magnetic properties (as discussed in chapter 4), which are crucial to developing an optical spintronic device and high-density magnetic storage media. Based on the material property investigations done in chapter 4 regarding Ni doping in

ZnO nanostructures, in this section, the origin of ferromagnetic behaviour at room temperature is discussed.

It is very well-recognized that for the extensive range of applications, the DMS materials should have a  $T_C$ , well above RT (300 K). The magnetization versus magnetic field (M-H) plots are shown in Figure 5.1. Figure 5.1(a) shows the M-H plot displaying the hysteresis loop for pure and Ni doped ZnO samples measured at 80 K. The experimental results of M-H curves (at 80 K) shows the typical weak ferromagnetic (FM) saturation behaviour of all the samples and saturation magnetization is found to increase from 0.02 to 0.17 emu/g with increasing Ni concentration. It can be noted from Figure 5.1(a) that the saturation tendency is not increasing with increasing the Ni concentration. Figure 5.1(b) shows the M-H plot of 5% Ni doped ZnO samples at different temperatures. It demonstrates that decrease in the temperature does not alter the important FM characteristic of the samples but significantly changes the saturated magnetic moments ( $M_s$ ) of the samples.

The origin of RT ferromagnetic property in Ni-doped ZnO is still a controversial issue. There are four possible reasons generally proposed for the ferromagnetic behaviour of the samples, *viz.* (i) Ni precipitation and the formation of NiO, (ii) at the nanoscale level, the formation of Ni-related secondary phase, (iii) extended defect due to the doping, and (iv) presence of magnetic impurity (due to the doped material) in the samples. The possibility of Ni precipitation or formation of secondary phase NiO in the present set of samples can be easily ruled out; as we did not find any evidence of NiO secondary phase in the sample from the XRD or XANES results (Chapter 4). Again the formation of Ni-related secondary phase at the nanoscale level is also ruled out because other measurements such as EXAFS, PL, and Raman spectroscopy magnificently suggested incorporation of Ni ions at Zn sites of ZnO. As discussed in chapter 4, all the above measurements manifest integration of  $Ni^{2+}$  ions in ZnO wurtzite and the formation of singly ionized oxygen vacancy, which can be considered to be the most important factor for the FM nature of the present samples. Thus, transition metals (TMs) as well as defects produced by TMs, especially single ionized oxygen vacancy, play a significant role in the observed FM.

However, for intrinsic ferromagnetism in TM-doped ZnO, the precise mechanism is still not established beyond doubt. A number of different theories and ideas have been

suggested for this, for example, (i) the mean-field Zener model [4] (ii) RKKY (Ruderman-Kittel-Kasuya-Yosida) mechanism (*i.e.*, carrier induced ferromagnetism), (iii) donor impurity band exchange model, where the FM in DMSs is due to an indirect exchange through shallow donor electrons and this forms BMPs, [22-24] and (iv) direct interactions (such as double or super exchange mechanism). RKKY is based on free electron, since ZnO is a semiconductor and merely a small doping cannot transform it into metal, so the RKKY is invalid here. Again, direct interactions between the magnetic ions required for the double-exchange mechanism are also not possible due to very dilute doping of the samples.

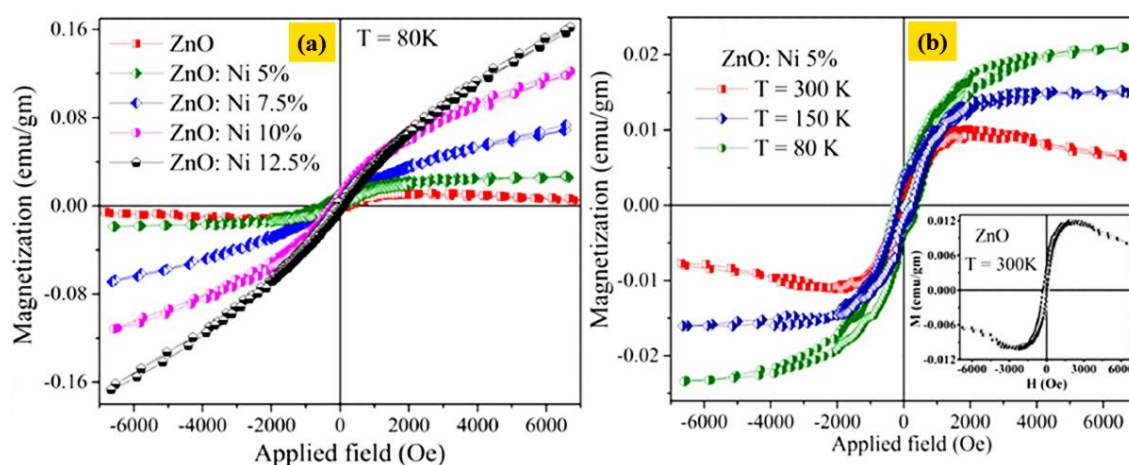


**Figure 5.1.** (a) *M-H* plot at 80 K showing the hysteresis loop for pure and Ni doped ZnO nano structure and (b) Shows the *M-H* plot of Ni 5% doped ZnO at 80 K, 150 K and 300 K and the inset shows *M-H* plot of ZnO at 300 K.

This suggests the intrinsic exchange interactions due to oxygen related defect which assisted BMPs and origin for the RT-FM in the present case. Therefore, we conclude that  $\text{Ni}^{2+}$  ions cannot just produce intrinsic ferromagnetism until and unless there are formation of point defects such as singly ionized oxygen vacancies assisted BMPs for room temperature FM.

### 5.1.2. Field emission (FE) application

The last few decades ZnO emerges as one of the most promising materials for FE devices. It is because of its high thermal stability, low electron affinity, as well as oxidation resistance in harsh environment [25, 26]. There are many reports on enhancement of FE from ZnO. Farid *et al.* have observed enhanced FE properties of Cu doped ZnO nanocomposite films synthesized by electrochemical methods [27] and Yu-Cheng Chang,

grown Ni-doped ZnO nano-tower arrays on a silicon substrate using thermal evaporation method ( $T = 1100\text{ }^{\circ}\text{C}$ ) and observed enhanced optical and field emission properties [28]. Similarly, Xing *et al.* have reported the growth of ultrathin single-crystal ZnO nano-belts by using an Ag catalyzed vapor transport method and studied their FE property [29].

The key issues in FE measurements are the operating voltage range and the emission current stability. As the turn-on or threshold field values (Turn-on field is defined as the applied field strength at which field emission from the material begins. Most popularly, the applied field at which the emission current density reaches to  $10\text{ }\mu\text{A}/\text{cm}^2$  is termed as Turn-on field) are dependent on the morphology (shape and size) as well as its intrinsic physical properties such as work function and electrical conductivity of the emitter. The approach towards improving the FE properties of semiconductors is either to tailor the geometry of the emitter or by modifying its electronic properties. The first approach has limitations on the reduction of the size and shape of the nanostructures. Although the synthesis of an array of well-spaced anisotropic nanostructures possessing a very fine apex radius (typically, 20 nm) is feasible, the mechanical sturdiness of such an emitter is questionable. It is predictable that the mechanical stress induced due to the presence of an intense electrostatic field may result in negative effects, such as bending/fracture of the emitters. Similarly, for the second approach, modified electronic properties by doping/mixing with suitable elements are very critical and sometimes the chemical reactivity of such structures may lead to a decline of their emission performance. Therefore, a suitable combination of both approaches is considered to be a promising method for improving the FE performance, which has been well attempted by several researchers.

As we have already explored the synthesis of Ni doped ZnO (0%, 5%, 7.5% 10%) by low temperature wet chemical methods and did a systematic study on their material properties, here we have made an attempt to use the Ni doped ZnO samples for FE applications.

1D and 2D ZnO nanostructures are considered as good field emitters because of their diverse nanostructures, which provide promising aspect ratios and appropriate work functions. FE properties can be altered by many factors, such as the curvature, uniformity, size, and density of emitter. The current density ( $J$ ) versus applied electric field ( $E$ ) characteristic of the pure and doped ZnO samples are shown in Figure 5.2(a). The values

of turn-on field and threshold field required for drawing emission current densities of 1 and 10  $\mu\text{A}\cdot\text{cm}^{-2}$  are found to be 2.5  $\text{V}\cdot\mu\text{m}^{-1}$  and 2.8  $\text{V}\cdot\mu\text{m}^{-1}$  in case of ZNi0 and 1.7  $\text{V}\cdot\mu\text{m}^{-1}$  and 2  $\text{V}\cdot\mu\text{m}^{-1}$  in case of ZNi10, respectively. The emission current density is found to increase rapidly with increase in the applied electric field, and emission current density of 326  $\mu\text{A}\cdot\text{cm}^{-2}$  and 872  $\mu\text{A}\cdot\text{cm}^{-2}$  has been obtained at an applied field of 3.8  $\text{V}\cdot\mu\text{m}^{-1}$  and 3.1  $\text{V}\cdot\mu\text{m}^{-1}$  for ZNi0 and ZNi10 respectively. FE characteristics of pure and doped ZnO samples are summarized in Table 5.1.

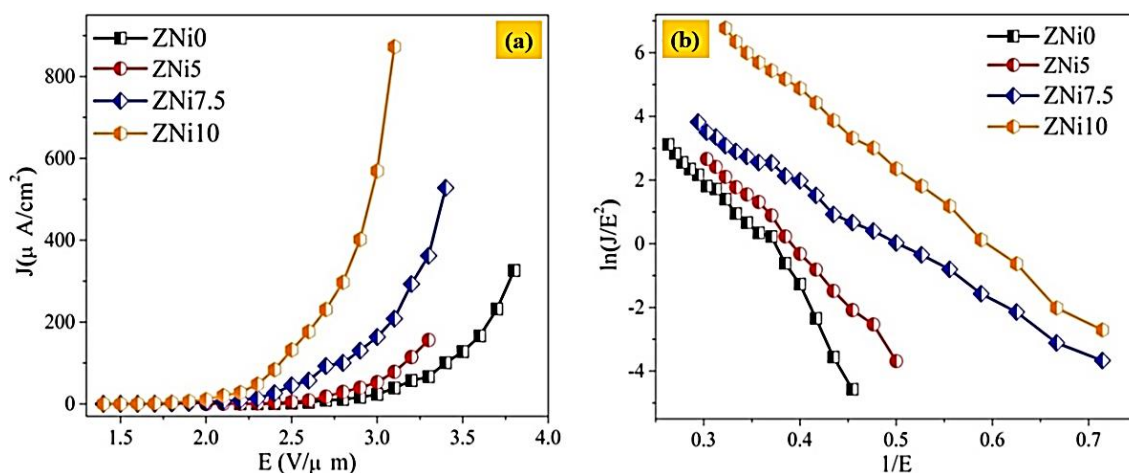


**Figure 5.2.** Shows Field emission of pure and Ni doped ZnO, (a) Applied electrical field as a function of emission current density, (b) Fowler-Nordheim (F-N) plot.

**Table 5.1.** Comparison of field emission characteristics of pure and Ni doped ZnO nanostructures.

Sr. No.	Sample Name	Turn on field ( $\text{V}\cdot\mu\text{m}^{-1}$ ) at 1 $\mu\text{A}/\text{cm}^2$	Threshold Field ( $\text{V}\cdot\mu\text{m}^{-1}$ ) at 10 $\mu\text{A}/\text{cm}^2$	Maximum current density ( $\mu\text{A}/\text{cm}^2$ ) at $\text{V}\cdot\mu\text{m}^{-1}$
1	ZNi0	2.5	2.8	$\sim 326$ at $\sim 3.8$
2	ZNi5	2.3	2.6	$\sim 156$ at $\sim 3.4$
3	ZNi7.5	1.8	2.2	$\sim 528$ at $\sim 3.4$
4	ZNi10	1.7	2	$\sim 872$ at $\sim 3.1$

The modified Fowler-Nordheim (F-N) equation in terms of the current density ( $J$ ) and the applied electric field ( $E$ ), is defined as [30, 31],

$$J = \lambda_M a \Phi^{-1} E^2 \beta^2 \exp\left(-\frac{b\Phi^2}{\beta E} v_F\right) \quad (5.1)$$

where  $E=V/d$ , where  $V$  is the applied voltage, and  $d$  is the separation between anode and cathode ( $\sim 2$  mm). Furthermore, the emission current density  $J$  is estimated as  $J=I/A$ ,

where,  $I$  is the emission current and  $A$  is the total area of the emitter,  $a$  and  $b$  are constants, typically  $1.54 \times 10^{-10}$  ( $\text{A-V}^{-2}\text{-eV}$ ) and  $6.83 \times 10^3$  ( $\text{V-eV}^{-3/2}\mu\text{m}^{-1}$ ) respectively,  $\phi$  is the work function of the emitter material,  $\lambda_M$  is the macroscopic pre-exponential correction factor,  $v_F$  is value of the principal Schottky–Nordheim barrier function (a correction factor), and  $\beta$  is the field enhancement factor. In the present study, the F-N plot is found to be nonlinear and such F-N plots have been reported for many semiconductor nanomaterials (Figure 5.2(b)).

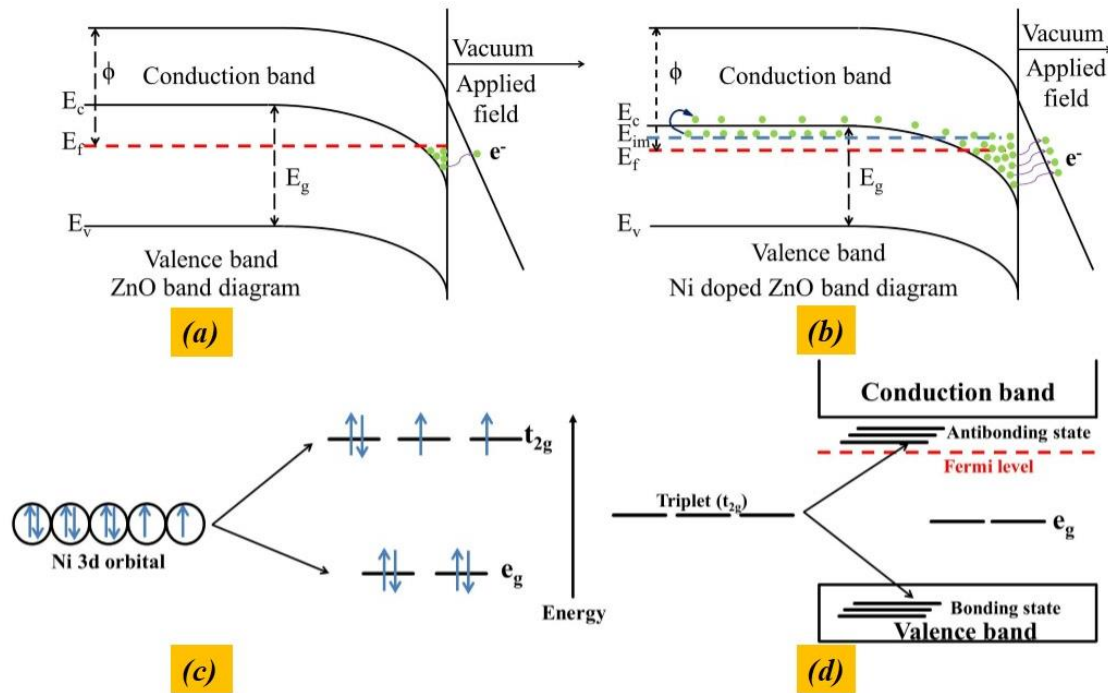


**Figure 5.3.** Shows the schematic (a) Electronic structure of transition metal at a substitution site in a wurtzite structure, (b) Splitting of impurity state under the influence of crystal field of host ZnO, energy band diagram of (c) ZnO, (d) Ni doped ZnO ( $E_g$ : Energy gap,  $E_f$ : Fermi level,  $E_c$ : Energy of Conduction band,  $E_v$ : Energy of Valance band,  $\phi$ : work function).

The enhancement in FE performance after doping with Ni in ZnO may be explained as follows: as we know, the turn-on and threshold fields depend upon the overall geometry of the emitter and also on its intrinsic electronic properties such as the charge carrier concentration, work function, *etc.* ZnO rods with Ni doping levels of 5% and 7.5% displayed an increase in diameter relative to that of pure ZnO, whereas ZnO rods with a Ni doping level of 10% exhibited a decrease. The overall morphology of ZNi5 and ZNi7.5 samples displayed a lower areal density with quite separate rods, which suggests a smaller screening effect in comparison to that of ZNi0. This decrease in screening resulted in a

reduction in the turn-on voltage in both cases. In the ZNi10 sample, the decrease in diameter and presence of few nano-sheets increased the number of emission centres; both these causes may result in a further decrease in the turn-on voltage. Another reason for a decrease in the turn-on voltage is an increase in the Ni doping level in ZnO, which increases the charge carrier concentration in the conduction band of ZnO, as well as causing a shift in energy levels, which has been proved by many experimental and theoretical studies [32].

In general, Ni is isoelectronic with Zn, so it should not behave as an acceptor or shallow donor into ZnO. Now the question is: where do these free electrons come from? Katayama-Yoshida and Sato [33] demonstrated using *ab initio* electronic structure calculations that semi metallic behaviour exists in transition metal-doped ZnO. In our samples, Ni<sup>2+</sup> partially substituted Zn<sup>2+</sup> in ZnO and as Zn<sup>2+</sup> ions in the ZnO structure are located at the center of a tetrahedra surrounded by four oxygen atoms. Under the influence of the tetrahedral crystal field of ZnO, the *d*-states of Ni split into a higher triplet (*t*<sub>2g</sub>) and a lower doublet (*e*<sub>g</sub>) state, as shown in Figure 5.3(a). The higher *t*<sub>2g</sub> state hybridizes with the *p*-orbital of the valence band and further splits into *t*<sub>bonding</sub> and *t*<sub>antibonding</sub> states (Figure 5.3(b)). The *t*<sub>bonding</sub> states participate in Ni-O bonding and are localized. However, the antibonding states have higher energy and contain some mobile electrons and also the energy of the antibonding states lies very close to the conduction band. Hence, there is a high probability that electrons from these antibonding states will jump (acting as an impurity state) into the conduction band with a small increase in potential difference. Owing to increase in the Ni concentration in ZnO, increasing numbers of electrons are promoted into the conduction band, which results in an increase in FE preformation, as shown in schematic form in Figure 5.3(c, d), in comparison to that of pure ZnO. In the present work, this effect has clearly been observed from the FE curve. Thus, an increase in the Ni concentration promotes a large number of electrons into the conduction band of ZnO, which ultimately results in a decrease in the turn-on voltage for ZNi5, ZNi7.5, and ZNi10 in comparison to that of ZNi0.

The current stability curves of pure and doped samples are also investigated at a pre-set value of 5  $\mu$ A over a period of 3 h (Figure 5.4). Successive current stability curves show no obvious decrease in current density. This is a very important feature, in particular for practical applications. The appearance of the “spike” type fluctuations observed in the

emission current may result from the adsorption/desorption and ion bombardment of residual gas molecules. The local work function of the emitter varies owing to the adsorption/desorption of gas molecules at the emitter surface and ion bombardment by residual gas molecules, which is due to the presence of a strong electrostatic field, which results in fluctuations. Typical FE images are shown in the insets of Figure 5.4. The images show a number of tiny spots, which correspond to the emissions from the most protruding edges of the emitters. These results indicate the excellent emission stability of Ni doped ZnO, which makes it highly valuable for practical applications as a field emitter. Furthermore, the field emission behaviour of other pure and doped ZnO nanostructures were compared with data for Ni doped ZnO, and are summarized in Table 5.2. The overall FE performances of Ni doped ZnO nanostructures prepared by a low-temperature wet chemical method in the present study, such as the turn-on and threshold fields, are better than those in previous reports on pure and doped ZnO nanostructures.

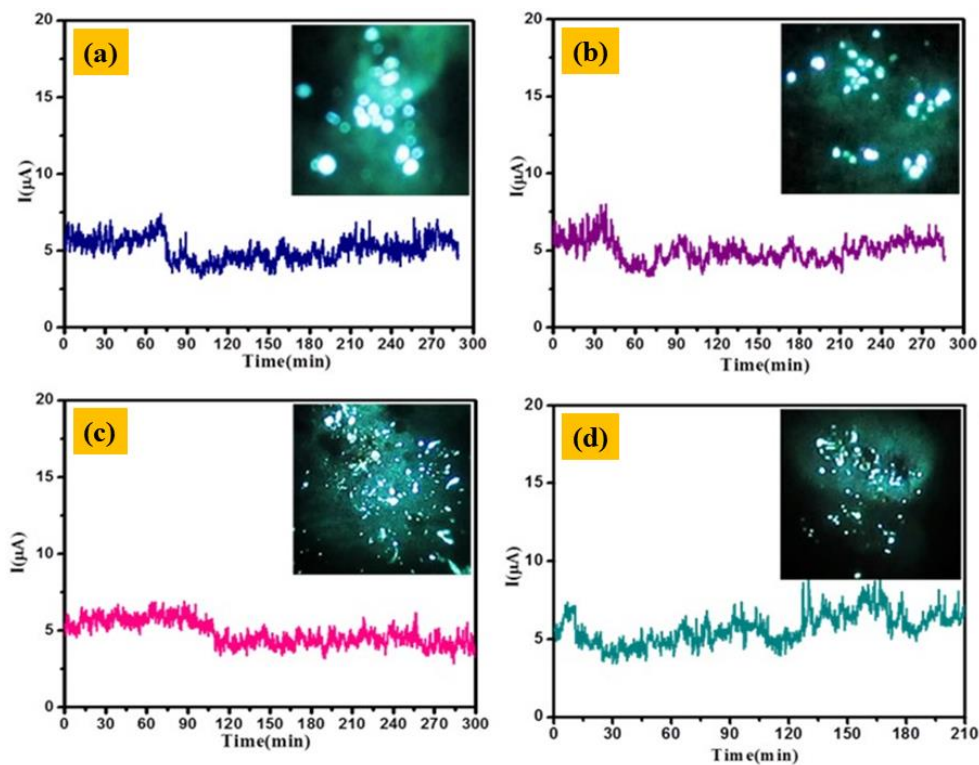


**Figure 5.4.** Shows typical field emission current stability recorded at  $5 \mu\text{A}$  indicating stable field emission current of (a) pure ZnO, (b) Ni 5% doped ZnO, (c) Ni 7.5% doped ZnO, (d) Ni 10% doped ZnO (inset of figures show field emission pattern taken during the long term current stability measurements of the emitter).

**Table 5.2.** Comparison of field emission characteristics of the pure and doped ZnO nanostructure with the present work.

Field emitters	Synthesis route	Turn on Field (V- $\mu\text{m}^{-1}$ )	Threshold Field (V- $\mu\text{m}^{-1}$ )	Ref.
ZnO nanoneedles	Vapor phase growth	2.4	6.5	[34]
ZnO nanowire	Vapor deposition method	6.0	11.0	[35]
Ga-doped ZnO	Vapor liquid solid process	3.4	5.4	[36]
In-doped ZnO	Chemical vapor deposition	2.4	3.5	[37]
N-doped ZnO	Solvothermal Synthesis	2.9	-	[38]
ZnO nanorods	Atomic layer deposition	2.85	-	[39]
ZnO nanowires/graphene	Hydrothermal method	2.0	-	[40]
Cu-doped ZnO quantum dot	Hydrothermal method	4.47	8.9	[41]
<b>Ni doped ZnO</b>	<b>Wet chemical methods</b>	<b>1.7</b>	<b>2</b>	<b>This work</b>

### 5.1.3. Two photon absorption

Recent advances in the chemical synthesis of ZnO have enabled to prepare them in complex nanocrystals with an increased degree of structural complexity and shape. [42] This opens up another degree of freedom to harness many optical phenomena that result from quantum confinement effects. Recently, two-photon absorption (TPA) induced UV emission is reported in ZnO nanowires [43] that can be used to fabricate low-cost nano-lasers for photonic circuitries and sensing systems. Although, extensive studies have been carried out toward revealing the size-dependent optical and nonlinear optical properties of ZnO nanocrystals, however, there were not many studies on the variation of such effects with the doping of transition metals. This led to the fact that their linear optical properties can be tuned just by doping. For example, various theoretical and experimental studies on the nonlinear optical absorption in semiconductors exhibit an inverse cubic relation with band gap for the two photon absorption coefficient ( $\beta$ ). Such studies are important to explore how the nonlinear optical properties of semiconductor nanocrystals (NCs) depend on the doping, which also provide insight to engineer it. Here we demonstrate that the two photon absorption coefficient ( $\beta$ ) increases by as much as 14 times with Ni doping in high-quality ZnO nanorods crystallized in wurtzite lattice which

named as ZnO0, ZnO5 and ZnO10 respectively. The significant increase in  $\beta$  is a result of the redshift in optical bandgap with Ni doping and follows the bandgap scaling.

To estimate the third order nonlinear optical properties, we have used the conventional open aperture Z-scan method, [44] which measures the total transmittance as a function of incident laser intensity. In the present Z-scan experiment, 5 ns pulses centered at 532 nm from the second harmonic of Nd-YAG laser was used to excite the sample. The repetition rate of the laser is kept at 10 Hz to avoid the heating effects. The beam was focused by a 50 cm focal length lens, and the sample is moved along the  $z$ -axis of the beam by using a computer controlled translation stage. The Rayleigh length ( $z_0$ ) and the beam waist in the experiment are 10 mm and  $\sim 84 \mu\text{m}$ , respectively. For the Z-scan measurements, all the samples were dispersed in ethanol and used a 1 mm path length cuvette. Open aperture Z-scan which measures the total transmittance as a function of incident laser intensity is employed to study the off-resonant third-order nonlinear optical properties of the Ni doped ZnO nanorods. The Z-scan results of the samples at the peak on-axis intensity of  $360 \text{ MW/cm}^2$  are presented in Figure 5.5(a). As the bandgap of all the samples ( $\sim 3 \text{ eV}$ ) are well above the single photon energy of 532 nm, it is reasonable to assume that a two photon process occurs in the samples. Expectedly, the Z-scan peak-shape response indicates the TPA for the samples. Importantly, the TPA shows a significant enhancement with the Ni concentration (Figure 5.5(a)). To derive the TPA coefficient ( $\beta$ ) of the samples, which is shown in Figure 5.5(b) the intensity-dependent normalized transmittance, where the input intensity is tuned from 10 to  $360 \text{ MW/cm}^2$ . From the figure, it can be seen that the transmittance decreases with increase in intensity that is consistent with the theory of TPA. To get more detailed information on the variation of  $\beta$  with Ni doping in ZnO nanorods, we have fitted the experimental data with the Z-scan theory. In the case of TPA, the normalized transmittance as a function of position  $z$  is given by:

$$T_N = \frac{1}{q_0 \sqrt{\pi}} \int_{-\infty}^{+\infty} \ln \left( 1 + q_0 e^{-t^2} \right) dt \quad (5.2)$$

where  $q_0 = \frac{\beta I_0 L_{eff}}{(1 + \frac{z^2}{z_0^2})}$  and  $L_{eff} = \frac{(1 - e^{-\alpha L})}{\alpha}$ ,  $I_0$ ,  $z_0$ ,  $L$  and  $\alpha$  are the peak intensity at

the focus ( $z=0$ ), the Rayleigh length, sample thickness, and linear absorption coefficient, respectively.  $\beta$  values from the best-fit to the normalized transmittance are shown in the

Table. 5.3. It can be seen from the table that  $\beta$  value shows a significant enhancement from  $7.6 \pm 0.4$  to  $112 \pm 6$  cm/GW with Ni doping, i.e. 14 times increase when the Ni concentration is increased from 0 to 10%.

**Table 5.3.** Experimentally calculated values of  $E_g$ ,  $\beta$ , and limiting threshold.

Sample	$E_g$ (eV)	$\beta \pm \text{Err. (cm/GW)}$	Limiting Threshold ( $\text{MW/cm}^2$ )
ZnO0	3.01	$7.6 \pm 0.4$	132
ZnO5	2.93	$41.8 \pm 3$	60
ZnO10	2.85	$112 \pm 6$	30

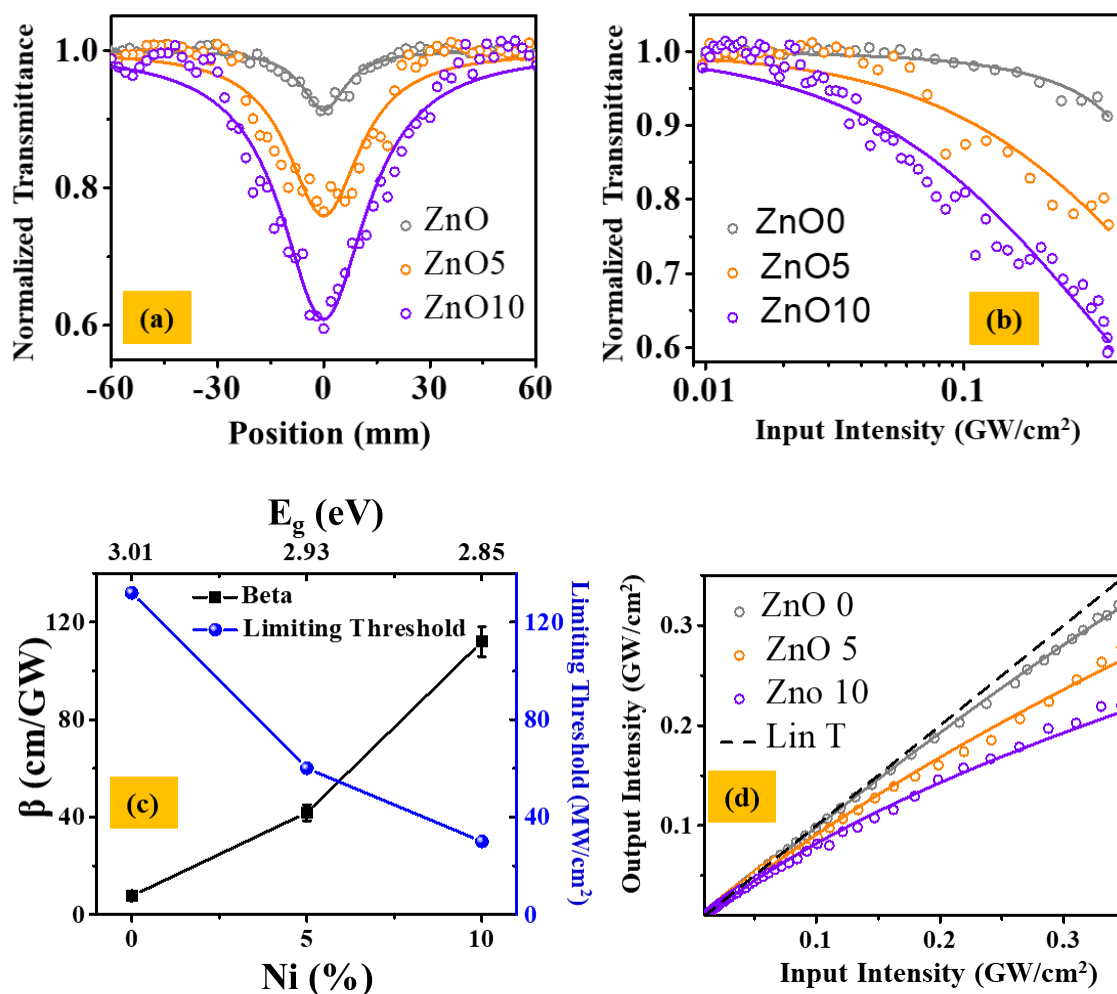


**Figure 5.5.** (a) Open aperture Z scan curves of the samples. (b) Normalized transmittance as a function of input intensity. (c) Variation of  $\beta$  (left axis) and optical limiting threshold intensity (right axis) as function Ni doping (bottom axis) and bandgap (top axis). (d) Optical limiting curve for the samples and the dashed line shows the linear absorption regime. The solid line represents the theoretical fit.

After demonstrating the substantial enhancement of the nonlinear optical response with Ni doping in ZnO nanorods, we have tried to explain the observed effects. For this,

we have assumed that the increase of  $\beta$  with doping is due to the decrease in optical bandgap ( $E_g$ ) of the sample. To get a consistent picture of this assumption, we have shown in Figure 5.5(c) the variation of bandgap and  $\beta$  as a function of the doping concentration. It can be seen from the Figure 5.5(c) that  $\beta$  increases and  $E_g$  decreases with increase in Ni concentration. Thus, we conclude that the large enhancement of  $\beta$  might be a result of bandgap reduction. Moreover, it has been theoretically and experimentally shown that the TPA in semiconductors follows an inverse cubic relation with bandgap, [45] *i.e.*

$$\beta = \frac{K\sqrt{E_p}F}{n^2E_g^3}. \text{ In this equation, } K \text{ and } E_p \text{ are material independent constants, and } n \text{ is the}$$

refractive index of the material.  $F$  is a band-structure dependent function, and its value depends on the ratio of photon energy and bandgap. For parabolic bands,  $F$  is given by

$$\text{the equation } F = \frac{[2h\nu/E_g - 1]^{3/2}}{[2h\nu/E_g]^5}. \text{ From the experimental results, it can be seen that } E_g$$

decreases with increase in Ni doping. Furthermore, a recent report [46] demonstrates that the refractive index decreases with Ni doping. Thus, the  $n^2E_g^3$  term decreases and consequently increases  $\beta$ . Additionally, Ni (transition metal) doping leads to the redistribution of electronic charge and increases the polarizability of the medium. The enhancement in the third-order optical susceptibility ( $\chi^3$ ) can be calculated from the rise in oscillator strength ( $R^3/X_b^3$ , where  $R$  is the crystallite size, and  $X_b$  is the exciton Bohr radius) [47]. From Table 5.3, it can be seen that the  $R$  increases with metal doping, which in effect increases the  $\beta$ . Here, we assumed that change in exciton Bohr radius is much smaller than the change in crystallite size with Ni doping. Expectedly, similar kind of enhancement in nonlinear absorption with metal doping is observed in semiconductor quantum dots [48]. For example,  $\beta$  shows 8 times enhancement with Cr doping and 11 times with Cu doping. Importantly, the nonlinear absorption and optical limiting properties of Ni doped ZnO nanorods are comparable or even better than other nanostructures such as liquid dispersion of carbon nanotubes (50 MW/cm<sup>2</sup>), [49] graphene nanostructures (60 MW/cm<sup>2</sup>), [50] and graphene/polyimide composites [51].

The remarkable observation of the substantial enhancement of TPA with Ni doping occurs at room temperature, is highly advantageous for potential applications in optical limiting and switching. The optical limiter is a nonlinear device that blocks the high-

intensity light while being transparent to the lower intensity beams. They are very critical in protecting various optoelectronic detectors and eye from intense laser beams. In this context, we have also shown in Figure 5.5(d) a plot of output intensity ( $I_{out}$ ) versus input intensity ( $I_{in}$ ). From the Figure 5.5(d), it can be seen that at low  $I_{in}$ ,  $I_{out}$  is linearly proportional to  $I_{in}$  (Lambert-Beer law). As the  $I_{in}$  increases, a stage reaches where the  $I_{out}$  is no longer linearly proportional to the  $I_{in}$ , *i.e.*, deviation of the curve from the linear transmittance (the dashed line in Figure 5.5(d)). The  $I_{in}$  at which the curve deviates from the linear behaviour is taken as the limiting threshold intensity that is an important performance parameter for an optical limiter. Further, it can be clearly seen from Figure 5.5(c) that the limiting threshold intensity decreases with Ni doping, meaning optical limiting can be even achieved at moderate intensity with Ni doping. The variation of limiting threshold intensity with Ni ratio is shown in Table 5.3. In contrast to normal optical designing techniques where only two dimensional structuring restricted to the material surface is possible, TPA technique has the capacity to perform three dimensional manipulations. This is because the interaction of light with material takes place only at very high photon flux such as at the focusing point of a lens. By suitable laser focusing setups, one can produce a well localized light matter interaction, precisely at any desired point inside the material. Thus, the high TPA in the doped samples brings many fold increase in its potentials and provides a way to engineer the material properties in three dimensions. Hence the improvement in TPA and optical limiting properties bring many fold increase in the technological potentials such as three dimensional patterning of this multifunctional material for the realization of various optoelectronic, magneto-optical, and integrated devices.

#### 5.1.4. Gas Sensing application: CO and CO<sub>2</sub> sensing tests

Doping of base metal oxide with various metallic elements, for example, noble metals, transition metal and metal oxides, had been proven to be also effective for this scope [52, 53]. Indeed, doping enhances the performance of gas sensor via controlling donor density, changing the acid-base properties and varying electronic properties so as to change the interaction between gases surrounding the sensor and sensing layer.

Here, we investigated ZnO nanorods doped with Sr (4% and 8%) and Ni (5% and 10%). Very few papers regarding Ni doped ZnO sensors are reported in the literature [54-58], whereas, to the best of our knowledge, only one paper deals with sensing properties

of Sr doped ZnO sensors [59]. Therefore, we decided to evaluate the sensing capability of ZnO nanorods doped with different loading of Sr and Ni synthesized by a simple wet chemical method. The morphology and microstructure of the synthesized materials are already investigated and discussed in chapter 4.

We have fabricated resistive gas sensors for monitoring CO and CO<sub>2</sub>. Sensors that measure accurately CO and CO<sub>2</sub> concentration in air are highly required for indoor air quality control. CO is a concern in indoor environments where poorly ventilated appliances are present or where outdoor air intakes are located in areas subject to high concentrations of vehicle exhaust [60]. OSHA (Occupational Safety and Health Administration) organization has established a permissible exposure limit for CO of 50 ppm as an 8-hour time-weighted average. CO<sub>2</sub> levels can be used as a rough indicator of the effectiveness of ventilation, and excessive population density in a structure. The eight-hour permissible limit for CO<sub>2</sub> is 5000 ppm [61]. Then, sensors with promising sensing characteristics to these two target gases are highly desired to be applied in electronic devices for monitoring indoor air quality and used to trigger an alarm, turn on a ventilation fan, or control a heating, ventilating and air conditioning (HVAC) system.

**Sensing Tests:** Sensing tests are carried out on resistive sensors having a planar configuration and based on alumina substrates (6 mm × 3 mm) with platinum (Pt) interdigitated electrodes and a Pt heater located on the back. The devices for electrical and sensing tests are prepared by printing films (~10 μm thick) of the nanorods dispersed in water. A picture of the final device with the Ni10% doped ZnO printed film after annealing at 350 °C is shown in Figure 5.6.

The sensors were then introduced in a Teflon test chamber for the sensing tests. The electrical measurements were carried out over the temperature range from RT to 350°C under a synthetic dry air (20% O<sub>2</sub>- 80% N<sub>2</sub>) stream of 100 sccm by collecting the electrical resistance of the sensitive films. An Agilent 34970A multimeter data acquisition unit was used for this purpose, while an Agilent E3632A dual-channel power supplier instrument was employed to bias the built-in heater of the device. Sensing tests are performed by injecting pulses of the analytic from certified bottles. The concentration of the target gas is varied by using mass flow controllers. The gas response is defined as the ratio  $R_{\text{air}}/R_{\text{gas}}$ , where  $R_{\text{air}}$  is the electrical resistance of the sensor in dry air and  $R_{\text{gas}}$  the resistance at different target gas concentrations.

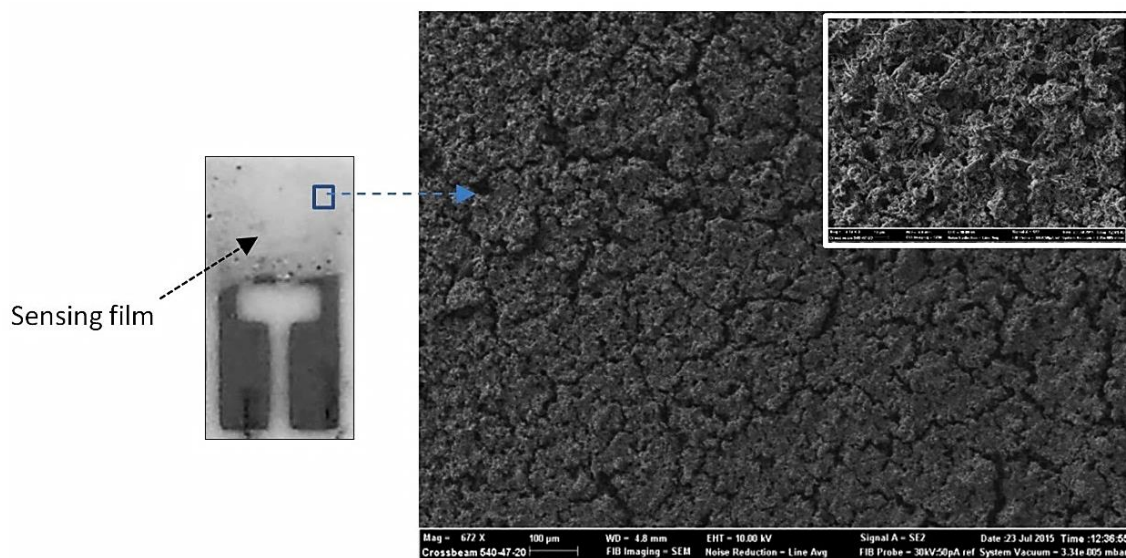


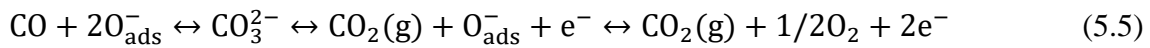
**Figure 5.6.** Photograph of the sensor device and micrograph of the sensing film surface. Inset shows a high magnification of the highly porous sensing film surface.

**CO and CO<sub>2</sub> sensing tests:** CO and CO<sub>2</sub> are major air pollutants whose concentration must be controlled as per international indoor air quality standards at industrial and public work places. Therefore, there is a high interest to fabricate efficient CO and CO<sub>2</sub> sensors. Resistive sensors having a planar configuration (Figure 5.6) have been fabricated by printing thick films of the synthesized samples on the Pt-inter digitated electrodes of an alumina support. The surface of the sensing layer shows a highly porous structure. Before sensing tests all the sensors prepared are heated up to 350°C and left to stabilize for a time of about 2 hours in order to stabilize the printed films. Figure 5.7 shows a panoramic view of the dynamic response of some samples investigated towards CO and CO<sub>2</sub> at different temperatures. The response to a decrease of oxygen, from 20% to 10% (v/v), is also shown. Operating temperature was found to play a crucial role in gas response of the investigated sensor. In the temperature range between 200°C and 350°C all samples show responses to CO and CO<sub>2</sub>. In accordance with *n*-type semiconductor behaviour of the samples, after pulses at different concentration of CO and CO<sub>2</sub> in synthetic air, a decrease of the electric resistance is observed. Indeed, when a reducing gas such as CO is added, the interaction of this gas with the surface, chemisorbed oxygen O<sup>2-</sup> can take place. The reducing gas readily releases electrons back to the conduction band, according eqn. (5.3), and the electrical resistance of the semiconductor decreases.



Different sensing mechanisms are responsible of the electrical behaviour of ZnO based materials towards CO<sub>2</sub>. Among these, the reactions of CO<sub>2</sub> with adsorbed OH<sup>-</sup> on the surface to form carbonates and hydroxyl carbonates are the most important. These intermediate species react with adsorbed oxygen on the ZnO surface, releasing electrons and, consequently decreasing the resistance. Furthermore, at removal of the target gas and subsequent exposure again to synthetic air, all the samples are able to recover the baseline. For example, even at the low operating temperature of 200°C, the dynamic response shown by the Ni-ZnO sensor is rather fast ensuring rapid response times of about 15 seconds and recovery less than 90 seconds. It is noteworthy that at lower temperature (200°C), the pure ZnO and Sr doped sensors exposed to CO pulses present an inversion of the response (Figure 5.8).

In the presence of O<sub>2</sub>, the O<sub>ads</sub><sup>-</sup> species becomes dominant at an operation temperature of 100 - 200°C. It is generally accepted that CO interacts with O<sub>ads</sub><sup>-</sup> to form carboxylate and bi-dententate carbonate (eqn. (5.4) & (5.5)), which helps in releasing electrons in the conduction band and thus decreasing conductance (*i.e.* increase in resistance) of Sr-doped ZnO nanorods [62].



Besides this the unusual sensing behaviour can be ascribed to the chemical reaction of CO molecule by the adsorption to the grain boundary of oxygen gas molecules which plays the key role in physical barrier for carrier's movement and increase the resistance [63]. The inversion of response indicate further that, at low temperature, the pure ZnO and Sr doped ZnO sensors behave as *p*-type semiconductors. In these materials, majority carriers are holes, so the electron released in eqn. (5.4) and (5.5) contribute to decrease their concentration and consequently the conductance decreases (resistance increases). Due to this fact, the response of the cited sensors is deteriorated. Instead, Ni doped samples work well also at lower temperature (up to 150°C for 10% Ni doped), showing no response inversion and are able to recover the baseline although with longer times.

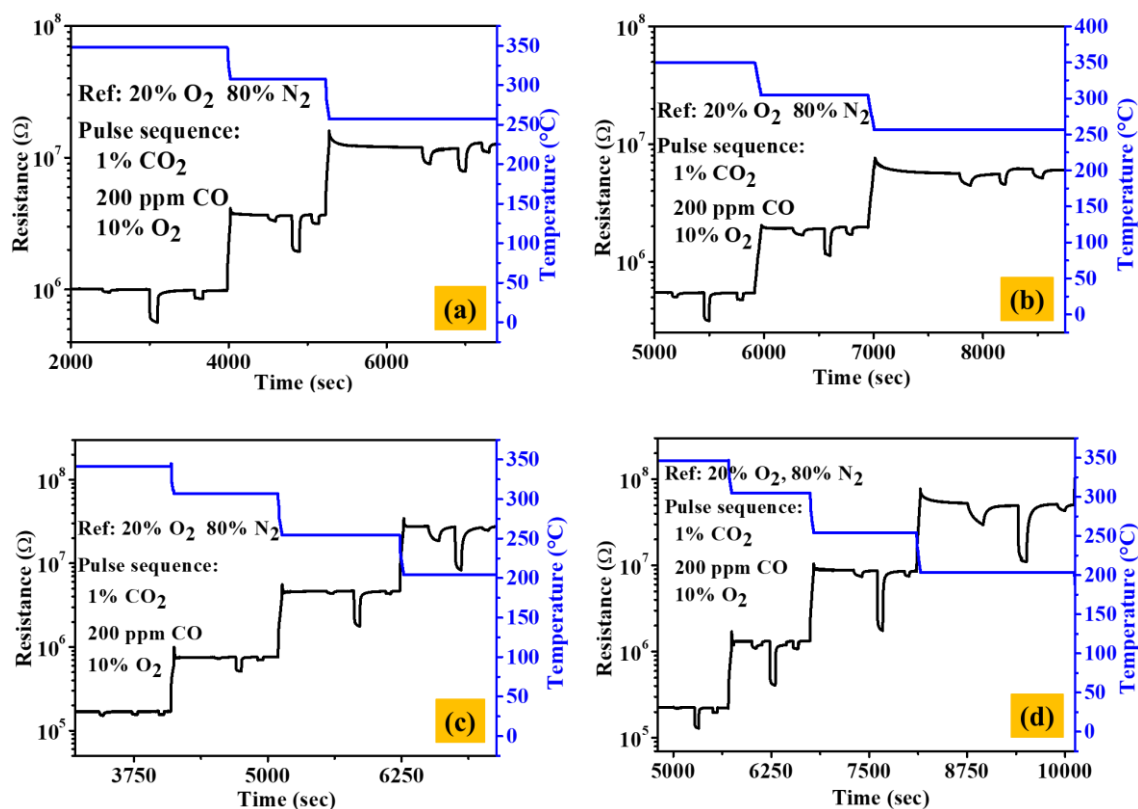


Figure 5.7. Dynamic responses of sensors: a) ZO; b) Sr8ZO; c) Ni10ZO; d) Ni5ZO.

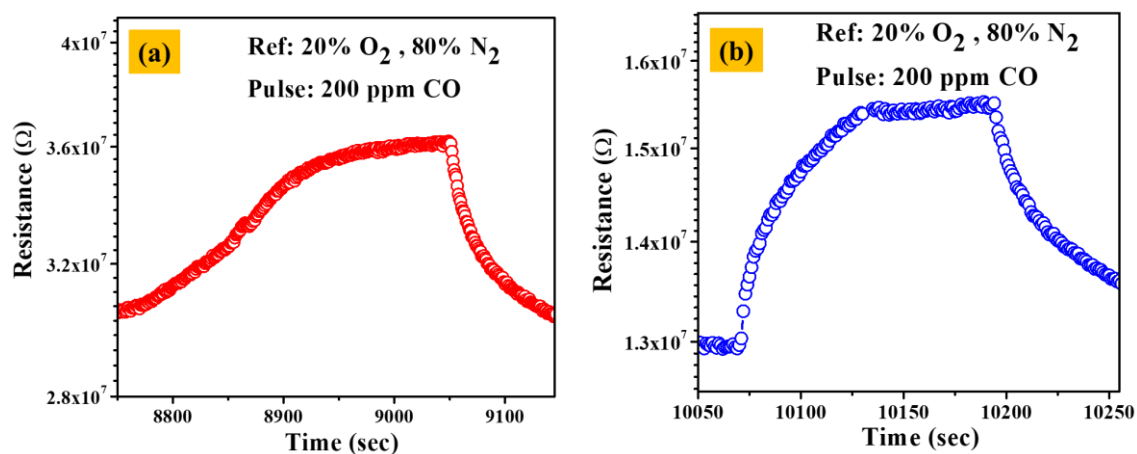
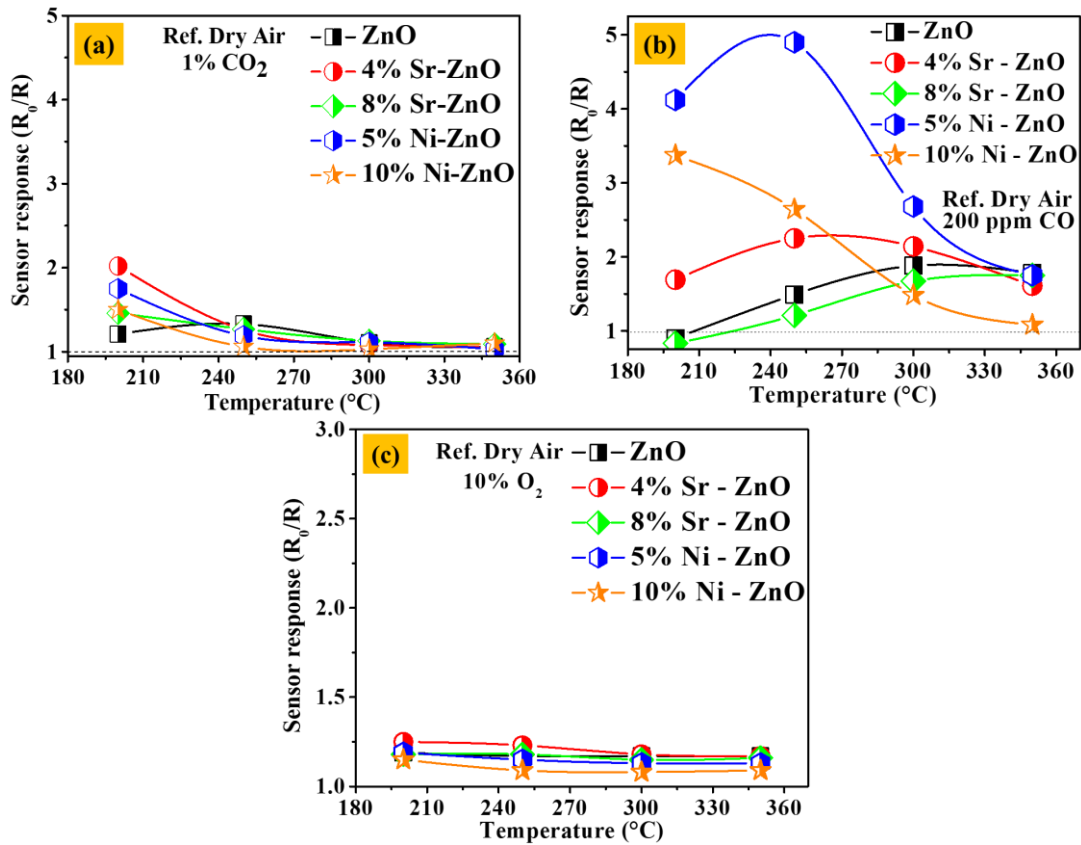


Figure 5.8. Dynamic responses of sensors (a) ZO and (b) Sr8ZO, to 200 ppm of CO at 200 °C.

Figure 5.9(a,b,c) summarizes the responses recorded at different temperatures for pure and doped sensors when exposed to 1% CO<sub>2</sub>, 200 ppm CO and 10% variation of O<sub>2</sub> concentration, respectively. At all temperatures, the sensors are little influenced by oxygen variation. For the two target gases, at temperature higher than 250°C, all sensors exhibit greater response to CO than CO<sub>2</sub>.



**Figure 5.9.** Sensor responses a) 1% CO<sub>2</sub>; b) 200 ppm CO; c) 10% O<sub>2</sub> at different temperatures.

Examining the trend of responses to target gases, it is observed that, for Ni-doped sensors, the response to CO is higher with respect the un-doped and Sr doped ZnO sensors and increase with decreasing the temperature. At the temperature of 200-250°C, their response is more than three times than that observed for the ZnO sensor. Hence, doping ZnO with Ni allows a remarkable enhancement of the gas sensing characteristics towards CO. Vice versa, Sr doped sensors display a CO sensing behaviour similar to un-doped ZnO sensor. In fact, as concerns CO gas, these sensors show a maximum of the response above 350°C, while a drastic loss of response is registered below 250°C. The possible reason for higher CO gas sensing response above 350°C is assumed to be due to higher thermal energy with increase in operating temperature which helps to overcome the activation energy barrier to the reaction and a significant increase in the electron concentration for the sensing reaction to happen [64]. It has been reported that the stable oxygen ions were O<sub>2</sub> below 100°C, O between 100°C and 300°C and O<sub>2</sub> above 300°C.

The relevant surface reactions can be listed as, [65]



Combining aforementioned facts and corresponding surface reactions, eqn. (5.8) turns out as most desirable for the gas sensing, because the reaction could release more number of electrons to follow a generalized sensing pattern and increase in the gas response. This is only possible when the operating temperature is maintained above 300°C but less than 400°C above which possibly degradation of doped ZnO causes decrease in CO response. In accordance to the equations it can also be explainable that the drastic loss of response for CO gas below 250°C is due to catalytic oxidation of CO by O<sub>2</sub> (eqn. (5.6)) [58]. Instead, the response to CO<sub>2</sub> is negligible at temperature higher than 250°C, and increases with decreasing the temperature. This opposite trend, indicates that Sr-doped ZnO sensors have the potential as CO<sub>2</sub> selective sensors at low operating temperatures. The dopant load has a great effect on the response against the tested gases. As shown in Figure 5.9, the 5% Ni-doped sensor shows higher response than the sample with higher Ni loading. This agrees with the reports of other authors. For example, Wang and co-workers [66] reported that the response to C<sub>2</sub>H<sub>2</sub> has been greatly enhanced by Ni-doping in ZnO at the optimal doping concentration of 5%. The samples with the excess Ni concentration deteriorate with worse response.

Ni 5% doped ZnO sensor is also tested at different low CO concentrations (5-80 ppm) at the best operating temperature of 250°C. The dynamic responses and related calibration curve of the sensor are reported in Figure 5.10(a). The sensor response, Figure 5.10(b) shows a linear behaviour in the log-log plot with CO concentration. The good response allows to reaching a lower detection limit of less than 2 ppm. The same finding has been observed for the CO<sub>2</sub>, being the Sr 4% doped ZnO sensor, with an intermediate loading of Sr, the most responsive. Figure 5.11(a) shows the dynamic response to pulses of different CO<sub>2</sub> concentration, in the range of 0.25-2% in volume, at a temperature of 250°C. In these operative conditions the sensor is able to detect CO<sub>2</sub> with fast dynamic response. The response of Sr 4% doped ZnO sensor to both gases at different temperatures

is also shown in Figure 5.11(c), evidencing as the selectivity towards  $\text{CO}_2$  for this sensor is maximized at the lower temperature tested ( $200^\circ\text{C}$ ).

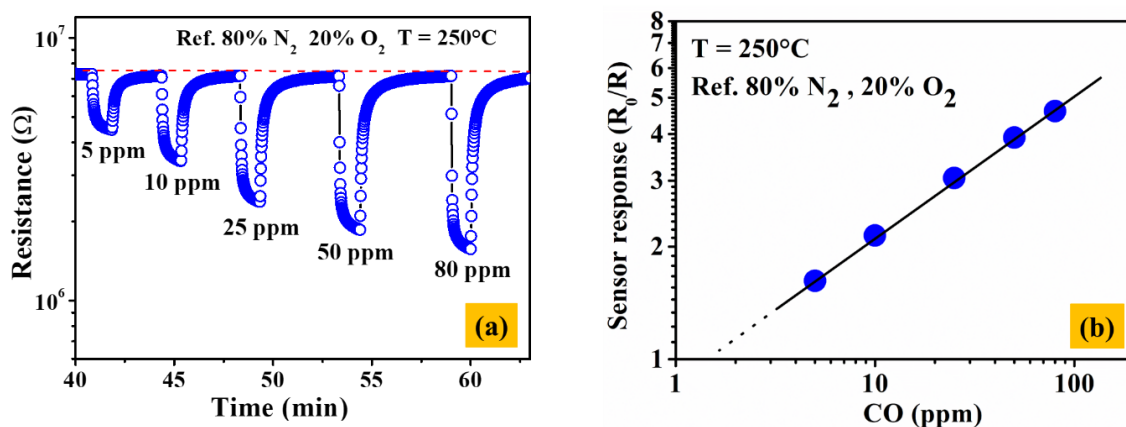


**Figure 5.10.** (a) Dynamic response towards different CO concentrations and (b) calibration curve at  $250^\circ\text{C}$  related to Ni5ZO sensor.

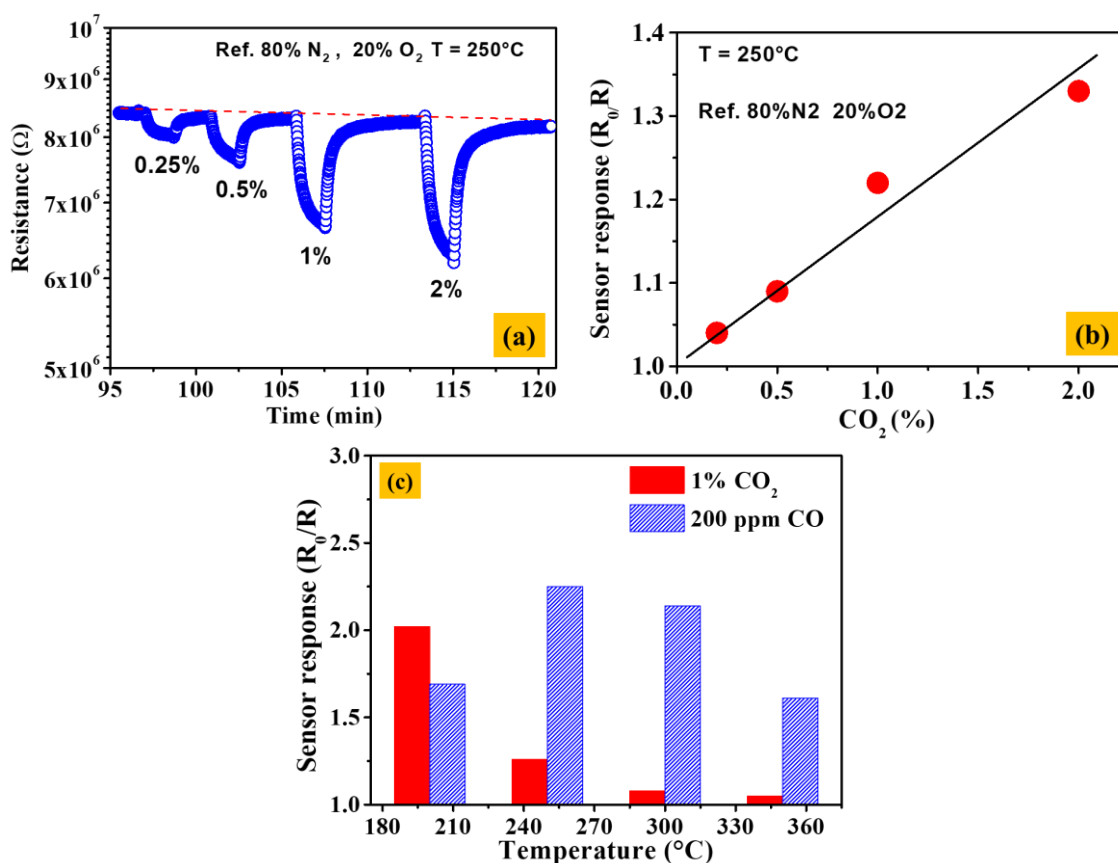


**Figure 5.11.** (a) Dynamic response towards different  $\text{CO}_2$  concentrations and (b) calibration curve at  $250^\circ\text{C}$  related to Sr4ZO sensor. c) Comparison of the response of Sr4ZO sensor to CO and  $\text{CO}_2$ , at different temperatures.

Overall results indicated that the Ni 5% doped ZnO sensor, operating at the temperature of 250°C, is highly sensitive to CO and inherently selective with respect to CO<sub>2</sub>. As regards the Sr 4% doped ZnO sensor, although decreasing the temperature, the response to CO decrease and that to CO<sub>2</sub> increases, we cannot achieve the required selectivity towards this latter specie. In this case, statistical and signal processing techniques are necessary, for example, developing adaptive searching algorithms to retrieve each gas concentrations with improved precision, training data set evaluated by the two-sensor array [67].

A comparison with the sensing performance of some recent CO sensors based on ZnO nanorods reported in the recent literature is shown in Table 5.4. It can be noted the higher response of our sensor compared to others where ZnO nanorods are doped with different dopants. The search has produced instead no literature data about CO<sub>2</sub> sensing using ZnO nanorods-based sensors.

**Table 5.4.** Comparison of ZnO nanorods-based CO sensors.

Sensing material	Temperature (°C)	CO (ppm)	Response (R <sub>a</sub> /R <sub>g</sub> )	Response/ppm × 100	Ref.
Ni-ZnO hexagonal plates	300	300	2.5	0.83	[68]
Co-ZnO electrodeposited nanorods Nanotubes	350	150	1.3	0.86	[69]
Au/ZnO nanorods	300	200	3	1.5	[70]
Al-ZnO nanorods	350	100	1.7	1.7	[71]
Ga-ZnO nanorods	75	200	1.1	0.55	[72]
CuO-ZnO nanorods	300	200	3.5	1.75	[73]
<b>Ni-ZnO nanorods</b>	<b>250</b>	<b>200</b>	<b>5</b>	<b>2.5</b>	<b>This work</b>

### Sensing response-samples characteristics relationships

The above reported results demonstrate that the gas sensing characteristics of Ni and Sr doped ZnO based sensors towards CO and CO<sub>2</sub> are remarkably enhanced compared to ZnO based one. Indeed, both Sr and Ni increase the response and also shift the maximum response at lower temperatures. An attempt is made to correlate this behaviour with the morphological and microstructural characteristics of the materials used as sensing layers. Characterization results give indication of the presence of a higher amount of crystal defects in the doped samples. The key role of crystal defects in gas sensing is highly accepted. Hu *et al.* proposed that the high sensing properties towards of transition metal doped ZnO nanorods are related to a higher content of donor related defects and a lower content of acceptor related defects, because the donors would provide electrons for the

adsorbed oxygen to produce the active ionosorbed oxygen [74]. PL data here (Chapter 4) reported show a decrease of  $I_{UV}/I_{green}$  PL peak ratio with increase of Sr- and Ni-loading, suggesting an increase of the concentration of oxygen vacancies, which can improve the sensing properties [75].

However, in our case, this factor cannot fully explain the decrease of response found on the Sr- and Ni-doped sensors with the higher dopant loading. This means that other factors, such as non-stoichiometry, lattice distortion and smaller grain size, are involved. On the basis of XRD characterization (Chapter 4) we can exclude the effects due to a decrease of particle size and to the formation of local  $p-n$  junction because in our case all  $Sr^{2+}$  and  $Ni^{2+}$  ions substitute the  $Zn^{2+}$  atoms in ZnO lattice and no SrO or NiO phase is found [48]. In order to account for a correlation between the surface area of nanostructure and the gas sensing properties, the surface area is calculated using Brunauer-Emmett-Teller (BET) technique as presented in Figure 5.12. The sensing characteristics reported for both Ni- and Sr-doped ZnO sensors do not correlate in any way with the surface area of the corresponding samples as summarized in Table 5.5.

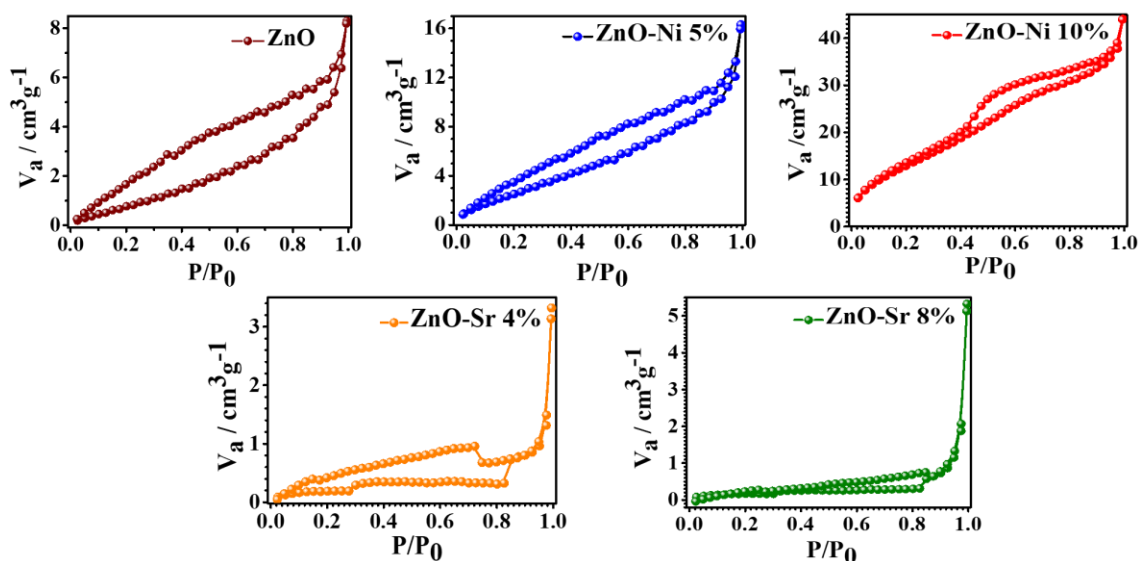


**Figure 5.12.**  $N_2$  adsorption/desorption isotherms of pure and doped ZnO (inset show the corresponding pore size distribution curve)

**Table 5.5.** Surface area values for the synthesized samples.

Sample	Surface Area ( $m^2/g$ )
ZnO	4.359
ZnO-Ni5%	12.029
ZnO-Ni10%	51.844
ZnO-Sr4%	0.729
ZnO-Sr8%	0.524

In case of CO response on Ni–ZnO sensors, a good correlation has been found taking into account the lattice distortion (Figure 5.13). Lattice distortion is advantageous for creating defects which are the sites for the interaction between test gas molecule and sensor surface [76].

For Sr-doped sensor, the decrease of operative temperature leads instead to a decrease of CO response and correspondingly to an enhancement of the response to CO<sub>2</sub>. As suggested by us for Ca-doped ZnO sensors, CO<sub>2</sub> sensing follows a mechanism relying on the adsorption of CO<sub>2</sub> on the sensing layer [77, 78]. On this basis, the CO<sub>2</sub> response enhancement for Sr doped ZnO could be related to the basicity of the dopant. In fact, as an acid molecule, the interaction of CO<sub>2</sub> with a solid material to form surface carbonates and hydroxyl carbonates is favoured if the surface basicity is increased. These intermediate species react subsequently with adsorbed oxygen species releasing electrons and consequently changing the resistance. Then, it seems that the improvement of the sensor response may be attributed to the higher adsorption of CO<sub>2</sub> provided by Sr-doped surface which is able to adsorb more strongly the acid CO<sub>2</sub> gas molecules compared to an un-doped and Ni-doped ZnO surface. On the basis of above report, these simply doped ZnO nanostructures are promising to be applied in electronic devices for monitoring indoor air quality.

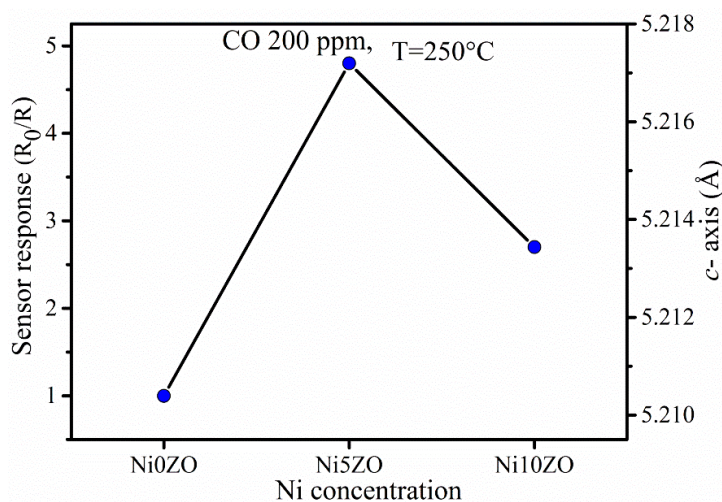


**Figure 5.13.** Sensor response as a function of lattice distortion for Ni-doped ZnO.

### 5.3. Summary

This chapter presents an investigation involving the physical properties of un-doped and doped ZnO nanostructures and demonstration of its unique properties for multifunctional

applications. We have explored the prepared ZnO nanostructures for magnetic, field emission, optical and gas sensing applications.

Initially, Ni doped ZnO nanostructures are directly utilized for magnetic application. The M-H plot displays the room temperature ferromagnetism and it enhances with increases in Ni concentration. The complementary studies on the material properties of Ni doped ZnO as discussed in chapter 4, suggests that the joint effects of the Ni ions as well as the intrinsic exchange interactions arising from the defect such as  $V_o^+$  assisted bound magnetic polarons are countable for RT-FM in  $Zn_{1-x}Ni_xO$  ( $0 \leq x \leq 0.125$ ) system. Second, the Ni doped ZnO nanostructures are realized for field emission applications. It has been observed that the Ni doping in ZnO decreases the turn-on field (from 2.5 to 1.7  $V \mu m^{-1}$ ) and the threshold field (from 2.8 to 2  $V \mu m^{-1}$ ), with a maximum current density of 872  $\mu A cm^{-2}$  at an applied field of 3.1  $V \mu m^{-1}$  for 10% Ni doped ZnO. Prolonged current stability was also observed for a period of 3 h at a preset value of 5  $\mu A$ . Third, we have investigated the role of Ni doping on the third order nonlinear optical properties of ZnO nanorods. It has been demonstrated that 10% Ni doping in ZnO nanorods enables a substantial enhancement of the two photon absorption coefficient ( $\beta$ ) as much as 14 times than that of the un-doped ZnO nanorods. The significant increase in  $\beta$  values is correlated with the reduction in bandgap energy by Ni doping, which is in accordance with the bandgap scaling. Further, we have also shown that the limiting threshold intensity decreases with doping, which makes this material an excellent optical limiter. Lastly, the gas sensing characteristics of the doped ZnO nanostructures are studied. We have developed chemo-resistive sensors with Sr and Ni doping in ZnO nanorods which acts as a sensing layer towards CO and CO<sub>2</sub> gases. The gas sensing properties are enhanced in Sr and Ni doped ZnO as compared to the un-doped ZnO based sensor. The enhanced CO response was attributed to the increased lattice distortion introduced by Ni which favours the interaction between CO gas molecules and the sensor surface. The CO<sub>2</sub> response enhancement for Sr doped ZnO could be instead related to the basicity of the dopant.

On all these notes, it can be concluded that this study opens a new insight into the physics of doped ZnO nanostructures to be applied in multifunctional ways. The effectiveness of such doped ZnO nanosystems serves as a potential candidate for various technologies particularly, optoelectronics, magneto-optical, flat panel displays and electron emitter devices.

**Reference**

- [1] Radzimska A. K., Jesionowski T. (2014), Zinc oxide-from synthesis to application: a review, *Materials*, 7, 2833-2881.
- [2] Gomez J. L., Tigli O. (2013), Zinc oxide nanostructures: from growth to application, *J. Mater Sci.* 48, 612-624.
- [3] Pan F., Song C., Liu X. J., Yang Y. C., Zeng F. (2008), Ferromagnetism and possible application in spintronics of transition-metal-doped ZnO films, *Mater. Sci. Eng. R: Rep.* 62, 1-35.
- [4] Meng-KeLi et al. (2007), Morphology and field emission from ZnO nanowire arrays synthesized at different temperature, *Mater. Sci. Eng.: A*, 452-453, 417-421.
- [5] Xu C. X., Sun X. W. (2003), Field emission from zinc oxide nanopins, *Appl. Phys. Lett.* 83, 3806.
- [6] Al-Harbi T. (2011), Hydrothermal synthesis and optical properties of Ni doped ZnO hexagonal nanodiscs, *J. Alloys Compd.* 509, 387-390.
- [7] Wolf S. A., Awschalom D. D., Buhrman R. A., Daughton J. M., Molnár S.V., Roukes M. L., Chtchelkanova A. Y., Treger D. M. (2001), Spintronics: A spin-based electronics vision for the future, *Science* 294, 1488-1495.
- [8] Pearton S. J., Abernathy C. R., Overberg M. E., Thaler G. T., Norton D. P., Theodoropoulou N., Hebard A. F., Park Y. D., Ren F., Kim J., Boatner L. A. (2003), Wide band gap ferromagnetic semiconductors and oxides, *J. Appl. Phys.* 93, 1-13.
- [9] Sarma S. D. (2001), Spintronics: A new class of device based on electron spin, rather than on charge, may yield the next generation of microelectronics, *Am. Sci.* 89, 516-523.
- [10] Dietl T., Ohno H., Matsukura F., Cibert J., Ferrand D. (2000), Zener model description of ferromagnetism in zinc-blende magnetic semiconductors, *Science* 287, 1019-1022.
- [11] Sato K., Yoshida H. K. (2000), Material design for transparent ferromagnets with zno-based magnetic semiconductors, *Jpn. J. Appl. Phys.* 39, L555-L558.
- [12] Sato K., Yoshida H. K. (2001), Material design of GaN-based ferromagnetic diluted magnetic semiconductors, *Jpn. J. Appl. Phys.* 40, L485-L487.

- [13] Samanta K., Bhattacharya P., Katiyar R. S. (2016), Optical properties of  $Zn_{1-x}Co_xO$  thin films grown on  $Al_2O_3(0001)$  substrates, *Appl. Phys. Lett.* 87, 101903.
- [14] Panigrahy B., Aslam M., Bahadur D. (2012), Effect of Fe doping concentration on optical and magnetic properties of ZnO nanorods, *Nanotechnology* 23, 115601.
- [15] Sans J. A., Sánchez-Royo J. F., Segura A., Tobias G., Canadel E. (2009), Chemical effects on the optical band-gap of heavily doped ZnO:MIII (M=Al, Ga, In): An investigation by means of photoelectron spectroscopy, optical measurements under pressure, and band structure calculations, *Phys. Rev. B: Condens. Matter Mater. Phys.* 79, 195105.
- [16] Kumar S., Mukherjee S., Singh R. K., Chatterjee S., Ghosh A. K. (2011), Structural and optical properties of sol-gel derived nanocrystalline Fe-doped ZnO, *J. Appl. Phys.* 110, 103508.
- [17] Schwartz D. A., Kittilstved K. R., Gamelin D. R. (2004), Above-room-temperature ferromagnetic  $Ni^{2+}$  doped ZnO thin films prepared from colloidal diluted magnetic semiconductor quantum dots, *Appl. Phys. Lett.* 85, 1395-1397.
- [18] Cong C. J., Hong J. H., Liu Q. Y., Liao L., Zhang K. L. (2006), Synthesis, structure and ferromagnetic properties of Ni-doped ZnO nanoparticles, *Solid State Commun.* 138, 511-515.
- [19] Wakano T., Fujimura N., Morinaga Y., Abe N., Ashida A., Ito T. (2001), Magnetic and magneto-transport properties of ZnO:Ni films, *Physics E* 10, 260-264.
- [20] Ueda K., Tabata H., Kawai T. (2001), Magnetic and electric properties of transition-metal-doped ZnO films, *Appl. Phys. Lett.* 79, 988-990.
- [21] Yin Z., Chen N., Yang F., Song S., Chai C., Zhong J., Qian H., Ibrahim K. (2005), Structural, magnetic properties and photoemission study of Ni-doped ZnO, *Solid State Commun.* 135, 430-433.
- [22] Coey J. M., Venkatesan M., Fitzgerald C. B. (2005), Donor impurity band exchange in dilute ferromagnetic oxides, *Nat. Mater.* 4, 173.
- [23] Kaminski A., Sarma S. D. (2002), Polaron percolation in diluted magnetic semiconductors, *Phys. Rev. Lett.* 88, 247202.

- [24] Sarma S. D., Hwang E. H., Kaminski A. (2003), Temperature-dependent magnetization in diluted magnetic semiconductors, *Phys. Rev. B: Condens. Matter Mater. Phys.* 67, 155201.
- [25] Fancher C. A. *et al.* (1998), Zinc oxide and its anion: A negative ion photoelectron spectroscopic study, *J. Chem. Phys.* 109, 8426-8429.
- [26] Ahmad M., Sun H., Zhu J. (2011), Enhanced photoluminescence and field-emission behavior of vertically well aligned arrays of In-doped ZnO nanowires, *ACS Appl. Mater. Interfaces*, 3, 1299-1305.
- [27] Farid *et al.* (2010), Electrochemical synthesis of Cu/ZnO nanocomposite films and their efficient field emission behaviour, *Appl. Surf. Sci.* 256, 2110-2114.
- [28] Chang Y.-C. (2014), Ni-doped ZnO nanotower arrays with enhanced optical and field emission properties, *RSC Adv.* 4, 56241-56247.
- [29] Xing *et al.* (2010), Ultrathin single-crystal ZnO nanobelts: Ag-catalyzed growth and field emission property, *Nanotechnology* 21, 255701.
- [30] Forbes R. G. (2008), On the need for a tunneling pre-factor in Fowler–Nordheim tunneling theory, *J. Appl. Phys.* 103, 114911.
- [31] Forbes R. G. (2006), Simple good approximations for the special elliptic functions in standard Fowler-Nordheim tunneling theory for a Schottky-Nordheim barrier, *Appl. Phys. Lett.* 89, 113122.
- [32] Pantha B. N., Sedhain A., Li J., Lin J. Y., Jiang H. X. (2010), Probing the relationship between structural and optical properties of Si-doped AlN, *Appl. Phys. Lett.* 96, 131906.
- [33] Katayama-Yoshida H., Sato K. (2003), Materials design for semiconductor spintronics by ab initio electronic-structure calculation, *Phys. B* 327, 337-343.
- [34] Zhao Q. *et al.* (2005), Morphological effects on the field emission of ZnO nanorod arrays, *Appl. Phys. Lett.* 86, 203115.
- [35] Lee C. J. *et al.* (2002), Atomic oxygen surface loss coefficient measurements in a capacitive/inductive radio-frequency plasma *Appl. Phys. Lett.* 81, 19.
- [36] Chang L. W. *et al.* (2011), Field emission and optical properties of Ga-doped ZnO nanowires synthesized via thermal evaporation, *Appl. Surf. Sci.* 257, 3145-3151.

- [37] Ahmad M., Sun H., Zhu J. (2011), Enhanced photoluminescence and field-emission behavior of vertically well aligned arrays of In-Doped ZnO nanowires, *ACS Appl. Mater. Interfaces*, 3, 1299-1304.
- [38] Gautam U. K. *et al.* (2009), Solvothermal synthesis, cathodoluminescence, and field-emission properties of pure and N-doped ZnO nanobullets, *Adv. Funct. Mater.* 19, 131-140.
- [39] Ahsanulhaq Q., Kim J. H., Hahn Y. B. (2007), Controlled selective growth of ZnO nanorod arrays and their field emission properties, *Nanotechnology* 18, 485307.
- [40] Hwang J. Ok *et al.* (2011), Vertical ZnO nanowires/graphene hybrids for transparent and flexible field emission, *J. Mater. Chem.* 21, 3432-3437.
- [41] Sun L., Lin Z., Zhou X., Zhang Y. Guo T. (2016), Synthesis of Cu-doped ZnO quantum dots and their applications in field emission, *J. Alloys Compd.* 671, 473-478.
- [42] Morkoc H., Ozgur U. (2009), Zinc oxide: Fundamentals, materials and device technology, Wiley-VCH Verlag GmbH & Co. KGaA, Weinheim, doi: 10.1002/9783527623945.
- [43] Zhang C., Zhang F., Xia T., Kumar N., Hahn J.-I., Liu J., Wang Z. L., Xu J. (2009), Low-threshold two-photon pumped ZnO nanowire lasers, *Opt. Express* 17, 7893-7900.
- [44] Sheik-Bahae M., Hutchings D., Hagan D. J., Van Stryland E. W. (1990), Sensitive measurement of optical nonlinearities using a single beam, *IEEE J. Quantum Electron.* 26, 760-769.
- [45] Van Stryland E. W., Woodall M. A., Vanherzeele H., Soileau M. J. (1985) Energy band-gap dependence of two-photon absorption, *Opt. Lett.* 10, 490-492.
- [46] Rajeh S., Mhamdi A., Khirouni K., Amlouk M., Guermazi S. (2015), Experiments on ZnO:Ni thin films with under 1% nickel content, *Opt. Laser Technol.* 69, 113-121.
- [47] Hanamura E. (1988), Very large optical nonlinearity of semiconductor microcrystallites, *Phys. Rev. B* 37, 1273-1279.
- [48] Sharma D., Malik B. P., Gaur A. (2015), Two and four photon absorption and nonlinear refraction in undoped, chromium doped and copper doped ZnS quantum dots, *J. Phys. Chem. Solids* 87, 163-170.

- [49] O'Flaherty S. M., Murphy R., Hold S. V., Cadek M., Coleman J. N., Blau W. J. (2003), Material investigation and optical limiting properties of carbon nanotube and nanoparticle dispersions, *J. Phys. Chem. B* 107, 958-964.
- [50] Feng M., Zhan H., Chen Y. (2010), Nonlinear optical and optical limiting properties of graphene families, *Appl. Phys. Lett.* 96, 033107.
- [51] Gan Y., Feng M., Zhan H. (2014), Enhanced optical limiting effects of graphene materials in polyimide, *Appl. Phys. Lett.* 104, 171105.
- [52] Sun Y.-F., Liu S.-B., Meng F.-L., Liu J.-Y., Jin Z., Kong L.-T., Liu J.-H. (2012), Metal oxide nanostructures and their gas sensing properties: A review, *Sensors* 12, 2610-2631.
- [53] Korotcenkov G. (2008), The role of morphology and crystallographic structure of metal oxides in response of conductometric-type gas sensors, *Mater. Sci. Eng. R Rep.* 61, 1-39.
- [54] Rambu A. P., Ursu L., Iftimie N., Nica V., Dobromir M., Iacomi F. (2013), Study on Ni-doped ZnO films as gas sensors, *Appl. Surf. Sci.* 3, 280, 598-604.
- [55] Ganbavle V. V., Inamdar S. I., Agawane G. L., Kim J. H., Rajpure K. Y. (2016), Synthesis of fast response, highly sensitive and selective Ni:ZnO based NO<sub>2</sub> sensor, *Chem. Eng. J.* 286, 36-47.
- [56] Bai Z., Xie C., Hu M., Zhang S. (2008), Formaldehyde sensor based on Ni-doped tetrapod-shaped ZnO nanopowder induced by external magnetic field, *Physica E*, 41, 235-239.
- [57] Woo H.-S., Kwak C.-H., Chung J.-H., Lee J.-H. (2015), Highly selective and sensitive xylene sensors using Ni-doped branched ZnO nanowire networks, *Sens. Actuators B* 216, 358-366.
- [58] Xu M., Li Q., Ma Y., Fan H. (2014), Ni-doped ZnO nanorods gas sensor: Enhanced gas-sensing properties, AC and DC electrical behaviors, *Sens. Actuators B* 199, 403-409.
- [59] Vijayan T. A., Chandramohan R., Valanarasu S., Thirumalai J., Subramanian S. P. (2008), Comparative investigation on nanocrystal structure, optical, and electrical properties of ZnO and Sr-doped ZnO thin films using chemical bath deposition method, *J. Mater. Sci.* 43, 1776-1782.

- [60] Neri G., Bonavita A., Micali G., Rizzo G., Callone E., Carturan G. (2008), Resistive CO gas sensors based on  $\text{In}_2\text{O}_3$  and  $\text{InSnO}_x$  nanopowders synthesized via starch-aided sol-gel process for automotive applications, *Sens. Actuators, B* 132, 224-233.
- [61] ASTM D6245, (1998), Standard Guide for Using Indoor Carbon Dioxide Concentrations to Evaluate Indoor Air Quality and Ventilation, 22, pp. 05.
- [62] Hahn S. H., Barsan N., Weimar U., Ejakov S. G., Visser J. H., Soltis R. E. (2003), CO sensing with  $\text{SnO}_2$  thick film sensors: role of oxygen and water vapour, *Thin Solid Films* 436, 17-24.
- [63] Kishimoto S., Akamatsu S., Song H., Nomoto J., Makino H., Yamamoto T. (2014), Carbon monoxide gas sensing properties of Ga-doped ZnO film grown by ion plating with DC arc discharge, *J. Sens. Sens. Syst.* 3, 331-334.
- [64] Gong H., Hu J. Q., Wang J. H., Ong C. H., Zhu F. R. (2006), Nano-crystalline Cu-doped ZnO thin film gas sensor for CO, *Sens. Actuators B* 115, 247-251.
- [65] Takata M., Tsubone D., Yanagida H. (1976), Dependence of electrical conductivity of ZnO on degree of sintering, *J. Am. Ceram. Soc.* 59, 4-8.
- [66] Wang X., Zhao M., Liu F., Jia J., Li X., Cao L. (2013),  $\text{C}_2\text{H}_2$  gas sensor based on Ni-doped ZnO electrospun nanofibers, *Ceram. Int.* 39, 2883-2887.
- [67] Frank M. L., Fulkerson M. D., Patton B. R., Dutta P. K. (2002),  $\text{TiO}_2$ -based sensor arrays modeled with nonlinear regression analysis for simultaneously determining CO and  $\text{O}_2$  concentrations at high temperatures, *Sens. Actuators, B* 87, 471-479.
- [68] Darvishnejad M. H., Firooz A. A., Beheshtian J., Khodadadi A. A. (2016), Highly sensitive and selective ethanol and acetone gas sensors by adding some dopants (Mn, Fe, Co, Ni) onto hexagonal ZnO plates, *RSC Adv.* 6, 7838-7845.
- [69] Li Y.-J., Li K.-M., Wang C.-Y., Kuo C.-I., Chen L.-J. (2012), Low-temperature electrodeposited Co-doped ZnO nanorods with enhanced ethanol and CO sensing properties, *Sens. Actuators B* 161, 734-739.
- [70] Rai P., Kim Y.-S., Song H.-M., Song M.-K., Yu Y.-T. (2012), The role of gold catalyst on the sensing behavior of ZnO nanorods for CO and  $\text{NO}_2$  gases, *Sens. Actuators B* 165, 133-142.

- [71] Lim S. K., Hong S. H., Hwang S.-H., Choi W. M., Kim S., Park H., Jeong M. G. J. (2015), Synthesis of Al-doped ZnO nanorods via microemulsion method and their application as a CO gas sensor, *Mater. Sci. Technol.* 31, 639-644.
- [72] Phan D. T., Chung G.-S., (2012), CO Gas sensing using Ga doping ZnO nanorods by hydrothermal method: Effects of defects-controlled, *IMCS 2012 – 14th International Meeting on Chemical Sensors, 2012*, pp. 1070-1073 doi:10.5162/IMCS2012/P1.7.6.
- [73] Rai P., Jeon S.-H., Lee C.-H., Lee J.-H., Yu Y.-T. (2014), Functionalization of ZnO nanorods by CuO nanospikes for gas sensor applications, *RSC Adv.* 4, 23604-23609.
- [74] Hu P., Han N., Zhang D., Ho J. C., Chen Y. (2012), Highly formaldehyde-sensitive, transition-metal doped ZnO nanorods prepared by plasma-enhanced chemical vapor deposition, *Sensors and Actuators B: Chemical* 169, 74-80.
- [75] Phan D. T., Chung G.-S. (2013), Effects of defects in Ga-doped ZnO nanorods formed by a hydrothermal method on CO sensing properties, *Sensors and Actuators B: Chemical* 187, 191-197.
- [76] Kapse V. D., Ghosh S. A., Chaudhari G. N., Raghuwanshi F. C., Gulwade D. D. (2008), H<sub>2</sub>S sensing properties of La-doped nanocrystalline In<sub>2</sub>O<sub>3</sub>, *Vacuum*, 83, 346-352.
- [77] Dhahri R., Hjiri M., Mir L. El, Fazio E., Neri F., Barreca F., Donato N., Bonavita A., Leonardi S. G., Neri G. (2015), ZnO:Ca nanopowders with enhanced CO<sub>2</sub> sensing properties, *J. Phys. D: Appl. Phys.* 48, 255503.
- [78] Dhahri R., Leonardi S. G., Hjiri M., Mir L. El, Bonavita A., Donato N., Iannazzo D., Neri G. Enhanced performance of novel calcium/aluminum co-doped zinc oxide for CO<sub>2</sub> sensors, *Sensors and Actuators B: Chemical* 239, 36-44.

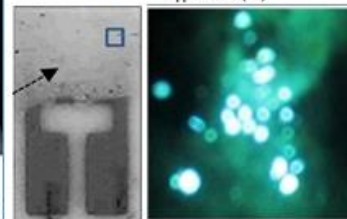
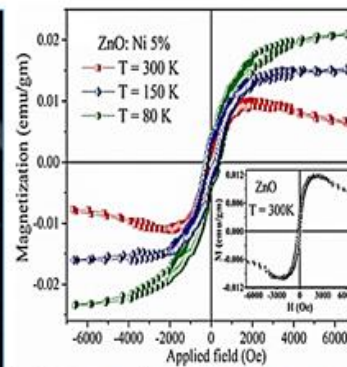


# CHAPTER 6

## Conclusion and Scope of Future Work



**MORPHOLOGY**



**APPLICATIONS**



# 6

---

---

## The Conclusion and Scope of Future Work

*The core basis of this thesis is to synthesize various nanostructures of zinc oxide (ZnO) for their potential application in multifunctional applications. Prominence is given to a comprehensive synthetic route based on a wet chemical method for its exploration in synthesizing ZnO nanostructured materials and understanding the fundamentals of their growth processes. Efforts have also been made by adopting two diverse geometries of ZnO nanostructures by doping with strontium (Sr) and nickel (Ni) to realize highly efficient and stable materials for magnetic, field emission, optical and gas sensors application.*

## 6.1. Thesis summary

A brief review of nanostructured materials, inorganic metal oxides: ZnO and diverse applications of ZnO are discussed in *Chapter 1*.

As stated in the introduction part (*Chapter 1*), there are a number of real and practical challenges surrounding the inorganic metal oxides which were difficult to overcome. However, progressive and excellent research have shown gradual improvement in device performance as reported by many scientists. But the biggest challenge of understanding the fundamentals of the growth mechanism of ZnO nanostructures are still far from accomplished. Therefore, this thesis took the opportunity to present a comprehensive approach to fabricate various nanostructures of ZnO with enhanced performance and to understand the material chemistry and to realize it for multifunctional applications.

*Chapter 2* describes the main experimental techniques that are employed in this thesis related to the material/device fabrication and characterization.

In *Chapter 3*, the synthesis and growth of the ZnO nanostructures are discussed. Here we have shown how to regulate the process parameters of chemical bath deposition (CBD) such as pH, concentration, time, and temperature, for controlling the morphology of ZnO and we also observed that the basic physical properties of ZnO are highly dependent upon the morphology of ZnO nanostructure. We have shown the controlled growth of ZnO nanostructures such as nanoneedles/flower, nanorods, nanotubes. The change in morphology is very helpful for constructing the possible growth mechanisms, for instances, the layer by layer and screw dislocation mechanism of ZnO nanostructure. We have also investigated the optical properties of ZnO which again depend on the morphology of the ZnO nanostructures, which is of prime importance for searching possible applications in the field of optoelectronics, sensors, *etc.*

In *Chapter 4*, the effect of doping on ZnO nanostructures is studied. The study conducted in chapter 3 for controlled growth of ZnO nanostructures encourage us to see the effect of doping on the structural, morphological, and optical properties. We have studied Sr- and Ni-doping in ZnO nanostructure and understood the effect on fundamental physical properties. The successful doping of large ionic radii Sr compare to Zn is confirmed using SIMS and XPS analysis that enables for further possible application of Sr-doped ZnO nanostructure. Furthermore, to study the origin of magnetic behaviour of

pure and Ni-doped ZnO nanostructures are reported. Through EXAFS, PL, UV and Raman spectroscopic analysis, we conclude that bound magnetic polaron is accountable for ferromagnetism in the ZnO nanostructure.

Lastly, in *Chapter 5*, the as synthesized un-doped and doped ZnO nanostructures are explored for multifunctional applications. The study of physical properties discussed chapter 4 on the effect of Ni- and Sr-doping in ZnO led us to show the possible application in the field of magnetic, field emission, two photon absorption and gas sensing. Started with magnetic nature, Ni-doped ZnO sample enhances the magnetic properties at room temperature, which is very helpful for future spintronic application of ZnO. As Ni doped ZnO shows the good enhancement in optical properties, which directly reflects in the field emission. Ni-doping enhances the field emission properties that make Ni-doped ZnO for cost-effective electron sources. Furthermore, the optical studies also encourage us to study the two photon absorption. Again with Ni doped ZnO, the two photon absorption coefficient increase by 14 times, *i.e.*,  $7.6 \pm 0.4$  to  $112 \pm 6$  cm/GW, when the Ni doping is increased from 0% to 10%. Here we predict that the strong nonlinear optical properties together with their dilute magnetic effects, they provide an important class of materials for potential applications in magneto-optical and integrated optical chips. Finally, the effect of Sr- and Ni-doping on the sensing properties of ZnO nanorods has been investigated especially toward CO and CO<sub>2</sub>. The effect of the operating temperature, nature and loading of the dopant on the sensibility and selectivity of the fabricated sensors towards these two harmful gases are also accounted. The gas sensing characteristics of Ni- and Sr-doped ZnO based sensors showed a remarkable enhancement (*i.e.* the response increased and shifted towards a lower temperature for both gases) compared to the pure ZnO, demonstrating that these ZnO nanostructures are promising for the fabrication of sensor devices for monitoring indoor air quality.

Overall, it is concluded that the controlled growth of ZnO nanostructures is very crucial for repeatable production of diverse prototypes with stable characteristics. The means to grow ZnO nanostructures in predefined sites with the most favourable morphology is of great importance for the scientific community. It is true that the robust control and reproducibility of the nanostructures can be achieved by vapour phase methods, however, the wet chemical methods are more suitable due to their low cost and great potential for scalability and compatibility. Several key aspects are addressed in the

present work. Firstly, the controlled growth of ZnO nanostructures by a simple wet chemical approach is discussed in details followed by understanding the nanostructure growth mechanism. Secondly, the effect of doping on ZnO nanostructures is highlighted for improving the structural, optical, vibrational and morphological properties. Finally, the growth of ZnO nanostructures are realized in multifunctional applications including magnetic, field emission, optical and gas sensing.

Thus, the verdict of the present study is a decent contribution in the inorganic semiconductor metal oxides. This study also fulfills the main objectives of the thesis and also the thesis title is quite well justified.

## **6.2. Outlook and Future Prospects**

Integrating the benefits from literature and different aspects of the present study, diverse proposals for future work are in line. A few among them are presented briefly:

Zinc oxide nanostructure's promising future is dependent on achieving *p*-type ZnO, which is still obstructing and most difficult to grow. This is beneficial to extend its application in the different field of optoelectronics. As we have shown, ZnO stands as a good candidate in providing electronic, photonic, and spin-based devices. However, there are a number of important issues related to its stability and reproducibility that are needed to be addressed by further research to form *p*-type ZnO for its commercialization.

As ZnO shows good biocompatibility and low cost, therefore it has shown recent exciting progress in the field of biomedical applications. This opens up the opportunity to use these nanostructure presented in this thesis in the field bio-sensing and drug delivery applications.

Besides this, with the help of the adopted growth method, the growth of nanobelts and alike nanostructure that are likely to have a significant impact on applications like nano-size optoelectronic devices, optical, sensors, and photodetector. Furthermore, for gas sensing application we have to explore these nanostructure for other harmful gases such as ammonia, sulphur dioxide, *etc.* with room temperature sensing, with high sensitivity and selectivity.

As the field of nano devices is nurturing, it becomes increasingly necessary to unravel the underlying working mechanisms of the material/device from both experimental and theoretical aspects. Therefore, there is an immediate need for a deeper

understanding of the fundamental mechanisms of the nanostructures before going for direct design.